Characterising ATP13A3 biological function and its role in pulmonary arterial hypertension

Bin Liu

St Catharine's College

August, 2020

The thesis is submitted for the degree of Doctor of Philosophy

Preface

This thesis is the result of my own work and includes nothing which is the outcome of work done in collaboration except specifically indicated in the text.
It is not substantially the same as any work that has already been submitted before for any degree or other qualification.
It does not exceed the word limit specified by the Faculties of Clinical and Veterinary Medicine Degree Committee.

Characterising ATP13A3 biological function and its role in pulmonary arterial hypertension

Bin Liu

Abstract

Pulmonary arterial hypertension (PAH) is a rare but devastating disease characterised by the progressive remodelling of the small pulmonary vessels. Although the causes may vary, similar pathobiological features are shared among different forms of PAH, with endothelial dysfunction, the hyperproliferation of smooth muscle cells and mesenchymal cells in the vascular wall, as well as inflammation contributing to this process. Despite the availability of licensed therapies, 5-year survival for patients remains less than 60%. To uncover additional fundamental mechanisms of PAH pathobiology, our group undertook whole genome sequencing in 1038 idiopathic or heritable PAH patients and identified disease-associated heterozygous mutations in *ATP13A3*, a P5B-type ATPase. P5 ATPases, namely ATP13A1-5, are putative transmembrane proteins that generate and maintain significant chemical gradients across biological membranes by active transport of cations. However, to date, studies of their functions are sparse. Therefore, the focus of my project was to characterise ATP13A3 in the pulmonary vasculature and to uncover the underlying mechanism of how mutations in this gene contribute to PAH pathogenesis.

Although the biological functions of ATP13A3 are elusive, its homologue *(CATP-5) in C. elegans* was previously reported as a polyamine transporter. Polyamines are a group of naturally existing polycations essential for many cellular processes. Therefore, my working hypothesis was that ATP13A3 loss of function might disrupt the polyamine homeostasis and hence contribute to the abnormal vascular remodelling in PAH. To address this, I first confirmed ATP13A3 as residing in the recycling endosome of endothelial cells. This

localisation of ATP13A3 suggested it might be related to polyamine transport since the endocytic pathway was recognised as a crucial route for polyamine trafficking. To expand this finding, I developed molecular tools to knockdown or to overexpress ATP13A3 in vascular cells and analysed how these affected polyamine transport. This led to the discovery of putrescine as the preferred substrate for ATP13A3 and also revealed a basal reduction of other polyamines in endothelial cells.

Further investigation highlighted an essential role of ATP13A3 in pulmonary vasculature with its deficiency restrained cell growth and predisposed endothelial cells to apoptosis. To validate these findings, blood outgrowth endothelial cells (BOECs) were isolated from a PAH patient bearing an ATP13A3 frameshift mutation (LK726X). Intriguingly, *ATP13A3*^{LK726X}, by causing ATP13A3 reduction, impaired polyamine uptake and induced apoptosis in BOECs. This provides the first evidence for the pathogenic effects of a PAH associated ATP13A3 mutation. In addition, using a lentiviral overexpression system, I also demonstrated impairments of other PAH-associated mutations on ATP13A3 mediated polyamine uptake, reinforcing the involvement of ATP13A3 in PAH pathobiology. To explore whether *ATP13A3* mutations can cause PAH, our laboratory has generated a mouse model harbouring a human *ATP13A3* mutation (P452Lfs) via the MRC Harwell Gene editing service. My colleague, Dr Ekaterina Legchenko and I have discovered that the *Atp13a3*$^{P452Lfs/P452Lfs}$ mice spontaneously develop PAH-like hemodynamic changes at 6-months of age. Preliminary data also revealed lower *Atp13a3* level and reduced polyamine content in the lungs of the mutant mice, suggesting that *Atp13a3* frameshift mutation (P452L) may contribute to PAH pathogenesis via the disruption of polyamine homeostasis in vivo.

In conclusion, my work characterises for the first time that ATP13A3 is a polyamine transporter in vascular cells with putrescine as its preferable transport substrate. *ATP13A3* mutations identified from PAH patients are highly likely to impair polyamine homeostasis and contribute to PAH progression.

These findings open up a new field for investigating PAH pathobiology and also highlight the potential role of rebalancing polyamine homeostasis in PAH treatment.

Acknowledgements

First and foremost, I would like to express my deepest gratitude to Prof. Nick Morrell and Dr. Paul Upton, for their considerate support and expert supervision for the design, execution and data analysis of my PhD project. Thank you very much Paul- you have been a great mentor, your attitudes towards science-precision, coherence and “well-planned” will be a great resource for the scientific career ahead of me. Great thanks to you Nick-you’ve been a fantastic supervisor, supportive whenever and wherever you can. Your sharp vision and practical advice have guaranteed me on the right track. The joint supervision from both of you is the most beneficial experience a PhD student could have ever asked for.

A massive thank you to all of the Morrell group members, especially the “cupboard crew”- Jenny, Josh, Joy, Emily and Iona, for covering cell feeding, for invitations to dinners and drinking, you are the best! Also, to Dr. Wei Li’s group-Jason, Zhen, Dong and Wei, thank you very much for your time as lunch companions and also your suggestions from a structural biology perspective. A specific appreciation to the “stem cell crew”- Moo for your passionate talks and supervision for the generation of the iPsc lines, Fedir and C-Hong for your patience about the troubleshooting, Baraa and Chris for your help on the cell maintenance. Moreover, a big thank you to Stefan and the bioinformatics group, without whom there might not be a project on ATP13A3. Last but not least, thank you Dr. Benjamin Dunmore for your valuable advice on tissue culture and Dr. Ekaterina Legchenko for your help on the in vivo study.

I would also like to take this opportunity to express my gratitude to the people outside of the Lab. A huge thank you to Professor Peter Vangheluwe and your group for your priceless inputs in my project and all the valuable reagents. Also,

a massive thank you to Dr. James West, who has performed extensive method development for the measurement of polyamines in cells. Furthermore, I would like to express my gratefulness to the funding body-Cambridge Trust and the China scholarship council-your generous support has been the greatest guarantee for my PhD study.

Finally, I would like to acknowledge my family for their loving support with the deepest gratitude goes to my girlfriend Yaqiong Liu. You have been the best partner, tolerating my immatureness and offering your love. Cannot even imagine my PhD journey without you.

Table of Contents

List of Abbreviation

AA	Amino acids
Ab	Antibody
ABCC8	ATP-binding cassette transporter sub-family C member 8
ACTB	Actin Beta
ACVRL1	Activin A Receptor Like Type 1
ALK	Activin receptor-like kinase
AMD1	Adenosylmethionine Decarboxylase 1
AQP1	Aquaporin 1
ARG1	Arginase 1
ATP13A1-5	Probable Cation-Transporting ATPase 13A1-5
AZIN1	Antizyme Inhibitor 1
B2M	Beta-2-microglobulin
BOEC	Blood outgrowth endothelial cell
BMP	Bone morphogenetic protein
BMPR2	Bone morphogenetic protein receptor type2
CAV1	Caveolin
CAD	Cadaverine
cDNA	Complimentary DNA
C. elegans	*Caenorhabditis elegans*
CDK	Cyclin-dependent Kinase
DMEM	Dulbecco's modified eagle medium
DFMO	2-difluoromethylornithine
EC	Endothelial cells
E. coli	*Escherichia Coli*
EGF	Epidermal Growth Factor
EGM	Endothelial growth medium
eIF5A	eukaryotic initiation factor 5A

EIF2AK4	Eukaryotic Translation Initiation Factor 2 Alpha Kinase 4
ENG	Endoglin
FBS	Foetal bovine serum
GDF2	Growth differentiation factor 2
gDNA	Genomic DNA
GFP	Green fluorescent protein
GWAS	Genome-wide associated study
HIF	Hypoxia induced factor
HMEC-1	Human Microvascular Endothelial Cell-1
hPAEC	Human pulmonary artery endothelial cell
hPASMC	Human pulmonary artery smooth muscle cell
HPRT	Hypoxanthine Phosphoribosyl transferase
HRP	Horse radish peroxidase
ID	Inhibitor of DNA binding/inhibitor of differentiation
IFN	Interferon
IL	Interleukin
IRES	Internal ribosome entry site
KCNK3	Potassium Two Pore Domain Channel Subfamily K Member 3
KD	Kilodalton
LB broth	Luria-Bertani broth
MCT	monocrotaline
mPAP	Mean pulmonary arterial pressure
mRNA	Messenger RNA
OAZ	Ornithine antizyme
ODC	Ornithine decarboxylase
ORF	Open reading frame
PAGE	Polyacrylamide gel electrophoresis
PAH	Pulmonary arterial hypertension
PAO	Polyamine oxidase

PBS	Phosphate buffered saline
PCR	Polymerase chain reaction
PDGF	Platelet-derived growth factor
PTS	Polyamine transport system
PUT	Putrescine
PVDF	Polyvinylidene difluoride
PVOD	Pulmonary veno-occlusive disease
qPCR	Quantitative real-time polymerase chain reaction
RIPA	Radioimmunoprecipitation assay
ROCK	Rho-associated, coiled-coil containing protein kinase
RVH	Right ventricular hypertrophy
RVSP	Right ventricular systolic pressure
SAT1	Spermidine/spermine N1-acetyltransferase 1
SDS	Sodium Dodecyl Sulfate
siRNA	Short interfering RNA
SLC	Solute carrier
SMA	Smooth muscle actin
Smad	Sma-Mothers Against Decapentaplegic
SMOX	Spermine oxidase
SMS	Spermine synthase
SRM	Spermidine synthase
SPD	Spermidine
SPM	Spermine
TNFα	Tumour necrosis factor alpha
TAE	Tris-acetate EDTA
TBE	Tris-Borate EDTA
TGFβ	Transforming growth factor beta
VEGF	Vascular endothelial growth factor/ Receptor

Chapter 1 Introduction

1.1 Pulmonary Hypertension

1.1.1 Clinical definition and classification

Pulmonary hypertension (PH) is a clinical condition characterised by elevated blood pressure in the pulmonary arteries. It was first defined by the WHO group as mean pulmonary arterial pressure (mPAP) ≥ 25mmHg measured at rest [1] and this definition has been used for decades. In 2009, a meta-analysis of the published data suggested that 20mmHg is the upper limit of the mPAP in the healthy population [2]. This makes mPAP between 21-24mmHg a “grey area”, although studies have suggested an increased risk of disease progression in patients with mPAP in this range [3-5]. Therefore, to address these recent findings, renewed PH definitions were proposed by the 6th World Symposium on Pulmonary Hypertension (WSPH) task force to redefine this clinical condition [6] (Table 1-1). However prospective studies are warranted to evaluate the benefits of management in this PH population. The updated clinical classification of PH was also released with minor changes while maintaining the 5 core groups [6] (Table 1-2).

Table 1-1 Hemodynamic definitions of pulmonary hypertension (PH)

Definitions	Characteristics	Clinical groups#
Pre-capillary PH	mPAP >20 mmHg PAWP ⩽15 mmHg PVR ⩾3 WU	1, 3, 4 and 5
Isolated post-capillary PH (IpcPH)	mPAP >20 mmHg PAWP >15 mmHg PVR <3 WU	2 and 5
Combined pre- and post-capillary PH (CpcPH)	mPAP >20 mmHg PAWP >15 mmHg PVR ⩾3 WU	2 and 5

mPAP: mean pulmonary arterial pressure; PAWP: pulmonary arterial wedge pressure; PVR: pulmonary vascular resistance; WU: Wood Units; # Group 1-5 PAH refer to the classification in Table1-2 [6].

Table 1-2 Updated clinical classification of pulmonary hypertension (PH)

1 PAH
1.1 Idiopathic PAH
1.2 Heritable PAH
1.3 Drug- and toxin-induced PAH
1.4 PAH associated with:
1.4.1 Connective tissue disease
1.4.2 HIV infection
1.4.3 Portal hypertension
1.4.4 Congenital heart disease
1.4.5 Schistosomiasis
1.5 PAH long-term responders to calcium channel blockers
1.6 PAH with overt features of venous/capillaries (PVOD/PCH) involvement
1.7 Persistent PH of the newborn syndrome
2 PH due to left heart disease
2.1 PH due to heart failure with preserved LVEF
2.2 PH due to heart failure with reduced LVEF
2.3 Valvular heart disease
2.4 Congenital/acquired cardiovascular conditions leading to post-capillary PH
3 PH due to lung diseases and/or hypoxia
3.1 Obstructive lung disease
3.2 Restrictive lung disease
3.3 Other lung disease with mixed restrictive/obstructive pattern
3.4 Hypoxia without lung disease
3.5 Developmental lung disorders
4 PH due to pulmonary artery obstructions
4.1 Chronic thromboembolic PH
4.2 Other pulmonary artery obstructions
5 PH with unclear and/or multifactorial mechanisms
5.1 Haematological disorders
5.2 Systemic and metabolic disorders
5.3 Others
5.4 Complex congenital heart disease

PAH: pulmonary arterial hypertension; PVOD: pulmonary veno-occlusive disease; PCH: pulmonary capillary haemangiomatosis; LVEF: left ventricular ejection fraction [6].

1.1.2 Pulmonary arterial hypertension

1.1.2.1 Overview

Pulmonary arterial hypertension (PAH) belongs to the group 1 pulmonary hypertension which is characterised by the progressive expansion of the muscle wall of small pulmonary arteries and the muscularisation of previously non-muscular arterioles. The resulting narrowing and occlusion of these vessels increases the pressures required to maintain blood flow and PAH is eventually lethal due to right heart failure if left untreated. Group 1 PAH can be idiopathic/heritable (I/HPAH), induced by drug/toxin, or secondary to other disease conditions. PAH patients who have a long-term response to calcium channel blockers were recently incorporated into group 1 PH (Table 1-2) to reflect the involvement of vasoconstriction in PAH pathophysiology. PAH is a rare disease with an incidence of 2.5-7.1 cases/million and a prevalence between 5-52/million in the adult population [7, 8]. Idiopathic and heritable PAH are the most common forms of PAH, accounting for approximately half of the patient population. This is followed by PAH secondary to other diseases, with connective tissue disease reported as the most prevalent aetiology [7, 9, 10].

1.1.2.2 Pathology

PAH mainly affects the small distal muscularised pulmonary vessels ranging from 70μm to 500μm in diameter [11]. The pathology of PAH typically manifests as a series of remodelling events in the vessel wall, including hyperplasic or fibrotic intima, hypertrophic media, hyperproliferative adventitia, and/or in situ thrombosis [11-16]. These histological changes can either occur alone in mild cases or together to form concentric lesions in severe cases (Figure1-1 g-j [11], Figure 1-2 [16]) or eventually developed into plexiform lesions in end-stage conditions (Figure 1-1 a-c [11]; Figure 1-2 [16]), which completely block the vessels. PAH can also be characterised by abnormal muscularisation and fibrosis in the microvasculature, leading to obliteration and ultimately loss of

pre-capillary arteries (Figure 1-3 [11]). Recent evidence has demonstrated perivascular infiltration and accumulation of inflammatory cells in the pathology of PAH (Figure 1-3 [11]), suggesting an important role for inflammation in disease development.

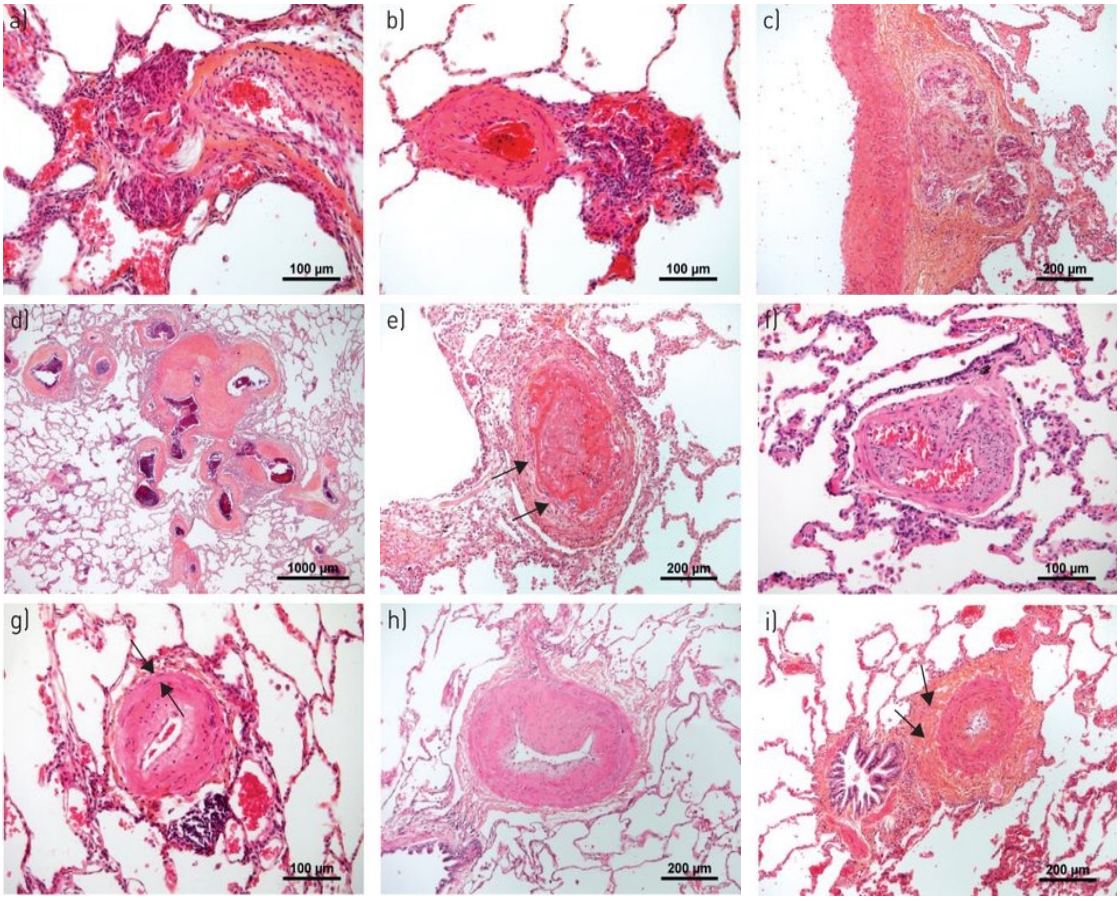

Figure 1-1 Representative vascular lesions typically detected in lungs of patients with pulmonary arterial hypertension (PAH)

a–c) Plexiform lesions. d) Atypical fibrovascular lesions e) Thrombotic lesion with fresh fibrin and fibroblasts involvement (arrows). f) Fully organised thrombotic lesion g) Concentric the intima with mild media thickening (arrows) h) Eccentric (cushion-like) intima i) media hyperplasia and adventitia fibrosis (arrows). Images adapted from Humbert, Marc, et al. European Respiratory Journal 2019 [11].

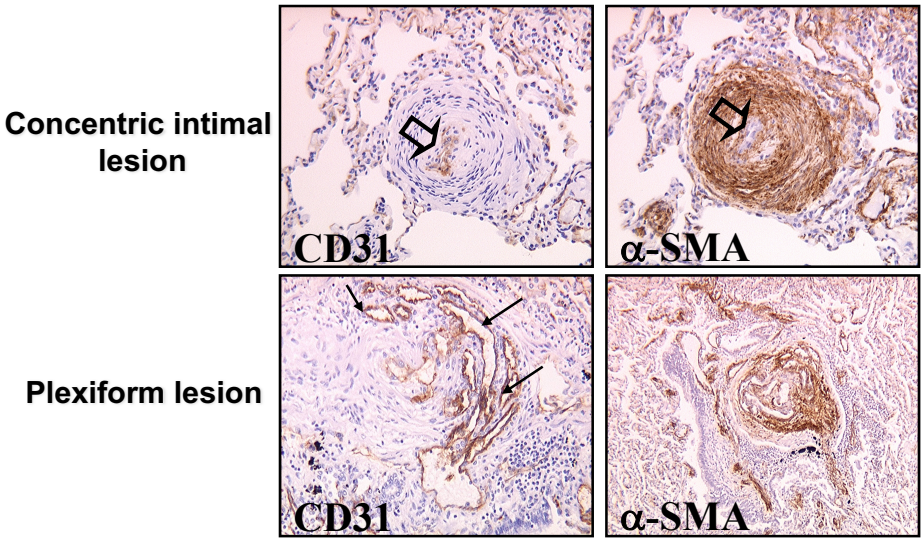

Figure 1-2 Pathology of vascular lesions in idiopathic pulmonary arterial hypertension Immunostaining of CD31 and α-smooth muscle actin (arrowed) demonstrating concentric intimal lesions and plexiform lesions in lung sections of idiopathic pulmonary arterial hypertension patients [16].

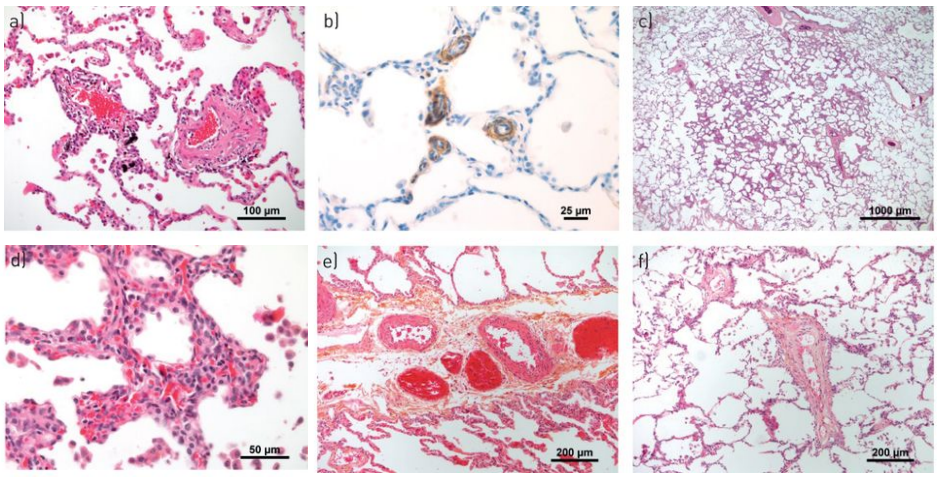

Figure 1-3 Lesions of the microvasculature in lungs of PAH or PVOD patients a) Inflammatory infiltration of micro-arteries or -venules b) Muscularised pulmonary vasculature (highlighted by α-SMA) in lungs of a PVOD patient. c) Patchy lung interstitial thickening in a PVOD patient d) Haemangiomatosis-like foci. e) Muscular hyperplasia and fibrous remodelling in pulmonary septal veins of a PAH patient. f) Fibrous intima thickening of small septal veins in a PVOD patient. Images readapted from Humbert, Marc, et al. European Respiratory Journal 2019 [11].

1.1.2.3 The genetics of PAH

Though familial occurrence was initially described in 1891 [17], Dresdale highlighted a family with primary pulmonary hypertension (currently referred to as IPAH) in 1954. More extensive families with primary pulmonary hypertension were described in 1984, with 6-10% of the cases found to be familial and exhibiting an autosomal dominant inheritance with incomplete penetrance [18]. Later in 2000, heterozygous germline mutations were identified in *BMPR2* [19] and since then, our understanding of the genetic architecture of PAH has steadily grown. It is now well established that mutations in *BMPR2* cause nearly 80% of familial PAH and approximately 20% of sporadic cases with reduced penetrance. In addition to *BMPR2,* mutations in genes encoding two other receptors of the TGFβ/BMP family, ALK1 and endoglin (ENG) were discovered in HHT families manifesting severe PAH symptoms [20, 21]. Later, DNA sequencing screening of genes downstream of the BMP signalling revealed rare variants in *Smad-1, -4* and *-9* in PAH patients [22, 23]. Interestingly, the initial genetic findings were mainly confined to TGF/BMP signalling, indicating an important role for disruption of this pathway in the pathogenesis of PAH. Over the last decade, advances in genetic techniques have substantially expanded our knowledge in the genetic causes of PAH. For example, whole exosome sequencing of blood samples uncovered rare mutations in *caveolin-1 (CAV-1)* and potassium channel subfamily K member 3 (*KCNK3*) in familial PAH cases [24, 25]. Mutations in T-box 4 (*TBX4*), a gene, previously reported in small patella syndrome, were also associated with childhood cases of PAH [26]. In 2014, mutations in *EIF2AK4*, the gene encoding eukaryotic translation initiation factor 2 alpha kinase 4 were reported in PVOD and PCH cases. Recently, whole genome sequencing of a European-wide cohort consists of over 1000 I/HPAH cased revealed rare variants in four novel genes, namely *ATP13A3*, *SOX17*, *AQP1* and *GDF2* [27]. In addition, two *BMP10* loss-of-function mutations were also identified in severe PAH cases, further expanding the spectrum of BMP signalling in PAH molecular genetic framework [28, 29].

In summary, 16 genes (Table1-3) to date have been identified as contributing to the genetic architecture of PAH. Mutations in these genes are inherited predominantly in an autosomal dominant manner with incomplete penetrance [30, 31].

Table 1-3 Genetic features of 16 PAH associated genes

Gene	Allelic series	Mutation number	MOI	Molecular mechanism
BMPR2	486	806	AD	Haploinsufficiency
EIF2AK4	58	101	AR/AD	Loss of function
ACVRL1	54	76	AD	Haploinsufficiency
TBX4	55	48	AD	NK
GDF2	30	34	AD/AR	Haploinsufficiency
SOX17	24	26	AD	NK
ENG	16	17	AD	NK
KCNK3	15	16	AD	Haploinsufficiency
ABCC8	12	12	AD	Haploinsufficiency
ATP13A3	11	11	AD	NK
SMAD9	10	11	AD	Haploinsufficiency
AQP1	5	9	AD	NK
CAV1	3	4	AD	Gain of function; Dominant negative
BMP10	2	2	AD	NK
SMAD4	2	2	AD	NK
SMAD1	1	1	AD	NK

AD, autosomal dominant; **AR**, autosomal recessive; **MOI**, mode of inheritance; **NK**, not known; **Allelic series**: number of distinct mutations, excluding recurrent variations. **Mutation number:** the total number of independent alleles reported, excluding related individuals. For biallelic mutations in EIF2AK4 and GDF2, each allele was counted as independent (that is, n = 2), except for five patients with documented consanguinity [31].

1.1.2.4 Pathogenesis of PAH

1.1.2.4.1 Dysfunctional pulmonary vascular endothelium

The pulmonary vascular endothelium is the inner layer of the pulmonary vasculature. This monolayer 'barrier" is formed mainly by the pulmonary vascular endothelial cells (ECs), separating the bloodstream from lung tissue and playing a pivotal role in maintaining vascular-tissue homeostasis.

Endothelial dysfunction was first recognised in the pathogenesis of PAH for mediating elevated vascular tone [32, 33]. Under physiological conditions, a low pulmonary vascular tone is maintained by a dynamic balance between vasoconstrictors and vasodilators. Pulmonary vascular ECs synthesise vasodilators, such as Nitric oxide (NO) and prostacyclin (PGI2), to favour vaso-relaxation. However, under disease conditions (e.g. PAH), the production of vasodilators is suppressed [34] while vasoconstrictors including Endothelin-1 (ET-1), Thromboxane A2 [35], Serotonin (5-HT) [36] are elevated, resulting in a high vascular tone. These findings led to the development of the current PAH specific therapies which mainly target the calcium channels, nitric oxide pathway, endothelin pathway and also prostacyclin pathway for promoting vasodilatation [32]. However, as vasoconstriction only accounts for disease in a small proportion of PAH patients [37, 38], whereas vascular remodelling remains the predominant pathogenic cause, new therapeutic strategies are required.

Apart from causing abnormal vascular tone, endothelial dysfunction also leads to an impairment of endothelial integrity, manifesting as increases of EC apoptosis and permeability [39]. Several lines of evidence have linked the initiation of pulmonary arterial hypertension to endothelial cell apoptosis [40-43]. The plant alkaloid monocrotaline (MCT), after being metabolised into MCT pyrrole, causes PH in rats, at least in part, via endothelial injury [44]. Vascular endothelial growth factor (VEGF) is a potent survival factor protecting endothelial cells from apoptosis. SU5416, a semi-selective tyrosine kinase VEGFR2 inhibitor, combined with hypoxia can also establish PH in rats by mediating EC apoptosis [45]. Gene-based VEGF overexpression [46, 47] attenuated both MCT- and Sugen/hypoxia-induced PH by decreasing EC caspase activities, further implicating EC apoptosis as a pivotal cause of disease development. Increased endothelial apoptosis is also linked to the dysregulation of PAH associated genes. Teichert-Kuliszewska et al. [48] showed that *BMPR2* loss-of-function predisposes hPAECs to apoptosis. In the

same study, BOECs derived from patients bearing *BMPR2* mutations failed to respond to the antiapoptotic effect of BMP2 under serum withdrawal. Our group also demonstrated that BMP9, by selectively targeting PAECs, prevented TNF-α induced apoptosis via BMPR2 and reversed experimental PAH related to endothelial injury [39]. Similar to BMPR2, preliminary data also suggest that *ATP13A3* silencing by small interfering RNA predisposed BOECs to apoptosis [27]. Interestingly, contrary to disease initiation, hyper-proliferative, apoptosis-resistant EC populations are also evident in PAH, mostly during the late stage of disease progression. Masri et al. [49] demonstrated that hPAECs isolated from PAH patients were more proliferative and inhibition of Janus Kinase (JAK) could attenuate their proliferation. Decreased miRNA-124 via affecting PTBP1 and PKM1/PKM2 in PAH patient-derived endothelial cells was recently demonstrated to be associated with abnormal pulmonary artery endothelial cell proliferation and glycolysis [50]. These hyper-proliferative, anti-apoptotic ECs arise as a result of the initial endothelial injury, as continuous apoptosis and renewal of endothelial cells may favour the selection of such a population [51]. However, the full mechanism underlying these divergent observations is still unclear as multiple factors including the genetic background, hypoxia and inflammation may be involved. Increased endothelial permeability has also been documented in PAH. BMP signalling holds great importance to endothelial homeostasis. si*BMPR2* was shown to mediate leakage and promote leukocytes transmigration in hPAECs under both static- and flow-based conditions [52]. Mice bearing a PAH associated mutation *Bmpr2-R899X* exhibited increased vascular leakage and spontaneously developed PAH at 6-months of age [39]. Recently, other than the BMP signalling, researchers have also demonstrated a transient receptor potential channel 4 (TRPC4)-dependent pulmonary vascular leakage, indicating a role of Ca^{2+} in endothelial permeability. These together suggest that increased endothelial permeability could be an important contributor to pulmonary vascular remodelling.

The pathobiology of PAH is also characterised by dysregulated angiogenesis. This is evidenced by the elevated plasma VEGF observed in severe PAH cases [53] and also the abundant expression of VEGF and its cognate receptor (VEGFR2) in complex PAH associated lung lesions [54]. BMP9 was also demonstrated to promote endothelial stability by suppressing this pathological angiogenesis [39]. These lines of evidence suggest PAH might be a proangiogenic disorder. However, the fact that combining SU4516 with chronic hypoxia can induce experimental PH, and loss of pre-capillary arteries is a feature of the pathology of PAH [40] suggest an anti-angiogenic mechanism underlies the disease pathogenesis. These seemingly paradoxical findings indicate that the pro- or anti-angiogenic events in the pathogenesis of PAH may be context-dependent and involve multiple pathways. For example, *Bmpr2* knockout mice exhibit impaired angiogenesis in the uterine decidua via repression of VEGF signalling [55]. On the other hand, the VEGFR3 receptor facilitates BMP signalling by promoting BMPR2 internalisation. In mice, endothelial-specific knockdown of *Vegfr3* exaggerated hypoxia-induced PH phenotypes by impairing the BMP signalling [56]. These findings provide evidence for an aberrant interplay between BMP and VEGF signalling in the context of angiogenesis, possibly contributing to the pathogenesis of PAH.

It has also been reported that endothelial dysfunction in the pathobiology of PAH is accompanied by an abnormal immune response. Overproduction of inflammatory cytokines or chemokines were observed in endothelial cells in hypoxia or with a genetic predisposition [57, 58]. The acquisition of pro-inflammatory phenotypes by PAECs has recently been described in PAH. Under disease-promoting conditions, endothelial cells upregulate the expression of E-selectin, intercellular adhesion molecule 1 (ICAM1) and vascular cell adhesion molecule 1 (VCAM1), resulting in the recruitment of leukocytes and the promotion of vascular remodelling [59]. In PAH, endothelial dysfunction, by mediating IL-6 and FGF2 overproduction, also leads to increased pericyte coverage of distal pre-capillary pulmonary arteries [60]. This

underpins the importance of communication between endothelial cells and other cells resident in the vessel wall for the maintenance of vascular homeostasis.

1.1.2.4.2 Dysfunctional smooth muscle cells and adventitial fibroblasts

Pulmonary vascular remodelling in PAH is also hallmarked by hyperproliferative and apoptosis-resistant pulmonary artery smooth muscle cells. hPASMCs harvested from PAH patients with *BMPR2* mutations were insensitive to the normal growth inhibitory response to BMP4 due to impairment of Smad1/5 signalling [61]. Moreover, TNF repressed BMPR2 expression and promoted BMP6 mediated hPASMC proliferation via dysregulated Src family signalling [62]. FoxO1, a critical transcription factor that regulates cell proliferation, was demonstrated to be downregulated in PAH patients. Inhibition of FoxO1 with the inhibitor, AS1842856, or transduction of cells with a constitutively active FoxO1 mutant increased PASMC proliferation [63]. Excessive levels of several growth factors have been demonstrated in vascular lesions in PAH and are suggested to contribute to vascular cell abnormalities. Factors produced by PAECs, such as serotonin [64] and endothelin-1 [65], also induce PASMC proliferation. Moreover, proliferation of PASMCs could be triggered by other growth factors, namely fibroblast growth factor 2 (FGF2), epidermal growth factor (EGF) and platelet derived growth factor (PDGF) [66, 67]. Among these, PDGF is a potent stimulus for pulmonary vascular abnormalities with both PDGF-A and PDGF-B found to be upregulated in the pulmonary arteries of severe PAH cases [68]. In addition, treating patients with Imatinib, a receptor tyrosine kinase inhibitor initially designed to target Abl kinase, but with activity towards PDGF receptors, improved pulmonary vascular resistance (PVR) and cardiac output (CO) in PAH patients, implying an important contribution of PDGF signalling to the pathology of PAH [69]. Moreover, other cancer-related signalling pathways are also implicated in the

hyperproliferative responses of PASMCs in PAH. Mammalian target of rapamycin 2(mTORC2) has been shown to activate mTORC1 via AMPK and contributes to PASMC proliferation [70]. Pulmonary artery adventitial hypertrophy, dominated by dysfunctional fibroblasts, is another hallmark of the pathological changes in PAH, contributing to increased pulmonary artery stiffness. Pulmonary artery adventitial fibroblasts, particularly under hypoxia, secrete a series of adhesion molecules and cytokines e.g. ICAM-1, VCAM-1, TGF-β which promote the recruitment of leukocytes into the adventitial compartment and together trigger subsequent inflammatory responses leading to vascular remodelling [71].

1.1.2.4.3 Immune disturbance

Inflammation and dysregulated immune responses have been implicated in the pathogenesis of PAH. Histological analysis revealed perivascular infiltration of inflammatory cells and lymphoid neogenesis in the precapillary arteries of PAH patients [72, 73]. Increased plasma cytokines and chemokines were also reported in PAH patients, with higher levels of IL1α/β, IL2, IL6, IL10, IL12 or TNFα associating with a poorer prognosis [74]. Overproduction of these inflammatory mediators leads to endothelial injury [75], abnormal recruitment of leukocytes [59] and smooth muscle/fibroblast proliferation [76, 77], thus contributing to vascular remodelling in PAH. Aberrant inflammatory responses also happen when BMP signalling is disrupted. LPS exposure promotes IL-6 and IL-8 production in both *Bmpr2*$^{-/+}$ mice and PASMCs isolated from *BMPR2* mutation carriers [58]. Moreover, loss of *BMPR2* increases the phosphorylated-p38 pathway, resulting in the overproduction of IL-6 [78]. Apart from being affected by BMP signalling, inflammatory factors also mediate the regulation of BMPR2. Our group has previously reported that TNFα promotes the development of PAH by transcriptionally suppressing *BMPR2* while enhancing its cleavage in hPASMCs [62]. The elevation of circulating TNFα in PAH

patients suggests an important role for TNFα as a modifier of disease penetrance.

1.1.2.4.4 Genetic mechanisms of PAH pathobiology

TGFβ/BMP signalling pathway It is recognised that the TGFβ/BMP signalling pathway is central to the molecular genetic framework of PAH, with mutations in *BMPR2*, the gene encoding the BMP type II receptor as the most common cause of HPAH [30, 31]. BMPR2 is widely expressed in different tissues and plays pivotal roles in the functions of several BMP ligands [79]. To mediate signal transduction, BMPR2 forms a heteromeric receptor complex with one of four type I receptors, ALK1, ALK2, ALK3 or ALK6 that dictate the selectivity of the receptor complex for particular BMP ligands. Upon binding of a dimeric BMP ligand, the constitutively active kinase domain of BMPR2 then transphosphorylates the kinase domain of the type I receptor, which in turn catalyses C-terminal phosphorylation of the downstream canonical Smad1/5/8 (receptor-regulated Smads(R-Smads)) proteins [80, 81]. Once activated, the R-Smads form a complex with the nuclear chaperone Smad4, and this complex then translocates into the nucleus to they control the transcriptional regulation of target genes [82]. BMPR2 is highly expressed on the cell surface of the pulmonary endothelial cells and mediates BMP9 and BMP10 signalling with the endothelial-specific type I receptor (ALK1) and co-receptor (ENG) [79]. Mutations in these genes cause aberrant BMP signalling, contributing to the endothelial dysfunction underlying PAH [31]. However, only 20-30% of the *BMPR2* mutation carriers develop PAH, indicating that other factors may contribute to the disease penetrance. Indeed, dysregulated oestrogen metabolism may account for the higher penetrance in female patients [83]. TNFα, a potent inflammatory cytokine, disrupts BMP signalling by suppressing the expression of BMPR2. This provides evidence for the potential involvement of inflammation as a factor in driving disease [62]. More recently, somatic

mutations acquired in PAH patients were reported as causing DNA damage and are a possible contributor to the disease penetrance of *BMPR2* mutations [84]. In addition to disrupting endothelial cell functions, hPASMCs bearing PAH-related *BMPR2* mutations also exhibit disease-associated phenotypes [85], suggesting that BMPR2 dysfunction contributes to disease by affecting multiple cell types. Apart from the receptors, mutations were also identified in the *SMAD1*, *SMAD9* and *SMAD4* genes, which encode the proteins responsible for canonical BMP signal transduction. Recently, mutations in *GDF2*, the gene encoding BMP9, were also identified in HPAH cases [27]. A follow-up study demonstrated that these *GDF2* mutations impair BMP9 processing and secretion and lead to reduced circulating levels of BMP9 and BMP10 [29].

Caveolin-1 (CAV1) *CAV1* encodes the scaffolding protein caveolin-1, which is the main component of the invaginations of the plasma membrane. So far, three protein truncated variants have been reported in PAH patients [24, 86, 87], suggesting that CAV-1 loss of function leads to the pathogenesis of PAH. Indeed, reduced CAV-1 levels were reported in the lung tissues of PAH patients [88], and CAV-1 deficiency perturbs BMP signalling by affecting BMPR2 localisation [89]. Cav1 knockout mice also exhibit an absence of caveolae in the pulmonary vasculature and an increased mPAP [90]. Taken together, these suggest a role for caveolin-1 in maintaining pulmonary homeostasis.

Potassium channel subfamily K member 3 (KCNK3) Ion channels play an important role in the regulation of vascular homeostasis. An aberrant resting membrane potential resulting from dysregulated ion channels could lead to vascular remodelling [91]. A genetic association of *KCNK3* mutations with PAH were first identified in 2013 [25] and further validated by other studies [92]. Mutations in *KCNK3* caused variable impairment of the potassium-channel current, causing membrane depolarisation in hPASMCs. These genetic changes affect vascular tone and hence contribute to the pathogenesis of PAH.

Eukaryotic Translation Initiation Factor 2 Alpha Kinase 4 (EIF2AK4) Unlike the other types of PAH, pulmonary veno-occlusive disease (PVOD) and

pulmonary capillary haemangiomatosis (PCH) exhibit autosomal recessive inheritance [30]. Genetic analysis in these patients revealed homozygous mutations in *EIFAK4.* Nearly 25% of the sporadic cases also harbour mutations in this gene, further suggesting a pathogenic role of *EIF2AK4* in PVOD [93]. The biological functions of EIF2AK4 mainly involve regulating the response to cellular stress [94]. Interestingly, EIF2AK4 mutations were also seen in HPAH patients, characterised by early onset of disease and poor clinical outcomes, and likely to represent cases of PVOD without typical clinical features [95].

T-box transcription factor 4 (TBX4) TBX4 is a transcription factor responsible for the regulation of mesoderm differentiation and embryogenesis. Genetic analysis revealed TBX4 as the predominant cause of childhood-onset PAH [96]. Interestingly, mutations identified from early-onset PAH cases clustered in the critical T-box domain, resulting in deleterious amino acid substitutions or premature stop codons [31]. These findings, at least in part, suggest TBX4 loss-of-function defects may contribute to the pathobiology of disease by affecting developmental progression.

Novel genes associated with PAH Aquaporin 1 (AQP1) is a water channel widely expressed in tissues and predominantly functions in maintaining the homeostasis of the kidney. Recently, inhibition of AQP1 was shown to alleviate hypoxia-induced PAH in mice [97]. Reduced angiogenesis was also observed in Aqp1 knockout mice [98]. Conversely, aquaporin 1 overproduction induced proliferation and migration of PASMC [99]. Collectively, these findings suggest an essential role of AQP1 in vascular homeostasis.

Sox17 is an endothelial transcriptional factor essential for development. Rare variants were recently identified in an I/HPAH cohort with the missense mutations clustering in the high-mobility group box of *SOX17* [27]. This suggests a potential pathogenic link between *SOX17* mutations and the regulation of developmental transcriptional programs in endothelial cells. Recently, a comprehensive GWAS study of over 2000 PAH patients of European ancestry revealed a significant association with the upstream region

of *SOX17* [100]. The same study also demonstrated an impairment of enhancer activity in the *SOX17* gene promoter by these PAH risk variants [100]. This, together with the previous findings [27] indicate that both common and rare variants in *SOX17* predispose to PAH. Later, two independent cohorts further revealed *SOX17* as a major risk factor accounting for PAH associated with congenital heart diseases [96, 101]. Collectively, these findings strongly suggest a potential role of *SOX17* in the pathobiology of PAH.

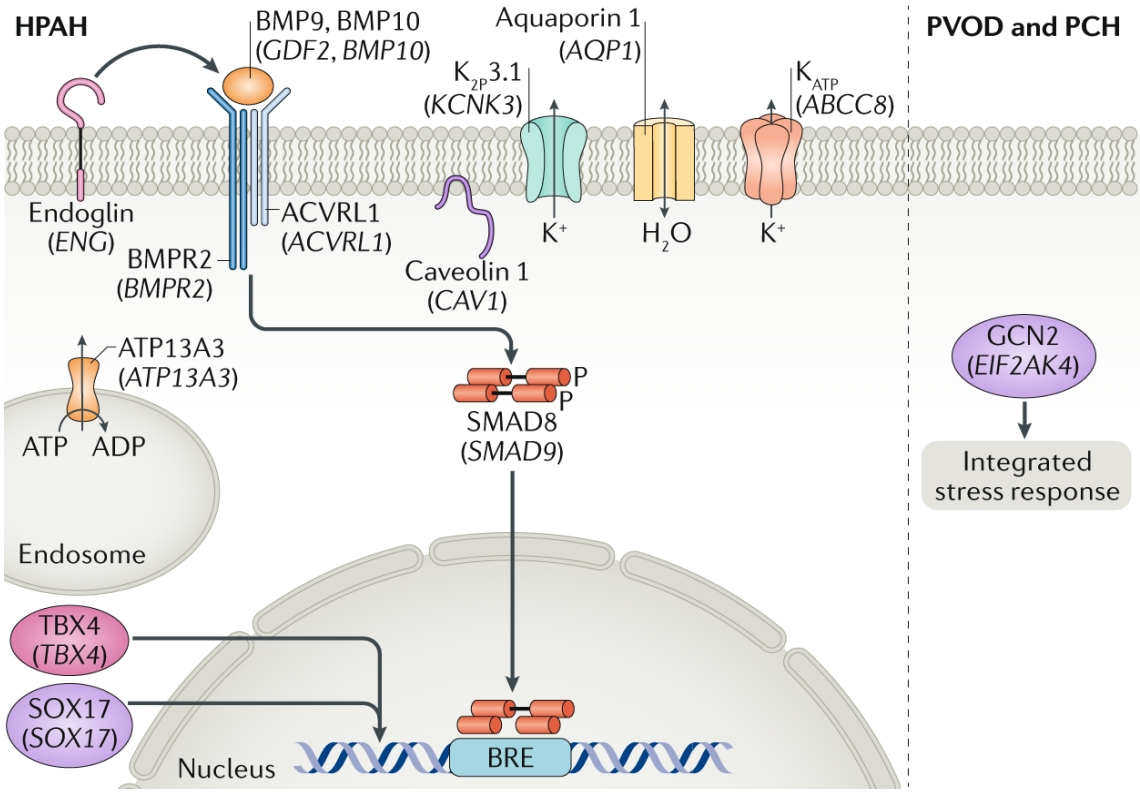

Figure 1-4 Schematic of the major pathway and associated genes in HPAH, PVOD and PCH

BMP9 and BMP10 signalling pathways centre the genetic causes of HPAH, with mutation identified in BMPR2, ACVRL1 (also known as ALK1), ENG, SMAD4 and SMAD9. Caveolin 1 (CAV1) mutations also potentially disrupt BMP signalling by affecting BMPR2. KCNK3 encodes the potassium channel and ABCC8 encodes a subunit of the ATP-sensitive potassium channel. ATP13A3 is a putative cation transporter resides on the endosomal compartment. SOX17 and TBX4 encode

transcription factors critical for organogenesis. Biallelic mutations in EIF2AK4, which encodes an important kinase essential for sensing cellular stress response, are implicated in the PVOD and PCH pathogenesis. ACVRL1, activin receptor-like 1; ATP13A3, probable cation-transporting ATPase 13A3; BRE, BMP-responsive element; BMPR2, bone morphogenetic protein receptor type 2; GCN2, eIF2α kinase GCN2; SMAD, mothers against decapentaplegic homologue. Schematic readapted from Southgate, Laura, et al. Nature Reviews Cardiology 2019 [31].

ATP13A3

Following whole genome sequencing and rare variant analysis, *ATP13A3* was recently identified as a novel PAH-associated gene, accounting for 1.1% of the I/HPAH cohort [27]. Later, additional variants were reported in whole-exome sequencing studies [102, 103]. To date, 26 unique *ATP13A3* variants have been identified in PAH patients (Table 1-4). Of these, the missense mutations are enriched within the catalytic domains, suggesting a potential disruption of normal ATP13A3 functions (Figure 1-5). Moreover, an overrepresentation of protein truncated variants was reported in a PAH cohort [27] suggesting that loss-of-function of ATP13A3 could contribute to the pathogenesis of PAH.

ATP13A3 is a P5B ATPase that is widely expressed in different cell types. The biological functions of this putative cation transporter are still unknown as very few studies of ATP13A3 have been reported. Some lines of evidence suggest a link between *ATP13A3* and the levels of polyamines, a group of small cations essential for cell growth, apoptosis [104-106]. Preliminary data I generated in BOECs showed that *ATP13A3* deficiency reduces cell proliferation and increases the rates of apoptosis under serum-deprivation [27]. As shown in my studies described in this Thesis, this is likely owing to the perturbation of endothelial polyamine homeostasis [107, 108] and indicates a pathogenic role of *ATP13A3* loss-of-function in the pathobiology of PAH.

Table 1-4 ATP13A3 rare variants identified in different PAH cohorts

Gene	Variant type	HGVS (cDNA)	HGVS (protein)	PAH classification	REF
ATP13A3	frameshift	c.2192dupC	p.Ala732CysfsTer4	IPAH	[27]
ATP13A3	frameshift	c.2176_2180delTTAAA	p.Leu726AlafsTer8	IPAH	[27]
ATP13A3	frameshift	c.1367delC	p.Pro456LeufsTer7	IPAH	[27]
ATP13A3	missense	c.2867T>C	p.Leu956Pro	IPAH	[27]
ATP13A3	missense	c.2573G>A	p.Arg858His	IPAH	[27]
ATP13A3	missense	c.2550G>A	p.Met850Ile	IPAH	[27]
ATP13A3	missense	c.2023T>G	p.Leu675Val	IPAH	[27]
ATP13A3	Splice donor	c.3402+1G>T	NA	IPAH	[27]
ATP13A3	Stop gained& Splice region	c.1558C>T	p.Arg520Ter	IPAH	[27]
ATP13A3	Splice region& Synonymous variant	c.1149A>G	c.1149A>G(p.%3D)	IPAH	[27]
ATP13A3	Stop gained	c.1654G>T	p.Glu552Ter	IPAH	[27]
ATP13A3	frameshift	c.158_159del; 163_167del	p.(Trp53Serfs*12)	APAH-CTD	[96]
ATP13A3	Stop gained	c.201_202del	p.(Cys67*)	IPAH	[96]
ATP13A3	missense	c.1222A>G	p.(Arg408Gly)	APAH-CHD	[96]
ATP13A3	frameshift	c.2189_2205del	p.(Thr730Argfs*4)	IPAH	[96]
ATP13A3	missense	c.2228G>T	p.(Arg743Leu)	IPAH	[96]
ATP13A3	frameshift	c.2549dup	p.(Met850Ilefs*13)	IPAH	[96]
ATP13A3	missense	c.2996C>T	p.(Ser999Leu)	FPAH	[96]
ATP13A3	missense	c.G3653A	p.G1218E	IPAH	[102]
ATP13A3	missense	c.T2755G	p.S919A	IPAH	[102]
ATP13A3	missense	c.G2686A	p.G896R	IPAH	[102]
ATP13A3	missense	c.T1427C	p.I476T	IPAH	[102]
ATP13A3	missense	c.G1228T	p.A410S	IPAH	[102]
ATP13A3	missense	c.T869C	p.V290A	IPAH	[102]
ATP13A3	missense	c.A511G	p.I171V	IPAH	[102]
ATP13A3	nonsense	c.1540C>T	p.Glu514*	APAH-MS (INFβ treatment)	[109]

HGVS: Human Genome Variation Society nomenclature APAH: Associated pulmonary arterial hypertension CTD: Connective tissue disease CHD: Congenital heart disease MS: Multiple sclerosis[27, 96, 102, 109]

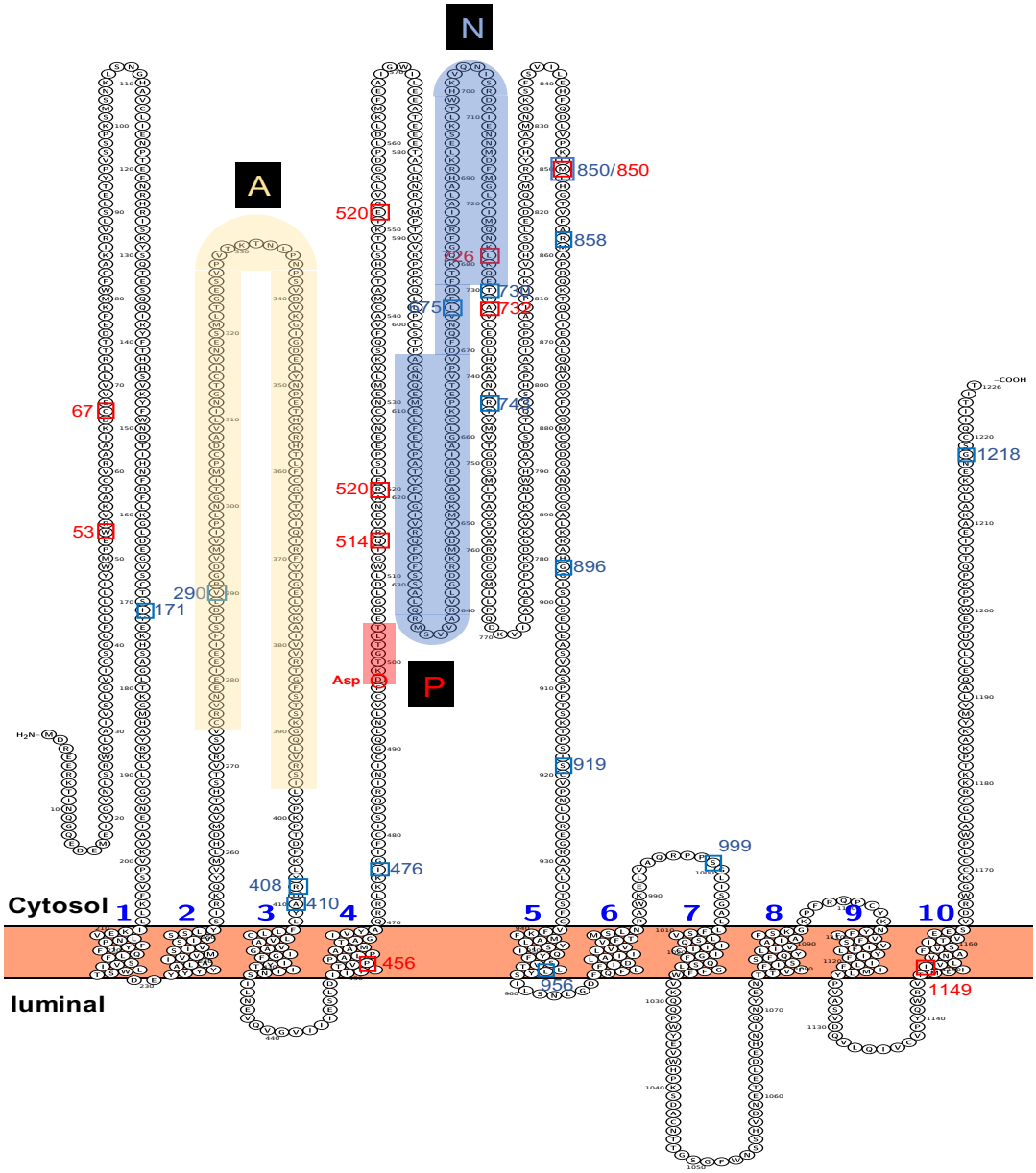

Figure 1-5 Summary of the reported PAH associated mutations in ATP13A3

Reported *ATP13A3* mutations found in PAH patients were plotted on ATP13A3 topology simulated from Protter (http://wlab.ethz.ch/protter). Residues affected by missense mutations are highlighted by a light blue square while protein truncated variants are marked by a red square. Cytosolic domains of ATP13A3, namely actuator "A", phosphorylation "P" and nucleotide-binding "N" domains are also marked in responding colours. The N-terminal Ma domain (Figure 1-6) is not shown as the actual amino acids inserted into the membrane are not known.

1.2 P-type ATPase

1.2.1 P-type ATPases

The P-type ATPases are a group of highly versatile membrane transporters. These may reside in the plasma membrane, facilitating transport between the extracellular space and the cytoplasm, or maybe present in organelle membranes, transporting substrates between the lumen of the organelle and the cytoplasm. By hydrolysing ATP to ADP, they serve as pumps for translocating ions, lipids or heavy metals across cell membranes or among cellular compartments [110]. The nomenclature of this superfamily, as “P-type”, comes from the phosphorylation intermediate formed during a catalytic cycle [110]. The first P-type ATPase was described by Skou [111] in 1956 as a sodium/potassium ATPase that transports ions across the shore crab nerve membrane. Later, more P-type ATPases were discovered and to date, five distinct subfamilies, namely the P1-P5 ATPases, have been characterised with respect to their sequence homology and substrate preferences.

Despite the low overall sequence conservation among P-type ATPases, they share highly conserved topology, probably owing to the sophisticated coupling of the cytoplasmic domains during substrate transport. P-type ATPases are transmembrane proteins, typically containing 10 membrane-spanning segments (Figure 1-6). The cytosolic domains of P-type ATPases are responsible for the coordination of protein phosphorylation and subsequent conformation change during the transport cycle. The transmembrane domains, on the other hand, contribute towards forming the substrate-binding sites, providing structural support for the P-type ATPase domains and mediating transport activities together with the cytosolic domains [110]. P-type ATPases generally consist of three cytosolic domains (Figure 1-6), the actuator domain (A), nucleotide domain (N) and the phosphorylation domain (P). The N domain, marked by a signature KGAPE motif, is linked to the P-domain and mainly

responsible for ATP binding. Following substrate binding to the transmembrane domains, the N domain mediates the phosphorylation of the P domain by exposing the γ-phosphate of ATP to the DKTG motif in the P domain. This highly conserved DKTG motif is the hallmark of the P-type ATPases and is crucial for their transport activity. Consequently, the A domain, which is a flexible phosphatase, contacts the first two (P1 ATPase) or three (P2-5 ATPase) transmembrane segments and dephosphorylates the P domain during the catalytic cycle. A signature TGE motif is conserved among the P-type ATPases in this domain, suggesting a shared catalytic function across these transporters.

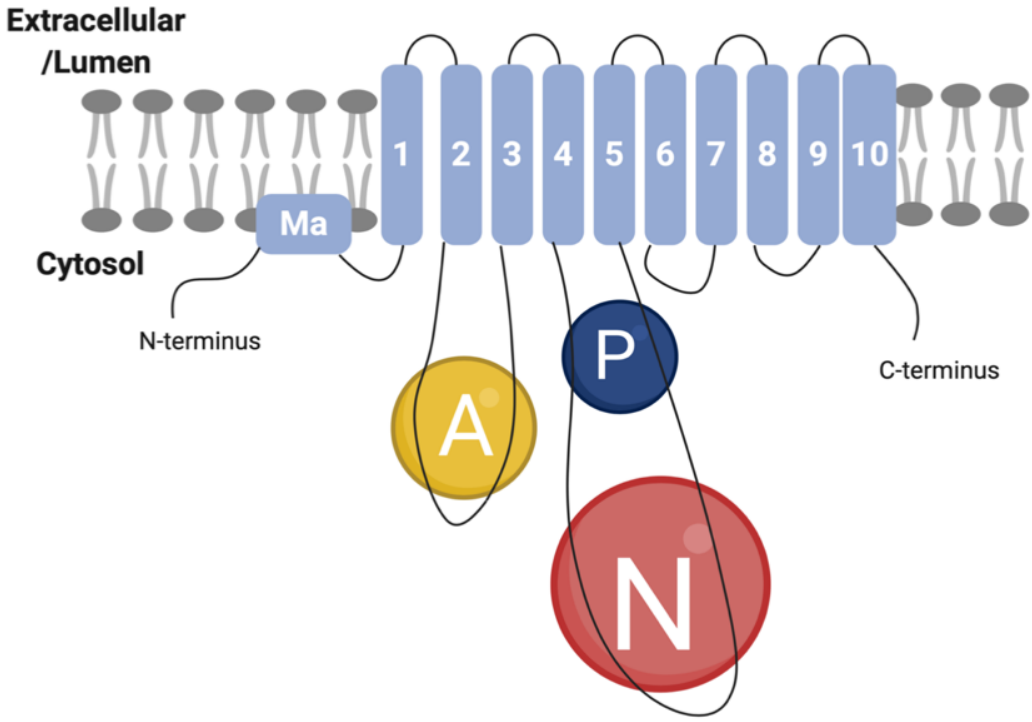

Figure 1-6 General topology of P-type ATPases

P-type ATPases consist of three cytosolic domains including the Actuator domain (A, yellow), nucleotide domain (N, red) and the phosphorylation domain (P, Navy). The transmembrane domain of the pump typically contains 10 membrane-spanning segments, responsible for substrate binding and provision of structural support. For P5B-ATPases, there is an additional N-terminal segment (Ma) embedded but not span across membrane.

1.2.2 General catalytic mechanism of P-type ATPase activity

P-type ATPases share high structural conservation and hence utilise a similar catalytic mechanism for moving substrates across membrane. A counter-transport theory ((Post-Albers cycle) was proposed based on the study of sodium, potassium-ATPases [112, 113].

In general, the P-type ATPases adopt two conformations, namely E1 and E2, that face the opposite sides of the membrane during a cycle (Figure 1-7). In the E1 state, substrate-binding site on the transmembrane domain of the P-type ATPases is faced to the cytosol, with a high affinity to the cytosolic substrate. Upon binding of the cytosolic substrate, the pump undergoes a structural rearrangement exposing an Mg^{2+} binding site near the conserved Asp site of the P domain. The binding of Mg^{2+} is crucial for the subsequent phosphorylation reaction, as it neutralises the electrostatic repulsion between ATP and the Asp residue in the P domain, facilitating the N-domain mediated phosphorylation of Asp residue (E1-P state). The phosphorylation of the P-domain leads to a forward bending, which in turn rotates the A domain by stretching the hinge between the transmembrane segments and the A domain. This conformational change reduces the affinity of the cytoplasmic substrate binding, releasing this cytosolic substrate to the extracellular/luminal side of the membrane (E2-P state). This step happens slowly and is recognised as the rate-limiting step of the catalytic cycle. The release of the cytosolic substrate triggers the binding of a counterion (extracellular/luminal substrate) on the extracellular/luminal side of the membrane and facilitates the dephosphorylation of the P-domain by the A-domain (E2). This is accompanied by a conformational shift from E2 back to E1, resulting in reduced affinity for the counterion substrate. There, the counterions are released into the cytosol, and the catalytic cycle can start again (Figure 1-7). However, it is noteworthy that not all the P-type ATPases function in a counter-transporting manner. Such examples are the heavy metal transporter P1 ATPase and the proton transporter P2 ATPase which are

responsible for single-direction transport [110]. Moreover, the transport mechanism of the P5-ATPases have yet to be characterised.

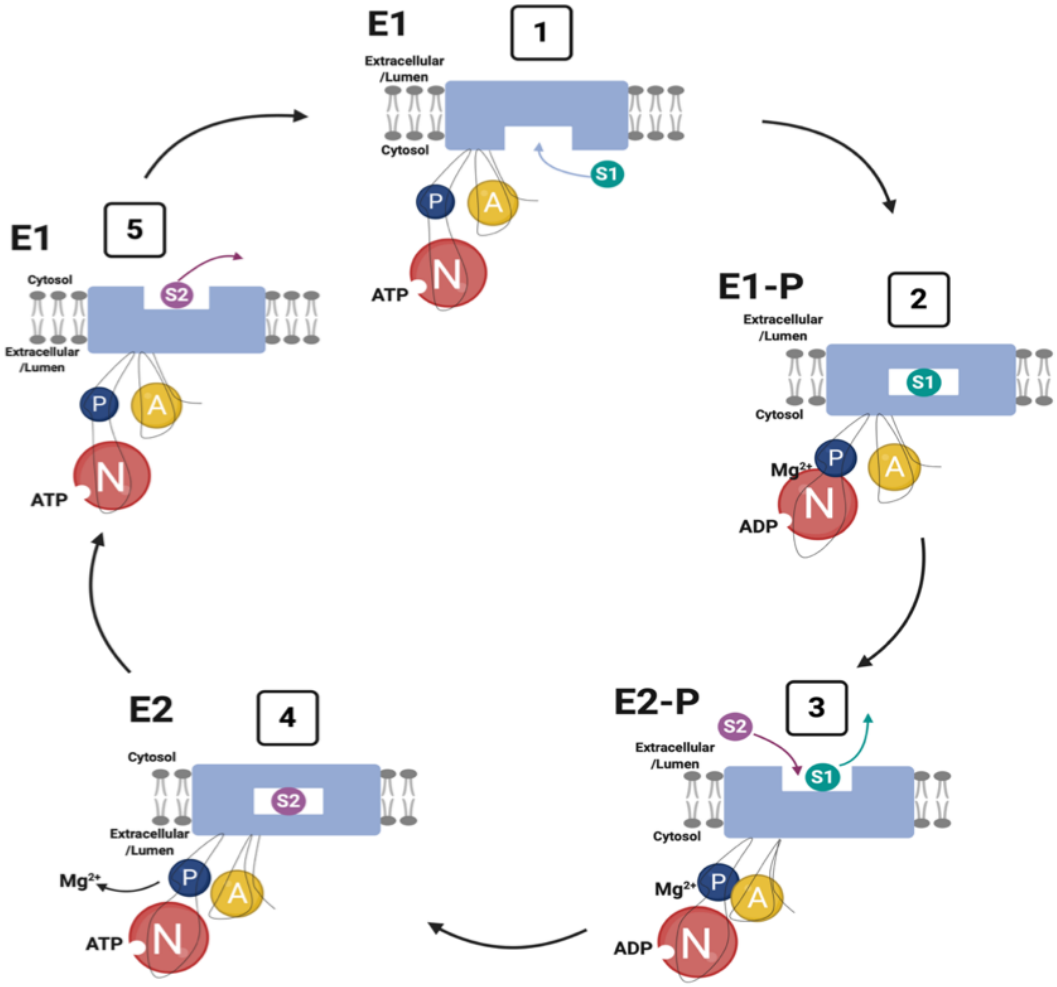

Figure 1-7 General catalytic mechanism of P-type ATPases during substrate transport

The catalytic cycle begins at the E1 conformation when the P-type ATPases have a high affinity for the cytosolic substrate (S1). The binding of this substrate induces a conformational change and initiates the phosphorylation of the P-type ATPase (E1-P). This leads to a decreased affinity and subsequent release of the cytosolic substrate while favouring a high affinity to the extracellular/luminal substrate (S2) (E2-P). The binding of the counterion triggers the dephosphorylation of the P-type ATPase (E2), subsequently resulting in the release of the counterion into the cytosol. The P-type ATPase then returns to the E1 state and is ready for the start of a new catalytic cycle.

1.2.3 P-type ATPase classification

As mentioned above, five subtypes of P-type ATPases exist in nature and participate in a set of biological functions by translocating substrates across membranes. So far, 36 P-type ATPases human homologues have been identified. Phylogenetic clustering of these cation transporters per their ancestry is detailed in figure 1-8.

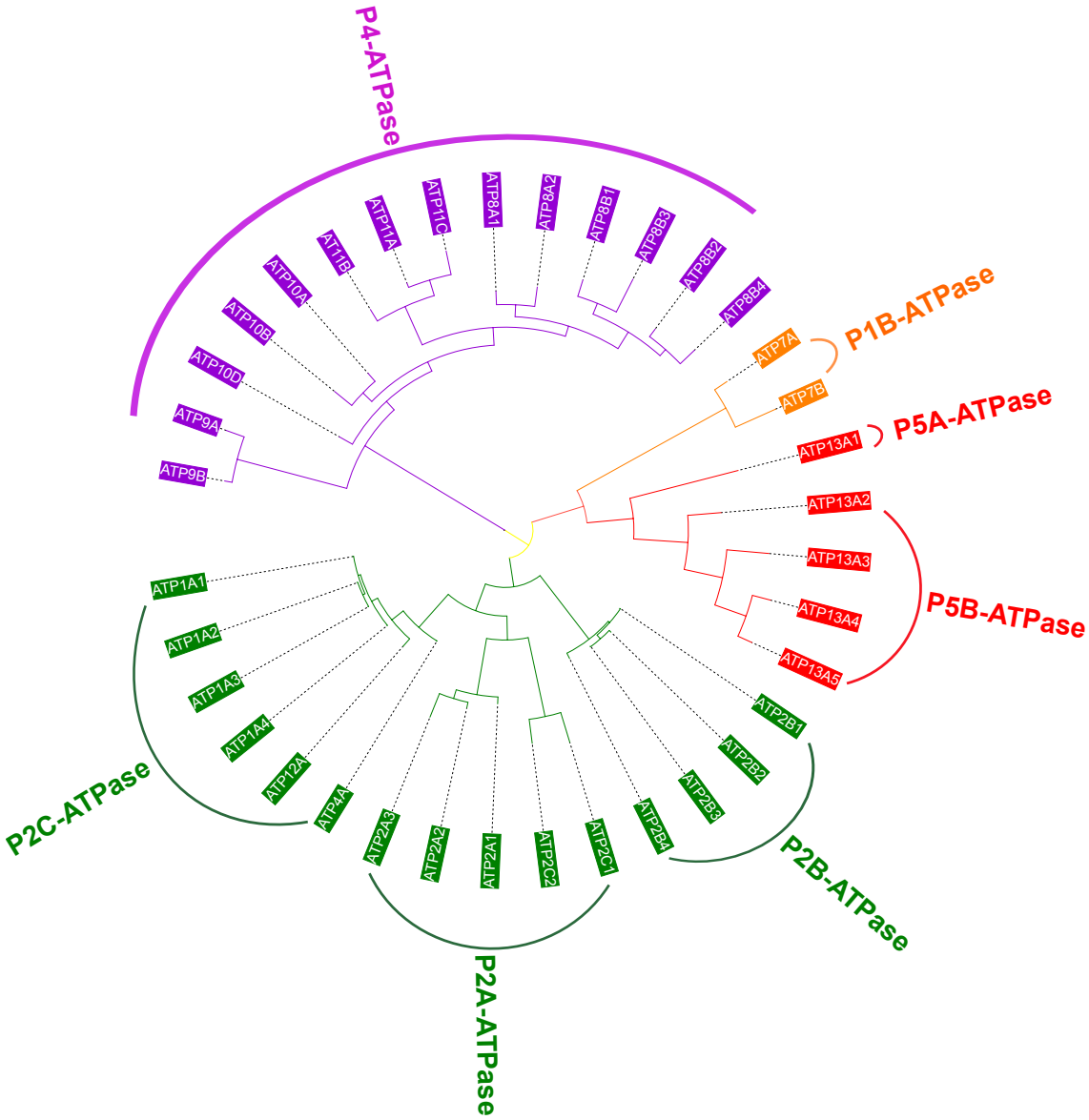

Figure 1-8 Phylogenetic clustering of human P-type ATPases Sequences of 36 mammalian P-type ATPases obtained from UniProt (https://www.uniprot.org) were further phylogenetically analysed with the iTOL (https://itol.embl.de) platform and clustered according to their ancestry.

1.2.3.1 P1-ATPases

P1-ATPases are recognised as the most ancient P-type ATPase subtype and can be further classified into the P1A and P1B subfamily. The P1A-ATPases are mainly found in bacteria with KdpFABC representing the most well-characterised ion pump responsible for K+ transport [114]. This Kdp-like K+ transporter complex is composed of 4 subunits (F, A, B, C). Among them, KdpB is the smallest P-ATPase identified so far, possessing all the core structures of a typical P-type ATPase. The P1B-ATPases, on the other hand, are a group of heavy metal pumps transporting monovalent and bivalent metals across the cell membrane [114-116]. They are essential in bacteria and animal cells as efflux transporters, preventing the intracellular accumulation of heavy metal ions. Two human homologues, namely ATP7A and ATP7B, were identified as copper exporters. Mutations in ATP7A were shown to cause Cu+ deficiency in Menkes disease[117] while genetic defects in ATP7B lead to Wilson disease by inducing excessive Cu2+ accumulation [118].

1.2.3.2 P2-ATPases

To date the P2-ATPases are most extensively characterised P-type ATPases, also known as Sarco(endo)plasmic Reticulum Ca2+-ATPases (SERCA) (P2A-ATPases), calmodulin-binding Ca2+-ATPases (P2B-ATPases) and sodium-potassium channels (P2C-ATPases). P2A-ATPases, namely ATP2A1-3, are calcium pumps responsible for recycling cytoplasmic calcium back to the sarcoplasmic reticulum during muscle relaxation [119]. This cation transport process is generally characterised by the efflux of two Ca^{2+} per catalytic cycle while counter-transporting H^{+} (less than four) into the cytosol. ATP2A1 (SERCA1) is predominantly expressed in skeletal muscle, while ATP2A2 (SERCA2) also exists in cardiac muscle (SERCA2a) and other types of tissue (SERCA2b) [120]. Loss-of-function mutations in *ATP2A1* have been found in patients with Brody myopathy. These mutations, by reducing ATP2A1 expression, impair skeletal muscle relaxation and hence cause muscle

cramping and stiffening during childhood (Table 1-5) [121]. ATP2A3 was initially identified in non-muscle cells, such as platelets, human lymphoblastoid Jurkat cells and rat mucosal mast cells [122]. However, a recent study also demonstrated its expression in cardiomyocytes [123]. P2B-ATPases, by binding to calmodulin, regulate cellular calcium homeostasis. In humans, four isoforms have been identified so far (ATP2B1-4) (Figure 1-8) [110]. These P-type ATPases reside on the plasma membrane of animal cells while localising to the vacuolar membrane or other intracellular compartments in plants or fungi [110]. A regulatory domain (R-domain) is typically present in the C-termini of these calcium pumps, and this negatively regulates their transport activity. Binding of calmodulin to the R-domain of a P2B-ATPase reduces this inhibition, substantially increasing the affinity for Ca^{2+} and hence facilitating calcium efflux [124].Unlike the P2A/B-ATPases, P2C-ATPases mainly mediate the translocation of sodium and potassium. ATP1A1, the first identified P-type ATPase, belongs to this subfamily [111]. A classic substrate transport process mediated by P2C-ATPases involves the efflux of three Na^+ while importing two K^+ into the cytoplasm [125]. This creates an electrochemical gradient across the plasma membrane and is pivotal for the formation of action potentials and other biological processes [126]. P3-ATPases do not exist in humans, with P3A functioning as membrane H^+-ATPases in plants [127] and P3B as $Mg2^+$-ATPases in bacteria [128].

1.2.3.3 P4-ATPase

P4-ATPases comprise the largest subfamily of P-type ATPases and are functionally distinct from the P1-3 subfamily, identified only in eukaryotes as phospholipid flippases [129]. P4-ATPases are physiologically important as they promote inward phospholipid translocation in the cell membrane [130]. So far, fourteen P4-ATPases have been identified in humans and are widely expressed across different human tissues. Among these, ATP8B1 is the most studied P4-ATPase, with mutations in *ATP8A1* causing severe cholestatic

disorders (Table 1-5) [131]. Both *in vitro* and *in vivo* data have shown that ATP8B1 translocates phosphatidylserine (PS) in the plasma membrane [132]. Interestingly, this requires the CDC50 protein to promote the release of ATP8A1 from the endoplasmic reticulum. P4-ATPases also mediate the trafficking of signalling lipids on cellular organelle membranes, regulating apoptosis, blood coagulation, cell fusion and other biological processes [132].

1.2.3.4 P5-ATPase

In the late 1990s, a fifth subtype of the P-type ATPases (P5-ATPases) existing exclusively in eukaryotes, were identified by phylogenetic analysis of the conserved sequence motif across genomes [129].

P5-ATPases are characterised by a signature PPxxP motif in the M4 transmembrane segment, distinguishing them from the conserved Pxxx(P/L) motif found in other P-type ATPases [133]. Moreover, sequencing analysis revealed that the subfamily could be further divided into P5A- and P5B-ATPases based on the conserved PP(E/D) x Px(E/D) motif and PP(A/V) x P(A/V) x motifs, respectively [134]. In humans, five distinct P5-ATPases have been identified, with ATP13A1 belonging to the P5A subfamily while ATP13A2-5 fall in the P5B- subgroup. It has been demonstrated in other P-type ATPases that residues in the Pxxx(P/L) motif play a pivotal role in unwinding the M4 segment and hence coordinating substrate binding during the catalytic cycle [134]. Due to the differences in this motif, it is rational to hypothesise that the substrate specificities may differ between P5A- and P5B-ATPases. Additionally, the P5-ATPases are also marked by the additional helices present in the N-termini of these pumps. Topology prediction indicates two N-terminal helices (Ma, Mb) in the P5A-ATPase while only one (Ma) is present in the P5B-ATPases [134]. Considering the fact that the N-terminal domain regulates the catalytic cycle of P1B-ATPases [135], these additional N-terminal helices may be functionally important for the P5-ATPases. Indeed, a recent study in Hela cells suggests that the N-terminal helix (Ma) of ATP13A2, by binding to

Phosphatidic Acid (PA) and Phosphatidylinositol (3,5) bisphosphate (PI (3,5) P2), regulates the autophosphorylation of the transporter [136].

Apart from the structural divergence, P5A- and P5B-ATPases also exhibit different cellular localisation. Studies in different species revealed an exclusive localisation of the P5A-ATPase to the endoplasmic reticulum (ER) [137, 138]. Unlike the P5A-ATPase, the P5B subgroup show a diverse cellular localisation. CATP5, the P5B orthologue in *C.elegans*, was demonstrated to localise to the apical membranes of intestinal cells [139], whereas the P5B-ATPase in yeast (Ypk9p) resides in the vacuole [140]. Recently, overexpression of the human P5-ATPases in Hela cells confirmed the ER localisation of P5A-ATPase (ATP13A1), while the P5B-ATPases (ATP13A2-5) localised to the endo/lysosome compartments, corresponding to the vacuole localisation in yeast [141].

Unlike other P-type ATPases, the substrate specificity of the fifth subgroup had not been fully elucidated, though several candidates were proposed. P5A-ATPase loss of function was shown to affect calcium homeostasis in yeast (Spf1p) [142] and in barley (HvP5A1) [143]. However, it is still unclear whether the pump is directly involved in the transport of Ca^{2+}. The substrate preferences of the P5B subgroup is even more elusive. ATP13A2, a human P5B-ATPase homolog, was reported to governing Zn^{2+} and Mn^{2+} homeostasis while its deficiency leads to lysosomal and mitochondrial dysfunction in mammalian cells [144, 145]. Moreover, deletion of YPK9p sensitised yeast to Cd2+, Ni2+ and Se2+ toxicity, indicating a role of P5B-ATPases in the transport of heavy metal ions [146]. However, no mechanistic evidence was provided with respect to how P5B-ATPases mediate the translocation of these substrates across the membrane. Polyamines, a group of polycations essential for cellular functions, have recently been proposed as potential substrates for P5B-ATPase. CATP-5 deletion increased the tolerance to nor-spermidine in *C. Elegans [139]*. Additionally, in pancreatic cancer cells, the expression level of ATP13A3 correlates to the ^{3}H Spermidine uptake capacity [147]. Most recently, a

comprehensive study revealed that ATP13A2, another human P5B-ATPase, is an endo/lysosomal polyamine transporter, primarily responsible for releasing spermine into the cytosol. Incubation with spermine increases the ATPase activity while reducing the phospho-intermediate of ATP13A2 [148]. This study described, for the first time, the transport mechanism of human P5B-ATPases with polyamines as the preferable substrate. Functional disruption of the P5-ATPases has been linked to several different diseases (Table 1-5). *ATP13A2* is predominantly expressed in brain tissues, and loss-of-function mutations in this gene have been implicated in Kufor-Rakeb syndrome [149] and early-onset Parkinson's disease [150]. Mutations in *ATP13A4* were linked to specific language impairment [151, 152] and autism spectrum disorders (ASD) [153], though its functions are still unclear. Recently, several lines of evidence have also revealed *ATP13A3* as a novel disease-associated gene mutated in pulmonary arterial hypertension, further expanding the spectrum of the disease association of P5-ATPases [27, 103, 109].

1.2.3.4.1 ATP13A3 overview

ATP13A3 is a human homologue of the P5B-ATPases with unknown function. Even though ATP13A3 has been identified for decades, it remains one of the least characterised of the P-type ATPases. The gene encoding ATP13A3 is located on chromosome 3q29 in close proximity to the other two P5B members, ATP13A4 and ATP13A5 [141]. Phylogenetic analysis based on the primary amino acid sequences indicates ATP13A4 and ATP13A5 are closely related to ATP13A3 (Figure 1-8). ATP13A3 is a single-chain protein consisted of 1226 amino acids, though the protein structure of ATP13A3 has not been elucidated. Previously, in silico prediction of the topology of the P5B-ATPases proposed a transmembrane (TM) domain consisting of 11 TM segments [134]. However, by overexpressing human P5B-ATPases in Hela cells, Sørensen et al. have demonstrated that ATP13A2-4 share a topology consisting of 10 transmembrane helices [141]. Instead of spanning across the membrane, the

N-terminal helix was shown to be embedded in the membrane and regulates the autophosphorylation of ATP13A2 [136]. As discussed earlier, the transmembrane domains of the P-type ATPase are responsible for substrate binding. Considering the highly similar TM domain topology shared by ATP13A3 and ATP13A2, it is highly likely that ATP13A3 may also function as a polyamine transporter in cells.

Table 1-5 Transport substrates and disease involvement of the human P-type ATPase

Protein name	Substrate	Involvement in disease
P1B-ATPase		
ATP7A (Q04656)	Cu^{2+}	Menkes disease (MNKD)
ATP7B (P35670)	Cu^{2+}	Wilson disease (WD)
P2A-ATPase		
ATP2A1 (O14983)	Ca^{2+}	Brody myopathy (BRM)
ATP2A2 (P16615)	Ca^{2+}	Acrokeratosis verruciformis (AKV)
ATP2A3 (Q93084)	Ca^{2+}	
ATP2C1 (P98194)	Ca^{2+}	Hailey-Hailey disease (HHD)
ATP2C2 (O75185)	Ca^{2+}	
P2B-ATPase		
ATP2B1 (P20020)	Ca^{2+}	
ATP2B2 (Q01814)	Ca^{2+}	Heriditary deafness
ATP2B3 (Q16720)	Ca^{2+}	Spinocerebellar ataxia, X-linked 1 (SCAX1)
ATP2B4 (P23634)	Ca^{2+}	
P2C-ATPase		
ATP1A1 (P05023)	Na^+/K^+	Charcot-Marie-Tooth disease 2DD (CMT2DD)
ATP1A2 (P50993)	Na^+/K^+	Migraine, familial hemiplegic, 2 (FHM2)
ATP1A3 (P13637)	Na^+/K^+	Dystonia 12 (DYT12)
ATP1A4 (Q13733)	Na^+/K^+	
ATP4A (P20648)	H^+/K^+	
ATP12A (P54707)	H^+/K^+	
P4-ATPase		
ATP8A1 (Q9Y2Q0)	Phospholipid	
ATP8A2 (Q9NTI2)	Phospholipid	Cerebellar ataxia, mental retardation, and dysequilibrium syndrome 4 (CMARQ4)
ATP8B1 (O43520)	Phospholipid	Cholestasis, progressive familial intrahepatic, 1 (PFIC1) Cholestasis, benign recurrent intrahepatic, 1 (BRIC1)
ATP8B2 (P98198)	Phospholipid	
ATP8B3 (O60423)	Phospholipid	
ATP8B4 (Q8TF62)	Phospholipid	
ATP9A (O75110)	Phospholipid	
ATP9B (O43861)	Phospholipid	
ATP10A (O60312)	Phospholipid	Angleman syndrome (AS)
ATP10B (O94823)	Phospholipid	
ATP10D (Q9P241)	Phospholipid	
ATP11A (P98196)	Phospholipid	
ATP11B (Q9Y2G3)	Phospholipid	
ATP11C (Q8NB49)	Phospholipid	Hemolytic anemia, congenital, X-linked (HAXL)
P5-ATPase		
ATP13A1 (Q9HD20)	unkown	
ATP13A2(Q9NQ11)	polyamine	Kufor-Rakeb syndrome (KRS) Neuronal ceroid lipofuscinosis (NCL)
ATP13A3 (Q9H7F0)	unkown	Pulmonary arterial hypertension (PAH)
ATP13A4 (Q4VNC1)	unkown	specific language impairment (SLI) Autism spectrum disorders (ASD)
ATP13A5 (Q4VNC0)	unkown	

1.2.3.4.2 Expression of ATP13A3

Human

RNAseq data from the GTEX platform (https://www.gtexportal.org/home/) indicates ATP13A3 is widely expressed across human tissues. Interestingly, apart from the thyroid gland, a relatively high level of *ATP13A3* gene expression is observed in systemic arteries and lung tissues (Figure 1-9). Single-cell RNAseq using lung tissues from healthy subjects indicated that *ATP13A3* expression is abundant in pulmonary macrophages, dendritic cells and vascular endothelial cells [154] (Figure 1-10). Our group also confirmed the expression of *ATP13A3* in primary cultures of pulmonary artery smooth muscle cells (PASMCs), pulmonary artery endothelial cells (PAECs) and blood outgrowth endothelial cells (BOECs) [27]. Collectively, these suggest a potential link between *ATP13A3* and the human pulmonary vasculature.

Mouse

Similar to the human, *Atp13a3* is also widely expressed in different mouse tissues, with the highest mRNA expression observed in the liver. A later developmental study in mice [155] demonstrated the existence of two *Atp13a3* transcript variants, with variant 1 highly expressed in brain, heart and lung and variant 2 in the kidney. *Atp13a3* was also shown to be highly expressed at early developmental stages, with a peak of expression at E7 [156]. This observation suggested a potential role of Atp13a3 in organogenesis. More recently, single-cell transcriptome analysis of various mouse organs revealed enriched *Atp13a3* expression in the lung epithelial cells [157], again suggesting *Atp13a3* has a role in pulmonary physiology.

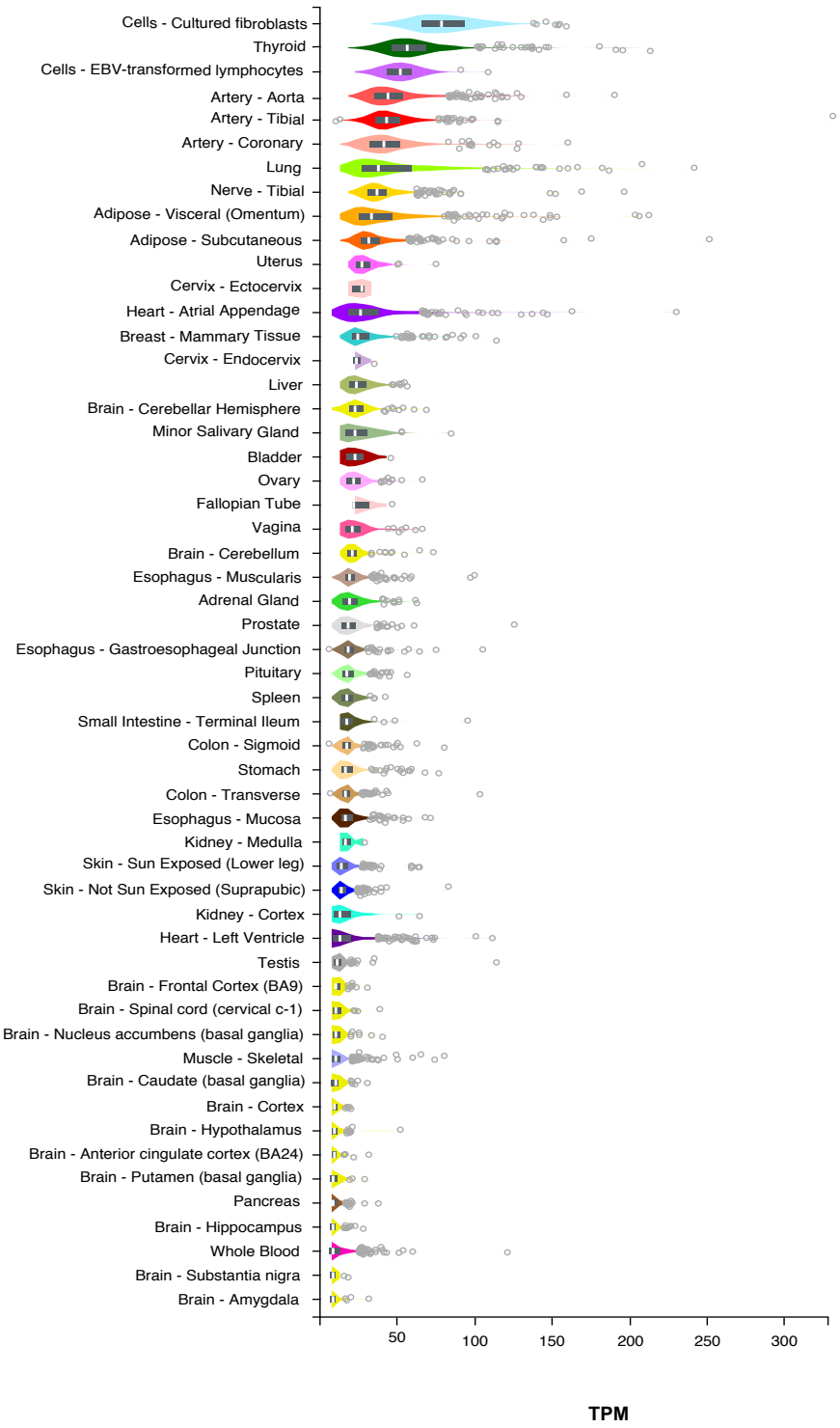

Figure 1-9 Gene expression of ATP13A3 in human cell and tissue samples

Gene expression of *ATP13A3* across 53 different types of human tissues was generated the RNA-seq data from the Genotype-Tissue Expression Consortium (GTEx V7) (https://www.gtexportal.org/home/). Expression level was presented as Transcripts per Million (TPM).

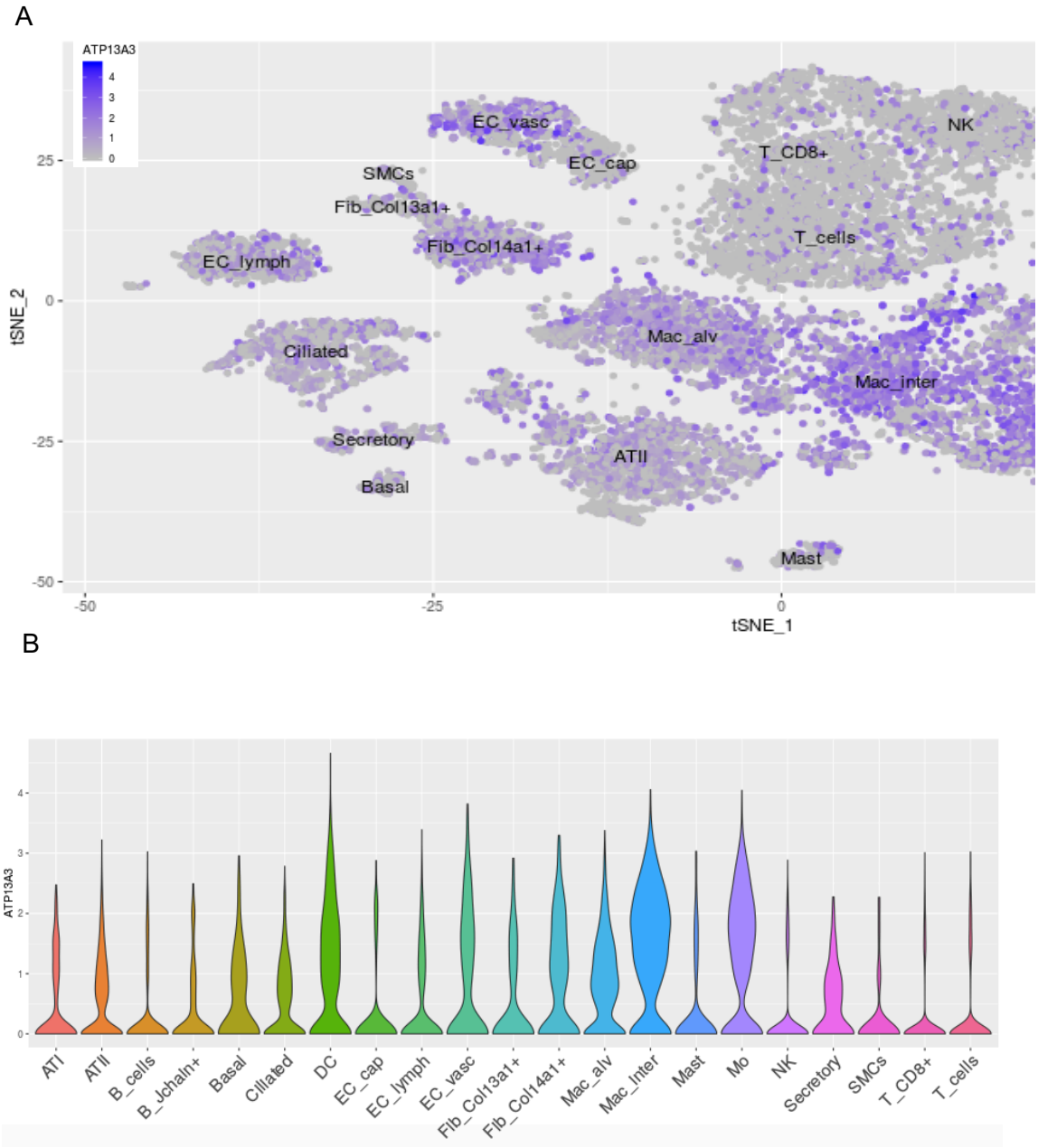

Figure 1-10 ATP13A3 expression pattern in single-cell RNAseq data from human lung tissues from healthy subjects

(A) *ATP13A3* expression clustering in 21 different types of human pulmonary cells. Data were generated from Lungconnectome [154] (http://www.lungconnectome.net.). The relative gene expression level is indicated by the colour intensity. (B) *ATP13A3* relative expression was plotted for different cell types.

1.2.3.4.3 Biological functions of ATP13A3

To date, studies of the biological functions of ATP13A3 are sparse. P-type ATPase activation is characterised by the phosphorylation of an aspartyl residue during the catalytic cycle. In Cos-8 cells, overexpressed human ATP13A3 was shown to be autophosphorylated at the conserved Asp_{498} site [141]. Classified as a P5B-ATPase, ATP13A3 is predicted to be a cation transporter, though the substrate specificity is still unclear. CATP-5, a *C. elegans* orthologue of three human P5B-ATPases (ATP13A3, ATP13A2, ATP13A4), localised to the apical membranes of intestinal cells and was linked to polyamine transport. CATP-5 loss of function led to reduced polyamine content and hence suppressed postembryonic development [139]. A recent study in human pancreatic cancer cells also revealed a positive correlation between the levels of *ATP13A3* expression and spermidine uptake [147]. These findings suggest polyamines may be potential substrates for ATP13A3. However, direct studies are necessary to establish the transport preference for particular polyamines and the mechanism of this transport.

In silico analysis, using a publicly available human gene expression database [158] (PathwayNet platform http://pathwaynet.princeton.edu) reveals a potential interaction between *ATP13A3* and several candidate genes. Among these, hypoxia inducible factor-1 α-unit (*HIF-1α*) has the highest confidence (0.95) of interacting with *ATP13A3* (Figure 1-11). HIF1α is a subunit of the transcriptional factor hypoxia-induced factor 1 (HIF1). In normoxia, HIF1α is constantly degraded through ubiquitin-mediated proteasomal degradation [159]. Hypoxia stabilises HIF1α expression by suppressing this ubiquitination [160]. By then dimerising with HIF1β and mediating transcription, a set of HIF1 target genes are transactivated [161]. Intriguingly, it has been reported that HIF1α can bind to the promoter region of ATP13A2 [162], another P5B ATPase sharing high homology to ATP13A3. Pharmacological inhibition of HIF1α hydroxylation increases *ATP13A2* expression by preserving HIF1α levels [163]. Therefore, studies to explore a potential regulatory link between HIF1α and ATP13A3 are

warranted. Moreover, by using subtractive suppression hybridisation, Habtemichael and co-workers showed upregulation of a homologous gene of the ATPase family (AFURS1) in senescent human parenchymal kidney cells [164]. AFURS1, localised to chromosome 3q26, encodes a 701 amino acids isoform with a high degree of homology to ATP13A3. Again, this suggests that a possible link between ATP13A3 and ageing might warrant further study.

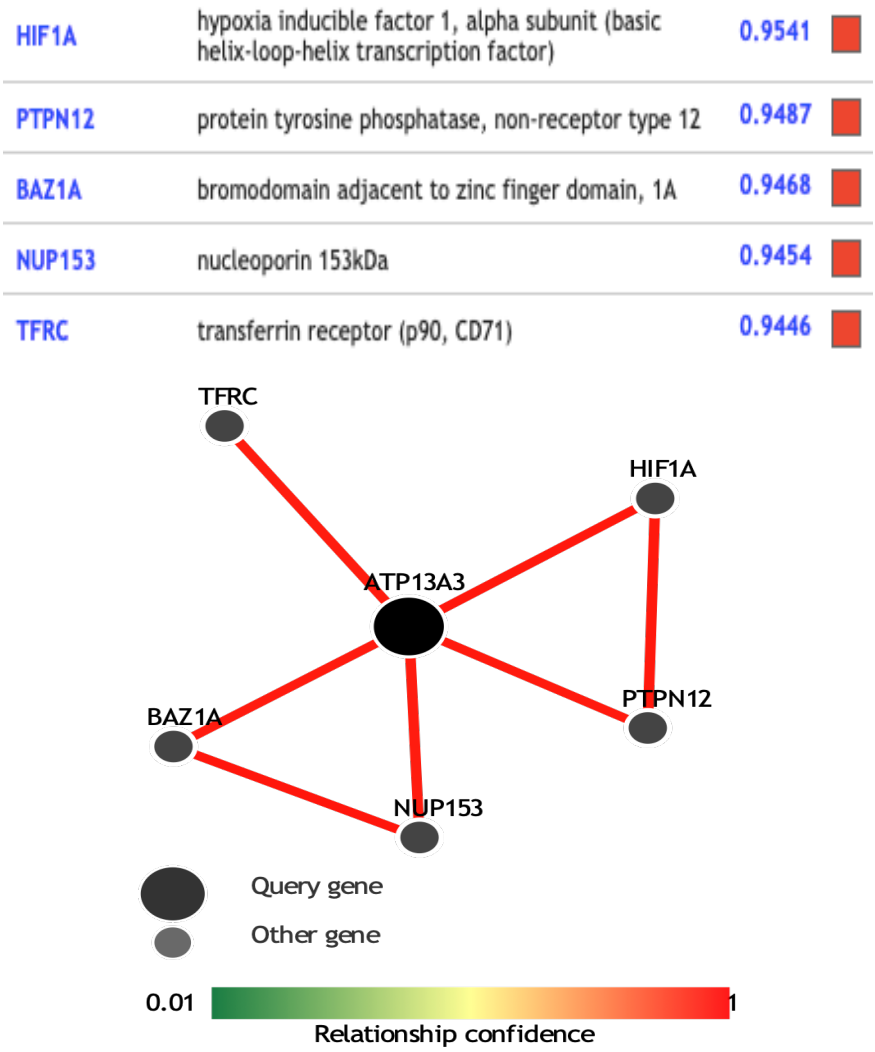

Figure 1-11 In silico prediction of the potential interactions between ATP13A3 and other genes.

Top 5 candidate genes potentially may interact with *ATP13A3* (confidence>0.94), as revealed by in silico analysis using the PathwayNet [158] platform (http://pathwaynet.princeton.edu).

1.2.3.4.4 ATP13A3 and PAH

Recently a large European-wide genetic study identified rare *ATP13A3* variants in blood samples from I/HPAH patients. These variants were inherited in an autosomal dominant manner with incomplete penetrance [27]. PAH patients with *ATP13A3* mutations were predominantly female (90.9%), with a similar age at diagnosis to those without mutations (47.5 years vs 52.6 years). The disease severity of *ATP13A3* mutation carriers was comparable to those bearing *BMPR2* mutations [27]. Later, other PAH genetic studies revealed additional variants in *ATP13A3*, further strengthening the link between *ATP13A3* mutations and the pathogenesis of PAH [102, 103]. Interestingly, an IFNβ-induced PAH case was reported recently in a multiple sclerosis patient bearing a nonsense mutation in *ATP13A3* [109]. This observation suggests the possibility that an additional pathological stimulus may be required to induce PAH on the background of *ATP13A3* mutations, explaining the reduced penetrance. In addition, ATP13A3 is potentially linked to dysregulated TGFβ signalling in PAH. Microarray analysis following 4-hour TGFβ incubation revealed upregulated *ATP13A3* expression in hPASMCs from HPAH patients bearing *BMPR2* mutations, but not in control cells [165]. However, no functional studies have been undertaken with respect to the role of ATP13A3 in the pulmonary vasculature.

1.2.3.4.5 ATP13A3 and cancer

Aside from PAH, ATP13A3 has also been implicated in cancer biology. As described above, ATP13A3 is associated with spermidine uptake in pancreatic cancer cells, with cells expressing higher levels of ATP13A3 showing high sensitivity to difluoromethylornithine (DFMO), an irreversible ODC inhibitor which binds to the ornithine substrate binding site. This suggests that cells with higher *ATP13A3* expression are more committed to polyamine transport. Therefore, plasma ATP13A3 levels were proposed as a clinical indicator for the

efficiency of DFMO treatment in pancreatic cancer patients [147]. ATP13A3 was also demonstrated as a prognostic marker in head and neck cancer, with those patients having higher *ATP13A3* overexpression in the tumour sites showing a lower overall survival rate (HR=1.45) [166]. However, no mechanistic insights were described in this study with respect to how increased levels of *ATP13A3* may affect the prognosis in head and neck cancer. To assess a potential link between ATP13A3 and survival of cancer cases in general, I have used the TCGA database to compare the overall survival between *ATP13A3* somatic mutation carriers and non-mutation carriers. In total, 10843 cancer cases were studied, including 1744 cases with mutations in *ATP13A3*. The overall survival rate between the two groups was statistically analysed by a log-rank test. Interestingly, without further cancer type stratification, ATP13A3 mutation carriers showed an overall poorer survival rate than those non-mutation carriers (Figure 1-12). This suggests a potential link between *ATP13A3* genetic defects and cancer prognosis, though further investigations are necessary.

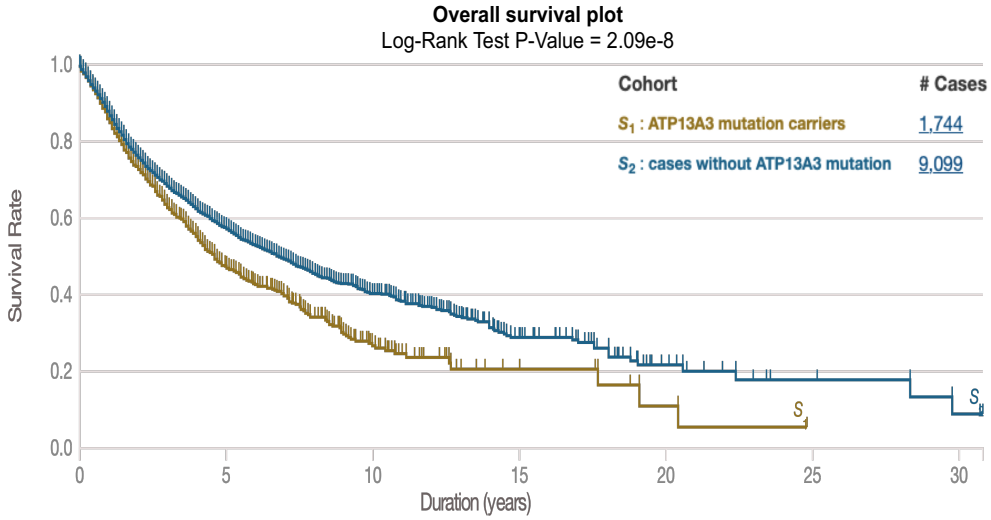

Figure 1-12 Overall survival rate of cancer cases with or without ATP13A3 mutations Survival rate of cancer cases with (1744 cases) or without (9099 cases) ATP13A3 mutations were extracted from the TCGA database followed by log-Rank test (P-Value=2.09e-8).

1.3 Polyamines in Biology

1.3.1 Polyamines

Polyamines are a group of highly charged aliphatic polycations ubiquitously existing in nature. The first report of polyamines dates back to 1678 when Leeuwenhoek observed crystals forming in seminal fluid [167], which were later demonstrated to be spermine phosphate [168]. Putrescine (PUT), spermidine (SPD) and spermine (SPM) are the three most common polyamines present in mammalian cells while cadaverine (CAD) is mainly found in bacteria and plant [169]. Though they are small molecules, these polycations are essential for many cellular processes, and their dysregulation could affect cell functions [104, 170, 171]. Therefore, to maintain a homeostatic balance, cellular polyamine levels are fine-tuned by two sophisticated pathways, polyamine biosynthesis and the polyamine transport system.

1.3.2 Polyamine biosynthesis

De novo polyamine biosynthesis is essential for maintaining the stable level of cellular polyamines. A detailed summary of polyamine biosynthesis is listed in Figure 1-13. Arginine, a substrate for several pathways including the nitric oxide synthase pathway, is converted to ornithine by Arginase 1. Putrescine, the first mammalian polyamine is synthesised from ornithine by the catalysis of ornithine decarboxylase (ODC). This is the rate-limiting step for polyamine biosynthesis[172]. Upon formation, putrescine is converted to spermidine by the addition of an aminopropyl group. This step is catalysed by spermidine synthase, with the aminopropyl group donated via the decarboxylation of S-adenosylmethionine by S-adenosylmethionine decarboxylase (encoded by *AMD1*). Spermine is formed in a similar manner, with spermine synthase catalysing the addition of an aminopropyl group to spermidine (Figure 1-13).

1.3.2.1 Transcriptional regulation of Ornithine decarboxylase (ODC)

As the key enzyme for the polyamine biosynthesis pathway, ODC is regulated at multiple levels to maintain a stable cellular polyamine level. Increased synthesis of *ODC* mRNA is seen in response to stimuli such as tumour promoters and hormones in a cell-context dependent manner. This is largely owing to the complexity of *ODC* promoter region which contains a binding motif for SP-1, a CAAT site, an LSF site, a cyclic AMP (cAMP) response element (CRE), multiple GC- boxes, and a TATA box (Figure 1-14). For example, the transcription factor SP-1 was shown to promote basal *Odc* expression in rat H35 hepatoma cells [173]. 17b-estra- diol (E2) was also reported to induce *ODC* expression in human breast cancer cells [174], whereas 12-O-tetradecanoylphorbol-13-acetate (TPA) upregulated *Odc* levels in mouse fibroblasts by binding to the TATA box in the promoter region [175]. Additionally, *ODC* is also well recognised as a downstream target of *c-Myc*, the potent oncogene which in tumour cells increases *ODC* expression by dimerising with *Max* to form a transcription complex (Figure 1-14). The myc/Max complex binds to the CACGTG E-boxes within the first intron of *ODC* gene and transactivates *ODC* mRNA overproduction. Interestingly, in BALB/c-3T3 fibroblasts under quiescent conditions, the CACGTG E-boxes is occupied by Mnt/Max, resulting in a lower level of *Odc* expression. Serum stimulation in these cells triggers the displacement of Mnt/Max by the Myc/Max complex and increases *Odc* expression [172].

1.3.2.2 Translational regulation of Ornithine decarboxylase (ODC)

ODC is also regulated at the translational level through a cap-dependent or independent internal ribosome entry site (IRES) mechanism. The *ODC* mRNA possesses a long 5'-UTR and hence needs eIF4E to unwind the extensive secondary structure for cap-dependent translation initiation. pMV7-4E cells (derived from NIH-3T3 cell) overexpressing *eIF4E* express high levels of *Odc1*

[176]. This long 5'-UTR also contains an inhibitory open reading frame (ORF) which suppresses ODC translation [172]. Apart from cap-dependent translation, ODC was also demonstrated to be translated via the internal ribosome entry site (IRES). It was shown in Hela cells that ODC translation alternates between cap-dependent and cap-independent mechanisms over the cell cycle. During the G2/M phase, Hela cells utilise the IRES for ODC translation and hence are insensitive to translational inhibition by rapamycin [177].

1.3.2.3 Post-translational regulation of Ornithine decarboxylase (ODC)

Although ODC regulation happens at both the transcriptional and translational level, the most extensively studied process is post-translational regulation. ODC protein is rapidly turned over, with a half-life of less than 30 minutes in mammalian tissues [178]. Upon synthesis, ODC is rapidly degraded via a ubiquitination-free 26S proteasomal degradation. This process is mediated by antizyme, which forms a non-covalent heterodimer with ODC and directs it to the proteasome [179] (Figure 1-15 A). The binding of antizyme (residue 106 –212) to ODC (residue 117– 140) prevents its enzymatic activity. However, this region is not sufficient for mediating ODC degradation, and the additional residues at positions 55-105 are required for directing ODC to the 26S proteasome [180]. Antizyme enhances the interaction of ODC with the proteasome without affecting the processing rate [181]. On the other hand, degradation of ODC does not induce the breakdown of antizyme. Instead, antizyme is released and binds to other ODC monomers to mediate their degradation [182]. Post-translational regulation of ODC is achieved by tightly controlled antizyme expression (encoded by *OAZ1*). The synthesis of antizyme is regulated through a unique frameshifting event caused by ribosome skipping during scanning of the antizyme mRNA (Figure 1-15 B). The antizyme mRNA has two overlapping open reading frames (ORF1 and ORF2). Typically, ORF1 can encode 68 amino acids and is terminated by a UGA stop codon (UCC UGA).

ORF2, which encodes the main part of antizyme, is in the +1 frame with respect to ORF1 and starts before the end of ORF1. ORF2 is only accessed by ribosomes that first translate ORF1 and is only translated when the ribosome skips to the +1 reading frame for translation. This frameshift event is induced by an increase in cellular polyamine levels, thus inducing the production of the full-length functional antizyme (Figure 1-15 B) [179, 183]. Increased cellular polyamine levels also block antizyme degradation by inhibiting ubiquitination [184] while polyamine depletion in Balb/C 3T3 cells via DFMO represses antizyme mRNA expression [185]. In 1982, another protein, antizyme inhibitor, was discovered in rat liver and heart tissues. This shares a high degree of homology to ODC but lacks enzymatic activity [186]. The antizyme inhibitor has a higher affinity for antizyme than ODC and hence can preserve ODC by releasing it from the antizyme-ODC heterodimer [187, 188]. The expression of antizyme inhibitor is also actively regulated by polyamines, with high levels repressing the production of the antizyme inhibitor [189] (Figure 1-15 A). Taken together, ODC expression is tightly controlled by the cellular polyamine level through the post-translational regulation orchestrated by antizyme and antizyme inhibitor.

1.3.3 Polyamine catabolism

In opposition to synthesis, spermine and spermidine can be metabolised to their precursors through acetylation and oxidation reactions mediated by polyamine catabolic enzymes. Spermine and spermidine are firstly acetylated by spermidine/spermine acetyltransferase (SSAT). The resulting metabolites, acetyl-spermidine/spermine, are then either excreted from cells or oxidised by polyamine oxidase (PAO) to form spermidine and putrescine, respectively (Figure 1-13). In addition, spermine can be directly oxidised by spermine oxidase (SMOX) to form spermidine (Figure 1-13). These oxidative reactions also produce amino aldehyde and H_2O_2, which can be cytotoxic when excessive quantities accumulate [170]. Similar to polyamine biosynthesis, the

catabolic pathway is tightly regulated by polyamine levels. For example, in cancer cells, higher polyamine levels increased the transcription of *SAT1* expression by binding to the 5' polyamine-responsive-element (PRE) in the *SAT1* gene, thus promoting to the catabolism of polyamines. These dynamic changes, together with the biosynthesis pathway, guarantees a carefully regulated narrow range of cellular polyamine levels.

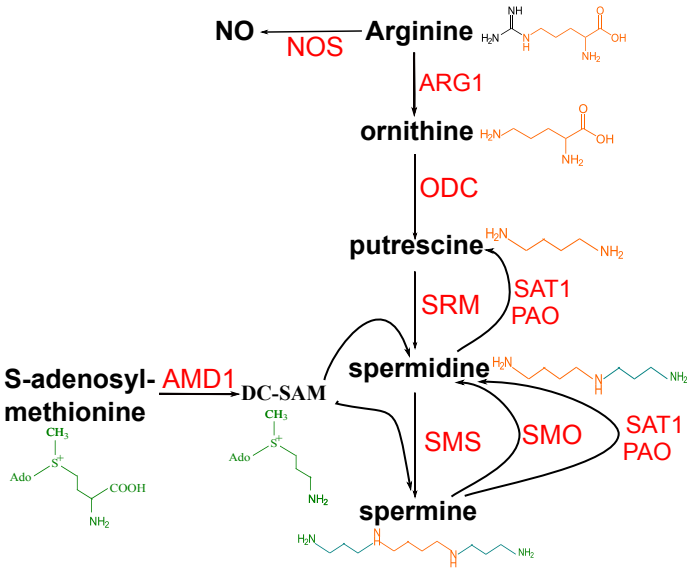

Figure 1-13 Schematic of the polyamine metabolism pathways Arginine can be turned into ornithine (by arginase) or serves as the precursor for NO (catalysed by NOS) in cells. Ornithine is then transformed into putrescine by the rate-limiting enzyme ODC. Spermidine and spermine are subsequently synthesised by receiving an aminopropyl from the decarboxylation of SAM. For the catabolism pathway, spermine and spermidine are interconverted to their precursors first by SAT1 mediated acetylation and then oxidisation by PAO. Uniquely, spermine can be directly oxidised by SMO to form spermidine. NOS, nitric oxide synthase; ARG1, arginase1; ODC, ornithine decarboxylase; DC-SAM, decarboxylated S-adenosyl-L-methionine; AMD1, Adenosylmethionine Decarboxylase 1; SRM, spermidine synthase; SMS, spermine synthase; SAT1, spermidine/spermine acetyltransferase; PAO, polyamine oxidase

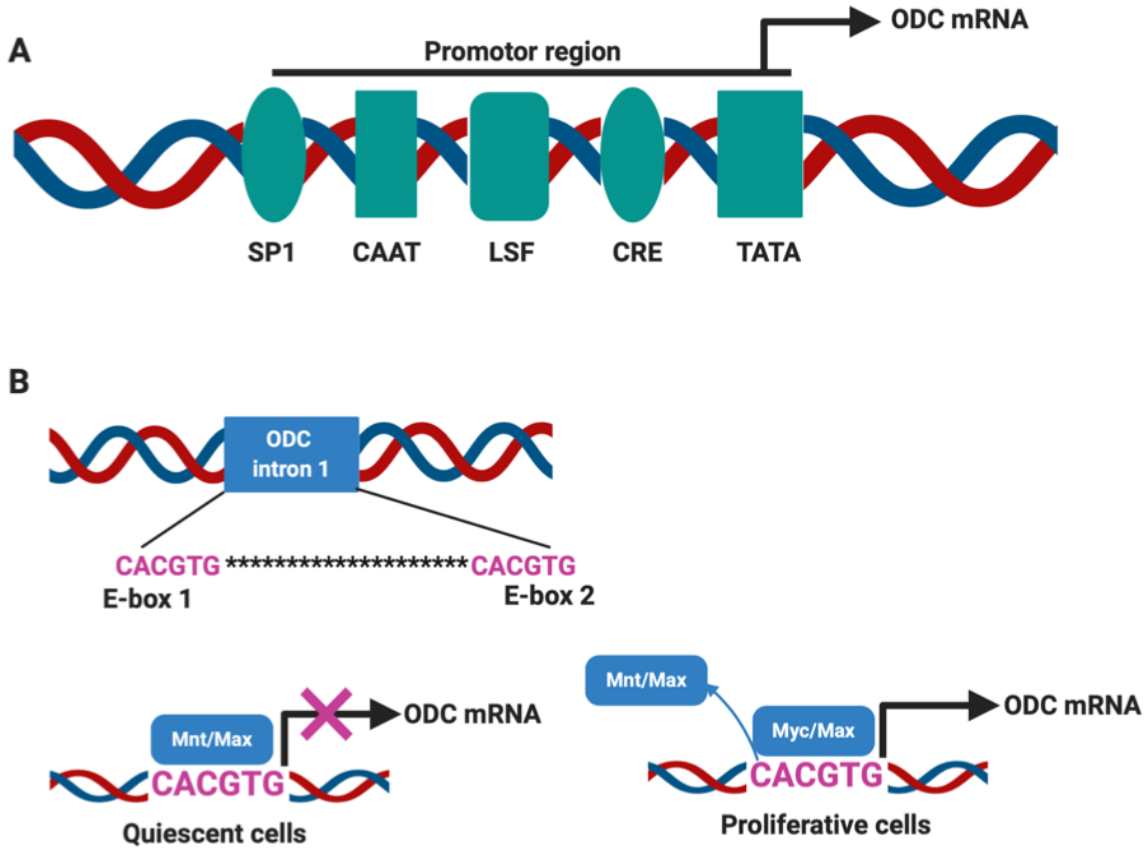

Figure 1-14 Transcriptional regulation of ornithine decarboxylase (ODC)

(A) The promoter region of the *ODC* gene contains several regulatory elements, including the SP-1 motif, a CAAT site, an LSF site, a cAMP response element (CRE), multiple GC- boxes, and a TATA box (TPA binding site). (B) Intron 1 of the *ODC* gene has two CACGTG E-boxes which can bind to *Myc.* Under quiescent conditions, these E-boxes are occupied by the Mnt/Max complex resulting in low *ODC* mRNA expression. However, when cells are proliferating (e.g. serum exposure), the Mnt/Max dimer is replaced by the Myc/Max complex, thus promoting ODC production. Figure 1-13 B readapted from (Pegg, Anthony E. JBC 2006)[172].

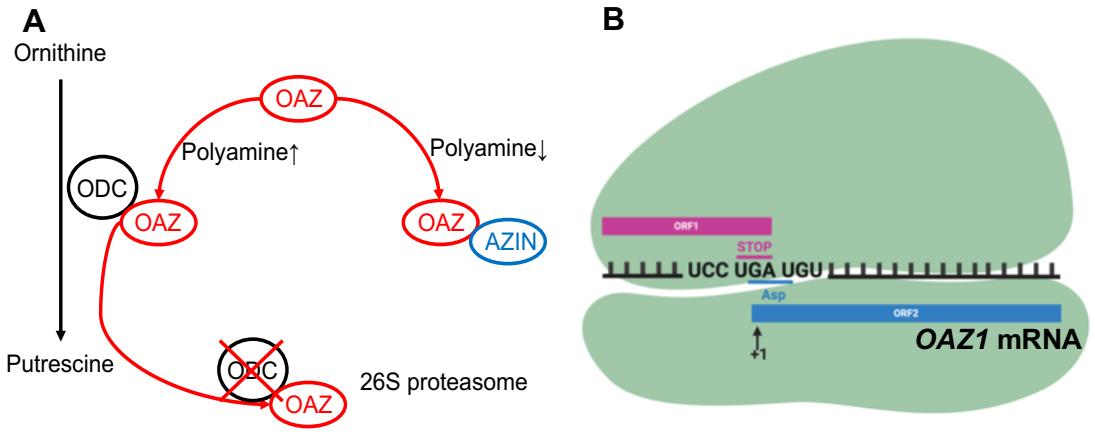

Figure 1-15 Antizyme / Antizyme Inhibitor regulation of ODC (A) Post-translational regulation of ODC is orchestrated by antizyme and antizyme inhibitor in a polyamine dependent manner. When polyamine levels are high, a unique ribosomal frameshifting event (B) is triggered to promote the production of the full-length functional antizyme. Conversely, when cellular polyamine levels drop, the expression of antizyme inhibitor is induced and ODC is liberated from the ODC-antizyme heterodimer, thus preserving its protein expression.

1.3.4 Polyamine transport

In addition to the biosynthesis/catalysis pathways, cellular polyamine levels are also tightly regulated by an energy-consuming, high-affinity and saturable polyamine transport system [190]. Although well described in simple life forms such as yeast and trypanosomatids [191], the molecules involved and mechanistic details of mammalian polyamine transport systems remain enigmatic. Over the past few decades, by using in silico identification combined with screening substrates of interests, polyamine transport activities were assigned to several members of the solute carrier (SLC) and ATP-binding cassette superfamily (Table 1-6). These membrane transporters are not primarily responsible for translocating polyamines. Instead, many of them also transport other basic amino acids which are structurally similar to polyamines [190]. Most recently, ATP13A2, a P5B-ATPase was uncovered as a spermine exporter residing in the endo/lysosomal compartment. Considering the high

homology shared by ATP13A2-5, this finding suggests the potential involvement of other P5B-ATPases in mammalian polyamine transport [148].

1.3.4.1 General characteristics of mammalian polyamine transporters

Though the mechanism is not fully understood, mammalian polyamine transporters seem to share some general characteristics which were elegantly summarised by Poulin and co-workers [190]. Contrary to the initial finding that polyamine transport is Na^+-dependent [192], subsequent evidence indicated that polyamine uptake is suppressed by high concentrations of monovalent cations (Na^+, Li^+), as a complete replacement of these cations with non-(sucrose) promoted putrescine uptake [193, 194]. Based on this property, polyamine transporters can potentially be classified into two groups: (a) Diamine transporters (e.g. putrescine) that are monocation-sensitive or (b) higher polyamine transporters (e.g. spermidine/spermine) that are less sensitive to these monocations [190]. Contrary to the inhibitory effect of Na^+, polyamine transporters seem to favour the binding of divalent metals, such as Mn^{2+}, Ca^{2+}, Mg^{2+}, Co^{2+}, to their exofacial portion for translocating polyamines, though the underlying mechanism is still unclear [193, 195]. Similar to other cation transporters, mammalian polyamine transport systems were also shown to be membrane potential dependent as seen in SLC22A1 and SLC22A3 [196]. In addition, pH is another parameter that affects polyamine transport in mammalian cells. It was demonstrated in L1210 mouse leukaemia cells that putrescine uptake was optimal at pH 7.2-8.0 while suppressed between 6.0-7.0. Spermidine transport, however, prefers mildly acidic conditions (pH 6.8-7.7) [193]. In addition to pH, polyamine transport is also affected by osmolality. It has been demonstrated that hypo-osmotic conditions increase putrescine uptake more efficiently than spermidine or spermine in L1210 mouse leukaemia cells [197] [198]. The presence of the carboxyl side group in the polyamine transporters was also shown to be essential for polyamine uptake as chemical

inhibition of the carboxyl group by N-ethylmaleimide suppressed polyamine uptake in CHO cells [199].

Table 1-6 Summary of mammalian polyamine transporters

Transporter	Tissue distribution	Substrate	Reference
OCT1 (encoded by SLC22A1)	Widely expressed High in liver	Spd/Spm/Agmatine	[196, 200, 201]
OCT2 (encoded by SLC22A2)	distal tubules of kidney	Agmatine PUT	[200]
OCT3 (encoded by SLC22A3)	Liver, skeletal muscle, heart, placenta	Agmatine	[201]
MATE1 (encoded by SLC47A1)	High in kidney	Agmatine	[200]
DAX (encoded by SLC3A2)	Widely expressed	PUT	[202]
CCC9a (encoded by SLC12A8A)	Lowly expressed across tissues	Polyamines	[203]
OCT6 (encoded by SLC22A16)	Highly expressed in testis	Polyamines	[204]
MDR1 (encoded by ABCB1)	small intestine, liver and brain	Spd	[205]
SLC18B1	predominantly in hippocampus	Spd/Spm	[206]
ATP13A2	Widely expressed High in brain and pituitary	Spm	[148]

1.3.4.2 Hypothetical models for mammalian polyamine transport

Although a unified theory of how polyamines translocate across mammalian cells is not yet available, several hypothetical models have been proposed to explain this biological enigma. As illustrated in Figure 1-16, the first model was a two-step process described by Soulet et al. [207]. By using Spd-C2-BODIPY, they demonstrated in CHO cells that polyamines were first imported through a

plasma membrane channel and subsequently sequestered into vesicles via a vesicular transporter. The vesicles sequestering polyamines mainly colocalised with acidic cellular compartments (lysosomes, late endosomes and multivesicular bodies), with inhibition of the vacuolar ATPase (V-ATPase) repressed by polyamine accumulation. This suggests that the V-ATPase, by creating an inward electrochemical H^+ gradient, sustains a H^+/polyamine exchange mediated by the vesicular transporter. Moreover, a relatively slower efflux pathway was also proposed in the same study, potentially through another vesicular channel, though they did not exclude the possibility of reverse transport through the same vesicular transporter. No transporters were specified in this model.

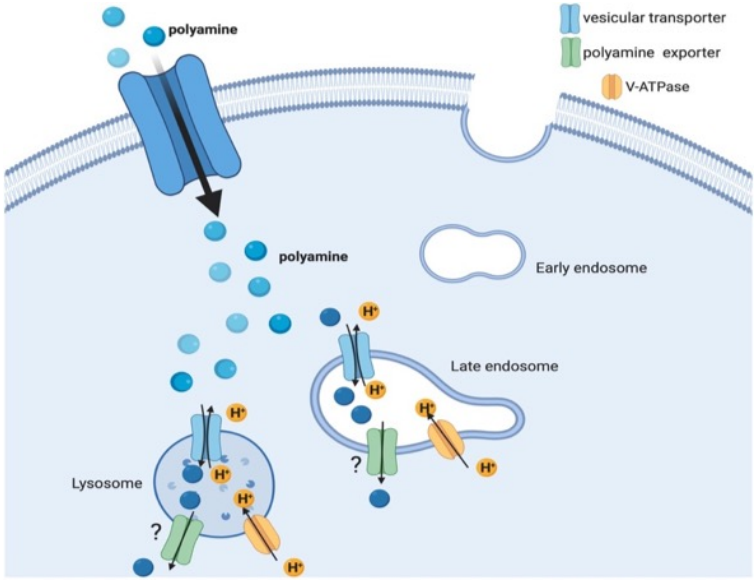

Figure 1-16 Schematic of the "two-step" polyamine transport model In CHO cells, polyamines enter cells via a plasma membrane channel and are subsequently sequestered into acidic vesicles through an unknown vesicular transporter. This process is facilitated by the H+ gradient created by the V-ATPase in these vesicles. A vesicular exporter may exist for polyamine efflux into the cytosol. However, it is also possible that the same vesicular transporter may export the polyamine in reverse.

A second model which mainly applies to spermine uptake was proposed by Beltings M and colleagues [208]. In this model, spermine import was mediated

by binding to the heparan sulfate (HS) chains of glypican-1 on the plasma membrane of CHO cells. Spermines were then internalised through the endocytic pathway. When reaching the late endosome, NO produced via the nitrosylation of glucosamine groups in glypican-1 by NO synthase 2 (NOS2), in the presence of copper, liberated spermine by the cleavage of spermine-HS binding. A detailed mechanism for the release of spermines from endosomes was not proposed in this model (Figure 1-17).

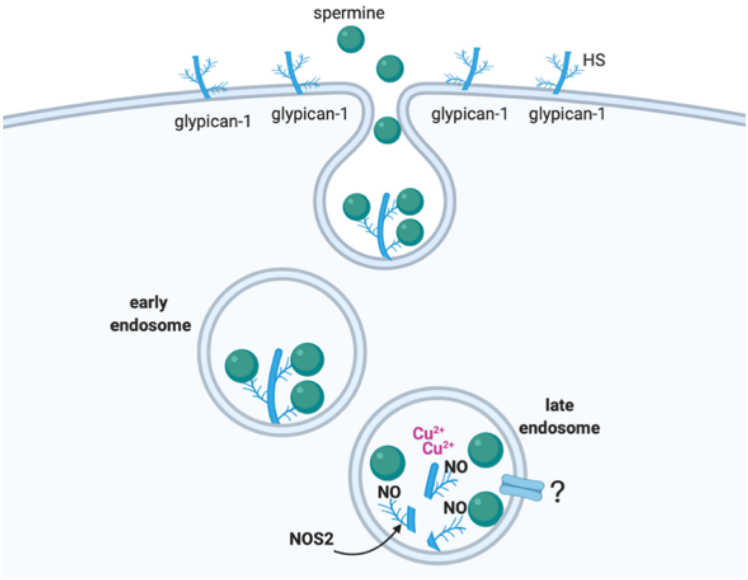

Figure 1-17 Glypican-1 mediated spermine uptake in CHO cells In CHO cells, spermine first binds to the heparan sulfate side chains of glypican-1 and is then internalised via endocytosis. Spermine is transported through the endocytic pathway, and when they reach the late endosome, spermine-HS binding is cleaved by NO (produced by NOS2) via a Cu2+ dependent process. This frees spermine from glypican-1, although the mechanism of spermine efflux was not discussed.

Based on the second of these models, a caveolin-mediated polyamine endocytosis mechanism was described by Gerner and colleagues [209]. In this model, polyamines first bind to an unspecified polyamine binding protein in the caveolin-1 rich region on the cell surface and are internalised through the caveolar endocytosis (Figure 1-18). Increased putrescine uptake was observed in human colorectal carcinoma cells with caveolin-1 knockdown and tissues

(small intestine, colon and liver) from caveolin-1 knockout mice. This was interpreted as an increase in caveolar endocytosis with caveolin-1 deficiency increased both the frequency and number of internalised caveolae. However, it is noteworthy that the caveolin-1-dependent regulation of caveola formation may differ between cells, as caveolae were absent in the pulmonary endothelium of caveolin-1$^{-/-}$ mice [210]. Therefore, further validation is required in the pulmonary circulation system. Similar to the glypican-1 model, NO produced by NOS2 was proposed to dissociate polyamines from the polyamine binding protein. This was supported by the observation that the *NOS2* knockout abolished putrescine import in mouse tissues. Again, this model does not address the pathway for polyamine release from the vesicle into the cytoplasm. Instead, SLC3A2 was proposed as a cell surface putrescine exporter (Figure 1-18).

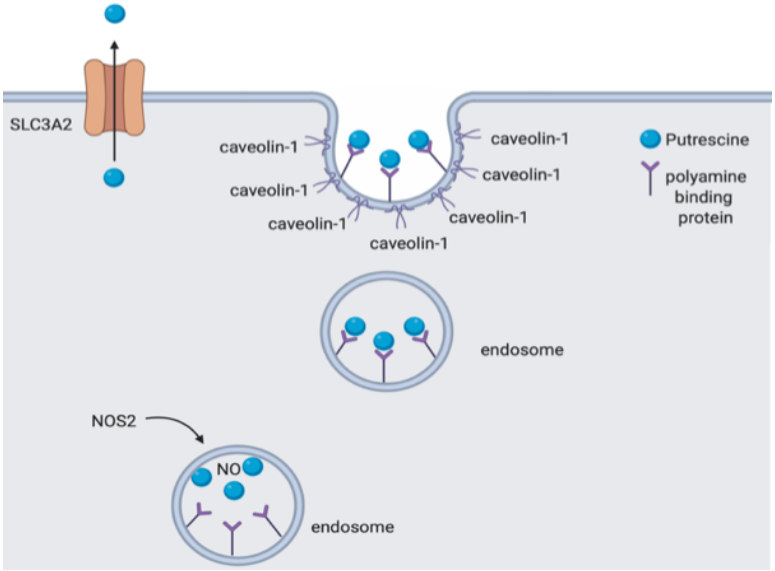

Figure 1-18 Caveolin-mediated polyamine endocytosis For entering cells, polyamines (PA), notably putrescine bind to the cell surface PA binding protein in the caveolin-1 rich region and internalise via caveolar endocytosis. NO released by NOS2 liberates polyamines from their binding proteins in endosomes. However, no vesicular efflux pathway for polyamines were proposed, although SLC3A2 was described as a cell surface exporter of putrescine

1.3.4.3 Regulation of the mammalian polyamine transport

It is well established that increased polyamine levels contribute to the hyper-proliferative phenotype of cancer cells. Considering that many of the growth factors and cytokines are upregulated in cancer cells or tumour tissues, it is not entirely surprising that these factors may promote polyamine transport in cancer. For example, both oestrogen and insulin were demonstrated to promote polyamine transport in human breast cancer cells [211], while IL-3 and IL-4 were shown to stimulate spermidine uptake [212]. Intriguing, it has also been reported that polyamine transport activities can be inhibited by antizyme. In rat hepatoma cells (Hz7), which exhibit high expression of antizyme in response to dexamethasone, J L Mitchell and colleagues demonstrated an inhibitory effect of antizyme on cellular spermidine uptake and ODC activities. However, the detailed mechanism was not determined in this study [213]. Whether antizyme directly binds to the cellular polyamine transporter to mediate this inhibitory effect or if it indirectly affects the endocytosis pathway remains elusive.

1.3.5 Biological functions of polyamine

Polyamines are small aliphatic polycations involve in multiple cellular processes. Owing to their highly-charged property, polyamines tend to bind to anionic molecules, such as DNA, RNA and phospholipids [214] and hence perform their biological functions.

1.3.5.1 Nucleotides structural and conformation

The binding of polyamines to DNA involves the ionic interaction between the amine groups in polyamines and the DNA phosphate groups. This interaction stabilises the DNA structure, protecting it from environmental insults (e.g. radiation) and can also facilitate DNA condensation [215]. Polyamines are also essential modulators for chromatin remodelling via the regulation of histone acetylation. In the skin of the k6/ODC transgenic mouse, ODC overexpression was reported to induce the activities of histone acetyltransferase and

deacetylase [216]. In addition to DNA, polyamines also bind to RNA such that up to 80% of cellular polyamines are associated with RNA [217]. Polyamines, by interacting with nucleotide bases, can also stabilise tRNA structure (with the affinity decreasing in order from spermine to putrescine) [218].

1.3.5.2 Gene expression regulation

It is well established that polyamines play important role in the transcriptional regulation of gene expression. By interacting with the polyamine-responsive element (PRE) in the promoter region of *SAT1* to induce expression, polyamines can trigger the polyamine catabolic pathway [219]. Moreover, polyamines also promote gene expression indirectly via transcriptional induction of transcription factors. For example, in rat kidney epithelial cells, spermidine stimulated the expression of *c-Myc*, whereas *c-jun* and c-fos were more sensitive to putrescine supplementation. The activation of these transcription factors, in turn, upregulated a set of downstream cell growth-related genes [220]. Polyamines also participate in the modulation of signal transduction by either directly stimulating protein kinase activities [221] or via promoting the expression of these protein kinases [222]. Putrescine and spermidine can also facilitate the phosphorylation mediated by tyrosine kinases, indicating an important role of polyamines in cell proliferation [222].

1.3.5.3 Protein synthesis

The association of polyamines with the regulation of protein synthesis was primarily investigated based on their RNA binding property. Indeed, in rat liver cell-free systems, these small polycations can either directly stimulate or decreased the optimal Mg^{2+} concentration for protein synthesis [223, 224]. As described above, cellular polyamine levels regulate antizyme translation via a ribosomal frameshifting event, thus regulating the rate of ODC degradation. A unique regulation comes from spermidine, as it serves as the aminobutyl group donor for the generation of hypusine, an amino acid only found in eukaryote, and essential for the activation of eukaryotic initiation factor 5A (eIF5A) [186].

This is achieved via a two-step catalytic reaction. Firstly, an aminobutyl moiety from spermidine is transferred to the lys_{50} residue in eIF5A by deoxyhypusine synthase (DHS) to form the eIF5A deoxyhypusine. Deoxyhypusine hydroxylase (DOHH) then mediates the hydroxylation of deoxyhypusine eIF5A, resulting in hypusinated eIF5A. Hypusinated eIF5A is essential for the ribosomal translation of the polyproline region in mRNA as the hypusine residue stabilises and orients the peptidyl-tRNA to read through these regions [225].

1.3.5.4 Proliferation and cell cycle progression

Polyamines have been well recognised as essential mediators of cell growth. Increased polyamine levels were observed in hyperproliferative tumour cells [226], regenerative tissues [227] and in response to growth stimuli [171]. Accumulated evidence also points to a pro-proliferative effect of polyamine supplementation in different cell types [228]. Conversely, polyamine depletion by DFMO was shown to induce cytostasis in rat hepatoma cells while putrescine and spermidine administration restored cell growth [229]. Similar findings were also observed in tumour cells, where combined inhibition of polyamine synthesis and transport effectively restricted neuroblastoma cell growth [230]. One possible explanation for the regulation of cell proliferation by polyamines is their ability to mediate cell cycle progression (Figure 1-19). Both polyamine related enzymes and cellular polyamine content seem to fluctuate during the cell cycle. Biphasic upregulation of ODC activities at the G1/S and S/G2 transitions was reported in both human dermal fibroblast and CHO cells [231]. A corresponding biphasic increase of all three types of polyamines was demonstrated by Heby et al. in CHO cells [232]. However, also in CHO cells, Fredlund, J. et al. [233] described that putrescine and spermine mainly increased during the S/G2 and G1/S phases respectively, while spermidine exhibited a consistent increase throughout the cell cycle (Figure 1-19). Several lines of evidence have pointed to the involvement of cyclins in the regulation of the cell cycle by polyamines. Polyamine depletion, depending on the treatment,

can result in cell cycle arrest in either the G1, S or G2/M phases via the regulation of cyclin expression [234]. For example, DFMO treatment of human melanoma cells induced the expression of p21, which inhibited cyclin-dependent kinases and led to cell cycle arrest in G1 [235]. Reduced expression of cyclin D1 was observed after the resulting cellular polyamine decrease, whereas an elevation of putrescine levels was associated with cyclin D1 upregulation [228]. Additionally, decreased cyclin E levels were attributed to reduced spermidine and spermine levels while cyclin A inhibition was induced by polyamine depletion via the inhibition of DNA synthesis [228].

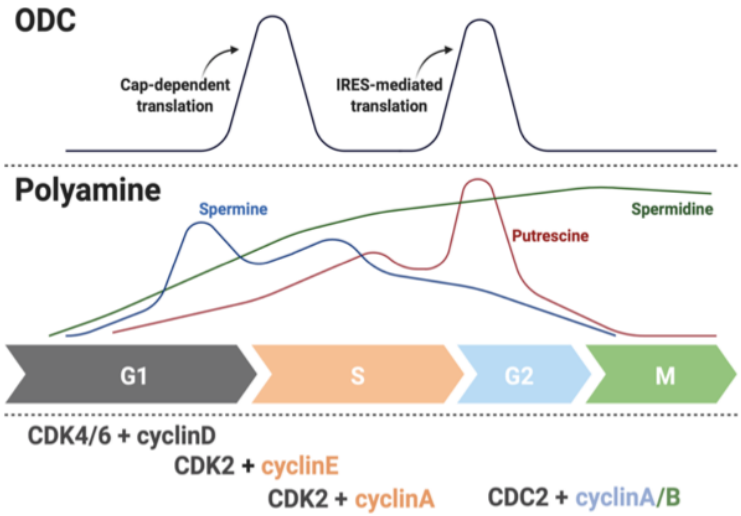

Figure 1-19 ODC and polyamine contents during cell cycle This figure summarises data from CHO cells. ODC expression fluctuates during the cell cycle with two expression peaks observed in the G1/S and S/G2 transition phase. Interestingly the translation of ODC is achieved through either cap-dependent or IRES-dependent mechanisms depending on the phase of the cell cycle. Corresponding to the fluctuation of ODC expression, putrescine level peaks at S/G2 phase whereas spermine doubling occurs in G1 and S phase. In contrast, spermidine levels increase over the course of the cell cycle. Readapted from Wallace, Heather M. Biochemical Journal 2003 [234]

1.3.5.5 Apoptosis

Compared to the relatively clear association of polyamines with cell growth, the regulation of cellular apoptosis by polyamines is complex, and cell type/context-dependent.

Anti-apoptotic role of polyamines: Polyamines have previously been reported to inhibit cell apoptosis. Reduced polyamine levels were associated with the apoptosis induced by heat-shock and γ-irradiation in rat thymocytes [236]. Decreased spermine levels sensitise both human and murine cells to TNF-induced cell apoptosis [237]. In addition, epidermal growth factor (EGF) induces apoptosis of breast cancer cells via the reduction of polyamine levels. This apoptotic phenotype was restored by supplementation with putrescine and spermidine, but not spermine [238].

Pro-apoptotic role of polyamines: In opposition to their reported anti-apoptotic effects, polyamines have also been demonstrated as inducers of apoptosis. Spermidine, through the activation of caspases, can induce apoptosis in rat cardiomyocytes (H9c2 cells) [239]. ODC activation, as a result of *c-Myc* overexpression, promoted 32D.3 murine myeloid cell apoptosis, though the cellular polyamine levels were not measured in this study [240]. Putrescine accumulation was shown to induce apoptosis in DH23A cells by affecting protein synthesis via the inhibition of hypusinated eIF5A formation [241]. H_2O_2 and amino-aldehydes resulting from the oxidation of spermidine and spermine oxidation are also inducers of cell apoptosis. In physiological conditions, these toxic products are removed by peroxisomal catalase [170] and aldehyde dehydrogenases [242] respectively. However, when an excess of polyamines accumulates, overproduction of H_2O_2 and aldehyde can lead to cytotoxicity [243].

1.3.5.6 Cell Junction regulation

Intercellular junctions, notably tight junctions and adherens junctions are indispensable in maintaining epithelial integrity. It has been demonstrated that polyamines are involved in the regulation of cell junctions in epithelial cells.

E-cadherin is a transmembrane adhesion molecule which, by binding to actin filaments, forms strong cell-cell adhesion between epithelial cells. In IEC-6 cells, polyamines were shown to regulate *E-cadherin* via the activation of c-Myc in a Ca^{2+} dependent manner. Increased polyamines induced both E-cadherin mRNA and protein expression while polyamine depletion by DFMO suppressed E-cadherin expression. Polyamine depletion substantially decreased the promoter activities of E-cadherin and increased the paracellular permeability of epithelial monolayers [244]. Moreover, polyamines were also implicated in the regulation of tight junctions. Polyamines deprivation impaired intestinal epithelial barrier function by affecting the synthesis and stability of occludin and transcriptionally downregulating *ZO1/2* and *claudin* expression [245] (Figure 1-20). Taken together, these findings suggest an important role for polyamines in the maintenance of epithelial cell-cell junctions.

Figure 1-20 Polyamine depletion affects epithelial cell-cell junctions Under physiological conditions, epithelial cells are tightly sealed by the tight junctions and adherens junctions to maintain epithelial monolayer integrity. Polyamine depletion by

DFMO suppresses the expression of several adhesion molecules and leads to the disruption of epithelial integrity.

1.3.6 Polyamines and disease

1.3.6.1 Polyamines and cancer

Owing to their essential roles in cell growth, polyamines have been intensively studied in cancer biology for more than 50 years. The first link between polyamines and cancer was reported in 1968, with elevated ODC activity observed in rat tumour tissues [227]. Further studies showing increased levels of polyamines in urine samples of cancer patients strengthened this theory [246]. However, the first biochemical evidence of a direct interplay between polyamines and oncogenes was revealed by the demonstration of ODC as the downstream target of the *Myc* in cancer cells [247]. Since then, this dysregulated Myc-ODC-polyamine axis was confirmed in several different cancer types, including lung cancer, breast cancer, leukaemia and colon cancers [248-250]. In addition to *ODC*, the *Myc* oncogene also transactivates *eIF5A* in multiple cancers. This, together with the increased spermidine from ODC upregulation, results in the overproduction of hypusinated-eIF5A and increased tumour cell proliferation [251]. Upregulation of other polyamine synthesis enzymes has also been described in cancer. In prostate cancer, mTORC1 was shown to increase AdoMetDC expression by phosphorylating and stabilising the AdoMetDC proenzyme, which consequently increased the levels of polyamines [252]. Apart from the biosynthesis pathway, reduced polyamine catabolism is another important mechanism contributing to the elevation of polyamines in cancer. K-Ras was shown to suppress SAT1 activation by interfering with PPARγ signalling. This resulted in a persistent elevation of the polyamine content in human colon cancer cells and hence promoted cell proliferation [253]. Moreover, as reported recently, *SAT1* expression can be induced by the potent tumour suppressor gene *p53*. By using a mouse embryonic fibroblast system, Ou, Y. et al. has shown that *p53*-

mediated ferroptosis is partly via the activation of *SAT1* [254]. In summary, cancer cells or tissues are generally characterised by increased polyamine content. This can be achieved via the activation of biosynthesis enzymes or the downregulation of catabolism enzymes.

1.3.6.2 Polyamines and PAH

PAH is a neoplastic growth disorder mainly affecting the small arteries in the lung. PAH has been frequently compared with cancer owing to the pathogenic similarity shared by these two diseases. Later than the discovery in cancer, a link between pulmonary hypertension and polyamine dysregulation was first demonstrated in 1984 when elevated polyamine levels were reported in lung tissues from rats exposed to monocrotaline (MCT) or chronic hypoxia [255, 256]. Intriguingly, these two rat PH models seemed to favour different mechanisms for their polyamine augmentation. Hyperactive *de novo* polyamine biosynthesis was mainly observed in MCT treated rats as reflected by the increased activities of both ODC and AMD. By targeting this polyamine biosynthesis with DFMO, the irreversible inhibitor of ODC, the elevated mPAP in this model was significantly attenuated. This suggests that MCT-induced PAH, at least in part, is driven by aberrant polyamine biosynthesis [255]. Conversely, chronic hypoxia repressed lung ODC activity, and hypoxic rats showed no response to the DFMO intervention [255]. This suggests a different mechanism, such as increased polyamine transport, may account for the elevation of polyamines in hypoxic rat lungs [255]. Indeed, a later study revealed increased putrescine uptake in rat lung explants under hypoxic conditions [256]. This theory was further supported by the observation that [^{14}C]-spermidine accumulated in the intimal and media layers of pulmonary arteries from hypoxic rats [257]. However, no polyamine transporters were identified in these studies. Taken together, these findings shed light for the involvement of polyamine dysregulation in the pathogenesis of PAH but suggest differences between

inflammation-dependent disease progression (MCT) compared to that mediated by hypoxic vasoconstriction.

Recently, owing to the advances in Multi-Omics techniques, more evidence suggesting polyamine dysregulation in PAH has been uncovered. A metabolomics study using human lung samples revealed increased levels of ornithine and putrescine in PAH patients compared with healthy subjects [258]. Plasma metabolomics profiling also demonstrated increased levels of polyamine metabolites in idiopathic or heritable PAH patients, with N-acetyl-putrescine being prognostic independent of the established prognostic markers [259]. Moreover, a study of the human lung transcriptome also identified that expression of ODC, the rate-limiting enzyme for polyamine biosynthesis, is negatively correlated to the mean pulmonary arterial pressure (mPAP) of PAH patients [260].

1.3.6.3 Polyamines and other diseases

Disease-associated genetic mutations were first linked to the polyamine pathway in 2003, with the discovery of a mutation in *SMS*, the gene encoding spermine synthase. This causes a rare X-linked recessive condition termed Snyder-Robinson, manifested with mental retardation as a result of spermine deficiency [261].

In addition to genetic disorders, polyamines have also been associated with neurodegenerative diseases. For example, reduced putrescine levels were identified in red blood cells from Parkinson's disease patients, while spermidine and spermine levels were elevated [262]. A metabolomics study of serum markers also revealed the prognostic value of polyamine alteration for predicting disease progression in Parkinson's disease [263]. Similarly, dysregulated polyamine levels were also reported in brain samples from Alzheimer's patients [264]. However most of these studies are observational and lack any detailed mechanism for the dysregulation of polyamine

metabolism in the disease pathogenesis. Recently, ATP13A2, a P5B-ATPase in which germ-line mutations had been implicated in Kufor-Recab syndrome, was comprehensively characterised as a late endo/lysosomal spermine exporter responsible for the releasing of spermine into the cytoplasm [148]. This provides mechanistic details on how defective lysosomal polyamine export may contribute to the pathogenesis of neurodegenerative diseases.

1.4 Hypothesis

The focus of this thesis is to investigate the biological functions of ATP13A3 in the pulmonary vasculature and to uncover the underlying mechanism of how mutations in *ATP13A3* contribute to the pathogenesis of PAH.

ATP13A3 is widely expressed across tissues with a relatively high expression observed in systemic vessels and lung tissues. Consequently, I hypothesised that ATP13A3 is also expressed in pulmonary vascular cells and is important for the regulation of vascular cell function. As a putative cation transporter, limited lines of evidence have suggested a link between ATP13A3 and polyamines, a group of versatile polycations essential for cell function. Therefore, I hypothesised that ATP13A3 is likely to function as a polyamine transporter in pulmonary vascular cells, with the substrate specificity to be determined. Cellular polyamine levels are homeostatically maintained within a narrow range to maintain normal biological processes. As a result, ATP13A3 dysfunction may affect the behaviour of pulmonary vascular cells, such as altering proliferation and apoptosis, via the disruption of polyamine homeostasis.

As mentioned earlier, rare variants in *ATP13A3* have been identified in PAH cohorts with an overrepresentation of protein-truncating variants and enrichment of missense mutations in the cytosolic functional region. The truncating mutations suggest a potential loss-of-function, which I predicted might affect polyamine transport mediated by ATP13A3. Therefore, I

hypothesised that genetic defects in *ATP13A3* could contribute to PAH pathogenesis by disruption of the polyamine homeostasis.

1.5 Thesis Aims

To address this hypothesis, the aims of this thesis are summarised as follows:

1. To assess the impacts of ATP13A3 loss-of-function in pulmonary vascular cells.
2. To investigate the roles of ATP13A3 in cellular polyamine homeostasis and determine the transport preference among different type of polyamines in human pulmonary vascular endothelial cells.
3. To perform a functional assessment on PAH associated *ATP13A3* variants
4. To further validate the pathogenic effects of ATP13A3 variants in BOECs isolated from a PAH patient (ATP13A3-LK726X) and a genetic mouse model bearing a frameshift mutation (P452L).

Chapter 2 Methods and Materials

2.1 CELL CULTURE PROTOCOLS

All cells were cultured and maintained in humidified incubators with an atmosphere of room air supplemented with 5% CO_2. All cells were routinely tested for mycoplasma contamination and were only used for experiments if negative. For cell passaging, cells were trypsinised with 0.25% trypsin (Sigma-Aldrich) and quenched with full growth media. The resulting cell suspension was then transferred into 50mL centrifuge tubes (Star Lab) before centrifuged at 400g for 5 minutes. For daily maintenance, cells were seeded into T75 culture flask at a variety of densities per different cell types.

Table 2-1 Cell seeding density in different formats

Format	Cell seeding density
96-well plate	10,000-15,000 cells/well
24-well plate	30,000 cells/well
6-well plate	
siRNA transfection	150,000 cells/well
Plasmid DNA transfection /lentiviral transduction	200,000 cells/well
Polyamine measurement	300,000 cells/well
6cm dish	300,000 cells/well
T75 flask	700,000-1,000,000 cells/flask

2.1.1 Cell culture of human pulmonary artery endothelial cells (hPAECs)

hPAECs were purchased from Lonza. Cells were grown in Endothelial Basal Medium (EBM-2) (Promocell) with the addition of Endothelial Growth Medium BulletkitTM (5 ng/ml hEGF, 0.2 µg/ml hydrocortisone, 0.5 ng/ml VEGF, 10 ng/ml h-FGFB, 20 ng/ml R3-IGF-1, 1 µg/ml ascorbic acid, 22.5 µg/ml heparin and 2% FCS) Promocell) and 1% A.A (EGM-2). For experiments, hPAECs were used between passage 4 to 7.

2.1.2 Cell culture of blood outgrowth endothelial cells (BOECs)

BOECs were isolated from 40-80ml of blood, as previously described [265]. For experiments involving BOEC generation, all blood donors provided informed consent under human study 07/H0306/134 (Cambridgeshire 3 Research Ethics Committee). BOEC lines listed below (Table 2-2) were used for experiments.

Table 2-2 Demographic information for Blood outgrowth endothelial cells used in these studies

Cell line	*ATP13A3* mutation	Gender	Age	Clinical details
C1	-	female	45	Healthy subjects
C2	-	male	20	Healthy subjects
C4	-	male	30	Healthy subjects
C7	-	male	41	Healthy subjects
C26	-	female	25	Healthy subjects
C35	-	male	33	Healthy subjects
OC0CQE	LK726X	male	46	PAH Patient

All lines were grown in EBM-2 supplemented with 5 ng/ml hEGF, 0.2 µg/ml hydrocortisone, 0.5 ng/ml VEGF, 10 ng/ml h-FGFB, 20 ng/ml R3-IGF-1, 1 µg/ml ascorbic acid (Promocell), 10%(v/v) Foetal Bovine Serum (FBS) and 1% A.A

and omission of heparin. Cells were maintained in T75 flasks and passaged when confluent. All cells were used for experiments at passage 4-7.

2.1.3 Cell culture of human pulmonary artery smooth muscle cells (hPASMCs)

Human pulmonary artery smooth muscle cells (hPASMCs) were isolated by explant culture from peripheral segments of pulmonary arteries obtained from patients undergoing lung transplantation following the protocol described previously [266]. Ethical approval of the hPASMCs isolation was obtained through the Papworth and Addenbrooke's Hospital Trust Ethical Committees. The hPASMC lines used for the experiment were listed below.

Table 2-3 Demographic information for human pulmonary artery smooth muscle cells used in these studies

Cell line	Gender	age
78MP	Male	68
79MP	male	69
103MP	Male	52

All hPASMCs were maintained in Dulbecco's Modified Eagle Medium (DMEM, Invitrogen) with 4.5 g/L glucose (Gibco) supplemented with 10%(v/v) Heat inactivated FBS and 1% A.A. Cells were used between passage 4 to 8.

2.1.4 Culture of the Human microvascular endothelial cell-1(HMEC-1) line

The immortalised (SV40-transformed) human microvascular endothelial cell-1(HMEC-1) line was purchased from ATCC [267]. HMEC-1 were grown in MCDB 131 medium (without glutamine) (Thermo Fisher Scientific) supplemented with 1 μg/ml Hydrocortisone (Sigma), 10mM Glutamine (Sigma), 10ng/ml Epidermal Growth Factor (EGF) (R&D systems), 10%(v/v) FBS and 1% A.A (HMEC1 full growth media). Cells were passaged twice a week to prevent over confluence.

2.2 NUCLEOTIDES DELIVERY PROTOCOLS

2.2.1 Transfection of small interfering RNA (siRNA)

Cells were seeded at different densities as described in Table 2-1 the day before siRNA transfection. Cells were preincubated in Opti-MEM-I reduced serum media (Invitrogen) for 2h before transfection. To prepare the lipoplexes, DharmaFect1 (Dharmacon, GE) was first added to Opti-MEM1(v/v 1 in 49) and incubated at room temperature for 5 minutes. Then, siRNA was diluted to a final concentration of 50nM in the tubes containing the DharmaFECT1/Opti-MEM pre-mixes and incubated for 20 minutes at room temperature to allow lipoplexes to form. During this time, appropriate volumes of fresh OptiMEM were added to the wells. The siRNA/DharmaFECT1 complex was added into each well at a 1:5 dilution such that the final siRNA concentration was 10nM. (i.e. for a 6-well plate, 400 µl of siRNA/DharmaFECT1 complex was added into 1.6ml OptiMEM in the well). The cells were incubated with the siRNA/DharmaFECT1 for 4h at 37℃ before the transfection media were replaced with full growth media. Cells were kept in growth media for 24h before further treatment. Knockdown efficiency was confirmed by mRNA expression or immunoblotting. To establish if the level of knockdown was retained in proliferation experiments, RNA was collected on day 0 and day 6. The siRNAs used for experiments were: oligos targeting *ATP13A3* from Sigma-Aldrich (#1, SASI_Hs02_00356805; #2, SASI_Hs02_00356806 and ON-TARGETplus non-targeting Control Pool (siCP) from GE Dharmacon.

2.2.2 Transient plasmid DNA transfection

The pcDNA6.2 expression plasmid encoding full-length wild type or missense mutant *ATP13A3* with N-terminal GFP tag was kindly donated by Prof. Peter Vangheluwe from KU LEUVEN (Leuven, Belgium) as listed below (Table 2-4). Prior to transfection, HMEC-1 cells were seeded at a density of $2.5x10^5$ cells/well into a 6-well plate and allowed to adhere overnight. The following

morning, cells were incubated in Opti-MEM-I reduced serum media (Invitrogen) for 2 hours before proceeding with transfection. To complete the transfection, 0.5-3 μg of plasmid DNA was delivered into cells using Lipofectamine LTX with Plus reagent (Thermo Fisher Scientific). Briefly, following 3-hour Opti-MEM incubation, 9 μl /reaction of Lipofectamine® LTX Reagent was diluted in 200 μl /reaction of Opti-MEM in a 15ml Falcon tube (Star Lab) labelled as Tube A. The required amount of plasmid DNA was diluted in a separate 15ml Falcon tube (Tube B) with 200 μl of Opti-MEM supplemented with 2.5 μl /reaction PLUS reagent before mixing thoroughly with the Lipofectamine® LTX reagent and incubated at room temperature for 5 minutes. The resulting lipoplexes were then added onto cells and incubated at 37°C for 4 hours before being returned to HMEC-1 full growth media. Twenty-four hours post-transfection, cells were trypsinised and reseeded into collagen-coated 4-chambered Nunc™ Lab-Tek™ II Chamber Slides™ (Thermo Fisher Scientific) or directly lysed for protein or RNA extraction.

Table 2-4 Wild type/mutant ATP13A3 plasmids

Plasmid Name
h*ATP13A3*-N-GFP-pcDNA6.2
h*ATP13A3*-D498N-N-GFP-pcDNA6.2
h*ATP13A3*-L675V-N-GFP-pcDNA6.2
h*ATP13A3*-M850I-N-GFP-pcDNA6.2
h*ATP13A3*-V855M-N-GFP-pcDNA6.2
h*ATP13A3*-R858H-N-GFP-pcDNA6.2
h*ATP13A3*-L956P-N-GFP-pcDNA6.2

2.2.3 Lentiviral transduction

Lentiviral vectors were kindly produced by Dr. Van Den Haute from Leuven Viral Vector Core facility (Leuven, Belgium). Briefly, Lentiviral vectors were generated by transfecting HEK293T cells with three plasmids:

1. A homemade transfer plasmid (pCHMWS-ires-puro) containing wild type or mutant *ATP13A3* coding sequencing as well as the cis-acting regulatory sequences
2. A packaging plasmid (8.91) encoding viral structural and replicative proteins
3. An envelope plasmid (VSV-G) which enables pseudotyping the glycoprotein of the Vesicular Stomatitis Virus, resulting in increased stability of the lentiviral vectors. The resulting lentiviral vectors were further concentrated and quantified with a p24 antigen ELISA.

Upon receiving the viral particles, lentiviral titer was assessed by real-time PCR based assay [268, 269] in hPAECs. Briefly, 75000/well of hPAECs were seeded into a 24-well plate followed by the transduction with Lentivirus media. An extra well of hPAECs with the lentiviral transduction was included for the normalisation of transduction copy numbers. Cells were harvested 72h post-transduction and genomic DNA was extracted as described in section 2.5.1. The resulting genomic DNA was then PCR amplified targeting *ATP13A3* and the lentiviral packaging cassette (GAG) with the following primers (*ATP13A3*-Forward-TGTTCGCCAGTTCCCATTTT, *ATP13A3*-Reverse-TTCATGTAGGCGTCCA
TTTTCCT, *GAG*-Forward- AAAGCGAAAGGGAAACCAGA, *GAG*-Reverse-AATTTTTGGCGTACTCACCAGTC). In the meantime, standard curves for *ATP13A3* and *GAG* gene copy number (Figure 2-1) were generated by amplifying the lentiviral plasmid DNA with known concentration (10^2 to 10^{10} copies/reaction). Standard curves were then used for calculating lentiviral copy number in hPAECs.

The lentiviral titer (TU/ml) was calculated according to the following equations [269]:

Lentiviral titer = (Cell number x Lentiviral copy number/cell) / volume of Lentivirus media

Lentiviral copy number/cell = (*GAG* copy number of $hPAEC_{transduced}$ / *ATP13A3* copy number of $hPAEC_{control}$) x 2

$hPAEC_{transduced}$: hPAECs transduced with lentiviral particles

$hPAEC_{control:}$ hPAECs without the transduction of lentiviral particles

Wild type and mutant *ATP13A3* lentiviral vectors displayed similar lentiviral titers (Table 2-5). When transduced at MOI=5, these lentiviral vectors showed optimal overexpression of *ATP13A3* without compromising the expression of other P5 ATPases.

For experiment involving lentiviral transduction, hPAECs were seeded into 6-well plates at a density of 200,000 cell/well and allowed for attaching overnight. The following day, cells were transduced with the lentiviral vectors diluted in EGM-2. hPAECs were left in EGM-2 media containing the lentiviral particles for 72 hours for the optimal transduction. Cells were then used for the following functional assays or lysed directly for extracting protein or RNA.

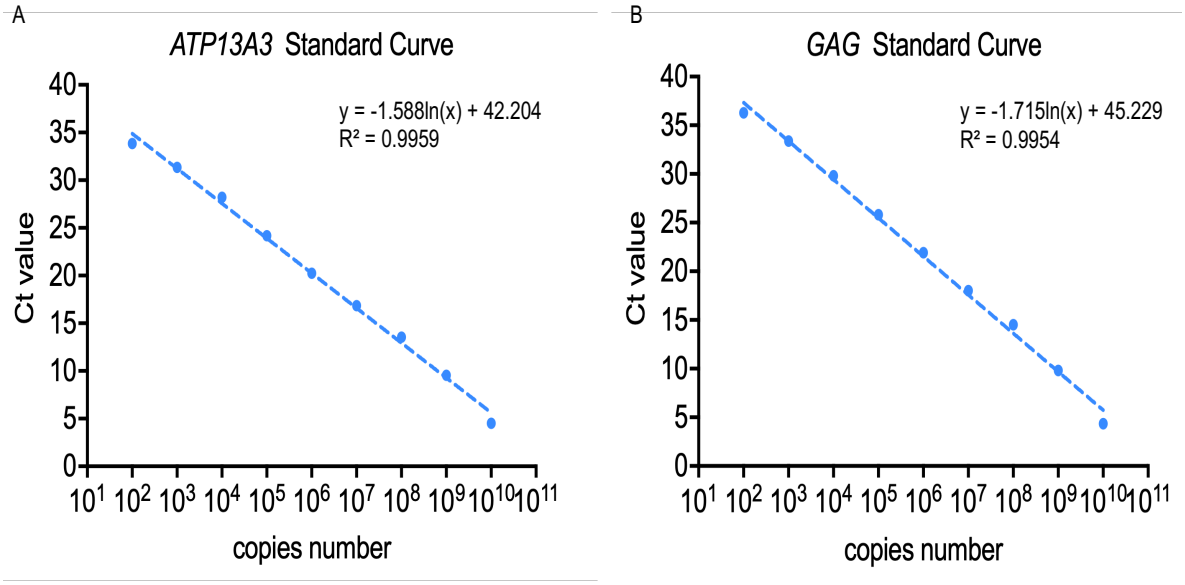

Figure 2-1 Standard curves of ATP13A3 and GAG gene copy number

Real-time PCR Ct values of (A) *ATP13A3* and (B) *GAG* amplified was plotted against the log value of the lentiviral plasmid DNA copies number. Linear regression analysis was performed to generate the standard curve equation of calculating the lentiviral copy number of hPAECs.

Table 2-5 Titers of wild type/mutant ATP13A3 lentiviral vectors

Plasmid Name	Lentiviral titers
pCHMWS-Hs *ATP13A3* WT-ires-puro	2.39 x 10^7 TU/ml
pCHMWS-Hs *ATP13A3* D498N-ires-puro	2.01 x 10^7 TU/ml
pCHMWS-Hs *ATP13A3* L675V-ires-puro	1.74 x 10^7 TU/ml
pCHMWS-Hs *ATP13A3* M850I-ires-puro	2.28 x 10^7 TU/ml
pCHMWS-Hs *ATP13A3* V855M-ires-puro	2.81 x 10^7 TU/ml
pCHMWS-Hs *ATP13A3* R858H-ires-puro	2.33 x 10^7 TU/ml
pCHMWS-Hs *ATP13A3* L956P-ires-puro	1.62 x 10^7 TU/ml

2.3 CELL FUNCTIONAL ASSAYS

2.3.1 Cell proliferation assay

Cells were seeded in 24-well plates at a density of 30,000/well and left to adhere overnight. Transfection of si*ATP13A3,* siCP or DharmaFECT1 reagent alone was performed in the following day and cells were returned to full growth media afterwards.

For assessment of BOEC proliferation, cells were serum-starved with EBM-2 containing 0.1%(v/v) standard grade FBS (EBM2/0.1% FBS) for 8 hours, followed by culturing in EBM-2 media supplemented with 5%(v/v) FBS (EBM-2/5% FBS) with or without the addition of 30ng/ml VEGF165(R&D Systems), 5ng/ml BMP9 (R&D Systems) for four days. Treatments were replenished every 48 hours.

For assessment of hPAEC proliferation, cells were quiesced in EBM-2/0.1% FBS for 8 hours before treating with 30ng/ml VEGF165(R&D Systems), 5ng/ml BMP9(R&D Systems) in EBM-2 media containing 2%(v/v) for six days. Treatments were replenished every 48 hours.

For assessment of hPASMC proliferation, cells were serum-restricted in DMEM containing 0.1%(v/v) FBS and A/A overnight, followed by treatment with either 1ng/ml PDGF or 10ng/ml PDGF (R&D Systems) in DMEM with 1%(v/v) FBS and A/A. In parallel, cells were treated with 5ng/ml TGFβ or 5ng/ml BMP9 (R&D Systems) in DMEM containing 5%(v/v) FBS and A/A for 6 days. Treatments were replenished every 48 hours. At day 6, all cells were trypsinised with 150 µl /well 0.5% trypsin (Sigma-Aldrich) and quenched with 60 µl /well of the relevant growth media, followed by 90 µl /well of trypan blue (0.4%, Sigma-Aldrich). All 300 µl of cell suspension was transferred into a newly labelled Eppendorf tube, and cells were counted using a haemocytometer.

2.3.2 Annexin V/PI Flow Cytometry Apoptosis assay

Annexin V has a high affinity for phosphatidylserine. Cells, while undergoing early apoptosis, expose this phospholipid from the cytoplasmic surface to the outer leaflet of the cell membrane, inducing binding of annexin V. PI on the other hand only enters dead cells that have become permeable and therefore distinguishes early apoptotic cells from cells in late apoptosis or necrosis. BOECs were plated at 150,000/well into 6-well plates and transfected with si*ATP13A3,* siCP or DharmaFECT1 reagent alone. Three extra wells of cells were seeded in a 6-well plate for unstained and compensation controls and maintained in BOEC media. Cells were then serum-starved in EBM-2/0.1% FBS for 8 hours before treating with EBM-2 containing either 1%FBS or 5%FBS for another 24 hours. For assessing the response to anti-apoptogens, cells were treated with or without 30ng/ml VEGF165 (R&D Systems) or 5ng/ml BMP9 (R&D Systems) in EBM-2/0.1% FBS for 24 hours. Cells were then trypsinised with 1ml/well 0.25% trypsin and quenched with 1ml/well BOEC media. The entire cell suspension was transferred into 15mL centrifuge tubes (Star Lab) prefilled with 3ml PBS, followed by centrifugation at 350g for 5minutes. Cells were washed with 1ml PBS and centrifuged at 350g for 5 minutes again. Cells were then resuspended with 100 µl 1x Annexin V binding buffer from FITC Annexin V Apoptosis Detection Kit I (BD Biosciences) and transferred into flow tubes (Fisher Scientific). For each condition, dual-staining was undertaken by adding 5 µl FITC conjugated Annexin V (BD Biosciences) and 5 µl propidium iodide (PI) (BD Biosciences) followed by incubation at room temperature for 15 minutes. For single staining compensation controls, either 5 µl FITC Annexin V or 5 µl PI was added into non-transfected cells and incubated for 15minutes. A further 400 µl 1x Annexin V binding buffer (BD Biosciences) was added to each tube. All samples were then analysed on a BD Accuri™ C6 Plus flow cytometer (BD Biosciences). FITC-Annexin V and PI fluorescence signal were collected in the FL-1 channel and FL-3 channel respectively. FlowJo (vX, Treestar) software was used for fluorophore compensation and data analysis.

2.3.3 Caspase-Glo 3/7 assay

Caspase activity is another indicator for cell apoptosis, as this is the executioner caspase that directly promotes chromatin condensation, cell lysis and DNA fragmentation.

To assess the caspase activities, cells were seeded at a density of 150,000/well into 6-well plates and transfected with si*ATP13A3*(Sigma-Aldrich), siCP (GE Dharmacon) or DharmaFECT1(GE Dharmacon) alone. For each condition, cells were trypsinised from 6-well plates, reseeded in triplicates into a 96-well plate at a density of 15,000-20,000/well and left to adhere overnight. Cells were quiesced in EBM-2/0.1% FBS for 24h before treating with or without 30ng/ml VEGF165(R&D Systems) or 5ng/ml BMP9(R&D Systems) in EBM-2/0.1%FBS for 16 hours. For measuring caspase-3/7 activities, 100 µl Caspase-Glo® 3/7 Reagent (G8091 Promega) as added into each well, then incubated and mixed on a plate shaker in the dark for 15 minutes at room temperature. The entire 200 µl from each well was transferred into the corresponding well of a white-walled 96-well plate and luminescence was read in a GloMax® luminometer (Promega).

2.3.4 Endothelial permeability assay

This assay measures the transit of horseradish peroxidase (HRP) across endothelial monolayers seeded in transwell inserts. hPAECs subjected to siRNA transfection were trypsinised and reseeded into Corning® Transwell® chambers polyester membrane cell culture inserts (0.4 µm pore size, Corning) at a density of 50,000 cells/insert and allowed to attach for 30 minutes before adding 1ml of EGM2 supplemented with 2% FBS (Promocell) to the lower 24-well plate chamber. Following overnight incubation at 37°C, hPAECs were serum-starved for 6 hours by replacing the media in the inserts with 200 µl, and the bottom chambers with 1ml of EBM2/0.1% FBS. Following serum-starvation, media was then replaced with 2% FBS supplemented EBM2 with or without the addition of 1U/ml Thrombin (Sigma) and incubated for an hour at 37°C. In the

meantime, 0.05 M Phosphate Citrate Buffer was prepared by dissolving one capsule of Phosphate-Citrate buffer with Sodium Perborate (Sigma) into 100ml of PBS. The o-Phenylenediamine dihydrochloride (OPD) developing solution was then made up by adding one OPD (Sigma) tablet into 50ml Phosphate-Citrate buffer. Prior to the assessment, media in the inserts was replaced with 100 µl of EBM2 supplemented with 2% FBS containing 25nM HRP(Sigma) with or without the addition of 1U/ml Thrombin. 3 x 15 µl medium from the bottom chambers were collected into a new 96-well plate at the following time points: 0min, 15min, 30min, 1hour, 1.5 hours and 2 hours. 150 µl /well of OPD buffer was then added into the 96-well plate and then read at 490nm on the plate reader over 10 to 20 minutes.

2.4 ANIMAL MODEL OF ATP13A3 DEFICIENCY

2.4.1 *Atp13a3* P452Lfs mice model

C57BL/6N genetic modified mice harbouring a PAH associated frameshift mutation(P452fls) in *Atp13a3* were created using a CRISPR-Cas9 genetic editing system by MRC-Harwell institutes. Mice were subsequently maintained on a C57BL/6N background.

2.4.1.1 Cardiopulmonary phenotyping in *Atp13a3* P452fls mice

Cardiopulmonary phenotyping of these animals by echocardiography and catheterisation was undertaken by Dr Ekaterina Legchenko (Morrell laboratory). Atp13a3 P452fls wild type, heterozygous and homozygous mice at 3-month and 6-month old were anesthetised with inhaled isoflurane for hemodynamic measurement. Mice were weighed and recorded before performing the right heart catheterisation using a Millar SPR-869 pressure-volume catheter system to measure the right ventricular systolic pressure (RVSP). Mice were sacrificed following measurement. The blood was collected through inferior vena cava followed by 30 minutes clotting at room temperature before centrifuging at

3000g for 10 minutes. Serum was collected into a new 1.5ml tube and stored in -80°C. Right ventricular hypertrophy was assessed using Fulton index. To achieve this, the mouse circulation system was flushed with 10ml of saline supplemented with heparin using a syringe. Whole heart tissues were collected before dissecting the right ventricle free wall (RV) out from left ventricle and septum (LV+S) and weighed respectively. The right ventricular hypertrophy was revealed using the ratio of RV/LV+S (Fulton index). The resulting heart tissues were transferred into cryo-vials and frozen in liquid nitrogen for protein and RNA extraction.

2.4.1.2 Tissue collection

Lung tissues: Following hemodynamic measurements by catheterisation under terminal anaesthesia, the right main bronchus was tied off with suture to prevent exposure to formalin. The gravity perfusion apparatus comprised a 22-gauge flexible cannula (0.9x25mm BD Venflon) connected via polypropylene tubing to a 5ml syringe placed with the base at a height of 6.5cm above the bench was inserted. The cannula and tubing were-pre-filled with 10% neutral-buffered formalin and the syringe was filled to the 3ml mark. The tubing was sealed with an artery clamp to prevent flow. The trachea was exposed and a partial incision was made, followed by insertion of the 22-gauge cannula, which was tied into place with suture. The clamp was released and the left lung lobes were fixed and inflated with 10% neutral-buffered formalin for 10 minutes. The left lobe was then excised and placed into 10% neutral-buffered formalin pots prior to tissue processing and paraffin wax embedding. The whole right lung lobes were excised, placed in cryovials and frozen in liquid nitrogen for RNA and protein extraction.

Liver and kidney: The mouse liver and kidney were also collected. Briefly, both kidneys were dissected with left kidney fixed in 10% neutral-buffered formalin

for histology assessment and right kidney snap-frozen in a cryovial in liquid nitrogen for later protein and RNA extraction. For mouse liver collection, the left lobe was snap frozen in a cryovial while the rest of the tissue was fixed in neutral-buffered formalin.

2.4.1.3 *Atp13a3*-P452Lfs mouse genotyping protocol

Mouse Genomic DNA extraction

Mouse genomic DNA was isolated from ear notches by digestion overnight with 350 µl of digestion buffer (50mM Tris-HCl, pH 8.0; 5mM EDTA, pH 8.0; 100mM NaCl; 1% sodium dodecyl sulfate (SDS)) supplemented with 9 µl of proteinase K (Biolab) in 1.5ml tubes at 50°C. Following digestion, 100 µl of 4.5M Sodium perchlorate (Thermo Fisher Scientific) was added and mixed by inversion before adding 600 µl /sample chloroform and further mixing. The homogenate was then centrifuged at 4000g for 1 minute at room temperature. The resulting ~300 µl of the upper aqueous phase was transferred into a new tube followed by adding 600 µl of ice-cold 100% ethanol. Samples were mixed thoroughly by inversion and centrifuged at 12,000g for 5 minutes at 4°C. After discarding the supernatants, pellets were washed with 1ml of 70% ice-cold ethanol and centrifuged at 12,000g for 5 minutes at 4°C. The supernatants were removed again, and pellets were left air dry for 5 minutes before resuspending in 100 µl of nuclease-free water.

Genotype determined by the polymerase chain reaction and restriction enzyme digestion

As described above, the *Atp13a3*-P452Lfs mutation was edited into the mouse genome using the CRISPR-Cas9 system. The introduction of the P452Lfs mutation as well as the addition of silent mutations for preventing Cas9 protein from the “re-cut”, created an additional BseRI restriction enzyme digestion site which was therefore used for mouse genotyping.

To achieve this, a DNA fragment was amplified from mouse genomic DNA using the following primers:

Atp13a3-P452Lfs-F: 5'-AGCCTAGGGCCTCAAACATTA -3'

Atp13a3-P452Lfs-R: 5'-AACAAACCGACCTTGTCAAAGC -3'

20 µl PCR reactions were set up as described below.

5x GoTaq® Buffer	4 µl
$MgCl_2$	1.2 µl
10mM dNTP	0.4 µl
Forward/Reverse Primer mix	1.2 µl
Nuclease-free water	11.8 µl
GoTaq® polymerase	0.12 µl
Genomic DNA	2 µl

Reactions were then run using the following program:

Step	Temp.	Time
Initial denaturation	95°C	2 minutes
30 cycles		
Denature	95°C	30 seconds
Anneal	64°C	30 seconds
Extend	68°C	1 minute

The resulting amplicon covering the P452Lfs region was then digested using the following reactions with BseRI (NEB) to determine mouse genotypes.

PCR product	5 µl
Cutsmart	2.5 µl
Nuclease free water	16.5 µl
BseRI	1 µl

The digestion reactions were performed at 37°C for an hour and inactivated at 80°C for 20 minutes. Following digestion, 2 µl of the reaction was used for electrophoresis in a 1.5% Agarose gel at 100V for 45 minutes before imaging.

Samples presented with digested bands were then sent out for Sanger sequencing (Genewiz) for genotype confirmation.

2.4.2 Monocrotaline (MCT) Rat model

Monocrotaline (MCT) is a pyrrolizidine alkaloid used for the establishment of pulmonary hypertension in rats. Once injected, the monocrotaline is dehydrogenated by rat liver into monocrotaline pyrrole, which is toxic. MCT induces pulmonary vascular injury through an inflammatory response [270].

This model was generated by Dr Elisabet Ferrer. Briefly, Male Sprague Dawley rats (~200 to 250 g, Charles River, Margate, UK) were randomised into two groups. Injections of saline were given to control rats as vehicle control. Rats in the experimental PAH group were given 40 mg/kg of MCT, which induces a progressive PAH phenotype over a 21-day period. To assess the disease progression of the MCT rat model, hemodynamic phenotyping was performed at week 0, week1, week 2and week 4. At each of the time point, rats were anaesthetised with inhaled isoflurane and right and left ventricular function were assessed using a Millar SPR-869 pressure-volume catheter. Hearts were dissected, and the weights of the right ventricle and left ventricle plus septum were recorded. Lung tissues were flushed before harvesting and snap-frozen in cryovials for downstream molecular analyses.

2.4.3 Sugen 5416/hypoxia rat model

Sugen 5416 is a semi-specific tyrosine kinase inhibitor that inhibits both vascular endothelial growth factor receptor 2 (VEGFR2) and VEGFR1. The combination of a weekly injection of Sugen 5416 followed by 3 weeks exposure to hypoxia causes rats to develop a progressively worsening pulmonary hypertensive phenotype when subsequently maintained in normoxia [270].

This model was generated by Dr Lu Long and Dr Xudong Yang. Briefly, Male Sprague Dawley rats (~150 to 200 g, Charles River) were randomised into four

groups. For the control group, rats were kept in normoxic conditions (21% O_2) for eight weeks; for the hypoxia (Hx) group, rats were maintained in 10% O_2 in normobaric chambers for three weeks. For the Sugen-Hypoxia model (SuHx) a single intraperitoneal -injection of Sugen (SU-5416, 20 mg/kg, Tocris, Bristol, UK) in the vehicle (0.5% carboxyl methylcellulose sodium, 0.4% polysorbate 80, 0.9% benzyl alcohol, all Sigma) was administered to each rat. After Sugen injection, rats were transferred to normobaric hypoxic chambers and maintained in hypoxia for three weeks, followed by maintenance for a further 5 weeks in normoxia over which time they develop progressive pulmonary hypertension. For the hypoxia+normoxia group, rats were maintained in hypoxia for three weeks, followed by five weeks of normoxia. At week 8, rats were assessed for cardiopulmonary phenotype and sacrificed for tissue collection as described above.

2.5 Molecular Biology Techniques

2.5.1 Cell genomic DNA extraction

Cell total genomic DNA was isolated using the DNeasy Blood & Tissue Kit (Qiagen). To achieve this, cells grown in 6-well plates were harvested and resuspended in 200 µl PBS supplemented with 20 µl of proteinase K (600 mAU/ml, Qiagen). 200 µl of lysis buffer AL (Qiagen) was then added and thoroughly mixed, followed by incubation at 56°C for 10 minutes. Following this incubation, 200 µl ethanol was added and well mixed before transferring into a DNeasy Mini spin column (Qiagen) and centrifuged at 6000g for 1 minute. After discarding the flow-through, 500 µl of washing buffer AW1(Qiagen) was added onto the column and centrifuged again at 6000g for 1 minute. The column was then washed again with 500 µl of buffer AW2 (Qiagen) and centrifuged at 6000g for 3 minutes to remove washing buffer completely. The column was then transferred into a new 1.5ml tube (Star Lab) and 200 µl of nuclease-free water was added before spinning down at 6000g for one minute for eluting DNA. The

final genomic DNA yield was determined by NanoDrop™ Lite Spectrophotometer (Thermo Fisher Scientifics).

2.5.2 Plasmid DNA preparation

2.5.2.1 Minipreparation of plasmid DNA

Small scale plasmid DNA was isolated using the GenElute™ Plasmid Miniprep Kit (Sigma). Following overnight culture, 5ml of recombinant *E. coli* was pelleted at 12000g for one minute and resuspended in 200 µl of resuspension buffer (Sigma). Lysis buffer (200 µl, Sigma) was then added, followed by mixing by gentle inversion 6-8 times. To precipitate cell debris, proteins, lipids and chromosomal DNA, 350 µl of neutralisation solution (Sigma) was added and the tube mixed by inversion 4-6 times before centrifuging at 12000g for 10 minutes. The aqueous phase was then carefully transferred into a GenElute Miniprep Binding Column (Sigma) and centrifuged at 12000g for one minute and the flow-through discarded. The column was then washed by adding 750 µl wash solution (Sigma) and centrifuged at 12000g for one minute. An additional two minutes centrifugation at 12000g was performed to remove excess ethanol. The column was then transferred into a new 1.5ml tube (Star Lab) and DNA was eluted with 50 µl of nuclease-free water by centrifuging at 12000g for one minute. The final DNA yield was assessed using a NanoDrop™ Lite Spectrophotometer (Thermo Fisher Scientifics).

2.5.2.2 Purification of DNA fragments from PCR reactions

DNA fragments from PCR reactions intended for Sanger sequencing or plasmid ligation were purified using the Invisorb® Fragment CleanUp kit (Stratec Molecular). To purify the DNA fragments, 250 µl or 500 µl binding buffer was added to 50 µl or reaction volume greater than 50 µl of PCR reactions. The resulting mixture was vortexed briefly before loading onto a spin filter column and incubated for 1 minute at room temperature. The column was then centrifuged at 12000g for four minutes and the flow-through discarded. The column was then transferred into a new 1.5ml tube, and 20-40 µl of elution

buffer (stratec molecular) was added and incubated for at least one minute at room temperature before being centrifuged at 12000g for one minute. The final DNA concentration was assessed using a NanoDrop™ Lite Spectrophotometer (Thermo Fisher Scientifics).

2.5.2.3 DNA fragment extraction from an agarose gel slice

Following agarose gel electrophoresis, DNA fragments at the intended size were rapidly excised from the agarose gel with a razor blade under UV light exposure and extracted using the Invisorb® Fragment CleanUp kit (Stratec Molecular). The resulting gel slices were then weighted and split into several reactions if they exceeded 300mg per slice. 0.5-1ml of Gel solubiliser S was used to dissolve gel slices at 50°C for 10 minutes. Binding Enhancer solution (250-500 µl) was then added with and the mix briefly vortexed before loading 800 µl onto a spin filter column and centrifuging at 11000g for two minutes. For volume higher than 800 µl, the residual volume was loaded and centrifuged again. The column was then washed with 500 µl of wash buffer, centrifuged at 11000g for one minute. After discarding the filtrate, the column was spun for an additional two minutes at 11000g before adding 20 µl elution buffer and incubating for five minutes at room temperature. To elute the DNA, the column was centrifuged at 11000g for one minute, and DNA concentration was assessed by NanoDrop™ Lite Spectrophotometer (Thermo Fisher Scientifics).

2.5.3 RNA extraction from cells/tissues

2.5.3.1 Cell RNA extraction

For RNA analysis, cells were seeded in 6-well plates at a density of 1.5×10^5/well and grown overnight in growth medium prior to transfection or exposure to treatments. Total RNA was extracted using RNeasy Mini Kit buffers (Qiagen, West Sussex, UK) and Silica Membrane Mini Spin Columns (EconoSpin). Briefly, cells were harvested and lysed in wells by scraping with 350 µl /well buffer RLT containing 0.1% (v/v) B-mercaptoethanol. The cell lysate was transferred into labelled RNase/DNase-free tubes and mixed with 350 µl /tube 70% (w/v) ethanol thoroughly. The entire 700 µl was then transferred into a mini-column (EconoSpin) and centrifuged at 8000g for one minute. The flow-through was discarded, and the columns washed with 350 µl /column RW1 buffer followed by centrifugation at 8000g for one minute. The flow-through was discarded, and 80 µl DNAse mix, comprising 70 µl RDD buffer (Qiagen) and 10 µl RNase-free DNase (Qiagen) was carefully added into the central filter of each mini-column for genomic DNA elimination. The columns were incubated for 15 minutes at room temperature and washed again with 350 µl /column RW1 buffer, centrifuging at 8000g for one minute. The flow-through was discarded, and the columns washed twice with 500µM/column RPE buffer, with centrifugation at 8000g for one minute followed by discarding the waste. The columns were then centrifuged for an additional two minutes at 8000g. The mini-columns were then transferred into the newly labelled RNase/DNase-free tubes. RNA samples were eluted by adding 30 µl RNase-free water into the central filter and incubating for two minutes at room temperature. The columns were centrifuged at 8000g for one minute and the RNA concentration measured using a NanoDrop Lite Spectrophotometer (Thermo Fisher Scientific). RNA samples were stored at -20°C and used as required.

2.5.3.2 Tissue RNA extraction

RNA from mouse lung tissues were extracted using QIAzol Lysis Reagent (Qiagen). To achieve this, one lobe of the mouse lung tissue was excised on dry ice and transferred into a sterile 2ml tube (Star Lab) containing a stainless-steel bead (Qiagen) that had been prechilled on dry ice. 1ml/tube of QIAzol Lysis Reagent (Qiagen) was then added. The tubes were transferred immediately into the prechilled TissueLyser racks and balanced before homogenising at 25Hz for 5 minutes. Tissues were then checked to confirm they were fully homogenised. An additional 5-minute homogenisation at 25Hz was applied if residual tissue chunks presented. Following homogenisation, tubes were transferred onto ice. In the meantime, 5PRIME Phase Lock Gel tubes (Quantabio) used for separating RNA from protein and lipid were prepared by centrifuging at 1500g for 30 seconds. The tissue homogenate was then warmed to room temperature, added into the corresponding Phase Lock Gel tube (Quantabio) and incubated for five minutes. 200 µl /sample of chloroform was then added, followed by vigorous shaking for 30 seconds to generate an emulsion. The samples were then centrifuged at 12000g for 10 minutes at 4°C. The aqueous layer containing the RNA was carefully transferred into a fresh 1.5ml tube (Star Lab) before adding 250 µl isopropanol (Sigma) and incubation at -70°C for 30 minutes. The samples were pelleted at 12000g for 10 minutes at 4°C followed by washing with 1ml 75% (v/v) ethanol (Sigma) and centrifuged at 7500g for 5 minutes at 4°C. After discarding the supernatant, tubes were left upside down to air dry for 10-15 minutes. RNA pellets were then dissolved in 100 µl /sample of nuclease-free water and concentration was measured using a NanoDrop Lite Spectrophotometer (Thermo Fisher Scientific). 1 µl of RNA samples were then electrophorised onto a 1% agarose gel. Only samples with distinct 28S/18S RNA bands were kept and stored at -20°C for future experiments.

2.5.3.3 cDNA synthesis

Equal amounts of RNA (500-1000ng) extracted as described above were added into labelled MicroAmp® Reaction Tubes (Applied Biosystems) and diluted with DEPC-treated Water (Invitrogen) to a final volume of 14.2 µl per tube. 5.8 µl /sample RT master mix (comprising 2 µl 10x RT buffer, 0.8 µl 100mM 25X dNTP, 2 µl 10x RT Random Primers and 1 µl MultiScribe™) Reverse Transcriptase from a High Capacity Reverse Transcriptase kit (Applied Biosystems) was prepared and added to each RNA sample tube accordingly. Single-stranded cDNA synthesis was performed on a Veriti® 96-Well Thermal Cycler (Applied Biosystems). Samples were initially incubated at 25°C for 10 minutes, followed by reverse transcription at 37°C for 120 minutes. The reaction was terminated at 85°C for 5 minutes and kept at 4°C before sample collection. cDNA samples were stored at -20°C and used as required.

2.5.3.4 Quantitative Reverse Transcriptase-PCR

cDNA (2 µl) together with 1.8 µl associated premixed primer sets (final concentration in mix = 200nM), 5 µl 2X SYBR Green JumpStart Taq ReadyMix (Sigma-Aldrich), 0.2 µl ROX reference dye (Invitrogen) and 1 µl DEPC-treated water were added into a well of a MicroAmp® Optical 384-Well Reaction Plate (Applied Biosystems), making a 10 µl /well reaction. Amplifications were performed on a QuantStudio 6 Flex Real-Time PCR System (Applied Biosystems). Reactions were initiated with a 2-minute pre-incubation at 95℃, followed by 50 amplification cycles of 30-second denaturation at 95℃, 30 seconds annealing at 55℃ and 30-seconds extension at 72℃. Melt curve analysis was performed to rule out nonspecific amplification, and no-template controls were included. Primers for human genes were designed using Primer-BLAST (http://www.ncbi.nlm.nih.gov/tools/primer-blast/), and primer efficiency confirmed to be between 90-110% before use. The relative expression levels of all target genes were calculated using the 2^-(△△Ct) method by normalizing

to the stably expressed housekeeping genes. Differences in gene expression are presented as the fold change relative to control. Relative expression of target genes in different cell lines or mouse tissues was determined as 2^-($CT_{target\ mean}$-CT_{3HK}). CT_{3HK} is calculated as the arithmetic mean of the CT value of *B2M*, *ACTB* and *HPRT*.

Table 2-6 Primer sequences for human genes analysed using qPCR

Gene name	**Forward 5' - 3'**	**Reverse 5' - 3'**
Human genes		
ATP13A1	AGTACGCCCATTGTGAAACT	TTGAACATCTGTAGCGTGGT
ATP13A2	AGCTCCTCAGTTTCATCCGT	TTCCAACGGAAGAGCAGCAA
ATP13A3	GAAAATAGGCACAGGATCAG	ATTTTACACTATGGTGGGTG
ATP13A4	ACCCTAAGCTGGTGCCTTTC	TGGCCAGGCTGAGAAGAATG
ATP13A5	ATTGATGGAAGCTGCGTGGT	TCTGGGGCAATGGTGTCTTT
ID1	CGAAGTTGGAACCCCGGGG	CAGGAACGCATGCCGCCTCG
ID2	GACCCGATGAGCCTGCTATAC	GGTGCTGCAGGATTTCCATCT
CCNA1	ACTAGAGCAGGGGGACAGAG	GTGTGCCGGTGTCTACTTCA
CCNB1	CTGCTGGGTGTAGGTCCTTG	TGCCATGTTGATCTTCGCCT
CCND1	TGTCCTACTACCGCCTCACA	CTTGGGGTCCATGTTCTGCT
CCNE1	CCACAGAGCGGTAAGAAGCA	TAAAAGCAAACGCACGCCTC
BMPR2	CAAATCTGTGAGCCCAACAGTCAA	GAGGAAGAATAATCTGGATAAGGACCAAT

ARG1	TGGGGAAGACACCAGAAGAA	AGTCCGAAACAAGCCAAGGT
ARG2	ACTGCCCAGACCTTTGTGTT	TGATGAAGTGGTAAGGGGTGTG
ODC1	ATATTGGCGGTGGCTTTCCT	TGCAAGCGTGAAAGCTGATG
AMD1	CTAGATGTCGATGCTGGGGG	CACAGCAAGAGTGGCAGAGA
SRM	ACCAAGTGTTACAAGCCCCA	ACACGTGTTTGGTGAGTGAG
SMS	TGGCAGGACCATGGCTATTT	TGAAGGTCCAGCAACACCAA
SMOX	TGGCCCTGTAGCTTTTCTTTT	AGGCACTTACAATAACAAGGCAG
APAO	AGGGTCCTCTGGTTTTTGGT	GCTGTGGCTGTAACTTGCTT
SSAT1	TGCTGTAGATGACAACCTCCATT	TCAAACATGCAACAACGCCA
SLC3A2	ACCAGAAGGATGATGTCGCT	TCCAGAATGACACGGATGCT
B2M	CTCGCGCTACTCTCTCTTTCT	CATTCTCTGCTGGATGACGTG
HPRT	GCTATAAATTCTTTGCTGACCTGCTG	AATTACTTTTATGTCCCCTGTTGACTGG
ACTB	GCACCACACCTTCTACAATGA	GTCATCTTCTCGCGGTTGGC

Table 2-7 Primer sequences for mouse/rat genes analysed using qPCR

Gene	Forward 5' - 3'	Reverse 5' - 3'
Mouse genes		
Atp13a3	TGAAGCTTCCGTGGCATCTC	GCACGACCTTCCCTGATA AGG
Odc1	ACTGTGCAAGCAAGACTGAA	ACTTTGCCTTTGGATGTGCT
Amd1	TCACGAAAATAGCCGGGAAA	TAGCGAACAACCAACAACCA
Srm	TGCGAGATTGATGAGGATGT	ACGTCAAAGGCATCTTGGTT
Sms	ACGTCAAAGGCATCTTGGTT	TTCCTTAAGAGGCAGCCAAA
Smox	TCACTGCCAAATGTGTTCCT	TACCCAGCCTGGAGAAAAAGAAA
Paox	TGGATTTTTGGTCCAGCCTT	AATTGTGGGTTTCCTGTCACTCT
Ssat1	TGCTGTAGATGACAACCTCCATT	TCAAACATGCAACAACGCCA
Slc3a2	AATTGTGGGTTTCCTGTCACTCT	AGGGTTTGTCTTGTTGGCTT
Oaz1	TCACACTCAAGTGTTGGCTT	TTTATTGGATTTGAGCCAGGGGA
Oaz2	AGCCTGTTTGTAGAAATCCCAGA	TCAAAGCCCAAGAAGCTGAA
Oaz3	AGAAGATGCTGCCTTGTTGT	AAGCTGGCTGTGGTCTTTTT
Azin1	TGTGGTCCAGAAATGCCAAA	TGGCAACTGATATGCCACAA
B2m	GTATACTCACGCCACCCACC	TGGGGGTGAATTCAGTGTGAG

Hprt	CTTCCTCCTCAGACCGCTTT	ATCGCTAATCACGACGCTGG
Actb	GGGAAATCGTGCGTGACAT	GTGATGACCTGGCCGTCAG

2.6 Immunoblotting

2.6.1 Whole-Cell Protein extraction

For protein extraction, 300,000 cells were plated in 6-cm dishes prior to experiments. Following the experiment procedure (e.g. transfection, transduction), cells were snap-frozen on an ethanol-dry ice bath and lysed in SDS-lysis buffer (125mM Tris (pH 7.4), 2% SDS, 10% glycerol) containing the EDTA-free protease inhibitor cocktail (Roche). The cell lysates were collected and sonicated for 10 seconds with a 10-micrometre amplitude on ice using a probe sonicator.

2.6.2 Tissue protein extraction

One lobe of mouse lung tissue was excised on dry ice and transferred into a sterile 2ml tube (Star Lab) containing a stainless-steel bead (Qiagen). 1ml/tube of SDS Lysis buffer (125mM Tris (pH 7.4), 2% SDS, 10% glycerol) containing EDTA-free protease inhibitor cocktail (Roche) was then added. The tubes were transferred immediately into the prechilled TissueLyser racks, balanced before homogenising at 25Hz for 5 minutes. Tissues were then checked if well homogenised. An additional 5-minute homogenisation at 25Hz was applied if residual tissue chunks presented. The resulting tissue homogenate was then sonicated before assaying for concentration using a modified Lowry assay as described below.

2.6.3 Lowry assay

A modified Lowry assay (Bio-Rad DC Assay, Bio-Rad) was performed for assessing protein concentration. A standard curve was constructed using BSA (20 µl /well) with the concentration ranging between 0 to 1mg/ml. A volume of 2 µl /well of cell lysate was pipetted in duplicate into a 96-well plate. To each well, 25 µl of A(S) reagent (comprising 20 µl of reagent S(Bio-Rad) in every 1ml

of reagent A(Bio-Rad)), was added into each well followed by 200 µl /well reagent B(Bio-Rad) and left to develop for 15 minutes. The absorbance of the samples and standards plate was read on a plate reader at 595nm, and protein concentration was calculated by linear regression in Graphpad Prism.

2.6.4 Protein separation by Sodium Dodecyl Sulphate-Polyacrylamide Gel Electrophoresis (SDS-PAGE)

Cell lysates(30-45 µg) were denatured at 99°C for 6 minutes with the addition of 5x Sample loading buffer. Samples were then rested on ice for two minutes before loading onto a 10% SDS-PAGE gels. All gels were freshly made using the recipe listed below. Following loading, cell lysates were separated by electrophoresis at 120V in stacking gel for 15 minutes before running at 150V in resolving gel for 60 to 90 minutes. 6 µl PageRuler™ Plus Prestained Protein Ladder (#26619 Thermo Fisher Scientific) was run in a separate lane for estimation of protein mass. Proteins were then transferred onto polyvinylidene fluoride membranes (GE Healthcare) by semi-dry blotting at 90mA for 120 minutes. Membranes were then blocked for an hour with either 5% (w/v) BSA(Sigma-Aldrich) or 5%(w/v) non-fat milk in TBST buffer (0.05% Tween-20 in TBS) before overnight incubation with primary antibodies as listed below. In the following morning, membranes were washed three times with TBST (0.05% Tween-20) for 10 minutes before incubating with corresponding secondary antibodies for an hour at room temperature. Membranes were again washed three times with TBST (0.05% Tween-20) for 10 minutes before rinsed with PBS to clear residual TBST before developing. For protein detection, 1.5ml/blot enhanced chemi-luminescence reagent mixture(A+B) (GE Bioscience) were added onto the membrane and developed for 20 minutes with X-ray film (GE healthcare) in the darkroom. For assessing loading controls, all blots were re-probed with mouse monoclonal anti-α-tubulin antibody (1:5000, T9026 clone DM1A, Sigma-Aldrich) for 30 minutes at room temperature followed by anti-mouse horseradish peroxidase antibody (1:5000, P0447, Dako) for 30 minutes

at room temperature. All blots were developed for 0.5 to 1 minute for visualising proteins.

Table 2-8 PAGE gel recipe

	10% Resolving Gel	4% Stacking Gel
PROTOGEL	5ml	1ml
Gel buffer	3.9ml	1.95ml
dH_2O	5.94ml	4.47ml
10%APS	150 µl	75 µl
TEMED	15 µl	7.5 µl

PROTOGEL (Bio-Rad): 30% acrylamide, 0.8% Bisacrylamide

Resolving gel buffer (Bio-Rad): 1.5 M Tris.HCl, 0.384% SDS; pH 8.8

Stacking buffer (Bio-Rad): 0.5 M Tris.HCl, 0.4% SDS; pH 6.8

APS (Sigma-Aldrich): Ammonium persulfate

TEMED (Sigma-Aldrich): N,N,N',N',-Tetramethylethylenediamine

Table 2-9 Antibodies utility in cell immunostaining

Antibody	Source	Dilution	Secondary	Dilution
Rabbit anti-ATP13A3	Sigma-Aldrich HPA029471	1:1000	anti-rabbit horseradish peroxidase antibody(P0448,Dako)	1:2000
Mouse Anti-Ornithine Decarboxylase/ODC	Abcam ab193338	1:300	anti-mouse horseradish peroxidase antibody(P0448,Dako)	1:2000

2.7 Immunocytochemistry

2.7.1 Slide coating

4-chambered Nunc™ Lab-Tek™ II Chamber Slides™ (Thermo Fisher Scientific) were pre-coated with 500 µl /chamber Type I Rat Tail Collagen (Type I Rat Tail Collagen 1:100 v/v diluted with 0.02N acetic acid, BD Biosciences) for 90 minutes before washing three times with PBS. Slides were then left in the tissue culture hood to dry and kept in the fridge before use.

2.7.2 Immunostaining

Following 48-hour transient siRNA or plasmid DNA transfection, Cells were then trypsinised and reseeded into collagen-coated 4-chambered slides and left to adhere overnight. On the following day, cells were washed with PBS and fixed in 4% (v/v) Paraformaldehyde solution (Sigma) at room temperature for 10 minutes before being permeabilised with 0.05%(v/v) Saponin in 0.5% BSA for a further 20 minutes. For blocking nonspecific binding, cells were incubated in 0.5% BSA/PBS for an hour. The plastic chambers were then removed from the slides, followed by overnight incubation with the intended primary antibodies listed below (Table 2-10). In the following morning, cells were washed three times with PBS before incubation with the corresponding fluorescent antibodies at room temperature for an hour, as shown below. Cells were then briefly washed twice with PBS before mounting with mount medium containing DAPI (Vector Laboratories) and kept in the dark at 4°C before imaging on Leica Sp5 confocal microscope platform (Leica microsystem).

Table 2-10 Antibodies utility in cell immunostaining

Antibody	Source	Dilution	Secondary	Dilution
Rabbit anti-ATP13A3	Sigma-Aldrich HPA029471	1:200	rabbit Alexa Fluor®488	1:200
Mouse Anti-Ornithine Decarboxylase/ODC	Abcam ab193338	1:200	rabbit Alexa Fluor®488	1:200
Mouse Anti-VE-Cadherin CD144	BD Biosciences 555661	1:200	Mouse Alexa Fluor®568	1:200
Mouse Anti-EEA1	BD Biosciences 610456	1:200	Mouse Alexa Fluor®568	1:200
Mouse Anti-Rab7	SANTA CRUZ sc-376362	1:200	Mouse Alexa Fluor®568	1:200
Mouse Anti-Rab11a	SANTA CRUZ Sc-166912	1:200	Mouse Alexa Fluor®568	1:200
Mouse Anti-Rab11a	SANTA CRUZ Sc-20011	1:200	Mouse Alexa Fluor®568	1:200
Mouse Anti-CD31	R&D Systems BBA7	1:300	Mouse Alexa Fluor®488	1:300
Rabbit Anti-Von Willebrand Factor (VWF)	Abcam Ab6994	1:200	rabbit Alexa Fluor®488	1:200
mouse anti-myosin (smooth)	Sigma-Aldrich M7786	1:200	Mouse Alexa Fluor®488	1:200
Rabbit Anti-Oct4	Reprocell, 09-0023	1:100	rabbit Alexa Fluor®488	1:100
Rabbit Anti-Nanog	Reprocell, 09-0020	1:100	rabbit Alexa Fluor®488	1:100

Mouse Anti-TRA-1-60	Reprocell, 09-0010	1:100	Mouse Alexa Fluor®488	1:100

2.8 Polyamine measurement by Liquid chromatography-mass spectrometry

2.8.1 Aqueous metabolites extraction

Adherent cells

To extract aqueous metabolites, cells were seeded at a density of 300,000cells/well into 6-well plates. Following the intended experiments, cells were then washed twice with phosphate-free buffer (162mM ammonium acetate 7.4) before being lysed with 350 µl 4:1 methanol: water. Cells were harvested from the plates with a cell scraper and carefully transferred into corresponding 2ml flat-bottom screw cap tubes. The resulting cell lysate was sonicated for 5 minutes in a water bath sonicator. An additional 5-minute sonication was applied if obvious cell debris was still present. The cell homogenate was then centrifuged at 21000g for 10 minutes at room temperature to pellet residual debris, and the supernatant was carefully transferred into new tubes. The resulting cell aqueous metabolites were then lyophilised using a centrifugal evaporator (Savant, Thermo Scientific) overnight and stored at -20 ºC prior to further preparation and analysis. For internal normalisation, the pellets remaining from the previous step were further lysed with SDS lysis buffer as described previously and assessed for protein concentration using Lowry assay.

Mouse lung tissues

Mouse lung tissues were homogenised in the TissueLyser II (Qiagen) followed by extraction in 4:1 methanol: water as described previously. To achieve this, one lobe of the mouse lung tissue was excised on dry ice and weighed before being transferred into a sterile 2ml tube (Star Lab) containing with a stainless-steel bead (Qiagen). All tubes were rested on dry ice prior to

lysing in 1ml/tube of 4:1 methanol: water. The tubes were transferred immediately into the prechilled TissueLyser racks, balanced before homogenising at 25Hz for 5 minutes. Tissues were then checked if well homogenised. An additional 5 to 10 minutes homogenisation at 25Hz was applied if residual tissue chunks still presented. The resulting lung homogenate was sonicated for one minute before centrifuged at 21200g for ten minutes at room temperature. Following centrifugation, the top aqueous layer was transferred into a fresh tube while the organic bottom layer was collected into a separate tube followed by a second extraction using 1ml 4:1 methanol: water. The resulting aqueous layer was combined and dried, as described previously. The residual pellets were lysed with SDS lysis buffer as described previously, and protein concentration was assessed using Lowry assay.

Targeted analysis of the metabolites was then performed by Dr. James West (Kaser Lab) using a Quantiva triple stage quadrupole mass spectrometer coupled to a Vanquish Horizon (all analytical instrument combinations supplied by Thermo Fisher Scientific). The resultant data were acquired, processed and integrated using Xcalibur (Version 3.0, Thermo Fisher Scientific) and Compound Discoverer (Version 2.1, Thermo Fisher Scientific).

2.9 Human induced pluripotent stem cell

2.9.1 Cell culture

Human induced pluripotent stem cells (iPSCs) were maintained in 6-well plates coated with gelatine to aid the attachment. To prepare the plates, 1.5ml/well of 0.2% (w/v) porcine gelatine (Sigma) solution in cell culture grade water (Hyclone) was added. After one-hour incubation at room temperature, the solution was replaced with DMEM supplemented with 10% FBS and incubated for at least 2 hours in the incubator before use. Prior to laying down cells, plates were washed once with PBS and replenished with respective growth media.

For feeder-dependent human induced pluripotent stem cells (hiPSCs), cells were grown on top of a 25% confluent irradiated mouse embryonic fibroblast (iMEF) cell layer in feeder-dependent hiPSCs media as described in the Appendix while feeder-free hiPSCs were cultured in BK media. For feeder-free H9 human embryonic stem cells (hESCs), cells were grown in CDM-BSA supplemented with activin A (10mg/ml) and FGF-2(12ng/ml) [271].

2.9.2 Generation of *ATP13A3*-R858H induced pluripotent stem cell lines

2.9.2.1 CRISPR-Cas9 genetic editing overview

The Clustered Regularly Interspaced Short Palindromic Repeat (CRISPR)/CRISPR association protein 9 (Cas9) genetic editing system[272] was used to introduce a PAH associated *ATP13A3* missense mutation (R858H) into the C2 iPSC line generated from BOECs from a wild-type individual without any previous history of PAH.

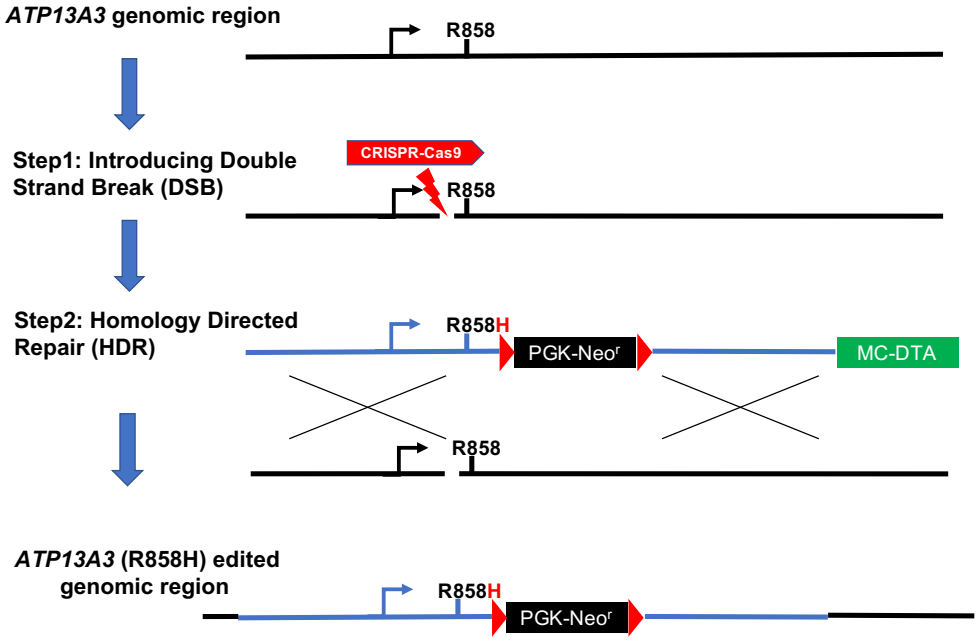

Figure 2-2 Strategy overview of introducing ATP13A3-R858H mutation using the CRISPR-Cas9 system.

The completion of the CRISPR-Cas9 directed genetic editing (*ATP13A3*-R858H) involves two steps: 1. To Introduce a double-strand break at the desired editing region (indicated by a red flash) with the CRISPR-Cas9 complex (red arrow). 2. The double-

strand break introduced by CRISPR-Cas9 complex is then repaired by the homology-directed repair (HDR) pathway with the direction of a repairing template bearing the R858H mutation.

2.9.2.2 Design of the CRISPR-Cas9 guide RNA

The CRISPR-Cas9 system is consist of two components: a guide RNA (gRNA) and a CRISPR endonuclease. A gRNA is a ~20bp nucleotide sequence shares the homology with the target genomic region. Following the binding of gRNA to the DNA target, a 3-bp protospacer adjacent motif (PAM) immediately downstream of the 3' end of the target region senses the signal for Cas9 endonuclease which then introduces a double stream break (DSB). CRISPR-Cas9 guide RNAs using in this study were designed using the online platform, benchling (www.benchling.com), based on the algorithm considering the target efficiency and off-target possibility. gRNA primers used for CRISPR Nuclease vector cloning were listed below (Table 2-11)

Table 2-11 Primers used for CRISPR-Cas9 cloning

Primer name	Forward 5' - 3'	Reverse 5' - 3'
gRNA primers		
ATP13A3-R858H-gRNA1	AGGTGCCATACGGGCAAACAgtttt	TGTTTGCCCGTATGGCACCTcggtg
ATP13A3-R858H-gRNA2	TGGCACCGTGTTTGCCCGTAgtttt	TACGGGCAAACACGGTGCCAcggtg
Repairing template homology arm primers		
ATP13A3-R858H-left homology arm	CGGCGAGCTAGCATTAGGTGACAGTATGTTGAC	GCGCAGCCTAGGGACACCAATACTTACTCAACATTTTGC
ATP13A3-R858H-right homology arm	ATATAACCCGGGTCACTTGTGGTCTGGTGCTG	AATATACCCGGGCTGTTTGCAAAGCAGCACAC
Cleavage detection primer		
Cleavage detection	GGTGTATGTGTGTGCTCAC	GCGCTTGTGCCTACAGTCTT
Side direct mutagenesis (SDM) primer		

ATP13A3-R858-SDM primer	GCATGGCACaGTcTTcGCCCaTATGGCACC	GGTGCCATAtGGGCgAAgACtGTGCCATGC

2.9.2.3 Generation of the *ATP13A3*-R858H CRISPR-Cas9 nuclease vector

To create the CRISPR-Cas9 complex targeting for *ATP13A3*-R858H editing, double-stranded oligonucleotides with the sequences listed in Table 2-11 were cloned into the GeneArt® CRISPR Nuclease Vector (A21174, Life technologies) (Figure 2-3) per the manufacturer's protocol. In Brief, 5 µl of each Forward/Reverse strand oligonucleotide at 200µM were reannealed in a 20 µl reaction containing 2 µl of annealing buffer and 8 µl of DNase/RNase-free water. The reaction was left at room temperature for 30 minutes before diluted 100-fold twice to make the 5nM working solution for ligation. 2 µl of Linearised GeneArt® CRISPR Nuclease Vector was ligated to 2 µl of 5nM double-stranded oligonucleotide solution at room temperature for 2 hours before proceeding to transformation. One Shot® TOP10 chemically competent E. coli was used for transformation, adding 3 µl of the ligation reaction to a vial of E.Coli. Tubes were left on ice for 30 minutes before heat-shock for 30 seconds at 42°C. 250 µl of S.O.C medium was added, followed by shaking on a Thermomixer for an hour at 500rpm. 50 µl of the transformation reaction was spread evenly on a prewarm LB agar plate containing 100 µg/ml ampicillin and incubated at 37°C overnight. Colonies were picked in the following day and cultured in 5ml of LB broth containing the appropriate antibiotics overnight. Plasmid DNA was then purified and stored at -20 ºC prior use. The GeneArt® CRISPR Nuclease Vector contains an orange fluorescent protein (OFP) to enable FACs enrichment of cleaved cell population and assessment of cleavage efficiency.

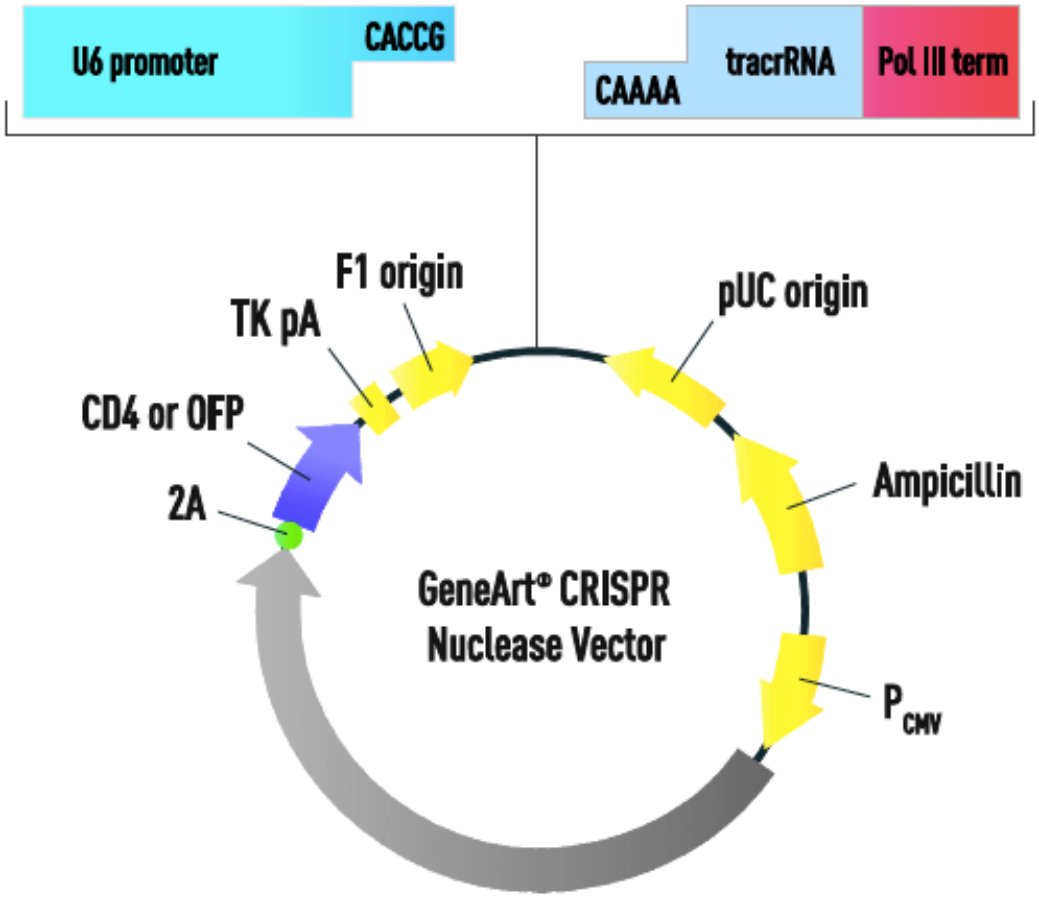

Figure 2-3 Schematic of GeneArt® CRISPR Nuclease Vector.

The GeneArt® CRISPR Nuclease Vector is a 9219bp plasmid constructed with the targeting CRISPR RNA (crRNA), a trans-activating crRNA (tracrRNA) as well as the Cas9 nuclease expression cassette. Double-strand oligonucleotides encoding the desired target CRISPR RNA (without PAM sequence) were cloned into the 3' downstream overhang of U6 promotor, ensuring the expression of Cas9 nuclease. The vector also contains an orange fluorescent protein (OFP) cassette, which following transfection, enables cell population enrichment with Fluorescence-activated cell sorting (FACs). The image was reproduced from (www.lifetechnologies.com).

2.9.2.4 Generation of the *ATP13A3*-R858H repairing template

The double-strand break introduced by CRISPR-Cas9 complex is repaired through either non-homologous end joining (NHEJ) or homology-directed repair (HDR). The NHEJ is an active but error-prone repairing pathway whereas the HDR is less efficient by has a high-fidelity. To introduce a precise modification in *ATP13A3*, a repair template containing the desired mutation was designed and delivered together with the CRISPR-Cas9 nuclease vector to maximise the utilisation of HDR for gene editing. To introduce the *ATP13A3*-R858H(G>A) mutation into the wild type C2 iPSC line, using AccuPrime™ Pfx DNA Polymerase kit (Invitrogen) as described below.

2.9.2.4.1 Cloning of LHA and RHA into pCR™-BluntII-TOPO® plasmid vectors

Two ~1kb DNA fragments namely Left homology arm (LHA), and right homology arm (RHA) were first cloned from the C2 genomic DNA and then subcloned into pCR™-BluntII-TOPO® plasmid vectors respectively using the Zero Blunt® TOPO® PCR Cloning Kit (Life technologies) as shown below.

Reagent	Volume
LHA/RHA PCR product	3 µl
Salt solution	1 µl
Nuclease free water	1 µl
pCR™-BluntII-TOPO®	1 µl

The cloning reaction was mixed and incubated at room temperature for an hour before proceeding to transform One Shot® TOP10 chemically competent cells.

2.9.2.4.2 Site direct mutagenesis in LHA-TOPO vector

As illustrated in Figure 2-2, the R858H mutation, together with three silent mutations aiming to prevent CRISPR re-cutting was introduced into the LHA using QuickChange II Site-Directed Mutagenesis (SDM) kit (Agilent Technologies). The pair of SDM primers were designed following the manufacturer's protocol.

Briefly, the criteria assigned were that the primer length should fall between 25 and 45 bases, with a melting temperature (Tm) of ≥78°C. The intended mutations should occupy the middle of the primers, leaving 10-15bp of correct sequence at each side. PCR reaction was set up as below:

10x buffer	5 µl
LHA-TOPO vector	50ng
SDM Forward primer	125ng (1.26 µl)
SDM Reverse primer	125ng (1.26 µl)
dNTP	1
Nuclease free water	36.48
Pfu ultra	1

Reactions were further amplified as follow:

95°C	30 seconds	1 cycle
95°C	30 seconds	18 cycles
55°C	1 minute	
68°C	5 minutes	

Following the mutagenesis PCR reaction, 1 µl of Dpn I restriction enzyme was added into the reaction and incubated for an hour at 37°C to digest parental methylated and hemi-methylated DNA. 1 µl of Dpn I treated reaction was then used for the transformation of 50 µl of XL-1 Blue cells. The cells were incubated on ice for 30 minutes before heat shocked for 45 seconds at 42°C. 500 µl of SOC medium was added and shaken in a Thermomixer at 500rpm for an hour at 37°C. 250 µl of transformation reaction was spread evenly onto two LB agar plates with 100 µg/ml Kanamycin followed by overnight incubation at 37°C. Plasmid DNA was prepared in the following day with the success of mutagenesis confirmed by Sanger sequencing (Genewiz) for the engineered LHA-TOPO vector.

2.9.2.4.3 Construction of RHA-LNDA vector

To complete the targeting repairing template, the two engineered DNA fragments, LHA and RHA in pCR™-BluntII-TOPO® were cloned into the Lox neo-DTA (A)(LNDA) plasmid backbone which contains a phosphoglycerate kinase promoter-driven neomycin resistance (PGK-NEO) positive selection cassette and an MC-1DTA (diphtheria toxin A) negative selection cassette as illustrated in Figure 2-2. LNDA vector was first linearised with SmaI (NEB) while the RHA fragment was cut out with the same restriction enzyme from the RHA-TOPO vector following the reaction listed below.

RHA-TOPO vector/LNDA	5 µg (11.5 µl /5 µl)
Cutsmart	5 µl
Nuclease free water	32 µl /38.5 µl
SmaI	1.5 µl

Both reactions were performed at 25°C for two hours for digestion and at 65°C for another 20 minutes to inactive the enzyme. 1.11 µl of Calf intestinal alkaline phosphatase (CIAP) (Promega) was added into the reaction and incubated for 10 minutes at 37°C, followed by inactivation for 2 minutes at 80°C to prevent the recircularization and re-ligation of RHA-TOPO vector and linearised LNDA vector.

Following the digestion step, RHA-TOPO reaction was loaded onto a 1.5% Agarose gel (low melting point) and ran for one hour before image by the Gel doc imaging machine. A band present at 1kb was excised under UV light and purified using the Invisorb® Fragment CleanUp kit (stratec molecular). RHA fragments purified from the previous step was ligated to the linearised LNDA vectors using the T4 DNA ligase Kit follow the manufacturer's protocol. ligation reaction was transformed using One Shot® TOP10 chemically competent E. Coli cells. The success of constructing the RHA-LNDA vector was confirmed by Sanger sequencing (Genewiz).

In comparison to the RHA fragments, the LHA fragments with the target mutation were cloned out by double digestion with NheI and AvrII restriction as described below (Table 2-11).

Briefly, 5 µg of LHA-TOPO vector was digested with NheI as listed above for an hour at 37°C followed by the inactivation of the enzyme at 65°C for 20 minutes. The linearised vector was then digested by adding 1.5 µl AvrII into the reaction and incubated for another hour at 37°C. In the meantime, The RHA-LNDA vector was linearised using the same restriction enzymes (Table 2-17). Both products were purified using the Invisorb® Fragment CleanUp kit (stratec molecular).

RHA-LNDA vector/ LHA-TOPO vector	5 µg (5 µl)/ 5 µg (10 µl)
Cutsmart	5 µl
Nuclease free water	37 µl / 33.5 µl
NheI	1.5 µl
AvrII	1.5 µl

To complete the construction of the final repairing template, the purified LHA fragments were ligated to the linearised RHA-LNDA vector in the reaction described below.

5x Ligase buffer	4 µl
Vector DNA	60 fmol
Insert DNA	180 fmol
T4 Ligase	1 µl

The ligation reaction was performed at 25 °C for 20 hours. 2 µl of the reaction was used for the transformation of One Shot® TOP10 chemically competent cells. The success of the construction of the LHA-RHA-LNDA vector was confirmed by Sanger sequencing (Genewiz).

2.9.3 Cell electroporation

Feeder-dependent C2 wild type iPSCs were removed from iMEF feeder cells and cultured in BK media as a feeder-free condition for a week before electroporated. 5 μg of the R858H targeting construct was linearised with 1.5 μl of NheI restriction enzyme digestion overnight followed by the purification of the linearised vector using Invisorb® Fragment CleanUp kit (stratec molecular).
3 μg of the linearised R858H targeting construct together with 2 μg of CRISPR vector was co-transfected into C2 wild type iPSCs using the Human Stem Cell Nucleofector Kit 1(Lonza). To achieve this, feeder-free C2 iPSCs growing in 6-well plates at ~70% confluence was washed twice with 1.5ml/well PBS before dissociation with 0.5ml/well of 1xTrypLE Select (Thermo Fisher Scientific) supplemented with 2 mM EDTA (Thermo Fisher Scientific) at 37°C for 5 minutes. 1ml/well of BK media was then added to the cell suspension to neutralise the TrypLE Select. Cell numbers were counted in the cell suspension before transferring $8x10^5$ cells into a 1.5ml Eppendorf tube and centrifuged at 150 x g for 3 minutes at room temperature. After discarding the supernatant, the cell pellet was gently resuspended with 100 μl of Nucleofector® Solution (Lonza). 3 μg of the linearised R858H targeting construct together with 2 μg of CRISPR vector were added into cell suspension before transferred into a cuvette. The cuvette was then inserted into the Amaxa Nucleofector machine (Lonza) and cells were electroporated with Program B-016 before being transferred back into a 24-well plate prefilled with 500 μl of prewarmed BK media. As a positive control, a separate set of C2 iPSCs were transfected with μg of pmaxGFP vector (Lonza) using the same electroporation protocol. To check the transfection efficiency, cell fluorescent imaging for assessing OFP expression was performed on a Leica DMI3000 B manual inverted microscope 24 hours post-transfection.

2.9.4 Fluorescence-activated cell sorting (FACs) enrichment of CRISPR targeted cells.

24-hour post-transfection, cells in 24-well plates were washed with 500 µl /well of PBS once and dissociated with 250 µl /well of 1xTrypLE Select (Thermo Fisher Scientific) supplemented with 2 mM EDTA (Thermo Fisher Scientific) at 37°C for 5 minutes before neutralizing with 0.5ml/well of BK media. The cell suspension was then transferred into a 5ml Falcon™ Round-Bottom Polystyrene Tubes (fisher scientific) and pelleted at 300g for 5 minutes at room temperature. The resulting cell pellet was then resuspended gently in 1ml of BK media before loaded onto the BD FACSAriaTM Fusion (BD) cell sorter. A separate set of C2 iPSCs without CRISPR transfection was harvested following the same protocol and run on the cell sorter for negative cell gating prior to the CRISPR cell enrichment. Forward Scatter Width (FSC-W) against Forward Scatter-Area (FSC-A) parameters were used for gating out cell debris and doublets. 561 582/15-A channel against 633 660/20-A channel was used for OFP positive cell gating. Following the negative cell gating, the CRISPR targeted cell suspension was run at 10 000 events/second on the platform, and single positive cell drops were collected into a 5ml Falcon™ FACs Tubes (fisher scientific) prefilled with 1ml BK media. After sorting, the enriched cell suspension was centrifuged at 300g for 5 minutes at room temperature. The cell pellet was resuspended in 1 ml of BK medium before transferred into a 10cm Corning® culture dish for iPSCs colony formation.

2.9.5 Genomic cleavage detection

The cleavage efficiency of the CRISPR-Cas9 system was assessed using the GeneArt® Genomic Cleavage Detection Kit (Thermo Fisher Scientific).
48-hour post-transfection, CRISPR targeted cells, as well as pmaxGFP control cells, were harvested from the 24-well plated and the resulting cell suspension

centrifuged at 200g for 5 minutes at 4°C. Cells were then lysed in 50 µl of Cell lysis buffer supplemented with 2 µl of Protein Degrader provided from the kit. The lysing process was performed in the thermal cycler following the program listed below.

68°C	15 minutes
95°C	10 minutes
4°C	Hold

Following lysing, the resulting genomic DNA from the targeted cells were used for PCR amplifying the region where the CRISPR had introduced a double-strand break using the primers listed in table 2-11. The reaction volume is described as followed.

Component	CRISPR-iPSCs	pmaxGFP-iPSCs
Cell lysate	2 µl	-
10uM F/R primer mix	1 µl	-
Control Template & primers	-	1 µl
AmpliTaq Gold® 360 Master Mix	25 µl	25 µl
Nuclease free water	22 µl	24 µl

The PCR reactions were run following the program below.

Enzyme activation	95°C	10 minutes	1x
Denature	95°C	30 seconds	40x
anneal	55°C	30 seconds	
Extend	72°C	30 seconds	
Final extension	72°C	7 minutes	1x
Hold	4°C	Hold	1x

The introduction of the double-strand breaks by the CRISPR-Cas9 system also created genomic insertions and/or deletions(indels) via the action of the NHEJ cellular repair mechanism. Therefore, the PCR amplicons from the previous step were denatured and reannealed to create mismatches which can be cleaved by Detection enzyme from the kit, resulting in two distinct bands after electrophoresis. To achieve this, 2 µl of PCR product together with 1 µl of 10X Detection Reaction Buffer and 6 µl of water were mixed thoroughly in a PCR tube and amplified using the program described below.

95°C	5 minutes	-
95°C-85°C	-	–2°C/sec
85°C-25°C	-	–2°C/sec
4°C	-	hold

1µl of detection enzyme from the kit was added to the mismatched product and incubated at 37°C for an hour before electrophoresis on a 2% agarose gel for an hour at 90V and imaging on a Geldoc imaging platform. The cleavage efficiency was calculated following the equation listed below:

Cleavage Efficiency = 1– [(1–fraction cleaved) ½]

Fraction Cleaved = sum of cleaved band intensities / (sum of the cleaved and parental band intensities)

2.9.6 *ATP13A3*-R858H genotyping

After FACs enrichment, the targeted C2 iPSCs were grown from individual single cells to reach individual cell colonies in 10cm dishes for two weeks. At day 14, cell colonies were hand-picked using 200µl pipette tips under a microscope and carefully transferred into 0.5ml sterile tubes prefilled with 60µl of 1xTrypLE Select (Thermo Fisher Scientific) supplemented with 2 mM EDTA (Thermo Fisher Scientific) to disperse the colonies before seeding into a 96-well plate prefilled with 150µl of BK media. Cells were grown to confluence and split 1 to 2 into a new 96-well plate with the remaining half of the cell suspension used for genomic DNA isolation. To assess the successful introduction of

R858H *ATP13A3* mutation, a pair of genotyping primers (Table 2-11), were used to amplify the LHA with the intended R858H mutation using the cell genomic DNA. 2µl of the resulting PCR product was used for positive genotype screening using NdeI restriction enzyme digestion as the introduction of R858H mutation will create a *de novo* NdeI cutting site in the amplicons. The positive PCR samples with two distinct bands were then purified using the Invisorb® Fragment CleanUp kit (stratec molecular) and submitted for Sanger sequencing to confirm the genotype.

2.9.7 Generation of iPSC-derived vascular cell-like cells

2.9.7.1 Generation of iPSC-derived endothelial cells(iPSC-ECs)

iPSCs-EC differentiation protocol

iPSCs-ECs derived from the R858H targeted as well as the C2 wild type iPSCs were generated using a 10-day differentiation protocol as described previously [273]. On day 0, 6 colonies/line were collected from the feeder-dependent iPSC lines and dispersed slightly in 1ml of 25% media (Appendix) before being seeded into a 0.2% gelatin-coated T25 flask (star lab) prefilled with 4ml of 25% medium. Following overnight attachment, the medium was aspirated and replaced with 5ml/flask of CDM-PVA supplemented with 20ng/ml FGF2, 10µM LY294002 (Sigma) and 10ng/ml BMP4 (Thermo Fisher Scientific). Cells were differentiated into the mesoderm phase with this conditioned media for 4 days. On day 5, the medium was replaced with 5ml/flask of CDM-PVA supplemented with 5ng/ml FGF2, 20ng/ml human $VEGFA_{165}$, 10ng/ml BMP4, 10µM SB 431542 and 5µM DAPT to differentiate cells towards the endothelial cell phase. On day 6 and day 7, cells were fed in E^+ media supplemented with 5ng/ml FGF2, 20ng/ml human $VEGFA_{165}$, 10ng/ml BMP4, 10µM SB 431542 and 5µM DAPT. On day 8 and day 9, cells were changed into E^+ media supplemented with 5ng/ml FGF2, 20ng/ml human $VEGFA_{165}$, 10ng/ml BMP4 and ROCK inhibitor (0.1%v/v) to prevent cell apoptosis. On day 10, the iPSC-

derived endothelial cell population was isolated using the Magnetic-activated cell sorting (MACS) system.

Magnetic-activated cell sorting (MACS) enrichment of iPSC-ECs

Following the endothelial cell differentiation process, cells were first dual-labelled with two endothelial-specific markers CD144 (CD144 MiroBeads, human, Miltenyi Biotec) and CD31 (CD31 MicroBead Kit human, Miltenyi Biotec) before isolation using the OctoMACS™ Separator (Miltenyi Biotec).

iPSCs from the T25 flask were washed twice with 3ml of PBS before dissociation with 1.5ml of 2xTrypLE Select (Thermo Fisher Scientific) supplemented with 2 mM EDTA (Thermo Fisher Scientific) at 37°C for 5 minutes. The detached cell suspension was then passed through a 50 μm cell filter before neutralization with 3ml of E^+ media supplemented with 2 mM EDTA (E^+ + EDTA media). The resulting cell suspension was then pelleted at 300g for 5 minutes followed by resuspending in 60μl of E^+ + EDTA media. 20μl of FcR blocking Reagent (CD31 MicroBead Kit human, Miltenyi Biotec) together with 20μl of CD31 Microbeads and 20μl of CD144 MicroBeads were added into the cell suspension followed by brief vortex and incubation at 4°C for 15 minutes. Following incubation, 1ml of E^+ + EDTA media was added to wash off excess microbeads and then centrifuged at 300g for 5 minutes. During the centrifugation step, the MS columns (Miltenyi Biotec) used for EC isolation were attached to the OctoMACS™ Separator with a 15ml Falcon tube (Starlab) prepared underneath each column for cell collection. The columns were then rinsed and equilibrated with 0.5ml of E^+ media before EC sorting. Following centrifugation of the cells, the resulting pellet was resuspended in 0.5ml of E^+ media and added straight away to the MS columns. After the cell suspension, had flowed through, columns were then washed three times with 0.5ml of E^+ media, resulting in a total of 2ml EC-negative cell suspension in the collection tube. Following washing, the MS columns were transferred into a new 15ml Falcon tube for EC-positive cells collection. 1ml warm E^+ FGM media was

added into the columns, and the iPSC-ECs immediately flushed out by firmly pushing the plunger into the column. Both the EC-negative and EC-positive cell suspensions were counted for calculation of the differentiation efficiency. iPSC-ECs were then seeded in tissue culture plates per the yield. iPSC-ECs were maintained for a maximum of 2 weeks in E^+ FGM media when endothelial marker staining, the cell apoptosis assay and mRNA/protein extraction were performed.

2.9.7.2 Generation of iPSC-derived smooth muscle cells (iPSC-SMCs)

To generate iPSC-SMCs, R858H targeted as well as the C2 wild type iPSCs underwent a 17-day differentiation protocol as described previously [273].

On day 0, 6 colonies/line were collected from the feeder-dependent iPSCs lines and dispersed slightly in 1ml of 25% media before seeding into a 0.2% gelatin-coated T25 flask (star lab) prefilled with 4ml of 25% media. To start smooth muscle cell differentiation, iPSCs were cultured in 5ml/flask of CDM-PVA supplemented with 20ng/ml FGF2, 10μM LY294002 (Sigma) and 10ng/ml BMP4 (Thermo Fisher Scientific) for 36 hours to induce early mesoderm differentiation. Subsequently, cells were cultured in 5ml/flask of CDM-PVA + FGF-2 (20 ng/ml) and BMP4 (50 ng/ml) for a further 3.5 days to induce late plate mesoderm formation. On day 5, cells were trypsinised and reseeded into new T25 flasks at a density of $5x10^5$ cell/flask to avoid over-confluence. Cells were cultured in CDM-PVA supplemented with PDGF-BB (10 ng/ml, Thermo Fisher Scientific), TGF-b1 (2 ng/ml, Thermo Fisher Scientific) and BMP4 (50 ng/ml) for a further 12 days to differentiate into Smooth muscle cells. iPSC-SMCs were then matured for another seven days in DMEM supplemented with 10%FBS.

Chapter 3 Results I-ATP13A3 and vascular cells

3.1 Introduction

Pulmonary Arterial Hypertension (PAH) is characterised by vascular remodelling caused by dysfunctional vascular cells. The disease pathogenesis is believed to be initiated by the disruption of endothelial functions [274, 275]. Teichert-Kuliszewska et al. [48] showed that *BMPR2* loss-of-function predisposes PAECs to apoptosis. An *in vivo* study also revealed that endothelial specific knockout of *Bmpr2* predisposed mice to PAH [276]. SU5416, a tyrosine kinase inhibitor, inhibits vascular endothelial growth factor receptors (VEGFR1 [277], VEGFR2 [278]) and in combination with hypoxia, induces endothelial injury in the rat pulmonary vasculature causing a progressive pulmonary vascular remodelling [45, 279]. Hyperproliferative and apoptosis-resistant pulmonary artery smooth muscle cells have been well documented as another important component contributing to vascular remodelling in PAH [40, 274, 275].

A recent whole genome sequencing study of a PAH cohort, led by the Morrell laboratory, revealed 11 ultra-rare heterozygous mutations in the gene encoding ATP13A3, a P5-type ATPase [27]. P-type ATPases are a group of membrane transporters which, by forming phosphorylated intermediates via ATP hydrolysis, translocate cations across cell membranes [110, 280]. Phylogenetic analysis has revealed five subgroups of this superfamily, namely P1-P5 ATPases [141, 280]. Among these, the P5-ATPases remain the least studied group with no known substrate specificity and ATP13A3 represents a P5B-ATPase of unknown cellular function.

Data from GTEX platform (https://www.gtexportal.org/home/) reveals ATP13A3 as widely expressed across human tissues. Interestingly, apart from the thyroid gland, a relatively high level of *ATP13A3* is observed in systemic arteries tissues and lung tissues (Chapter 1 Introduction). Single-cell RNAseq using lung tissues from healthy subjects [154] further indicates abundant

ATP13A3 expression in pulmonary macrophages, dendritic cells and vascular endothelial cells (Chapter I Introduction). These suggest a potential link of ATP13A3 to the functions of the pulmonary vasculature. Here in this chapter, I will assess the expression of ATP13A3 and other P5-ATPases in pulmonary vascular cells and investigate the impacts of ATP13A3 deficiency to cell functions.

3.1 Results

3.1.1 ATP13A3 is highly expressed in pulmonary vascular cells.

I first assessed the mRNA expression of *ATP13A1-5* by qPCR in human pulmonary artery endothelial cells (hPAECs), human pulmonary artery smooth muscle cells (hPASMCs) and blood outgrowth endothelial cells (BOECs). As illustrated in Figure 3-1, *ATP13A3* was expressed in all three types of cells with highest levels observed in hPAECs, slightly lower levels in hPASMCs and lowest levels in BOECs. hPAECs also showed the highest *ATP13A1* and *ATP12A2* mRNA expression, though the levels were only 15% of the *ATP13A3* expression. Unlike *ATP13A1-ATP13A3, ATP13A4* and *ATP13A5* were barely expressed in these cell types (data not shown).

3.1.1 Validation of ATP13A3 siRNA knockdown efficiency in different cell types

ATP13A3 loss of function is thought to participate in in the pathobiology of PAH [27]. To characterise this in human vascular cells, two siRNA oligonucleotides targeting different regions of the human *ATP13A3* mRNA were tested for their knockdown efficiency in both hPASMCs and BOECs. Forty-eight hours post-transfection, cells were harvested and assessed for *ATP13A3* mRNA expression by qPCR. In comparison with siRNA control pool, hPASMCs transfected with si*ATP13A3*#1 exhibited an average of 80% reduced *ATP13A3* expression while the mean knockdown efficiency of si*ATP13A3*#2 was only 40% (Figure3-2). Similarly, si*ATP13A3*#1 transfection in BOECs also yielded a higher knockdown efficiency (~85%) than si*ATP13A3*#2 transfection (~50%)

(Figure3-3). Therefore, si*ATP13A3*#1 was chosen for further experiments. In addition, to assess the specificity of si*ATP13A3* #1, mRNA expression of other P5-ATPases was also examined in BOECs. As shown in Figure 3-4, si*ATP13A3*#1 yielded an average of ~90% knockdown of *ATP13A3* without affecting the expression of *ATP13A1* and *ATP13A2.* Basal expression of *ATP13A4*, *ATP13A5* were undetectable and were therefore not included in the panel.

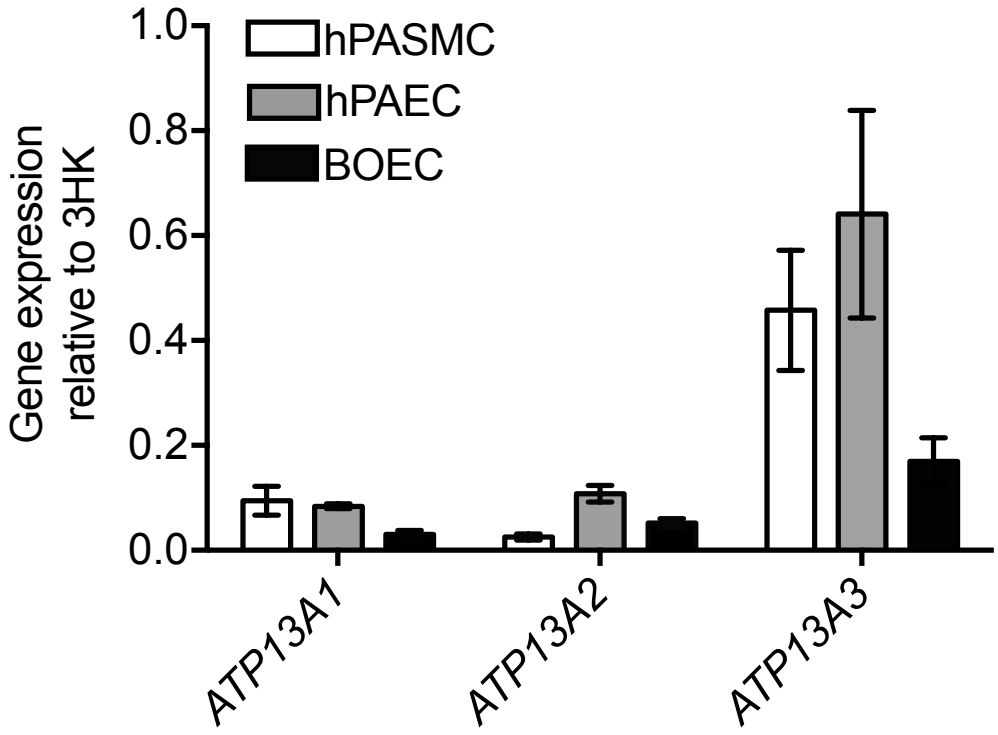

Figure 3-1 P5-ATPase family gene expression in vascular cell types

Relative expression of *ATP13A1-3* in hPAECs, hPASMCs and BOECs were assessed by qPCR (n=4). Data are presented as fold-change normalised to the arithmetic mean of the Ct values of three different housekeeping (3HK) genes *B2M, ACTB, HPRT*. One-way ANOVA with Tukey's post hoc test was used for multiple comparisons among the mRNA expression of P5-ATPases in different cell types.

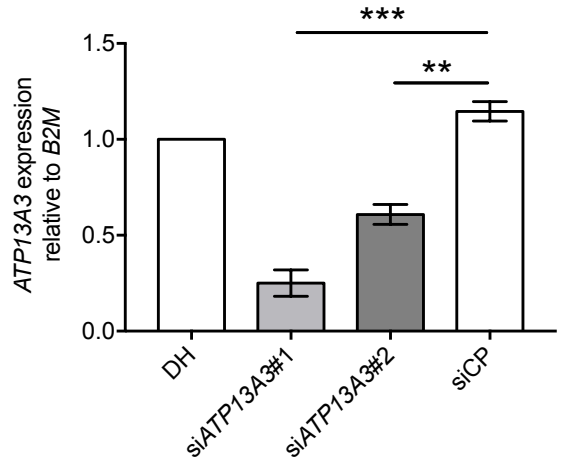

Figure 3-2 si*ATP13A3* knockdown efficiency in human pulmonary artery smooth muscle cells.

hPASMCs (78MP, 79MP, 103MP) were transfected with 10nM ATP13A3 siRNA (#1, #2) and assessed for knockdown efficiency 48-hour post-transfection. *ATP13A3* mRNA was presented as fold-change relative to *B2M* and further normalised to DH. One-way ANOVA with Tukey's post hoc test for multiple comparisons was used for data analysis **P<0.01, ***P<0.001 compared with siCP.

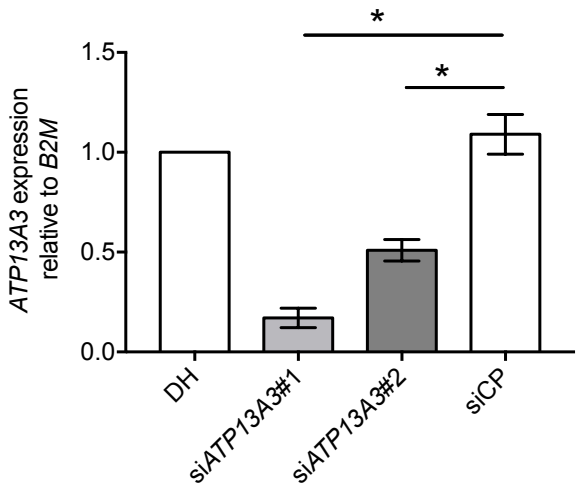

Figure 3-3 si*ATP13A3* knockdown efficiency in blood outgrowth endothelial

BOECs (C4, C7, C26) were transfected with ATP13A3 siRNA (#1, #2) and assessed knockdown efficiency 48-hour post-transfection. ATP13A3 mRNA was presented as fold-change relative to B2M and further normalised to DH. One-way ANOVA with Tukey's post hoc test for multiple comparisons was used for data analysis *P<0.05, compared with siCP

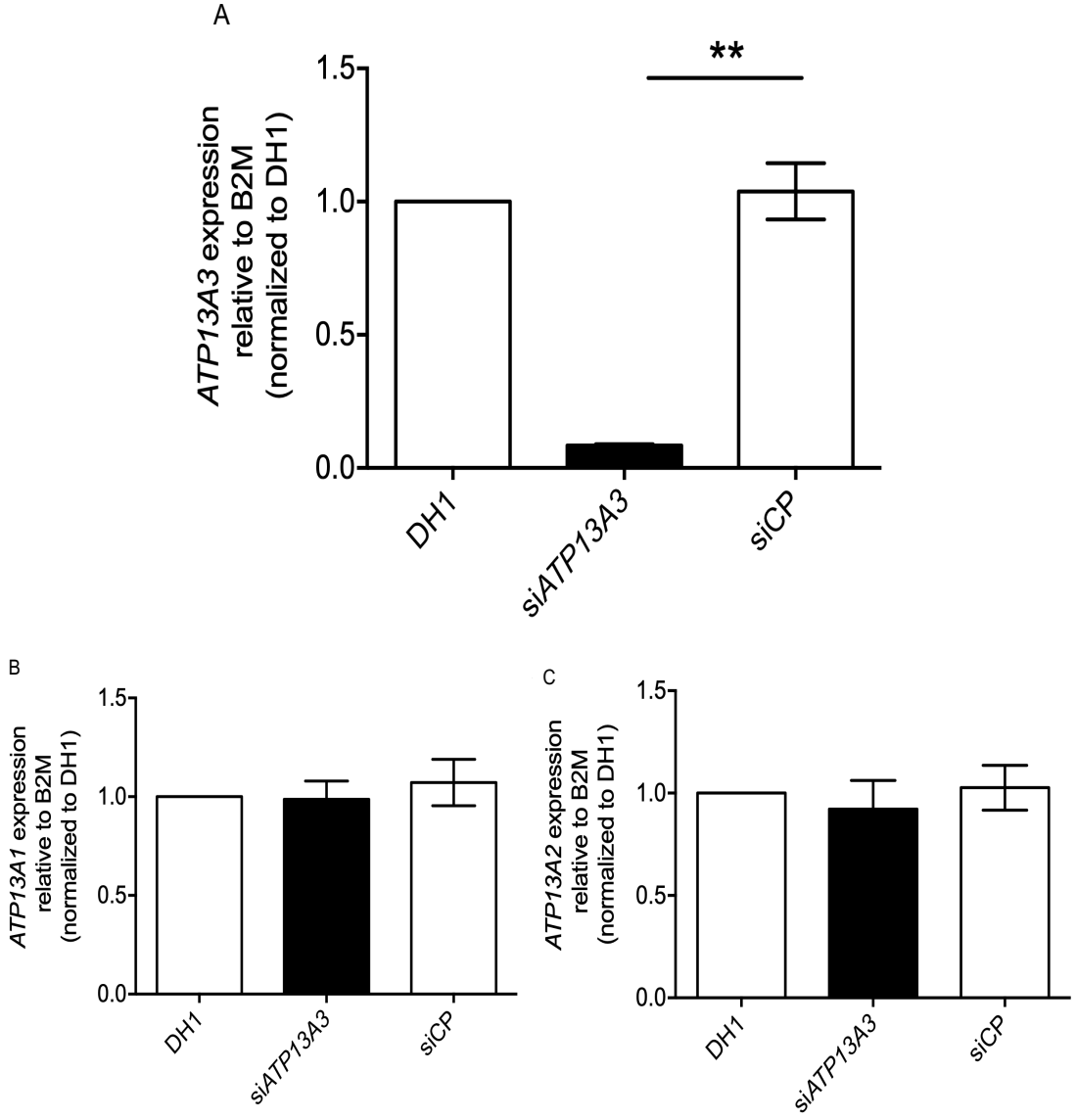

Figure 3-4 ATP13A3 depletion in BOECs did not alter mRNA expression of other P5-ATPases

mRNA expression of (A) *ATP13A3*, (B) *ATP13A1*, and (C) *ATP13A2* in BOECs transfected with DharmaFECT1 (DH1) alone, si*ATP13A3* or non-targeting siRNA control (siCP) (n=3). Data are presented as fold-change relative to *B2M* and further normalised to DH1. Mean ± SEM was shown and data were analysed using a One-way ANOVA with Tukey's post hoc test for multiple comparisons. **P<0.01, compared to siCP.

3.1.2 Characterising the impact of ATP13A3 loss-of-function in cell proliferation

3.1.1.1 *ATP13A3* deficiency impaired the proliferation of pulmonary artery smooth muscle cells.

Having shown that *ATP13A3* is expressed in hPASMCs, I then questioned whether manipulating *ATP13A3* expression could alter hPASMC proliferation. As shown in Figure 3-5, *ATP13A3* silencing in hPASMC restrained cell proliferation both in 1% FBS or 5% FBS DMEM (Figure 3-5 A). The efficiency of si*ATP13A3* knock-down was confirmed at the mRNA level both at day 0 (81.70% ± 0.63% reduction) and day 6 (67.50% ± 2.28% reduction) (Fig3-5 B). The proliferation of hPASMC is induced by cytokines such as PDGF [281] and inhibited by TGFβ [282] and BMP6 [61, 62], with responses to these ligands thought to be dysregulated in PAH [283]. Therefore, I assessed hPASMC proliferation in response to these cytokines after si*ATP13A3* transfection. In general, the proliferation of hPASMCs transfected with or without *ATP13A3* siRNA was enhanced to a similar extent by 10ng/ml PDGF (2.49 versus 2.28-fold change, si*ATP13A3* and siCP) (Figure 3-5 C). On the other hand, 10ng/ml TGFβ suppressed the proliferation of si*ATP13A3* transfected hPASMCs by 22.1% and siCP transfected cells by 25.4%. BMP6 also showed a similar degree of growth suppression in si*ATP13A3* (15.6%) and siCP (12.2%) transfected hPASMC (Figure 3-5 D).

3.1.2.1 *ATP13A3* knockdown impaired human endothelial cell proliferation

Endothelial dysfunction is a key feature in the pathogenesis of PAH [274, 275]. Therefore, I first sought to examine whether *ATP13A3* deficiency affected the proliferation of human pulmonary artery endothelial cells (hPAECs). Again, the si*ATP13A3* knockdown efficiency was confirmed at both day 0 and day 6 with an average of ~90% and ~65% mRNA reduction respectively (Figure 3-6 B). Similar to hPASMCs, si*ATP13A3* significantly reduced hPAEC proliferation by approximately 20% comparing to cells transfected with non-targeting siRNA control (siCP). (Figure 3-6 A). To further characterise the impact of *ATP13A3* deficiency on proliferation in the context of cytokine supplementation, transfected hPAECs were cultured with the addition of either 30ng/ml VEGF-A or 5ng/ml BMP9. VEGFA-165, an isoform of vascular endothelial growth factor, is an angiogenic endothelial mitogen [284]. BMP9 is a potent vascular quiescence factor crucial for maintaining endothelial homeostasis [285]. Although BMP9 was shown to promote angiogenesis in cancer cells [286], it has been demonstrated that BMP9 exerted anti-angiogenic effect and suppressed the proliferation of PAECs [39]. Interestingly, hPAECs transfected with si*ATP13A3* were less responsive to VEGF-A when compared to the siCP group (Figure3-6 A). Consistent with our previous finding, BMP9 treatment slightly reduced basal hPAEC proliferation and si*ATP13A3* transfection further decreased cell number. Similar findings were also observed in blood outgrowth endothelial cells (BOECs) transfected with si*ATP13A3* (Figure 3-7). *ATP13A3*-deficient BOECs restrained cell proliferation with or without the addition of 30ng/ml VEGF-A or 5ng/ml BMP9, further indicating an important role of *ATP13A3* in maintaining cell growth.

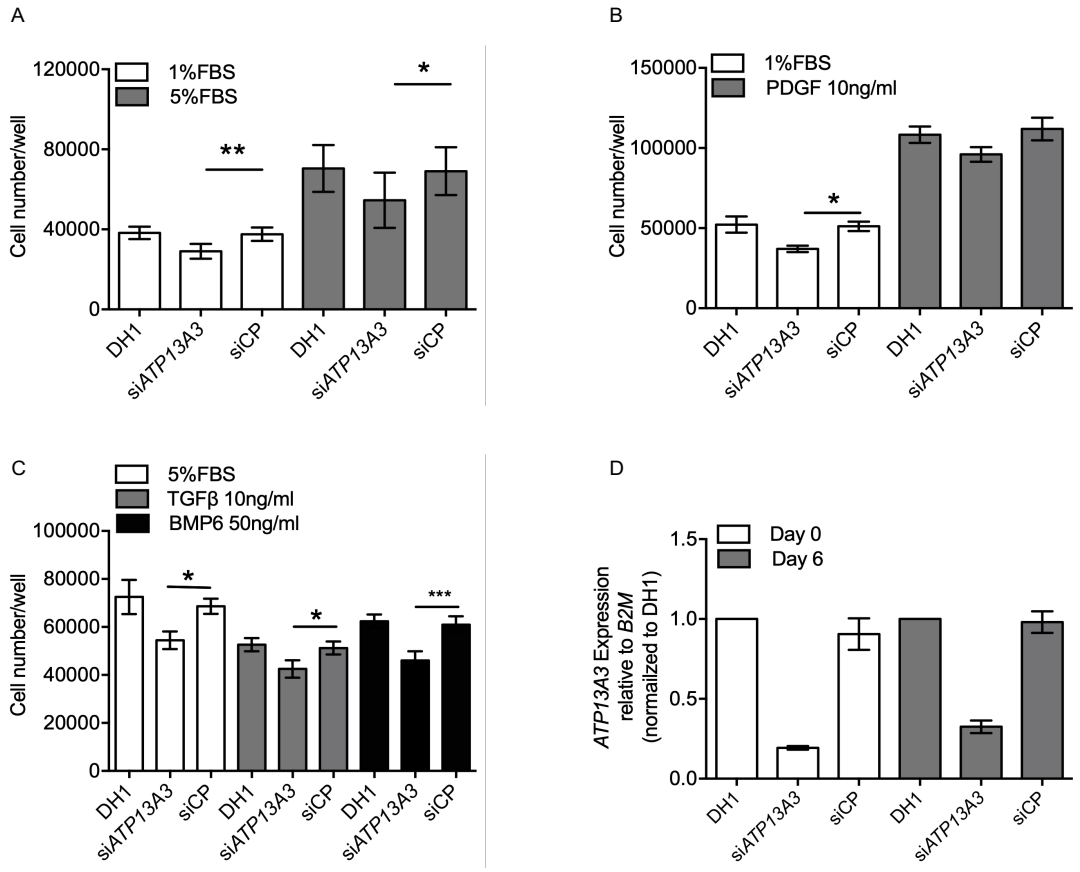

Figure 3-5 *ATP13A3* knockdown impaired the proliferation of pulmonary smooth muscle cells

(A) Cell number of transfected hPASMCs following 6-day incubation in DMEM containing either 1%FBS or 5%FBS (n=3) (B-C) The proliferation of post-transfected hPASMCs treated with or without the addition of (B) 10ng/ml PDGF, (C)10ng/ml TGFβ or (C) 50ng/ml BMP6 in 1% FBS over a 6-day period (n=4). (D) Relative expression of *ATP13A3* mRNA normalised to DH1 group at both day0 and day6 (n=3). Data are presented as mean ± SEM. One-way ANOVA with Tukey's post hoc test for multiple comparisons was used for data analysis among DH1, si*ATP13A3*, and siCP under different treatments. *P<0.05 and ***P<0.001 compared with siCP.

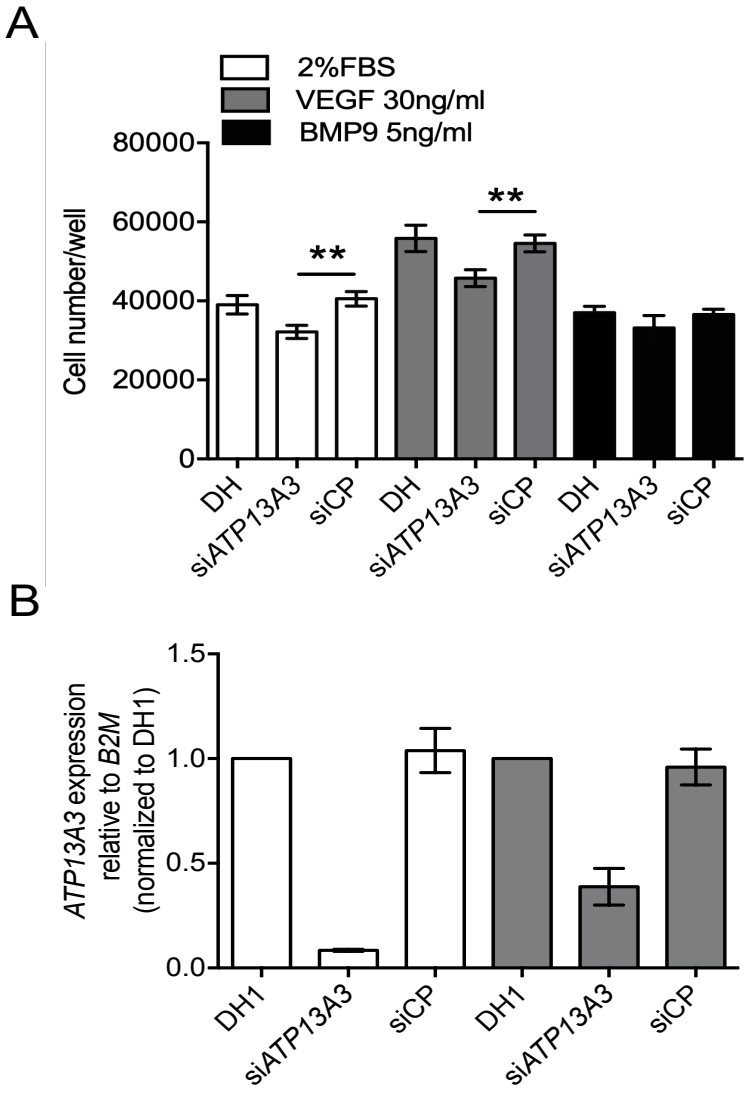

Figure 3-6 *ATP13A3* deficiency impaired pulmonary artery endothelial cell proliferation

(a) Proliferation of transfected hPAECs following 6-day incubation in EBM2 media supplied with 2%FBS alone, or with the addition of 30ng/ml VEGF-A or 5ng/ml BMP9 (n=3) (b) Relative expression of *ATP13A3* mRNA normalised to DH1 group at both day 0 and day 6 (n=3). Data are presented as fold change normalised to DH1 at different time points (mean ± SEM). One-way ANOVA with Tukey's post hoc test for multiple comparisons was used for data analysis. **P<0.01, compared with siCP

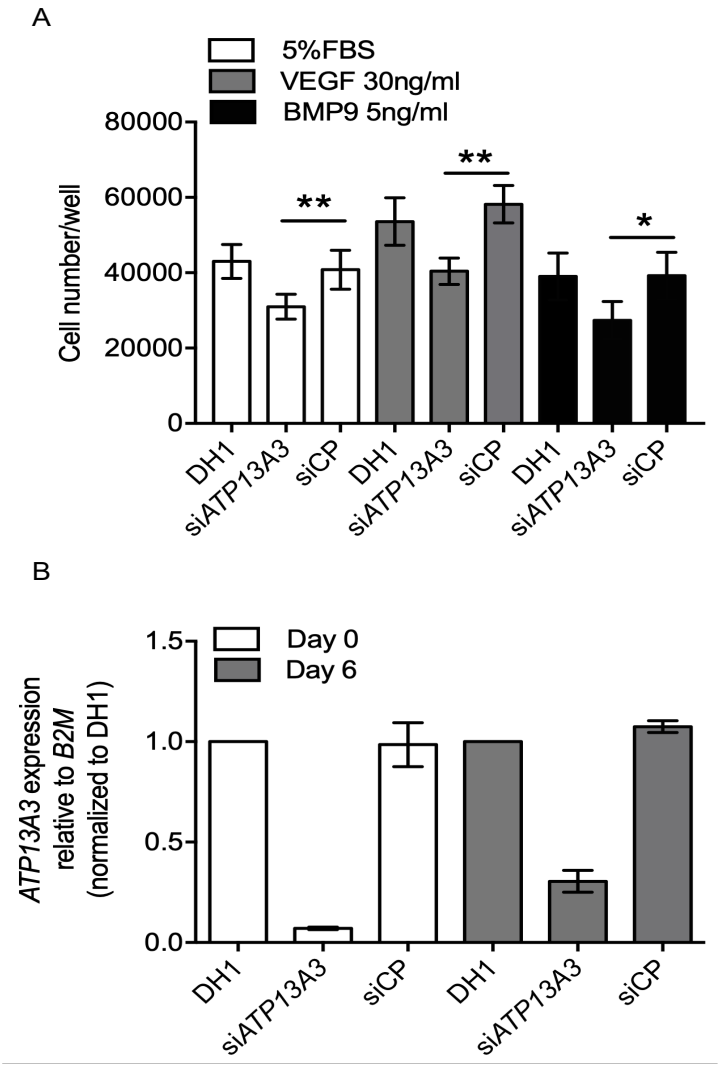

Figure 3-7 *ATP13A3* knock-down impairs blood outgrowth endothelial cell proliferation

(a) Proliferation of transfected BOECs followed 6-day incubation in EBM2 containing 0.1%FBS alone, or with the addition of 30ng/ml VEGF-A or 5ng/ml BMP9 (n=3 biological replicates) (b) Relative expression of *ATP13A3* mRNA normalised to DH1 group at both day 0 and day 6 (n=3 biological replicates). Data are presented as mean ± SEM. One-way ANOVA with Tukey's post hoc test for multiple comparisons was used for data analysis. *P<0.05 and **P<0.001 compared with siCP.

3.1.2.2 *ATP13A3* deficiency attenuated *CCNE1, CCNA1, CCNB1* expression in endothelial cells.

Cyclins are proteins involve in the regulation of the cell cycle progression. With the observation that *ATP13A3* deficiency restrains BOECs proliferation, I then questioned whether this effect was related to changes in the expression of cyclins. To test this hypothesis, 48-hour post-transfection cells were synchronised in EBM-2 containing 0.1% FBS for 28 hours before treating with or without 30ng/ml VEGF-A or 5ng/ml BMP9 for an additional 12 hours. Intriguingly, although *CCND1* mRNA expression was increased by approximately 48% with the addition of VEGF-A, it was downregulated by 40% with 5ng/ml BMP9, indicating a potential role of BMP9 in suppressing G1 phase progressing (Figure 3-8). *CCNE*, though not regulated with the addition of either VEGF-A or BMP9, was significantly reduced by si*ATP13A3* transfection (Figure 3-8 A) when compared to siCP. Similarly, both *CCNA1* and *CCNB1* were also negatively regulated by si*ATP13A3* (Figure 3-8 A) regardless of VEGF-A or BMP9 treatment. *CCND1*, on the other hand, was not altered by *ATP13A3* deficiency (Figure 3-8 A). Collectively, these data suggest a potential impairment of the *ATP13A3* deficiency on cell cycle progression.

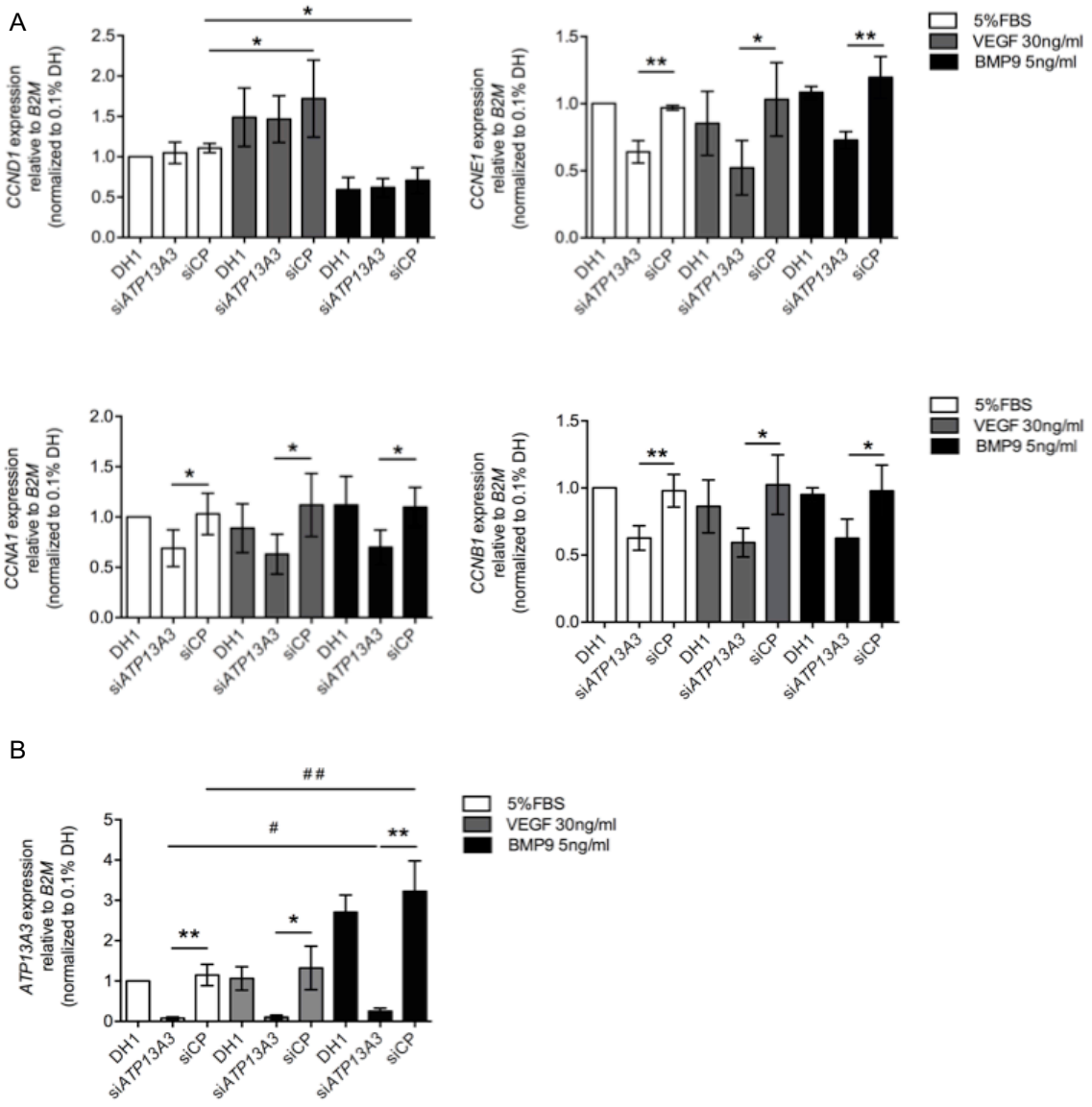

Figure 3-8 *ATP13A3* knockdown attenuated *CCNE1, CCNA1, CCNB1* expression in BOECs. (a) Relative expression of *CCND1, CCNE1, CCNA1* and *CCNB1* in transfected BOECs cultured with or without the addition of 30ng/ml VEGF-A or 5ng/ml BMP9 for 12 hours. Data were presented as fold-change relative to *B2M* and further normalised to DH1 in 0.1% FBS (n=4) (b) Knockdown efficiency of si*ATP13A3* in BOECs incubated with or without 30ng/ml VEGF-A or 5ng/ml BMP9. Mean ± SEM was shown. One-way ANOVA with Tukey's post hoc test for multiple comparisons was used for data analysis. *P<0.05 and **P<0.01 compared with siCP.

3.1.3 Characterising the impact of *ATP13A3* deficiency in endothelial cell apoptosis

3.1.3.1 Loss of *ATP13A3* induced blood outgrowth endothelial cells apoptosis at low serum levels.

As *ATP13A3* knockdown reduced BOECs cell numbers at day 6, I questioned whether this observation is due to increased apoptosis induced by loss of *ATP13A3*. Both annexin V/propidium iodide (PI) staining and caspase-3 activity were used to evaluate cell apoptosis. Quantified by flow cytometry, early apoptotic cells were defined as the annexin V+/PI- cell population. As assessed by Annexin V/PI staining, *ATP13A3* deficiency in BOECs, when grown in EBM-2 containing 0.1% FBS, led to a more pro-apoptotic response (16.8% ± 3.3% in si*ATP13A3* versus 11.5% ± 3.4% in DH1 and 10.9% ± 2.9% in siCP) whereas, in 5% FBS, loss of *ATP13A3* did not induce apoptosis (figure 3-9 A, B).

These findings were also confirmed by assaying for caspase activity using the Caspase-Glo® 3/7 Assay, which utilises a luminogenic substrate that is cleaved by caspase-3. The luminescent signal, representing caspase-3 activity, was significantly increased in BOECs transfected with si*ATP13A3* under 0.1% FBS (Figure 3-9 C). VEGF inhibits endothelial cell apoptosis both through the PI3K-Akt pathway [287] and by inducing Bcl-2 expression [288]. BMP9 has also been demonstrated by our group to inhibit endothelial cell apoptosis [39]. Therefore, I examined whether the apoptosis induced by *ATP13A3* deficiency under low serum levels can be restored by VEGF and BMP9. With the addition of 30ng/ml VEGF-A, BOECs transfected with si*ATP13A3* showed a decreased percentage of AV+/PI- cell population (7.9% ± 2.3% versus 16% ± 1%, VEGF-A versus 0.1%, $P < 0.01$). Although BMP9 prevents endothelial cell apoptosis via a different mechanism, still at a concentration of 5ng/ml, it reduced the AV+/PI- population in si*ATP13A3* transfected cells by around 10% (Figure 3-10 A, B). Again, the Caspase-Glo® 3/7 Assay showed a similar result, with both

VEGF-A and BMP9 reducing apoptosis in si*ATP13A3* transfected BOECs (Figure 3-10 C).

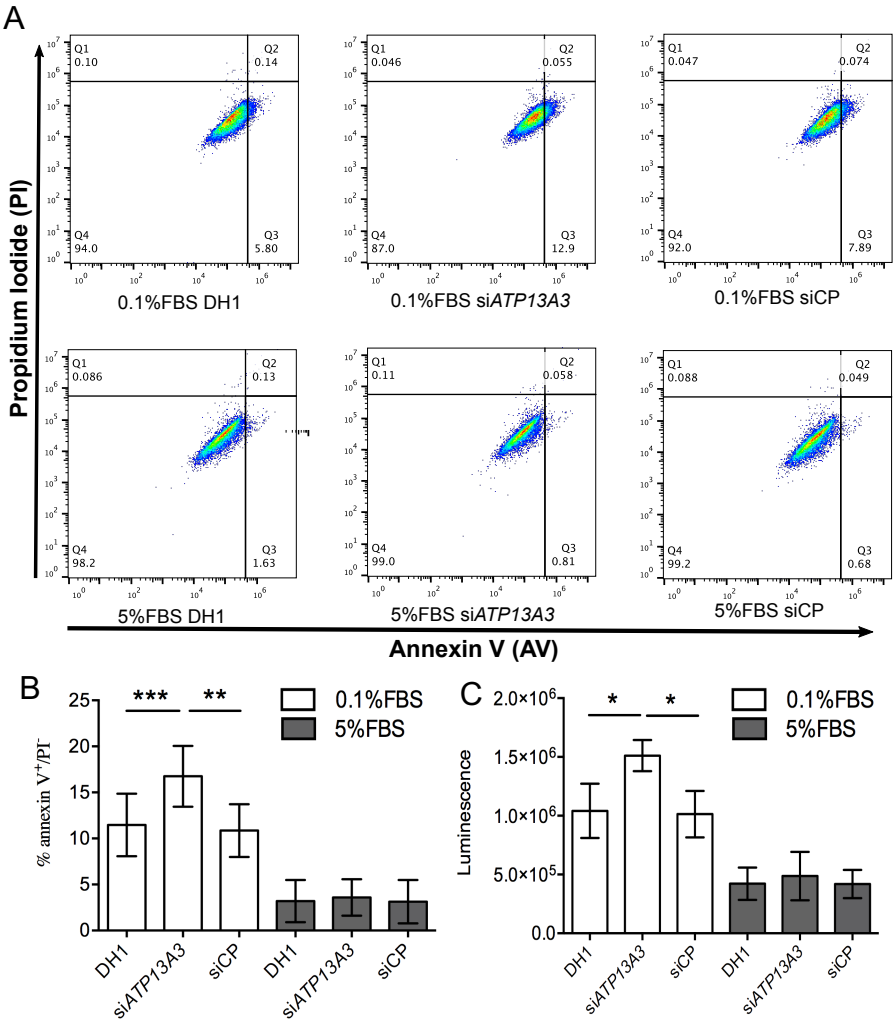

Figure 3-9 Loss of *ATP13A3* induced BOECs apoptosis at a lower serum level

(A) Following transfection, BOECs were treated for 24 hours in 0.1%FBS or 5%FBS (n=4) before assessing for cell apoptosis by Annexin-V (AV) and propidium iodide (PI) staining. (B) Quantification of early apoptosis (defined as Annexin V^+/PI^-). (C) Assessment of caspase-3 activity with Caspase-Glo® 3/7 assay. Data are presented as Mean ± SEM. One-way ANOVA with Tukey's post hoc test for multiple comparisons was used for data analysis. *P<0.05, **P<0.01, ***P<0.001 compared with siCP.

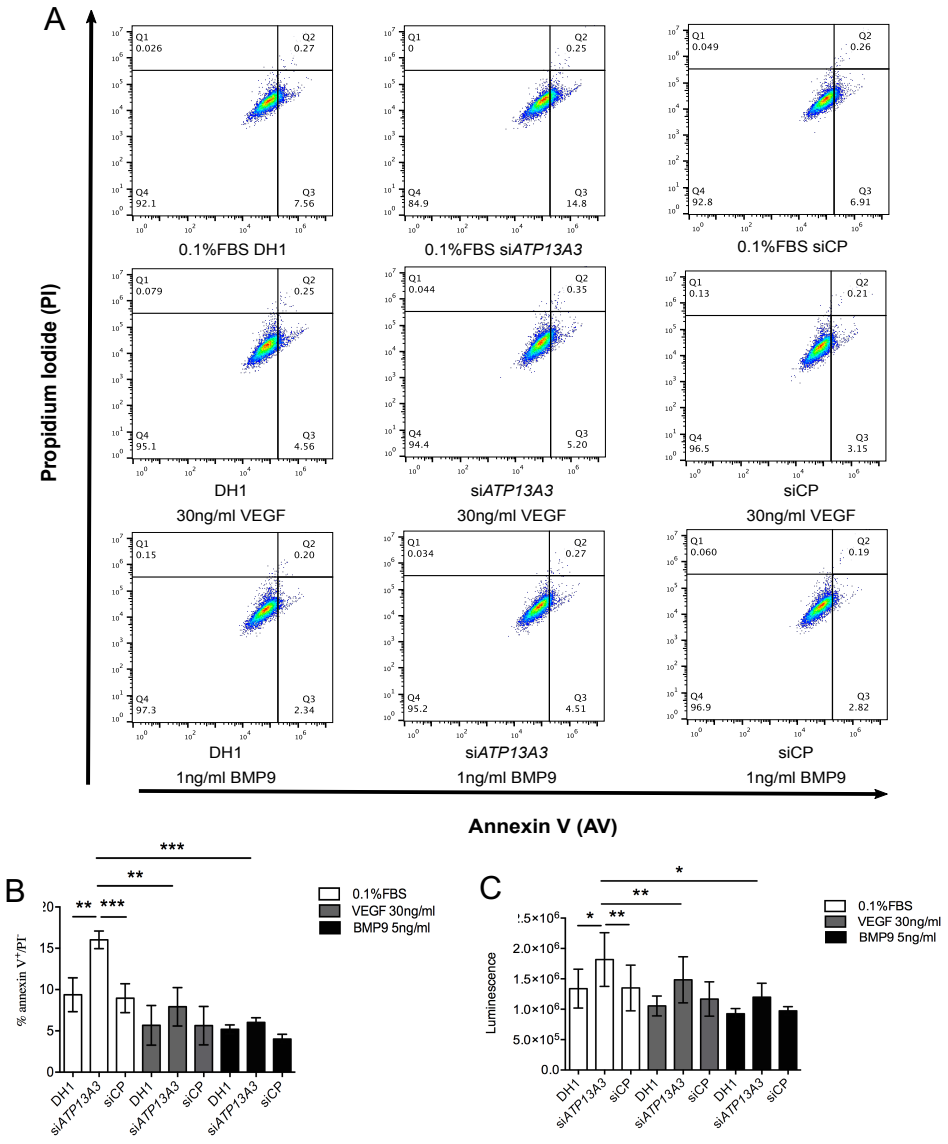

Figure 3-10 Apoptosis induced by loss of *ATP13A3* could be rescued by VEGF and BMP9

(A) Following transfection, BOECs were treated for 24 hours in 0.1%FBS or 5%FBS with or without the addition of 30ng/ml VEGF-A or 5ng/ml BMP9 (n=4) before assessing for cell apoptosis by Annexin-V (AV) and propidium iodide (PI) staining. (B) Quantification of early apoptosis (defined as Annexin V^+/PI^-). (C) Assessment of caspase-3 activity with Caspase-Glo® 3/7 assay. Data are presented as Mean ± SEM. One-way ANOVA with Tukey's post hoc test for multiple comparisons was used for data analysis. *P<0.05, **P<0.01, ***P<0.001 compared with siCP.

3.1.3.2 *ATP13A3* deficiency induced apoptosis in human pulmonary artery endothelial cells at low serum level.

Having demonstrated that loss of *ATP13A3* in BOECs led to enhanced apoptosis in low serum, I then questioned if hPAECs behave in a similar way to BOECs. As expected, loss of *ATP13A3*, led to increased activation of caspase-3 in hPAECs as detected by Caspase-Glo® 3/7 Assay. Again, this effect could be restored with the addition of either VEGF-A or BMP9 (Figure 3-11).

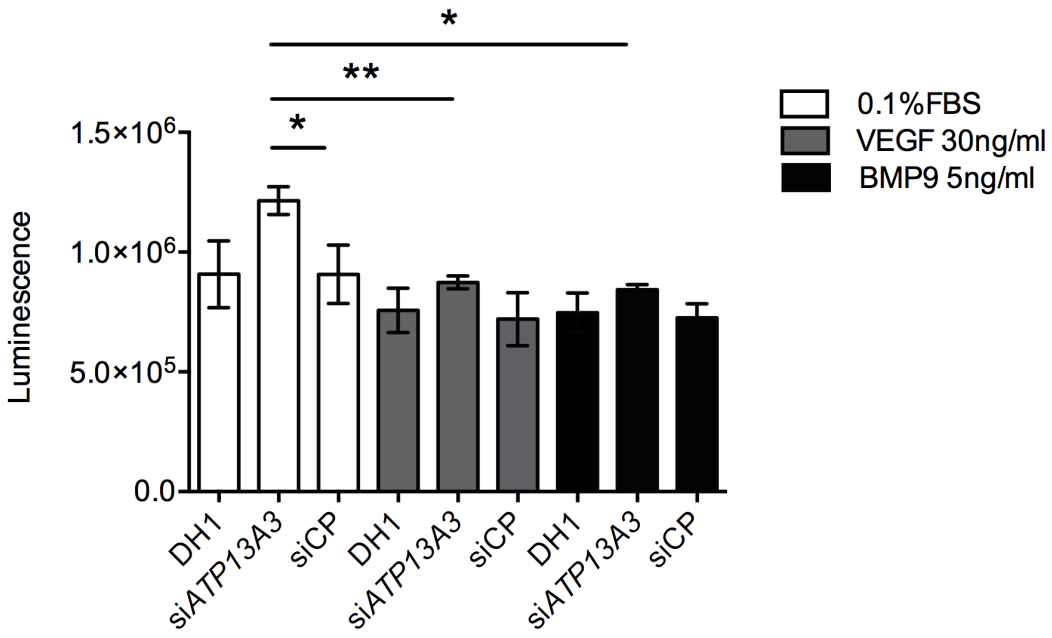

Figure 3-11 ATP13A3 deficiency induced apoptosis in human pulmonary artery endothelial cells

Cellular caspase activity was assessed by the Caspase-Glo® 3/7 assay (Promega). hPAECs were treated for 24 hours in 0.1%FBS with or without the addition of 30ng/ml VEGF-A or 5ng/ml BMP9 (n=3). Data are presented as Mean ± SEM. One-way ANOVA with Tukey's post hoc test for multiple comparisons was used for data analysis among DH1, si*ATP13A3*, siCP transfected cells in 0.1% FBS, *P<0.05 compared with siCP, and among si*ATP13A3* transfected cells treated with or without VEGF and BMP9. *P<0.05 and **P<0.01 compared with si*ATP13A3* in 0.1% FBS.

3.1.4 Characterising the impact of *ATP13A3* deficiency on endothelial cell permeability

The pulmonary artery endothelium represents a barrier crucial for maintaining vascular homeostasis. The disruption of endothelial integrity has been recognised as an important contributor to PAH pathogenesis, promoting the vascular remodelling and disease development [39, 289-291]. As described in the previous section, *ATP13A3* deficiency led to reduced endothelial cell proliferation and increased apoptosis under low-serum condition. Therefore, I sought to assess if this also affect the integrity of hPAECs monolayer. To ensure that we were assessing intact monolayers, hPAECs were initially plated at different densities in transwell chambers and stained with a VE-Cadherin antibody to assess the optimised number for confluent cell monolayer formation. As presented in Figure 3-12, when plated at 0.5 x 10^5 / chamber, hPAECs formed a clear and integral monolayer as revealed by the formation of adherens junctions (VE-cadherin) across the endothelial cells. hPAECs plated both at 1.0 x 10^5, and 1.5x10^5/chamber presented uneven staining for cellular junctions and cell clumps at several regions, suggesting overloading of the transwell membrane (Figure 3-12). Therefore, cells were plated at 0.5 x 10^5/ chamber for all further permeability assays.

3.1.4.1 Validation of endothelial permeability assay

Inflammatory factors (e.g. TNFα) [39, 292] or thrombogenic mediators (e.g. thrombin) [293, 294] have been reported to increased endothelial permeability. Therefore, after seeding into the transwell chambers, hPAECs were treated with either TNFα or Thrombin at a range of concentrations to assess their ability to induce increased endothelial permeability. As shown in Figure 3-13, hPAECs incubated with 1U/ml thrombin displayed a significantly higher permeability at 60 minutes when compared to cells without treatment. This effect was continuously exaggerated by exposure to 1U/ml thrombin until the end of the 2-hour time point. However, when incubated with 10U/ml thrombin, the

permeability of hPAEC monolayers was not significantly increased compared to the hPAECs treated with 1U/ml thrombin (Figure 3-13). On the contrary, TNFα treatment did not induce overt leakage in hPAECs, even at the highest dose (1ng/ml) (Figure 3-13).

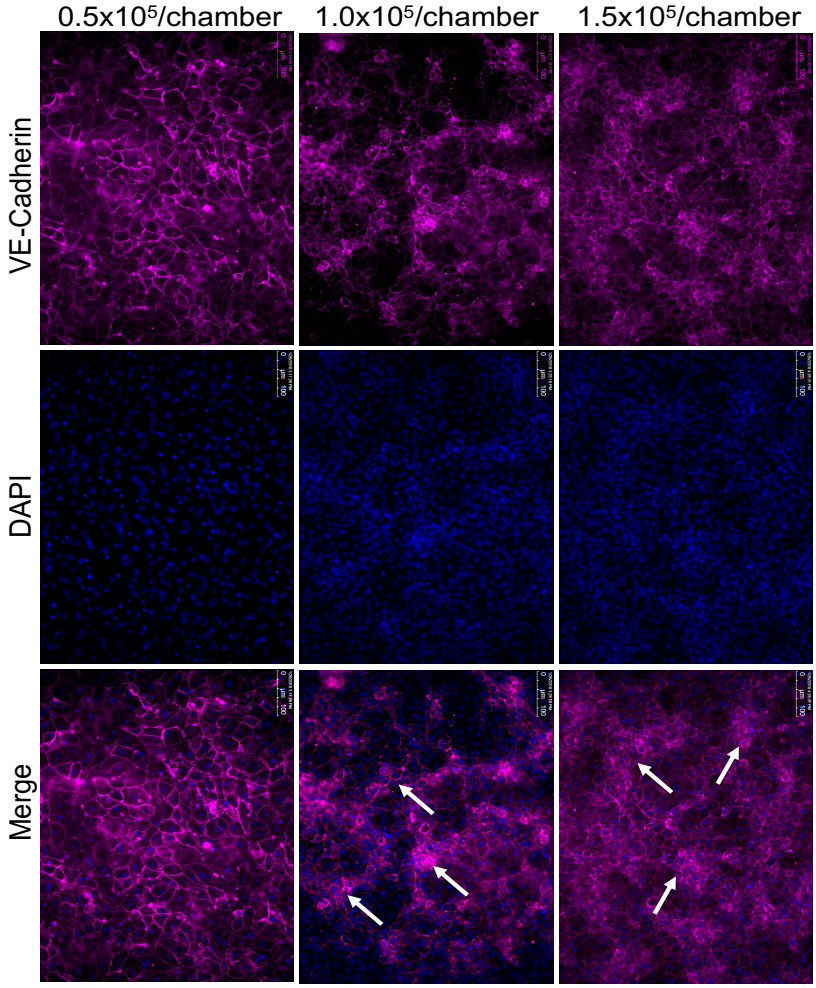

Figure 3-12 VE-Cadherin staining of human pulmonary artery endothelial cells (hPAECs) seeded in transwell chambers Representative images of cellular adherens junction (VE-Cadherin, magenta) staining of hPAECs seeded in transwell chambers (10X). Nuclei were stained with DAPI (blue). Cell clumps (white arrow) were apparent at seeding densities of $1.0x10^5$ and $1.5x10^5$.

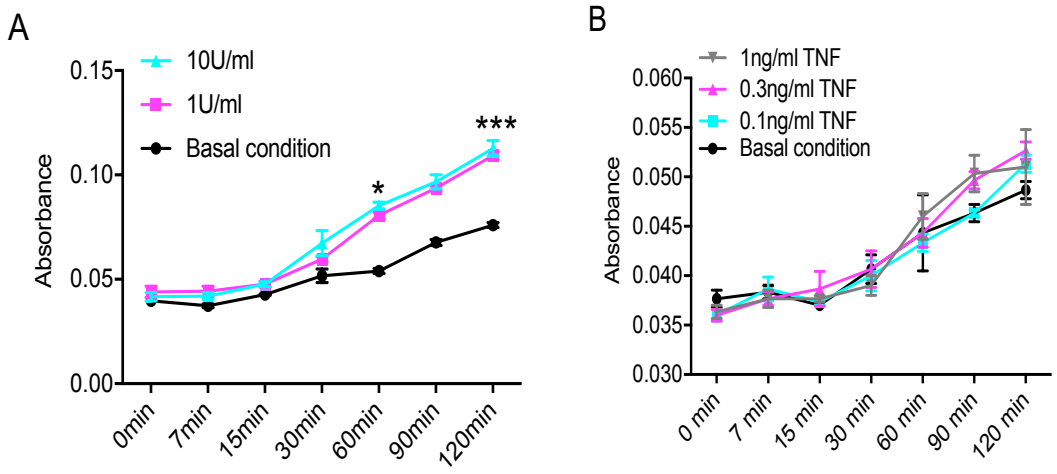

Figure 3-13 Thrombin induces increased permeability of hPAECs.

hPAECs were treated with or without (A) thrombin (1U/ml or 10U/ml) or (B) TNFα (0.1ng/ml, 0.3ng/ml, 1ng/ml) over a 2-hour period. 15µl of the medium was collected three times from the bottom wells at the indicated time points followed by the detection of horseradish peroxidase (HRP) activity. Raw absorbance was presented (n=3 technical repeats), and One-way ANOVA with Tukey's post hoc test for multiple comparisons was used for analysing data at each time point. *P<0.05 and ***P<0.001 compared with the basal condition.

3.1.4.2 *ATP13A3* deficiency increased hPAECs permeability in the present of thrombin

To assess the impact of *ATP13A3* deficiency on endothelial permeability, endogenous *ATP13A3* expression was knocked down by siRNA transfection. Following 6-hour serum-starvation in 0.1% FBS EBM2, transfected hPAECs were cultured in EBM2 supplemented with 2% FBS and assessed for endothelial permeability. As illustrated in Figure 3-14, *ATP13A3* deficient cells exhibited similar monolayer permeability compared to cells transfected with siCP or without transfection. Intriguingly, after 30 minutes of exposure to 1U/ml thrombin, si*ATP13A3* started to enhance hPAECs permeability compared to DH1 or siCP, and the difference continue to exaggerate and peaked at the 2-hour time point (figure 3-15 *P<0.05). Together, these data suggest an

important role of *ATP13A3* in maintaining endothelial integrity, especially under the exposure to pathogenic insults.

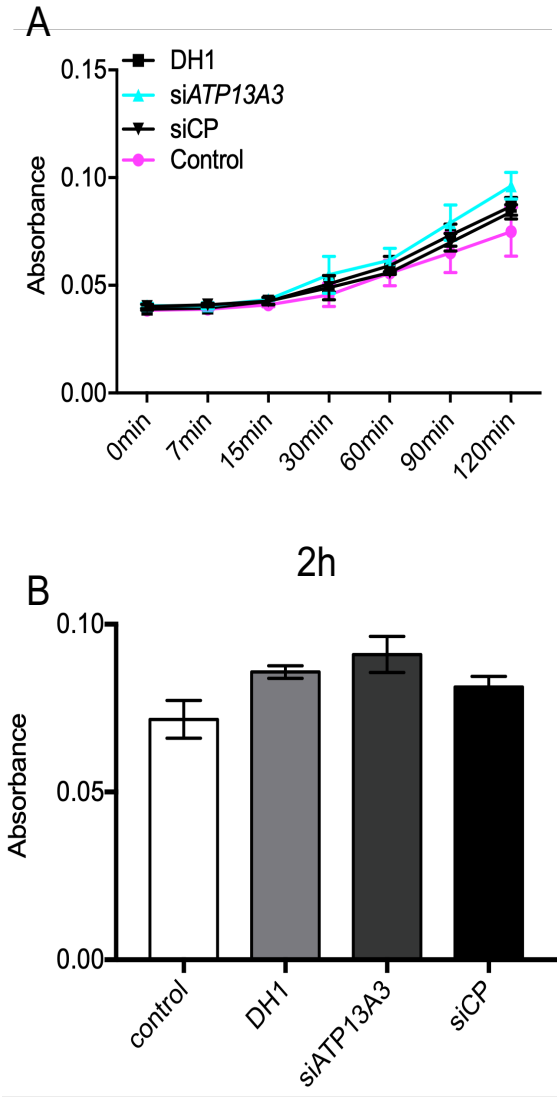

Figure 3-14 *ATP13A3* deficiency alone did not induce leakage in hPAECs (A) Transfected hPAECs were cultured in EBM2 supplemented with 2% FBS in the transwell chambers. 15µl of the medium was collected three times from the bottom wells at the indicated time points followed by the detection of horseradish peroxidase (HRP) activity. Raw absorbance values are presented (n=4). One-way ANOVA with Tukey's post hoc test for multiple comparisons was used for analysing data at each time point. (B) Raw absorbance of the different groups at the 2-hour time point.

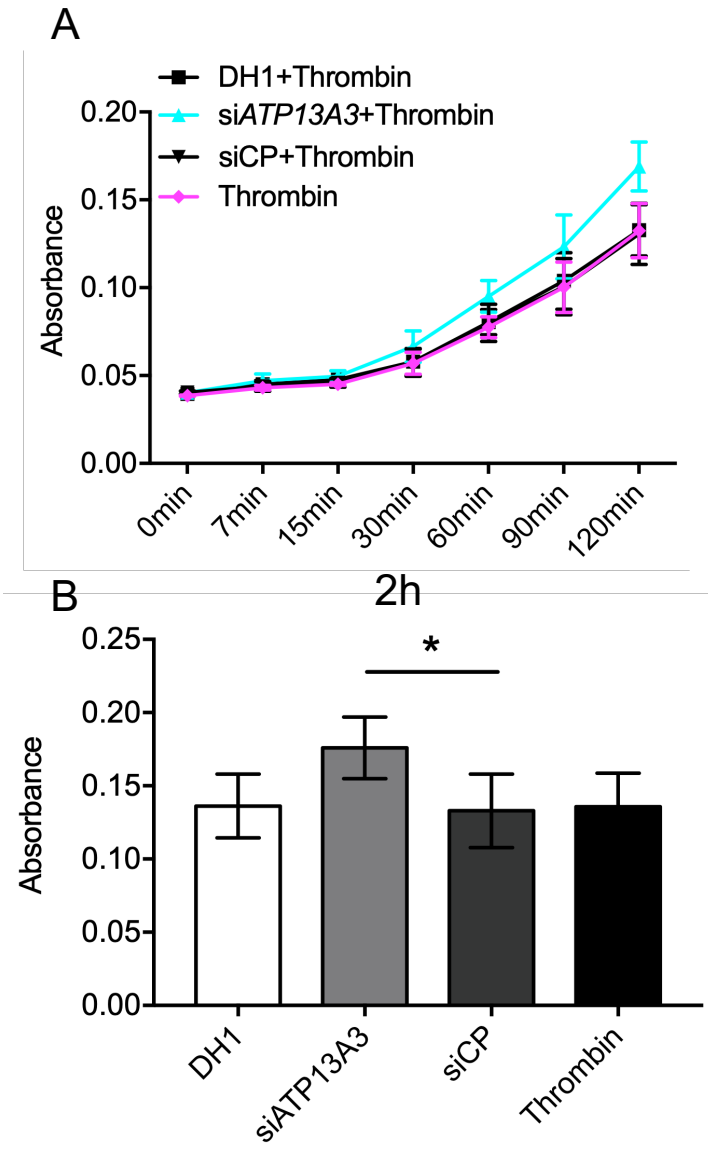

Figure 3-15 *ATP13A3* deficiency in combination with Thrombin triggered hPAEC leakage (A) Transfected hPAECs were culture in transwell chambers in the EBM2 supplemented with 2% FBS with the addition of 1U/ml Thrombin. 15µl of the medium was collected three times from the bottom wells at the indicated time points followed by the detection of horseradish peroxidase (HRP) activity. Raw absorbance values are presented (n=4). (B) Breakdown of the Raw absorbance at the 2-hour time point. One-way ANOVA with Tukey's post hoc test for multiple comparisons was used for analysing data at each time point. *P<0.05 when compared siATP13A3 to siCP.

3.2 Discussion

In this Chapter, I have investigated the expression pattern of *ATP13A3* in different vascular cells and assessed the impacts of *ATP13A3* deficiency on vascular cell functions.

Comparison of the mRNA levels of different P5-ATPases in hPAECs, hPASMCs and BOECs revealed *ATP13A3* as the highest expressed P5-ATPase gene. This observation indicated a potential role of *ATP13A3* in pulmonary vascular physiology, especially in the endothelial cell as hPAECs displayed a higher level of *ATP13A3* than the other two cell types. Based on these data, I moved on to assess the impacts of *ATP13A3* deficiency on vascular cell functions.

The pathology of pulmonary arterial hypertension is characterised by hyper-proliferative and anti-apoptotic pulmonary vascular cells that lead to progressive vascular occlusion and elevated blood pressure[40, 274, 275]. However, the underlying primary cellular defect is thought to reside in the endothelium. Evidence both *in vivo* [44, 45] and in *vitro* [39, 48] suggests that endothelial cell apoptosis may contribute to disease initiation by reducing the integrity of the pulmonary artery endothelium. Here, I have shown that *ATP13A3* deficiency (achieved by si*ATP13A3* transfection) reduces cell proliferation in both hPAECs and BOECs. Loss of *ATP13A3* probably affects cell cycle progression as *ATP13A3* deficiency down-regulates the mRNA expression of *CCNE*, *CCNA* and *CCNB.* Loss of *ATP13A3,* at a low serum level (0.1%FBS), increased the Annexin V+/PI- cell population and promoted caspase-3 activity in both hPAECs and BOECs, indicating a protective role of *ATP13A3* in cell viability under conditions of stress. These observations initiate the idea that *ATP13A3* is involved in endothelial homeostasis. However, the underlying mechanism is still unclear. It is likely the phenotypic changes led by *ATP13A3* deficiency is independent of or not directly regulated by the VEGF or BMP signalling, though other pathways such as TGFβ or inflammatory signalling should be examined for the regulation of *ATP13A3* in vascular cells.

In addition, although snapshot (48-hour post-transfection) qPCR data suggested that *ATP13A3* deficiency affect cyclins expression, further investigations are still needed to reveal its role on the full cell cycle progression. Increased endothelial permeability has also been implicated in the pathobiology of PAH. Endothelial cells with *BMPR2* deficiency displayed increased permeability [39] and altered leukocyte translocation across the vascular wall[289]. Intriguingly, loss of *ATP13A3* in hPAECs showed exacerbation of endothelial leakage in the presence of thrombin stimulation, indicating an important role of *ATP13A3* in maintaining endothelial integrity.

Depletion of *ATP13A3* in PASMCs*,* opposite to the expectation, presented a hypo-proliferative rather than a hyper-proliferative phenotype. However, PASMCs with depleted *ATP13A3* showed a similar response to a pro-proliferative mitogen (PDGF) and an anti-proliferative factor (TGFβ), implicating the reduction in proliferation caused by *ATP13A3* loss of function in PASMCs is likely to be independent of these two pathways.

In summary, *ATP13A3* loss of function impairs the cellular function of pulmonary vascular cells, yet the mechanism underlying these observations remains unclear. *ATP13A3* and its orthologs have been implicated as putative polyamine transporters in pancreatic cancer cells [147] and *C.elegans* (CATP-5)[139]. Polyamines are a group of aliphatic cations ubiquitous exist in nature and participate in a broad spectrum of the cellular processes, including proliferation, apoptosis [104, 295]. Together with the above observations in vascular cells, I hypothesised that *ATP13A3* loss of function is likely to cause cellular dysfunction by affecting cellular polyamine homeostasis. The evidence of ATP13A3 functioning as a polyamine transporter in maintaining endothelial cell polyamine homeostasis will be described in the next chapter.

Chapter 4 Results II-ATP13A3 and Polyamine Homeostasis

4.1 Introduction

P-type ATPases are transmembrane proteins, by forming phosphorylated intermediates, transport substrates across cellular membranes [110, 280]. While *ATP13A3*, a P5B-ATPase, is widely existing in eukaryotes, the biological functions of this putative transporter are still elusive. CATP-5, an orthologue of ATP13A3 in *C.elegans*, was demonstrated to translocate polyamine across the apical membrane of the intestinal cells [139]. Additionally, a study in cancer biology revealed a correlation between *ATP13A3* level and polyamine uptake in pancreatic cancer cells [147]. However, no study to date has directly addressed whether ATP13A3 is involved in polyamine transport and nor a transport substrate is proposed.

Polyamines are highly charged polycations widely exist in nature. Putrescine, spermidine and spermine are the three main types of polyamine found in mammalian cells. These highly charged molecules are essential in many cellular processes, including cell growth, apoptosis, transcription and translation regulation, as well as stress responses [104, 171, 191, 296-298]. Cellular polyamine levels are tightly governed by the coordination between the polyamine biosynthesis/catabolism pathways and the transport system. As shown in Figure 4-16, polyamine biosynthesis is initiated by the rate-limiting enzyme ornithine decarboxylase (ODC), which converts ornithine into putrescine. ODC levels are highly regulated by polyamine concentrations, as described in the paragraph below. The higher polyamines, namely spermidine and spermine, are generated by spermidine synthase (SRM) or spermine synthase (SMS) through the addition of aminopropyl groups to their precursors (putrescine and spermidine respectively). Decarboxylated S-

adenosylmethionine produced by S-adenosylmethionine decarboxylase (AMD) serves as aminopropyl groups donor for these reactions.

As the critical polyamine biosynthesis enzyme, ODC is dynamically regulated at multiple levels [172]. Increased *ODC* mRNA was seen in response to tumour promotors and hormones in a cell-context dependent manner [174, 299]. For example, activation of *c-Myc* results in the overexpression of ODC in cancer cells [122, 300]. Moreover, translational regulation of ODC alternates between the cap-dependent and internal ribosome entry site (IRES)-dependent mechanisms [301, 302], with the latter happens mainly during G2/M phase [302]. Upon translation, ODC protein is rapidly turned over via the antizyme-mediated degradation. Antizyme 1 (OAZ1), which non-covalently binds to ODC monomers, directs it to 26S proteasome for degradation [179]. This process is independent of ubiquitination but dynamically regulated by intracellular polyamine levels. Elevated polyamines trigger a unique ribosomal frameshifting event [179, 183], resulting in the translation of full-length antizymes. Polyamine depletion, however, represses this frameshifting event and hence preserved ODC expression via reducing antizyme production [185]. Antizyme inhibitor (AZIN), a protein structurally homologous to ODC but lacking the decarboxylase activity, also participates in ODC regulation by liberating it from the ODC-antizyme complex, thus prevents it from degradation [186-188].

As shown in Figure 4-16, to maintain homeostasis, polyamines can also be interconverted back into their precursors via the catabolic pathway. Spermine and spermidine are first acetylated by spermidine/spermine acetyltransferase (SSAT) to form N1-acetylspermine or N1-acetylspermidine. These metabolites are then oxidised back to spermidine or putrescine respectively by the polyamine oxidase (PAO). Spermine can also be interconverted directly into spermidine by spermine oxidase (SMOX). These oxidative reactions result in toxic metabolites (H_2O_2 and amino aldehyde), which under physiological conditions can be resolved by peroxisomal catalase [170] and aldehyde

dehydrogenases [303]. However, when polyamines accumulation happens, the resultant H_2O_2 overproduction may cause cytotoxicity [243].

The polyamine transport systems (PTS) is another essential pathway for regulating intracellular polyamine levels. Although well described in simple life forms such as *E. coli* and trypanosomatids [304, 305], the PTSs in mammalian cells remains elusive. Previous studies have demonstrated polyamine transport activities in members of the solute carrier (SLC) and ATP-binding cassette superfamily [190, 206] (Summarised in Chapter 1, Table 1), though these transporters are primarily responsible for translocating amino acid. Most recently, ATP13A2, a P5B-ATPase was uncovered as a spermine exporter resided in the endo/lysosomal compartment. Considering the high homology shared by ATP13A2-5, this may suggest the potential involvement of other P5B-ATPases in transporting polyamines [148].

As molecules essential for many cellular processes, polyamine, when dysregulated, can cause diseases, such as cancer [171], neurodegenerative diseases [262-264]. Similarly, aberrant polyamine contents were also reported in PAH. For example, increased polyamine accumulation has been demonstrated in the lungs of monocrotaline (MCT)- and hypoxia- treated rats. These changes tracked closely the hemodynamic elevation and right ventricular remodelling in both models [255, 256]. Intriguingly, the two models seemed to favour different mechanisms for their polyamine augmentation. MCT treatment significantly induced the upregulation of *de novo* polyamine biosynthesis [255] while hypoxia promoted polyamine accumulation in rat lungs via increased transport [256]. These findings shed lights for the involvement of polyamine dysregulation in PAH pathogenesis, but suggest differences between inflammation-dependent disease progression (MCT) compared to that mediated by hypoxic vasoconstriction. In addition, a human lung metabolomics study revealed ornithine and putrescine upregulation in PAH patients [258]. Plasma metabolomics profiling also demonstrated increased polyamine metabolites in idiopathic or heritable PAH patients, with N-acetyl-putrescine (in

relation to bilirubin) being prognostic independent of other established prognostic markers [259]. Taken together, these suggest a link between polyamine dysregulation and PAH pathogenesis.

As described in the previous chapter, *ATP13A3* deficiency leads to endothelial dysfunction. To further expand these findings, in this chapter, I will describe explore the link between *ATP13A3* and polyamine homeostasis in endothelial cells and provide functional assessment for PAH-associated *ATP13A3* mutations.

4.2 Result

4.2.1 Cellular localisation of ATP13A3

To understand the biological functions of ATP13A3 in human vascular cells, I first sought to characterise its cellular localisation. As a putative transmembrane transporter, I initially hypothesised that ATP13A3 might be expressed on the plasma membrane of pulmonary vascular cells.

4.2.1.1 Validation of the anti-ATP13A3 antibody in endothelial cells

To address the hypothesis, I first sought to test the specificity of the anti-ATP13A3 antibody (Sigma) in visualising the endogenous ATP13A3 localisation by transfecting human pulmonary artery endothelial cells with si*ATP13A3* followed by immunofluorescent staining. 90% of *ATP13A3* mRNA knockdown was achieved in hPAECs at 48-hour post-transfection (Figure 4-1B). hPAECs transfected with DH1 or siRNA control pool (siCP) displayed ATP13A3 fluorescent staining both in the cytoplasm and nuclei, while the expression level was significantly reduced in cells transfected with si*ATP13A3* (Figure 4-1 A). The reduced fluorescent ATP13A3 signal indicated that the antibody was specific and therefore it was used for all the following immunostaining.

4.2.1.2 Endogenous ATP13A3 is localised to the nuclei and perinuclear area in endothelial cells

I then sought to characterise the localisation of endogenous ATP13A3. To achieve this, hPAECs were co-stained with anti-ATP13A3 and anti-VE-Cadherin antibodies for visualising cell surface. Contrary to my hypothesis, as shown in Figure 4-2, little overlap was revealed between endogenous ATP13A3 and VE-Cadherin. Instead, ATP13A3 mainly presented within the cytoplasm (perinuclear) or nuclei, indicating an intrinsic cellular compartments localisation of this transmembrane protein (Figure 4-2).

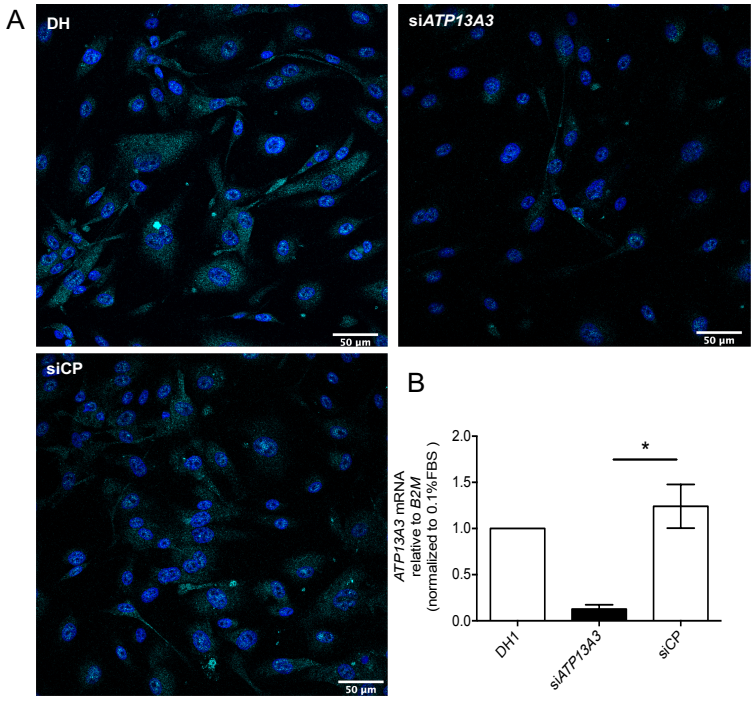

Figure 4-1 Immunostaining of ATP13A3 in transfected hPAECs

(A) Transfected hPAECs at a density of 50,000 cells/chamber were stained with an anti-ATP13A3 antibody (Sigma, 1:200, turquoise). Nuclei were visuaised with DAPI (blue). Representative images were taken at 20X magnification using a Leica Sp5 confocal microscope (Leica microsystem). (B) *ATP13A3* mRNA expression was presented as fold change relative to B2M expression and normalised to the DH1 (N=3). One-way ANOVA with Tukey's post hoc test for multiple comparisons was used for analysing data. *P<0.05 when compared siATP13A3 to siCP.

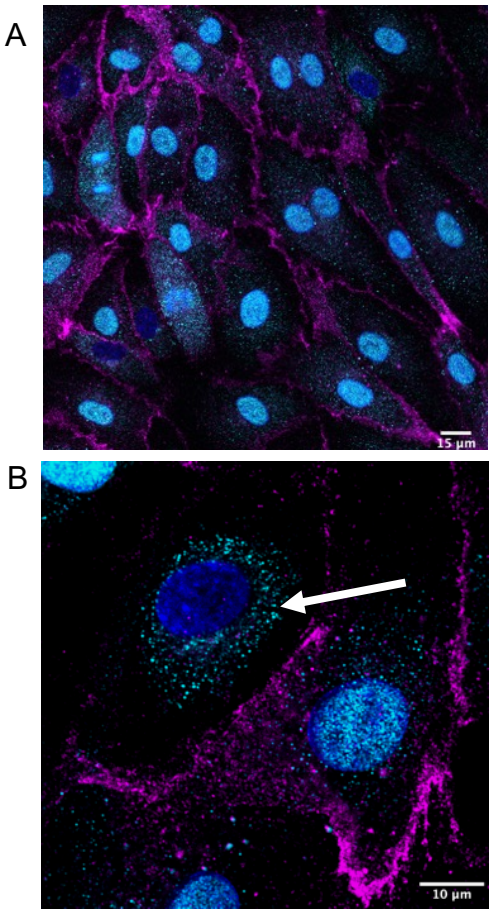

Figure 4-2 Endogenous ATP13A3 is mainly localised to the perinuclear region and nuclei of hPAECs

hPAECs were co-stained with anti-ATP13A3 (1:200) and anti-VE-Cadherin (1:200). Representative images were taken at (A) 40X (B) 63X magnification using the Leica Sp5 confocal microscope platform (Leica microsystem). ATP13A3 (turquoise) signal was indicated by the white arrow while the cell plasma membrane was visualised by VE-cadherin (magenta) staining. Cell nuclei were stained with DAPI (blue).

4.2.1.3 Overexpressed *ATP13A3* colocalised with endogenous ATP13A3 in HMEC-1

To further characterise the cell compartmentalisation of ATP13A3, GFP-tagged *ATP13A3* (GFP-*ATP13A3*) was transiently overexpressed in HMEC-1 cells using *hATP13A3*-N-EGFP-pcDNA6.2 donated by Prof. Peter Vangheluwe (KU Leuven). Before proceeding with cell compartmentalisation characterisation, the over-expression pattern of GFP- *ATP13A3* was compared to the endogenous ATP13A3 staining pattern in HMEC-1. As presented in Figure 4-3, the GFP-*ATP13A3* signal produced by plasmid overexpression (green) presented mainly in the perinuclear region. It also overlaid with the endogenous ATP13A3 (red), indicating a good correlation with the localisation of transiently overexpressed ATP13A3 (figure 4-3 A).

4.2.1.4 ATP13A3 colocalised with the recycling endosome marker Rab11 in endothelial cells

As described in the last two sections, both endogenous and overexpressed ATP13A3 were localised mainly to the perinuclear region of hPAECs or HMEC-1 cells. These findings suggest distinct compartmentalisation of ATP13A3 in endothelial cells. Interestingly, the previous study from Sørensen et al. [141] showed that in Hela cells, transiently overexpressed ATP13A3 colocalised with the endosomal markers Rab11 and EEA-1. To characterise its cellular localisation, GFP-ATP13A3 was transiently overexpressed in HMEC-1 cells followed by immunostaining with endo/lysosomal markers. Cells overexpressing GFP-ATP13A3 did not present apparent morphological abnormalities under the microscope.

Similar to the previous study, GFP-ATP13A3 colocalised with the recycling endosome marker Rab11 in HMEC-1 cells (Figure 4-4). Any overlap with the early endosome marker EEA-1, late endosome marker Rab7 or lysosomal

marker LAMP1 was minimal (Figure 4-4). These findings suggest a biological role of ATP13A3 in the cellular endosomal system.

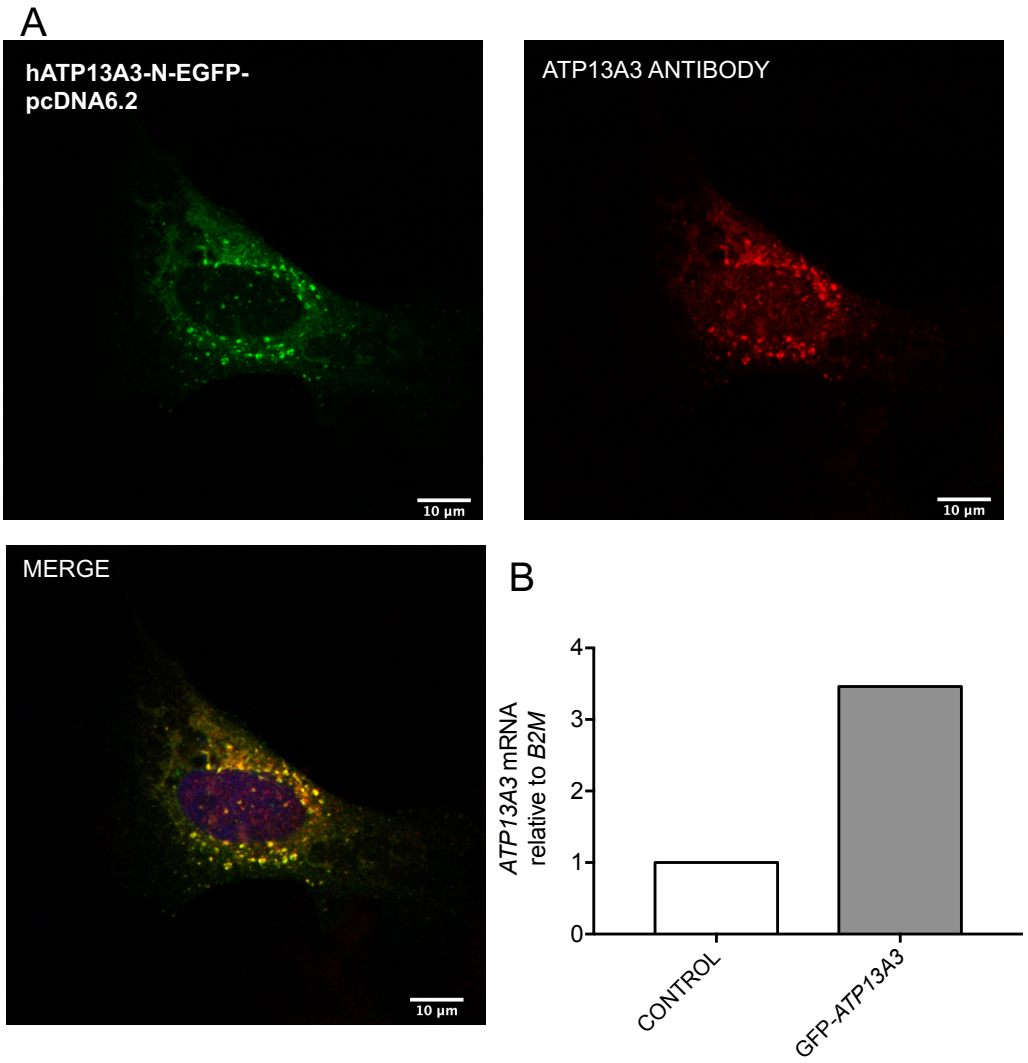

Figure 4-3 Fluorescent images of HMEC-1 overexpressing hATP13A3-N-EGFP-pcDNA6.2

(A) h*ATP13A3*-N-EGFP-pcDNA6.2 was transiently overexpressed for 48 hours in HMEC-1 cells followed by staining with the anti-ATP13A3 antibody. Representative images were taken at 63X magnification using the Leica Sp5 confocal microscope platform (Leica microsystem). GFP-*ATP13A3* overexpression is represented by the green fluorescent signal, whereas endogenous ATP13A3 staining is indicated by the red fluorescent signal. (n=3) (B) *ATP13A3* mRNA expression is presented as fold change relative to *B2M* expression and normalised to control.

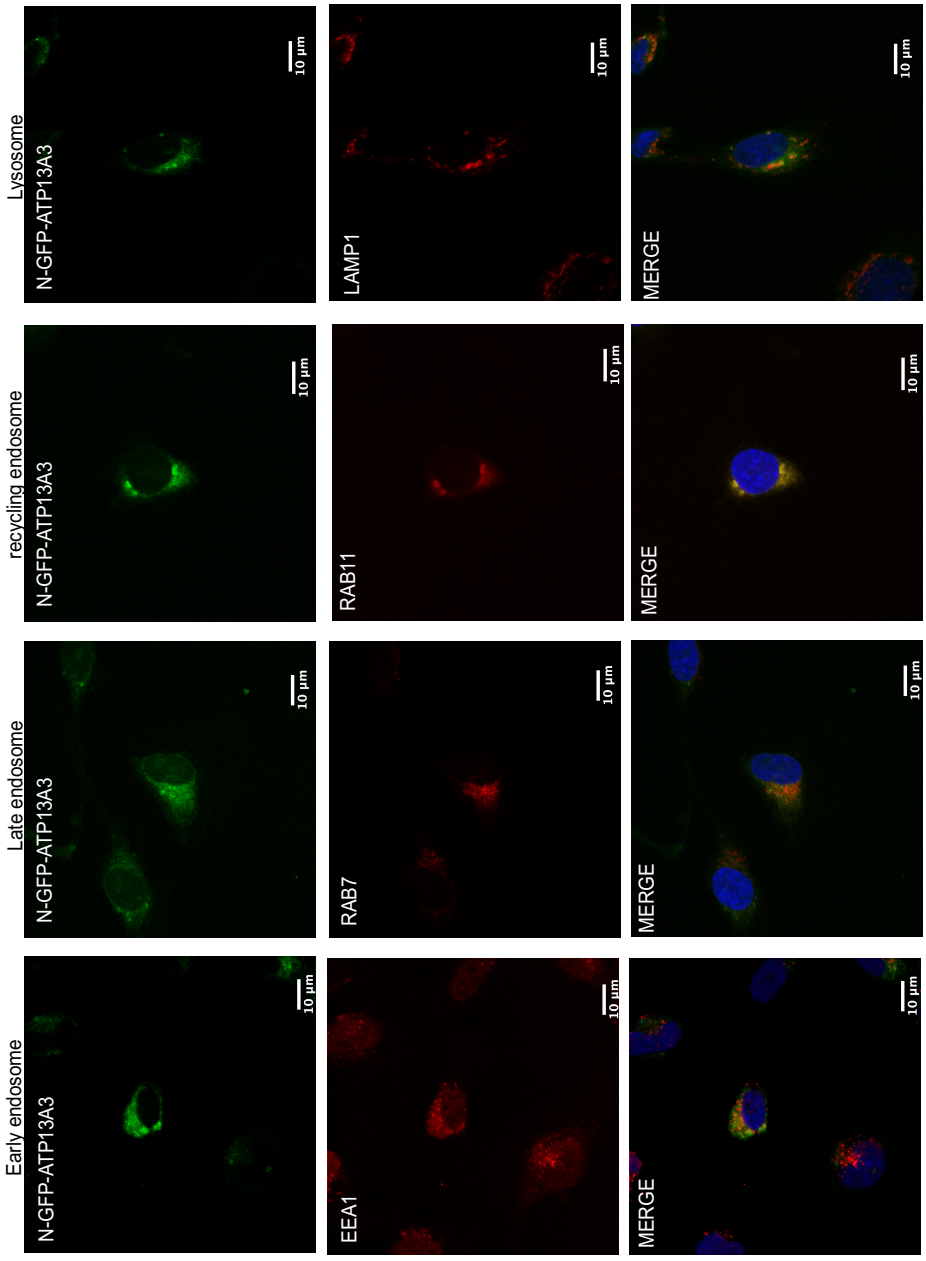

Figure 4-4 ATP13A3 is localised to the recycling endosome in HMEC1 cells

hATP13A3-N-EGFP-pcDNA6.2 (1 µg DNA) was transiently overexpressed in HMEC-1 cells of for 48 hours before being stained with anti-EEA1(1:200), anti-Rab7(1:200), anti-Rab11 (1:200) and anti-LAMP1 (1:200). Representative images were taken at 63X magnification using the Leica Sp5 confocal microscope platform (n=4) (Leica microsystem).

4.2.1.5 Disease-associated *ATP13A3* mutants do not display cellular compartmental mislocalisation in HMEC-1 cells.

After showing the colocalisation of ATP13A3 with the recycling endosome marker Rab11, I then assessed if the PAH-associated *ATP13A3* mutations led to compartmental mislocalisation in HMEC-1 cells. The hypothesis stemmed from the observation by Podhajska et al. [306] that overexpression of the Parkinson-related *ATP13A2* mutations in human SH-SY5Y neural cells, another P5-ATPase from the same family as *ATP13A3*, displayed mislocalisation from the lysosome to the endoplasmic reticulum. To characterise the cellular localisation of the PAH associated *ATP13A3* mutations, five missense heterozygous mutations (L675V, M850I, V855M, R858H, L956P) identified from the PAH cohort were transiently over-expressed (plasmids donated by Prof. Peter Vangheluwe) in HMEC-1 cells. Cells overexpressing the wild-type or mutant GFP-ATP13A3 did not exhibit any overt cell toxicity. Unlike *ATP13A2* mutants expressed in SH-SY5Y cells, PAH related missense mutants expressed in HMEC-1 cells did exhibit a different localisation when compared to the wild-type ATP13A3. The different GFP-ATP13A3 mutants still colocalised with Rab11 while overlap with other endo/lysosomal markers was minimal (Figure 4-5) low. However, in comparison to wild type GFP-ATP13A3, overexpression of mutations such as L675V, M850I and V855M led to enlarged and condensed vesicles indicating a potential disruption of cell vesicular homeostasis by *ATP13A3* mutations (Figure 4-5).

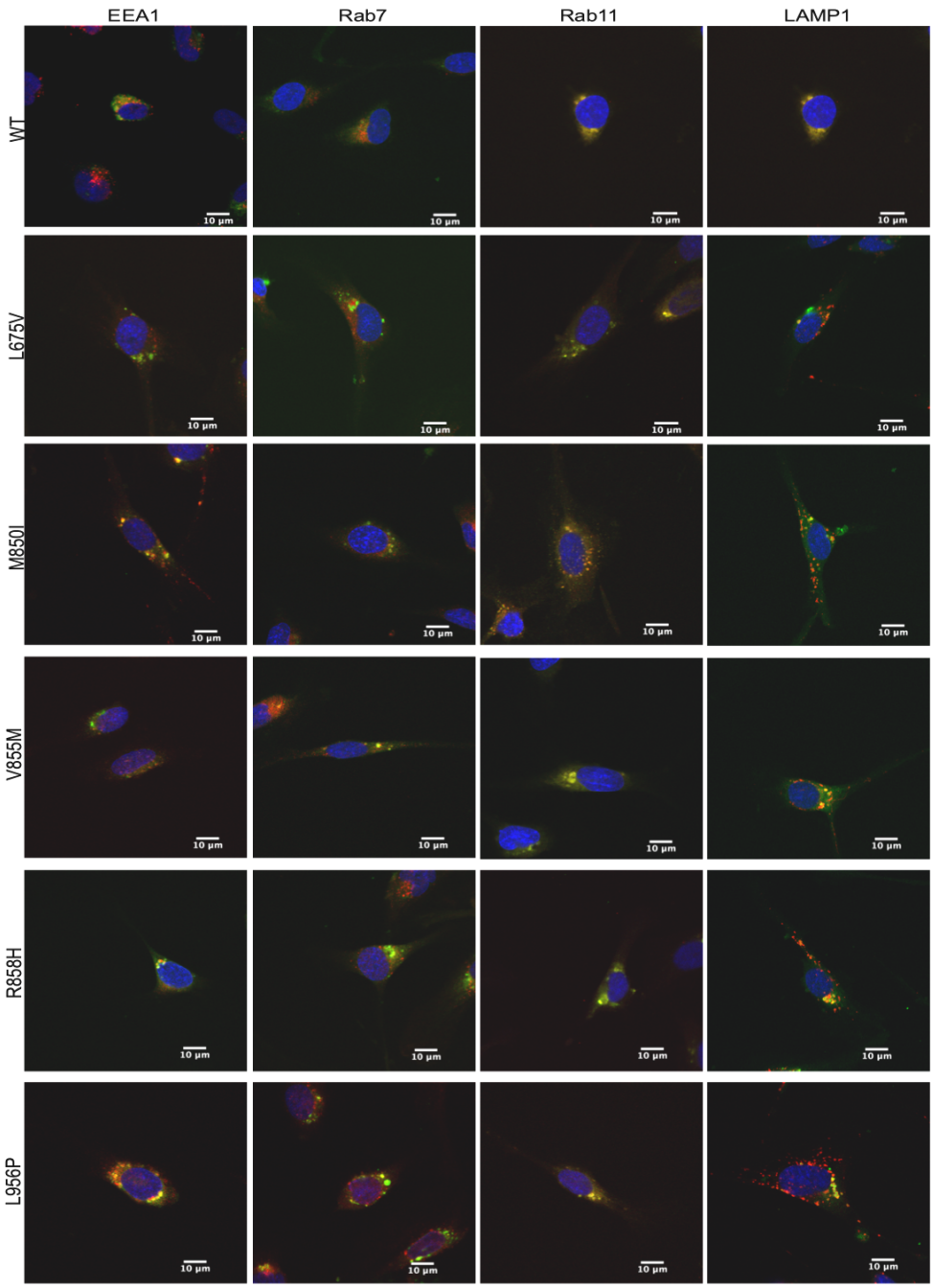

Figure 4-5 Disease-associated ATP13A3 mutants do not display cellular mislocalisation in HMEC-1 cells.

Wild type or disease-associated mutant h*ATP13A3*-N-EGFP-pcDNA6.2 (1 µg DNA) were transiently over-expressed in HMEC-1 cells for 48 hours before being stained with anti-EEA1(1:200), anti-Rab7(1:200), anti-Rab11 (1:200) and anti-LAMP1 (1:200). Representative images were taken at 63X magnification using the Leica Sp5 confocal microscope platform (n=4) (Leica microsystem).

4.2.2 ATP13A3 and polyamine transport

4.2.2.1 *ATP13A3* deficiency reduced the cellular polyamine content in human pulmonary artery endothelial cells (hPAECs)

ATP13A3 has previously been implicated in polyamine transport. To assess its link with polyamine homeostasis in vascular cells, the cellular polyamine contents were measured by liquid chromatography-mass spectrometry (LC-MS) in hPAECs with or without *ATP13A3* deficiency. si*ATP13A3* yielded an average of 90% reduction of *ATP13A3* mRNA in hPAECs (Figure 4-6 D). Notably, when compared to cells transfected with siCP, si*ATP13A3* transfected hPAECs showed approximately 35% lower cellular putrescine levels (Figure 4-6 A). Spermidine and spermine, were less affected by *ATP13A3* deficiency in hPAECs, with an average reduction of 20% and 18% respectively (Figure 4-6 B, C). Consistent with my previous findings (Chapter 3), the mRNA expression of other P5-ATPases was not altered by si*ATP13A3* in hPAECs (Figure 4-7). These findings suggest that *ATP13A3* is likely to play an essential role in maintaining the polyamine homeostasis in endothelial cells, with a bias towards putrescine.

4.2.2.2 *ATP13A3* loss of function reduces the putrescine uptake capacity

To assess the polyamine uptake capacity, transfected hPAECs were incubated with or without the addition of 1mM putrescine, 10μM spermidine, or 10μM spermine overnight and measured for cellular polyamine contents. As shown in Figure 4-8, consistent with the previous findings, *ATP13A3* deficiency reduced the basal level of putrescine, spermidine and spermine in hPAECs. Interestingly, unlike ATP13A2, which favours a higher transport selectivity to spermine, *ATP13A3* showed a higher preference to putrescine, manifesting by a sharp decrease of putrescine uptake in *ATP13A3*-deficient hPAECs. Spermidine and spermine were less affected (Figure 4-8 B, C). Taken together, these findings reinforce the hypothesis that *ATP13A3* is involved in polyamine

homeostasis, as achieved by favouring a higher transport preference for putrescine than spermidine or spermine.

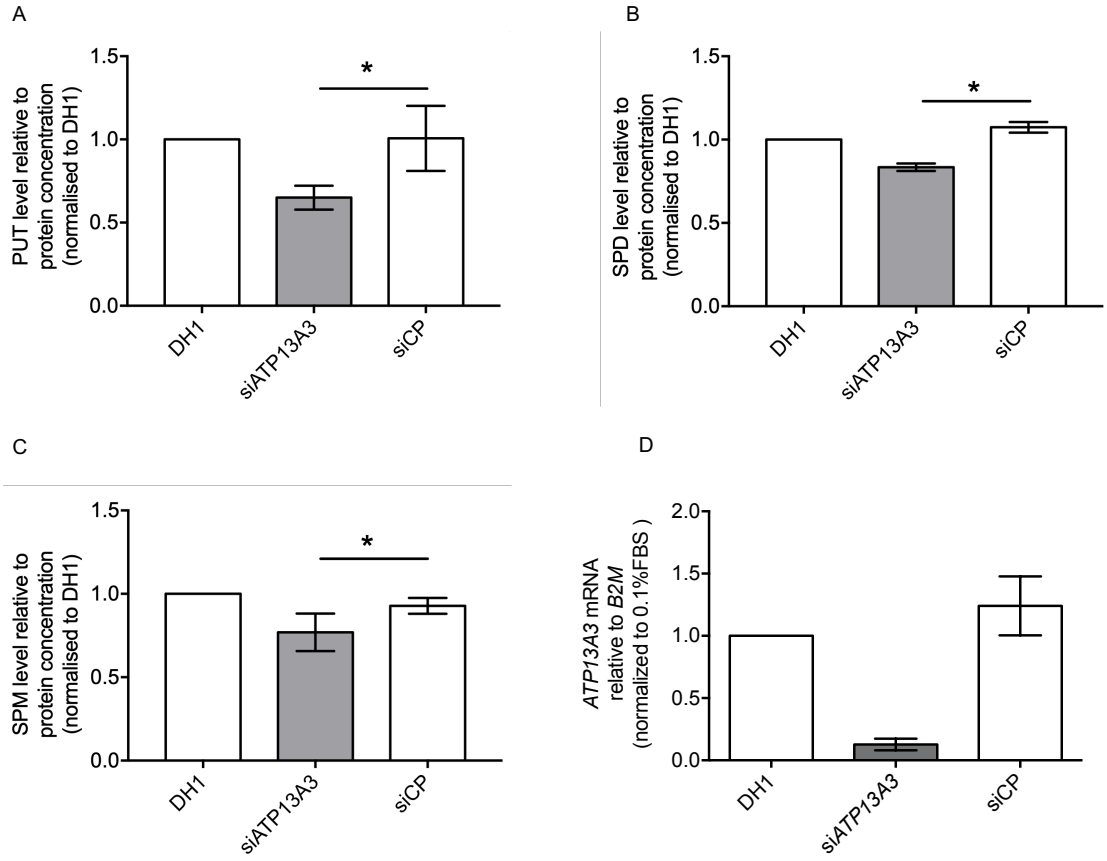

Figure 4-6 ATP13A3 deficiency reduces the cellular polyamine levels in hPAECs

Cellular Putrescine (A), Spermidine (B), or Spermine (C) contents of hPAECs transfected with DharmaFECT1(DH1) alone, si*ATP13A3* or non-targeting siRNA control (siCP) were assessed by Liquid chromatography-mass spectrometry (LC-MS) forty-eight hours post-transfection (N=3). Data are presented as the polyamine peak area ratio relative to sample protein concentration, and further normalised to DH1. Mann–Whitney U test was applied for data analysis. *P<0.05 compared with siCP. PUT: putrescine; SPD: spermidine; SPM: spermine (D) mRNA expression of *ATP13A3* relative to *B2M* and normalised to DH1.

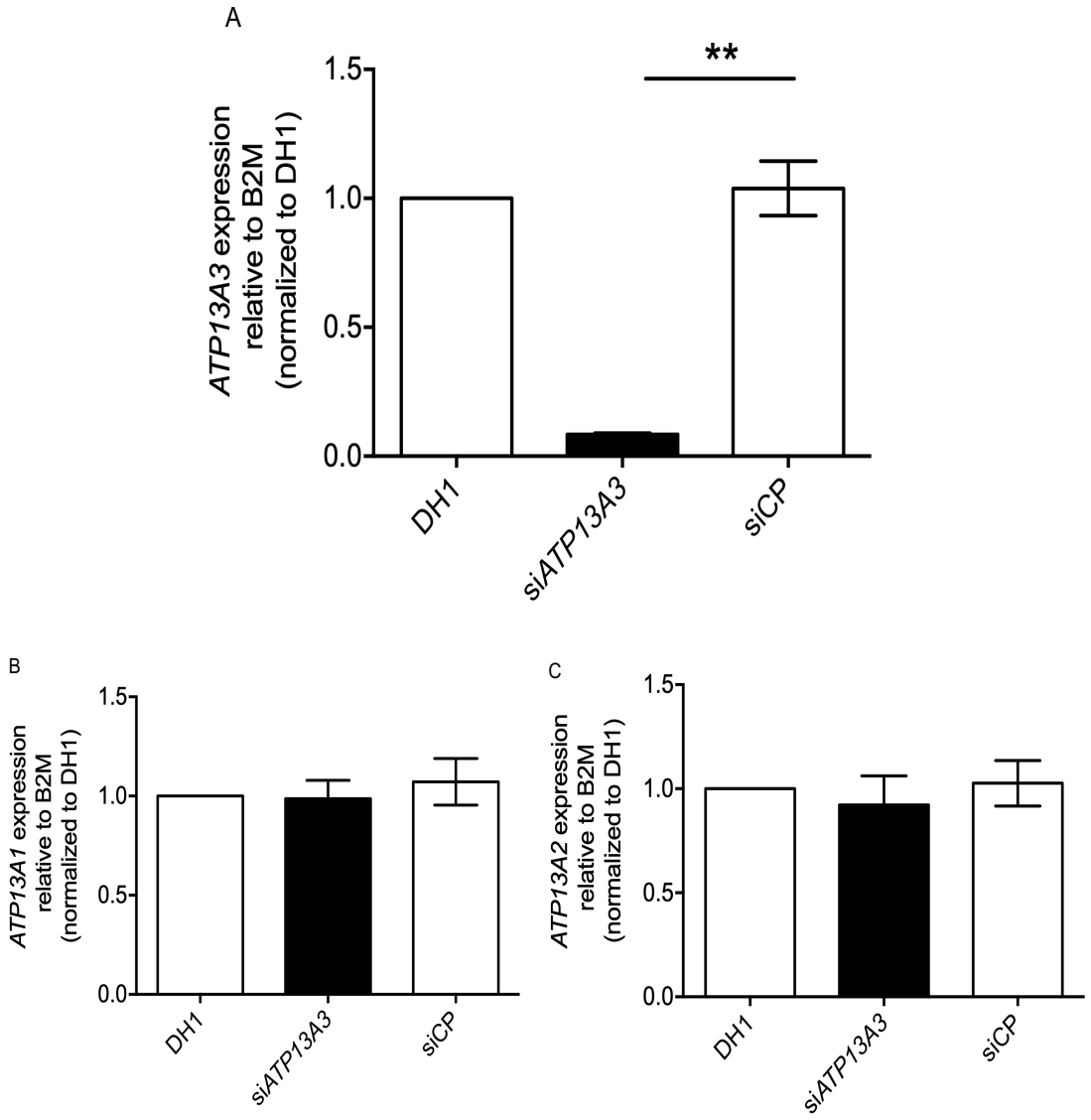

Figure 4-7 ATP13A3 depletion did not affect the mRNA expression of other P5-ATPases in PAECs

mRNA expression of (A) *ATP13A3*, (B) *ATP13A1*, and (C) *ATP13A2* of hPAECs transfected with DharmaFECT1 (DH1) alone, si*ATP13A3* or non-targeting siRNA control (siCP). Data are presented as the fold-change relative to *B2M* and further normalised to DH1(n=3). Mean ± SEM are shown, and data were analysed using a one-way ANOVA with Tukey's post hoc test for multiple comparisons. **P<0.01, compared to siCP.

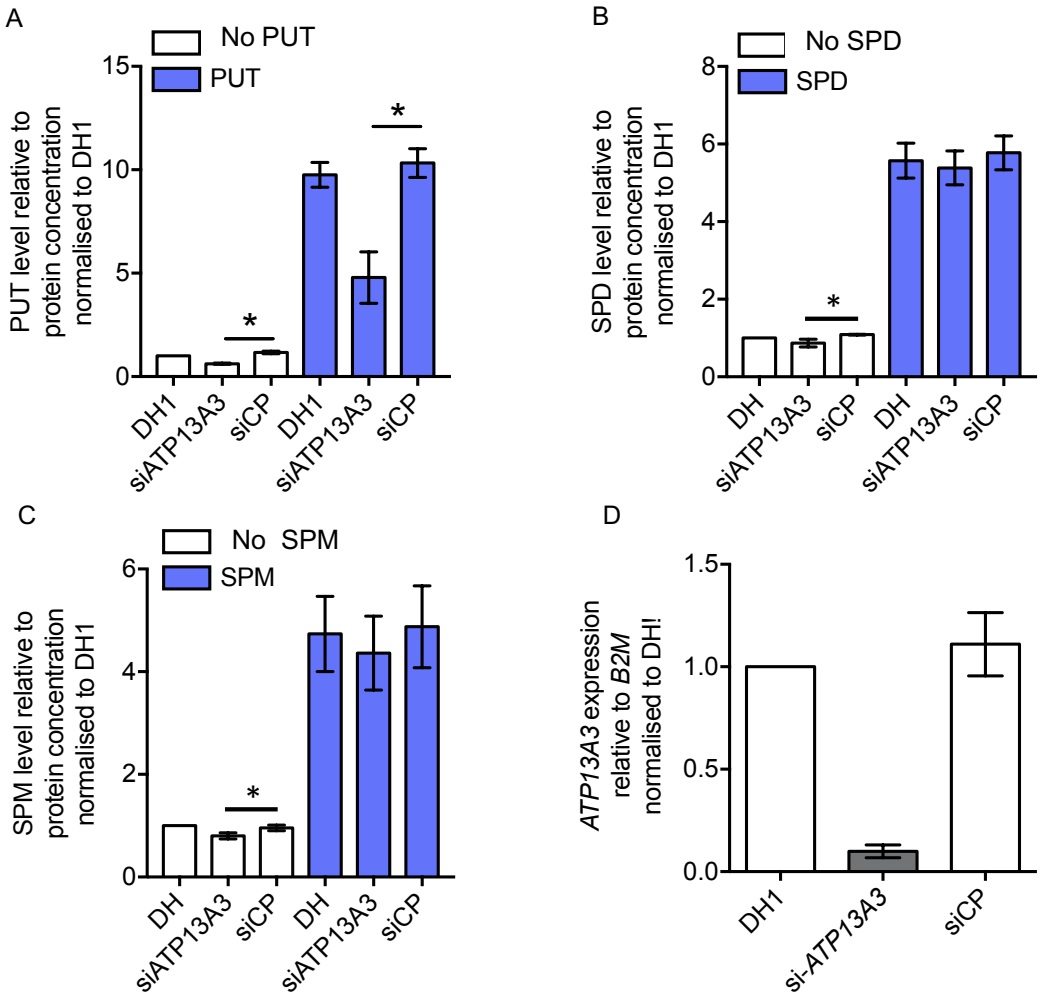

Figure 4-8 ATP13A3 deficiency reduces the cellular polyamine content and putrescine uptake in hPAECs

Cellular Putrescine (A), Spermidine (B), or Spermine (C) levels of hPAECs cultured overnight in EBM2 containing 2%FBS and supplemented with or without 1mM putrescine, 10μM spermidine, or 10μM spermine. Cellular polyamine content was measured by Liquid chromatography-mass spectrometry (LC-MS) (N=3). Data are presented as polyamine peak area ratio relative to sample protein concentration, and further normalised to 0.1% FBS DH1. Mann–Whitney U test was applied for comparison between si*ATP13A3* and siCP in basal or different polyamine supplementation group. *P<0.05 compared with siCP. (D) mRNA expression of *ATP13A3* relative to *B2M* and normalised to DH1.

4.2.2.3 PAH associated *ATP13A3* missense mutations display impaired polyamine uptake capacity in hPAECs

I then assessed if PAH-associated mutations affect ATP13A3 mediated polyamine uptake. For comparison, wild type (WT), a catalytic-dead mutant (D498N) and the PAH associated missense mutations of *ATP13A3* (L675V, M850I, V855M, R858H, L956P) were transiently overexpressed with lentiviral transduction in hPAECs. The overexpression efficiency for each construct was comparable, with an approximately three-fold increase of *ATP13A3* mRNA observed in transduced hPAECs (Figure 4-9 A). hPAECs were further incubated with or without 1mM Putrescine overnight before measuring for polyamine by LC-MS. In the basal condition (without putrescine supplementation), neither wild type nor mutant *ATP13A3* altered the cellular polyamine content (Figure 4-10 B). However, when supplemented with putrescine, WT-*ATP13A3* overexpression significantly increased putrescine uptake by 2-fold compared to GFP-tagged empty vectors (Figure 4-10 A).

ATP13A3 overexpression in hPAECs did not overtly alter ATP13A2 or ATP13A1 mRNA (Figure 4-9 B), so the changes I observed strongly suggested a specific effect of ATP13A3 on putrescine uptake. The presence of the conserved catalytic site (D498) is crucial for this effect as catalytically dead mutation (D498N) substantially reduced putrescine uptake compared to wild type *ATP13A3* (Figure 4-10 A). Interestingly, the PAH-associated mutants, L675V, M850I, and V855M significant impaired the putrescine uptake mediated by ATP13A3 (42-60%) (Figure 4-10 A) while R858H and L956V exerted a milder disruption (20% and 21% respectively) (Figure 4-10 A). Taken together, these results provide strong evidence for ATP13A3 as a putrescine transporter in endothelial cells and demonstrate impairment of PAH associated mutations on ATP13A3 mediated polyamine uptake.

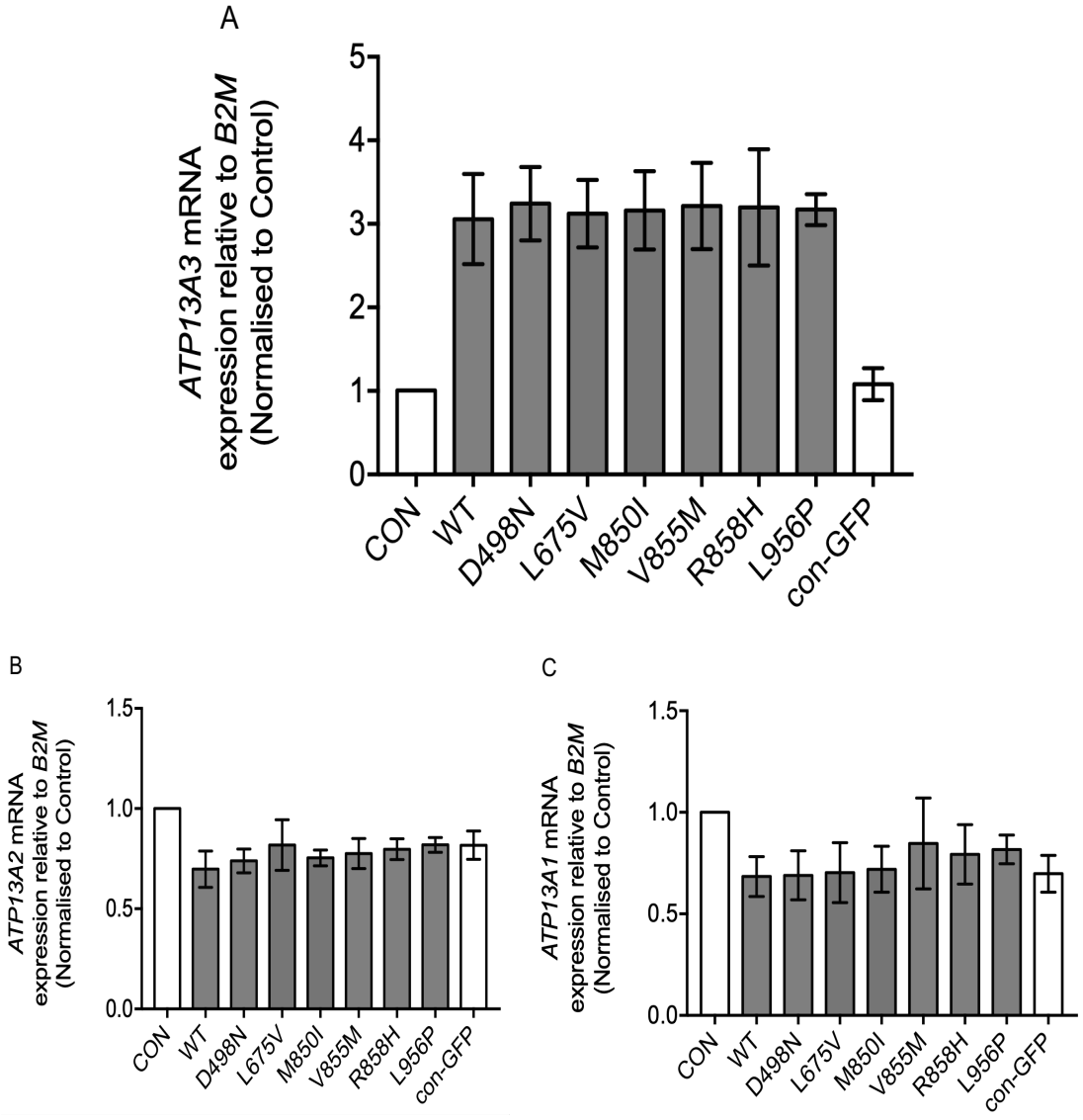

Figure 4-9 mRNA expression of P5-ATPases in hPAECs transiently overexpressing lentiviral-transduced WT and mutant ATP13A3

mRNA expression of (A) *ATP13A3*, (B) *ATP13A1*, and (C) *ATP13A2* in hPAECs transiently overexpressing lentiviruses encoding wild type (WT), catalytically dead mutant (D498N), PAH-associated mutants (L675V, M850I, V855M, R858H, L956P) *ATP13A3* or GFP-tagged empty vectors (n=3). Data are presented as fold-change relative to *B2M* and further normalised to non-transduced control.

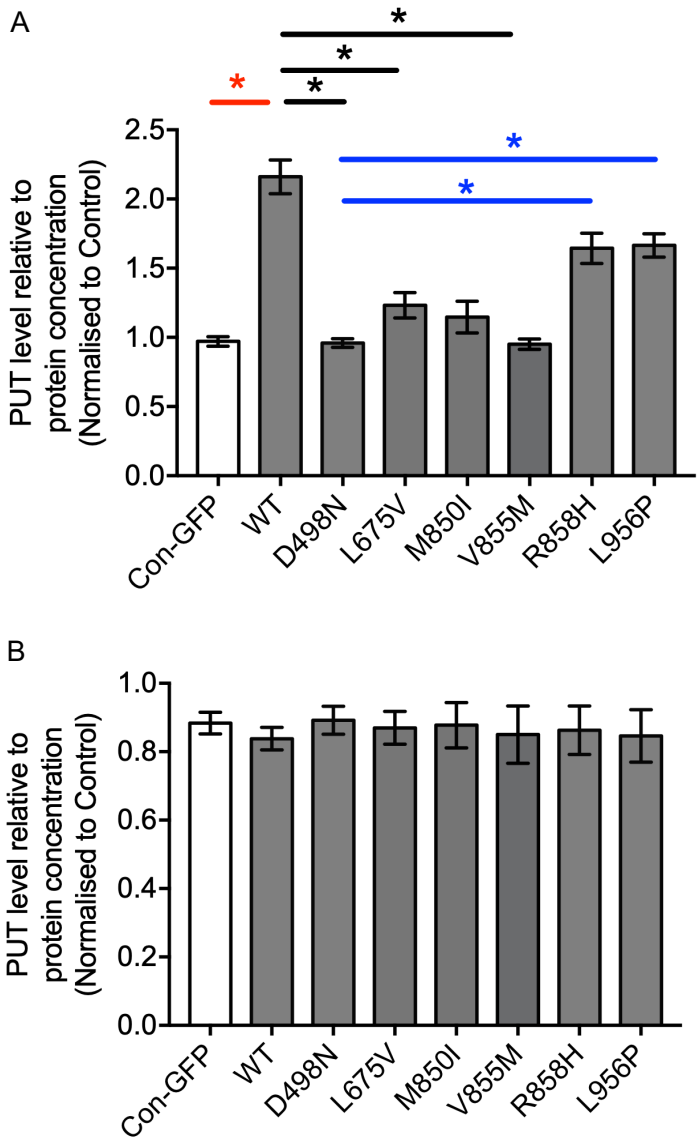

Figure 4-10 Cellular putrescine levels in hPAEC overexpressing lentiviral wild type or mutant ATP13A3

Cellular putrescine in hPAECs transiently overexpressing lentiviruses encoding wild type (WT), catalytically dead mutant (D498N), PAH-associated mutants (L675V, M850I, V855M, R858H, L956P) *ATP13A3* or GFP-tagged empty vectors followed by overnight incubation with (A) or without (B) the presence of 1mM Putrescine (N=4). Data are presented as polyamine peak area ratio relative to sample protein concentration, and further normalised to GFP-empty vector. Mann–Whitney U test was applied for data analysis. *P<0.05 compared with con-GFP. *P<0.05 compared with WT, *P<0.05 compared with D498N. PUT: putrescine.

4.2.2.4 Generation of HMEC-1 lines stably expressing short-hairpin RNAs targeting *ATP13A3*

Although the disease-associated mutants L675V, M850I, and V855M substantially reduces putrescine uptake capacity, the other two mutants assessed (R858H and L956P) exerted a milder effect. This could potentially be interpreted as a less deleterious phenotype being masked by the endogenous *ATP13A3* expression. Therefore, to overcome this, I sought to generate an HMEC-1 cell line with low basal *ATP13A3* expression by stable expressing a short-hairpin RNA (shRNA) targeting *ATP13A3.* In total, four shRNAs (MiR1-4) targeting different regions of *ATP13A3* were tested for their knockdown efficiency (Figure 4-11). In parallel, a control cell line expressing shRNA targeting firefly luciferase was generated (HMEC-1-MiR-fluc). All four *ATP13A3* short-hairpin RNAs significantly reduced the *ATP13A3* mRNA expression in HMEC-1 cells, with MiR-2 yielded the highest knockdown efficiency (~80%) (Figure 4-11 A). However, MiR-2 also caused reduction of *ATP13A1* (~30%) and *ATP13A2* (35%) mRNA (Figure 4-11 B, C). In contrast, the HMEC-1 line expressing MiR-1, though only exhibiting around 50% reduction of *ATP13A3* mRNA, preserved the expression of *ATP13A1* and *ATP13A2* mRNA. Additionally, unlike MiR2-4 which target the *ATP13A3* cDNA region, MiR-1 targets the 3' UTR region of *ATP13A3* cDNA and is unlikely to affect the *ATP13A3* overexpression achieved by plasmid or lentiviral transfection. Taken together, MiR-1 outweighed other shRNAs and the HMEC-1 line stably expressing MiR-1 (HMEC-1-MiR-1) was chosen for further experiments. Of note, the HMEC-1-MiRfluc line did not alter expression of *ATP13A1-3* (Figure 4-11 A-C).

4.2.2.5 Overexpression of *ATP13A3* in HMEC-1 suppressed ATP13A1 and ATP13A2 mRNA expression

Having generated the HMEC-1-MiR-1, I then assessed the overexpression efficiency of pcDNA6.2-h*ATP13A3* in these cells. To optimise experimental conditions, 0.5 µg -3 µg of plasmid DNA was transfected into HMEC-1-MiR-1 and assessed for the *ATP13A1-3* mRNA. Again, HMEC-1-MiR-1 displayed 50% reduction of *ATP13A3* mRNA compared to HMEC-1-MiR-fluc (Figure 4-12 A). *ATP13A3* mRNA showed a dose-dependent increase with the transfection of pcDNA6.2-h*ATP13A3*, with 3 µg plasmid DNA displayed the highest overexpression level (35-fold change) (Figure 4-12 A). Interestingly, pcDNA6.2-h*ATP13A3* transfected at 2 µg and 3 µg amounts substantially suppressed the mRNA expression of both *ATP13A1* and *ATP13A2*. 1 µg of pcDNA6.2-h*ATP13A3*, while yielding a 5-fold *ATP13A3* mRNA increase, did not affect the expression of other P5 ATPases (Figure 4-12 B, C). Therefore, 1 µg of pcDNA6.2-h*ATP13A3* was used for characterising the putrescine uptake capacity of wild type or mutant *ATP13A3* in HMEC-1-MiR-1 cells.

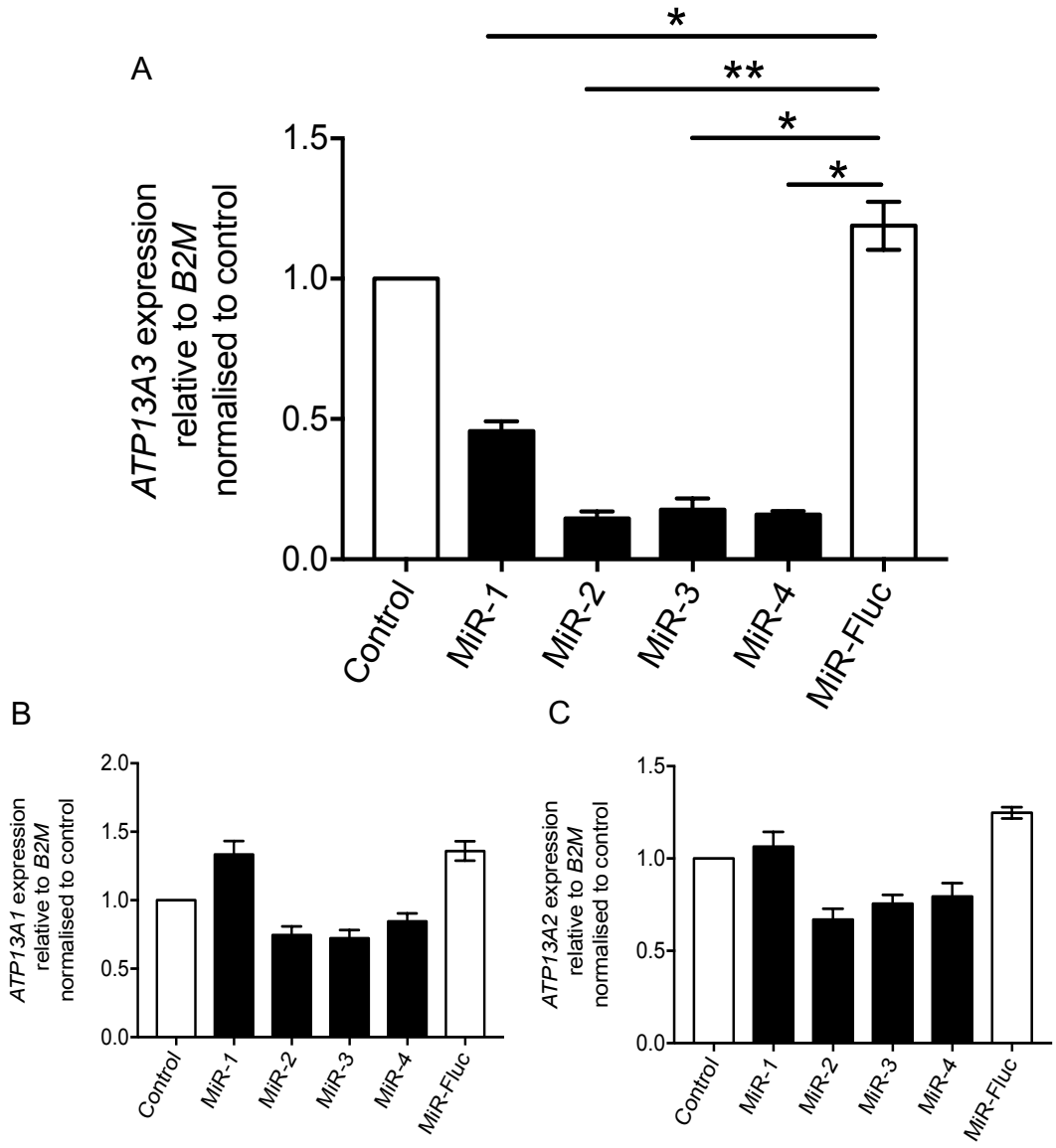

Figure 4-11 mRNA expression of P5-ATPases in HMEC-1 stably expressing different ATP13A3 shRNAs

mRNA expression of (A)*ATP13A3,* (B)*ATP13A1*, (C)*ATP13A2* in control HMEC-1 or HMEC-1 stably expressing MiR-1, MiR-2, MiR-3, MiR-4, non-targeting control (MiR-Fluc) (n=4). Data are presented as fold-change relative to *B2M* and further normalised to control HMEC-1. Mean ± SEM are shown and data were analysed using a One-way ANOVA with Tukey's post hoc test for multiple comparisons. *P<0.05, **P<0.01 compared to MiR-Fluc.

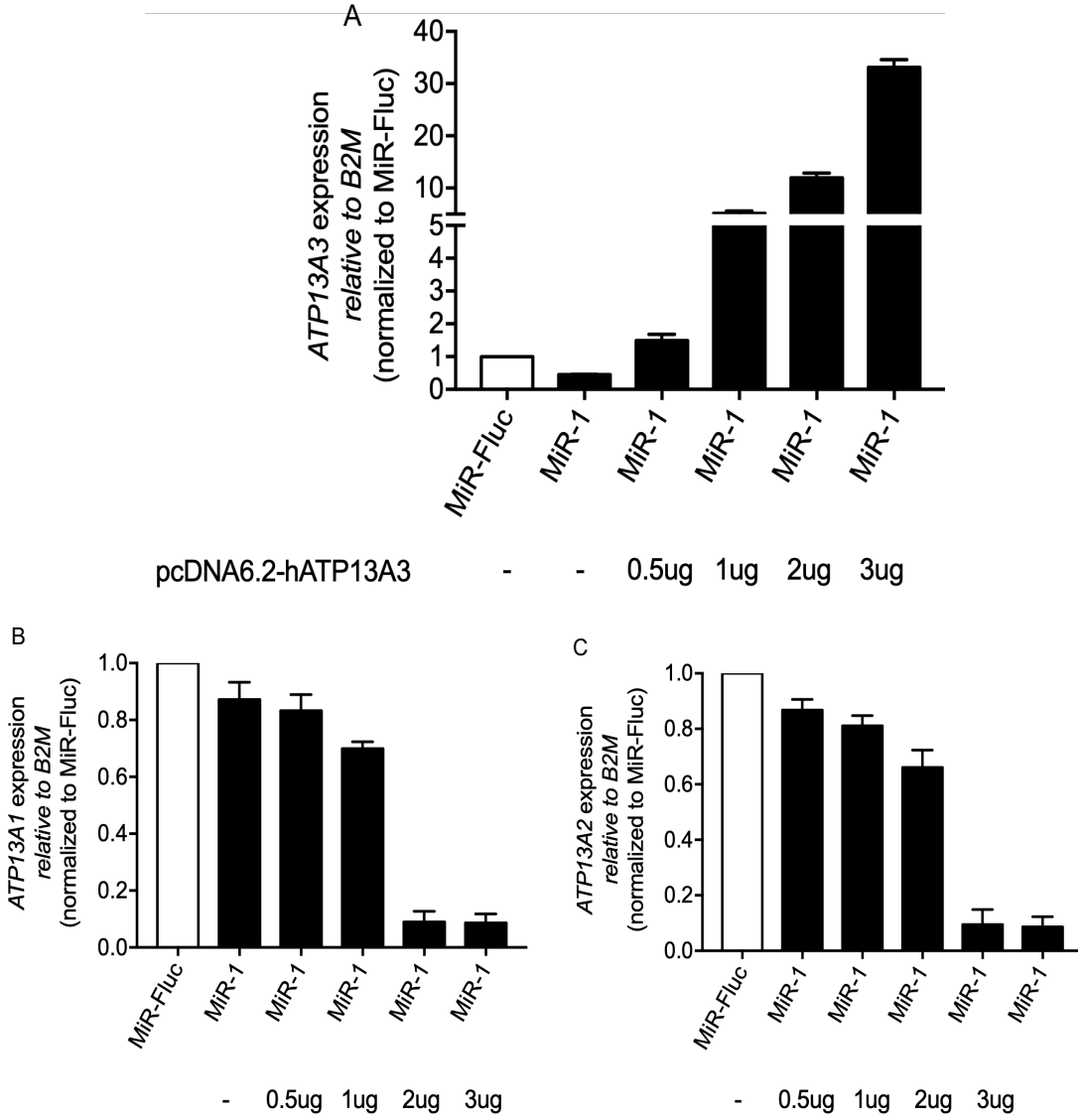

Figure 4-12 *ATP13A3* mRNA expression of HMEC-1-MiR-1 transiently overexpressing pcDNA6.2-hATP13A3

mRNA expression of (A)*ATP13A3,* (B)*ATP13A1*, (C)*ATP13A2* in HMEC-1-MiR-1 transiently transfected with 0.5 µg -3 µg of pcDNA6.2-h*ATP13A3* or MiR-Fluc (n=2). Data are presented as fold change relative to *B2M* and further normalised to MiR-Fluc.

4.2.2.6 PAH associated missense *ATP13A3* mutation display impaired polyamine uptake capacity in HMEC-1

Having shown that PAH associated mutations displayed impaired putrescine uptake capacity, I then assessed if HMEC-1 cells can recapitulate the previous findings in hPAECs. To achieve this, 1 µg of wild type or mutant *ATP13A3* (D498N, L675V, M850I, V855M, R858H, L956P) was transiently overexpressed in HMEC-1-MiR-1 cells. As shown below, HMEC-1-MiR-1 cells displayed a 50% basal reduction of *ATP13A3* mRNA compared to HMEC-1-MiR-fluc cells (Figure 4-13 A). Overexpression of *ATP13A3* mediated by the wild type and mutant *ATP13A3* plasmid DNA was comparable in HMEC-1 without affecting *ATP13A1-2* (Figure 4-13 A). Similar to siRNA knockdown in hPAECs, HMEC-1-MiR-1 also displayed reduced basal putrescine level, though to a lesser extent (18%) (Figure 4-13 A). Overexpression of wild type *ATP13A3* in HMEC-1-MiR-1 cells significantly increased their putrescine uptake by 4-fold while the D498N mutant displayed a similar uptake capacity to cells without overexpression (Figure 4-13 B). Again, PAH-associated mutants showed impairment of putrescine uptake in comparison to the wild type, with V855M exhibiting the most significant reduction. Though the reduction of putrescine uptake caused by R858H and L956P mutants was less prominent than the other disease-related mutants, they displayed a more significant reduction in uptake by HMEC-1 cells than observed in hPAECs when compared to wild type *ATP13A3* (Figure 4-13 B).

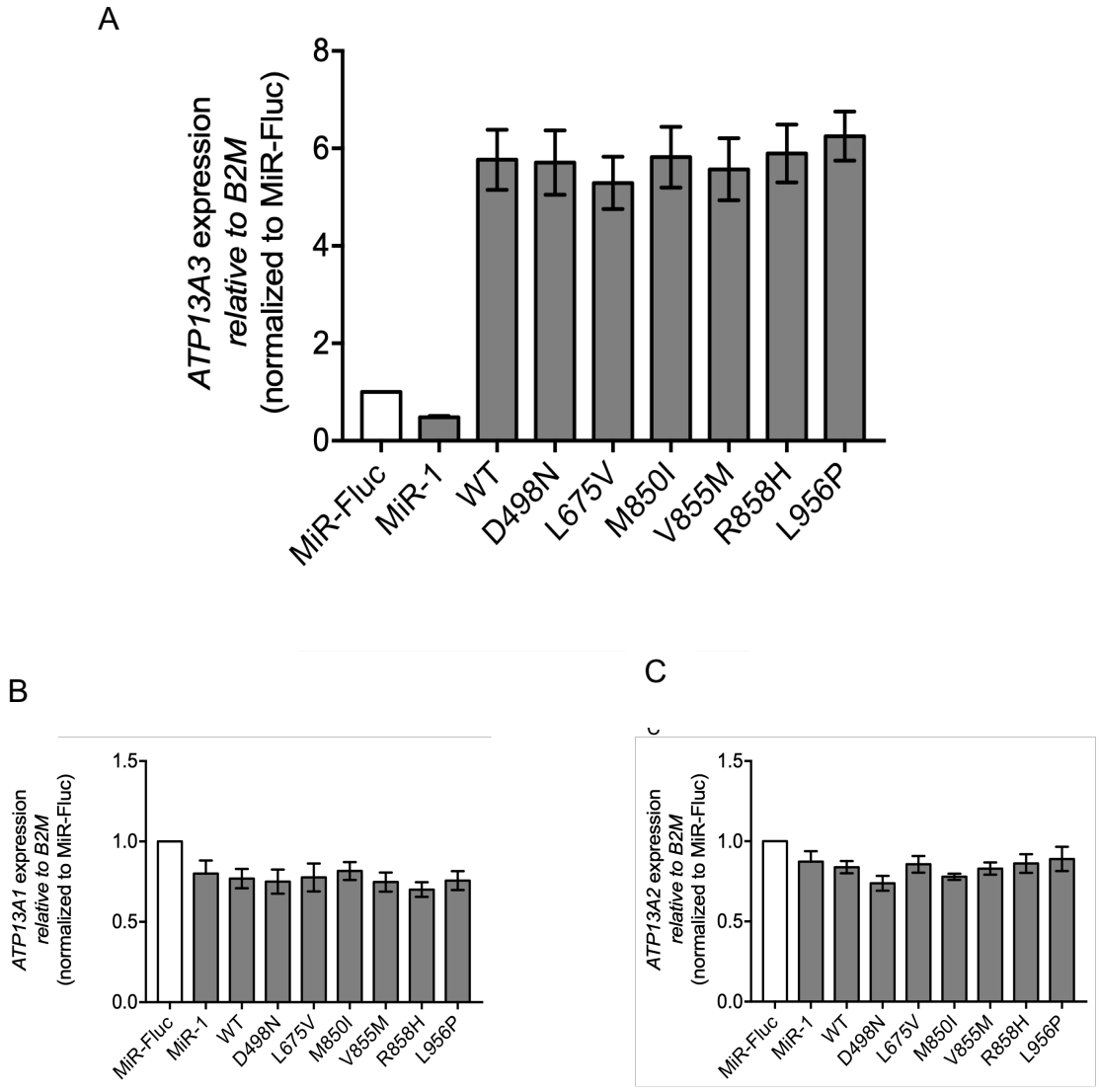

Figure 4-13 P5-ATPase mRNA expression in HMEC-1-MiR-1 transiently overexpressing WT and mutant ATP13A3

mRNA expression of (A) *ATP13A3*, (B) *ATP13A1*, and (C) *ATP13A2* in HMEC-1 MiR-Fluc cells or HMEC-1-MiR-1 cell stransiently overexpressing the *ATP13A3* wild type (WT), the catalytically dead mutant (D498N) or PAH-associated mutants (L675V, M850I, V855M, R858H, L956P) n=2. Data are presented as fold-change relative to *B2M* and further normalised to MiR-Fluc.

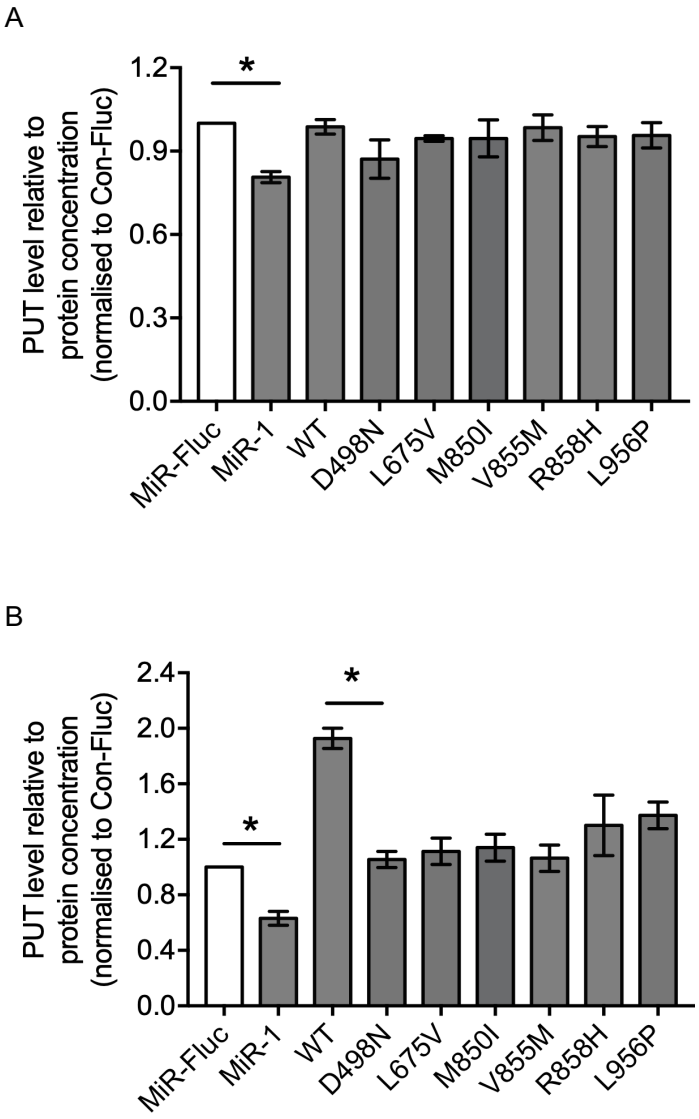

Figure 4-14 Cellular putrescine levels of HMEC-1 cells overexpressing wild type or mutant ATP13A3

Cellular Putrescine in HMEC-1-MiR-fluc cells or HMEC-1-MiR-1 cells transiently overexpressing *ATP13A3* wild type (WT), the catalytically dead mutant (D498N) or PAH-associated mutants (L675V, M850I, V855M, R858H, L956P) followed by overnight incubation with (A) or without (B) 1mM Putrescine (N=4). Data are presented as polyamine peak area ratio relative to sample protein concentration, and further normalised to MiR-Fluc. Mann–Whitney U test was applied for data analysis. *P<0.05 compared with MiR-Fluc. PUT: putrescine

4.2.2.7 hPAECs overexpressing PAH-associated *ATP13A3* mutations showed reduced sensitivity to polyamine accumulation

Although polyamines are essential for many cellular processes, it has been shown that excessive polyamines accumulation (especially spermidine and spermine) can be toxic and lead to apoptosis [106] or oxidative stress [307]. To further evaluate the functional impacts of PAH associated mutations, hPAECs overexpressing wild-type or mutant *ATP13A3* were exposed to putrescine(10mM), spermidine(1mM) and spermine(1mM) and assessed for cellular caspase activity. In control hPAECs (transduced with GFP-tagged empty vector), putrescine did not induce cell toxicity whereas both spermidine and spermine overnight incubation caused approximately 50% increase of caspase activity (Figure 4-15). Interestingly, wild type *ATP13A3* but not the D498N mutant sensitised hPAECs to putrescine, causing nearly 60% increase in caspase activity when compared to control hPAECs (Figure 4-15 A). The magnitude of the increased apoptosis caused by wild type *ATP13A3* under spermidine (~30%) and spermine (~20%) incubation was less profound than putrescine (Figure 4-15 B, C). The caspase activity induced by spermidine was ~15% lower in hPAECs overexpressing the D498N-*ATP13A3* mutant than in cells expressing wild type *ATP13A3*, while the difference under spermine incubation was negligible (less than 5%) (Figure 4-15 B, C). Similar to the polyamine uptake observations, PAH-associated mutants, namely L675V, M850I and V855M, were less sensitive to putrescine toxicity, with the V855M-*ATP13A3* showed the highest tolerance to putrescine. In contrast, the R858H and L956P mutants behaved more closely to wild type *ATP13A3* (Figure 4-15 A). Intriguingly, all PAH-associated mutants showed similar sensitivity to spermidine or spermine incubation in comparison to wild type *ATP13A3* (Figure 4-15 B, C).

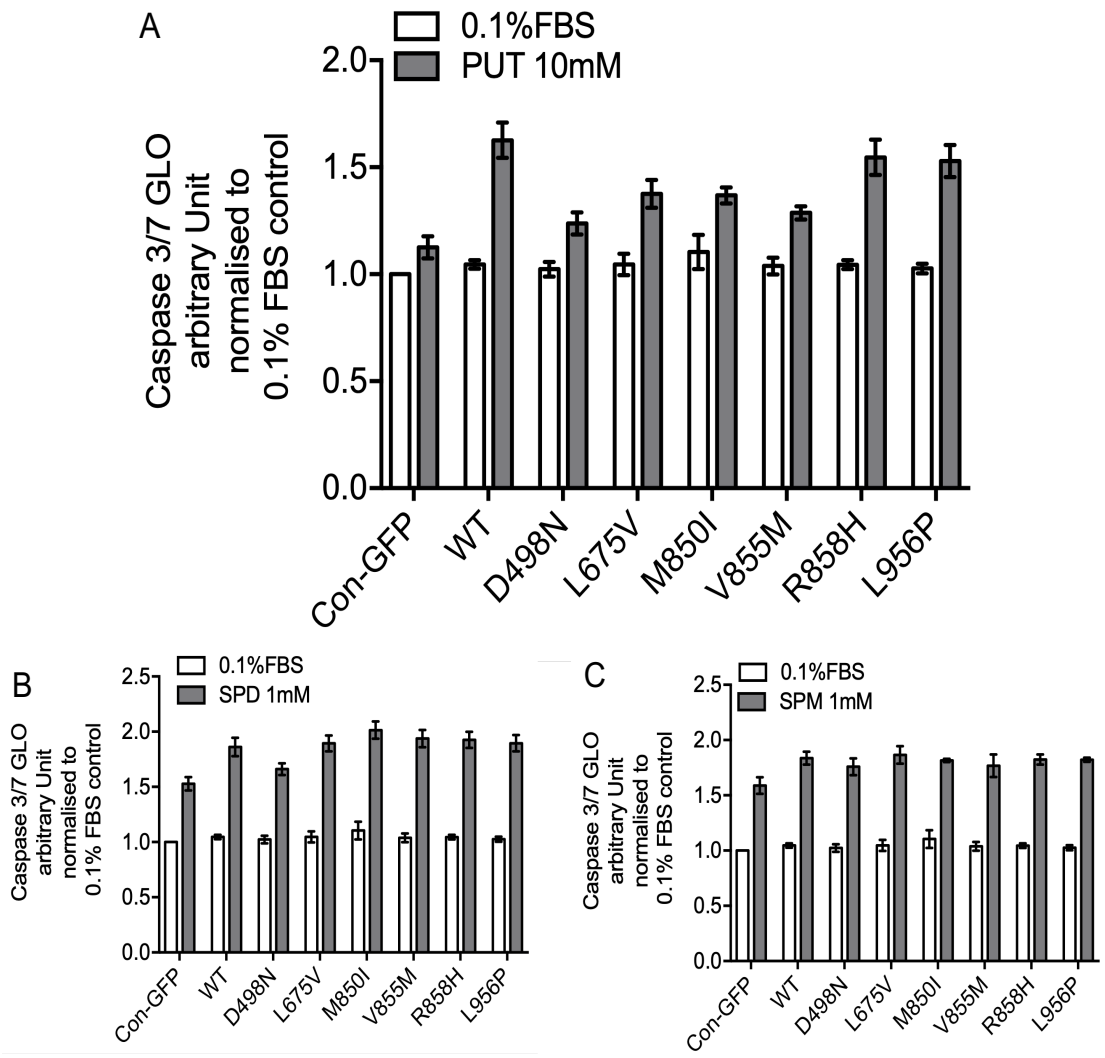

Figure 4-15 PAH associated mutations presented resistance to putrescine-induced apoptosis in hPAECs

hPAECs were transiently transduced with wild type (WT), catalytically dead mutant (D498N), PAH-associated mutants (L675V, M850I, V855M, R858H, L956P) *ATP13A3* or GFP-tagged empty vectors. Cells were then cultured overnight with or without the presence of (A)10mM Putrescine, (B)1mM Spermidine or (C)1mM spermine and assessed for cellular caspase activity (N=3). Data are presented as fold change relative to con-GFP cultured in 0.1%FBS.

4.2.3 ATP13A3 and polyamine metabolism

4.2.3.1 *ATP13A3* depletion in endothelial cells affects polyamine metabolic enzymes

From the data presented in this result chapter earlier, ATP13A3 may function as a polyamine transporter as *ATP13A3* deficiency in endothelial cells substantially impaired putrescine uptake capacity. Interestingly, endothelial cells with reduced *ATP13A3* mRNA expression displayed lower basal polyamine content (Figure 4-6 A; Figure 4-14 A). This indicates a potential regulation of *ATP13A3* on polyamine metabolism.

To test this hypothesis, the mRNA expression of polyamine biosynthesis and catabolism enzymes (Figure 4-16) was compared among hPAECs transfected with or without si*ATP13A3*. As previously shown, *ATP13A3* depletion did not affect the expression of other P5-ATPases (Figure 4-7). Strikingly, 48-hour post-transfection, si*ATP13A3* significantly suppressed the expression of the polyamine catabolic enzymes in hPAECs. Specifically, spermine oxidase (SMO) was reduced by 35%, polyamine oxidase (PAO) by 30% and spermidine/spermine acetyltransferase (SSAT) by 52% (Figure 4-16 C). Interestingly, the expression of two polyamine biosynthesis enzymes, spermidine synthase (SRM) and spermine synthase (SMS) was also downregulated by 31% and 30% respectively (Figure 4-16 B). Taken together, these findings suggest that *ATP13A3* depletion not only reduces polyamine uptake capacity but could also affect the polyamine-associated metabolic enzyme expression.

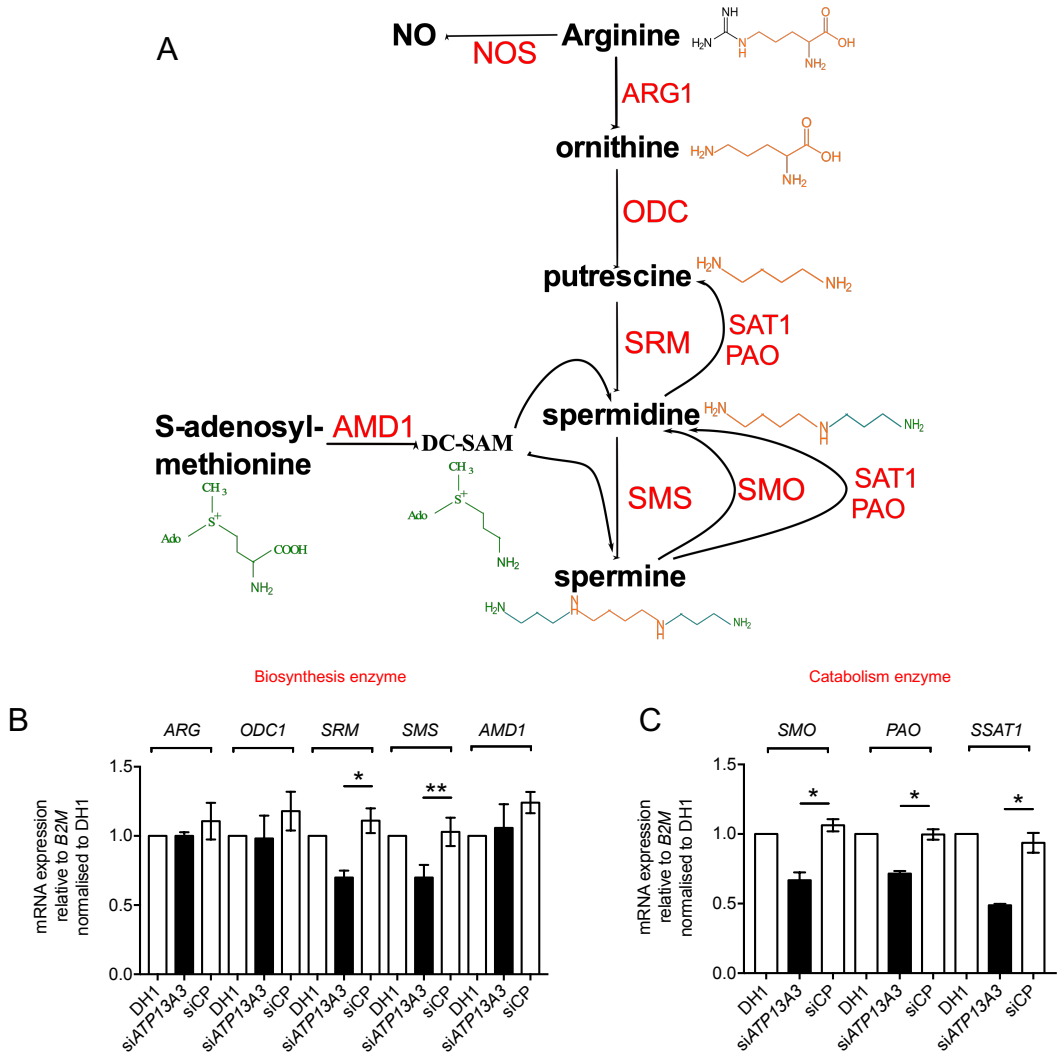

Figure 4-16 *ATP13A3* deficiency affects the mRNA expression of polyamine metabolic pathway enzymes in hPAEC (A) Schematic of cellular polyamine metabolism. Arginine from the urea cycle is converted into ornithine by arginase 1. The resulting ornithine is then decarboxylated into putrescine by the rate-limiting enzyme of polyamine synthesis ornithine decarboxylase (ODC). Spermidine synthase and spermine synthase catalyse the transfer of the aminopropyl moiety from S-adenosyl-methionine to mediate the production of spermidine and spermine respectively. mRNA expression of polyamine biosynthesis enzymes (B) and catabolic enzymes (C) of hPAECs (n=4). Data are presented as fold-change relative to B2M and further normalised to DH1. Mean ± SEM are shown and data were analysed using a One-way ANOVA with Tukey's post hoc test for multiple comparisons. *P<0.05, **P<0.01 compared to siCP.

A similar effect was recapitulated in BOECs, with mRNA expression of the polyamine metabolic enzymes being reduced by si*ATP13A3*. *ATP13A3* depletion in BOECs decreased the expression of both SRM and SMS by 50% and 43% respectively (figure 4-17 A). Additionally, the polyamine catabolic enzymes, SMO, PAO, and SSAT1 also displayed reduced mRNA expression (figure 4-17 B). This is likely to be a specific effect for *ATP13A3* as si*ATP13A3* transfection did not alter the mRNA expression of other P5-ATPases (Figure 4-18). Taken together, these findings suggest a potential regulatory role of *ATP13A3* in cellular polyamine metabolism.

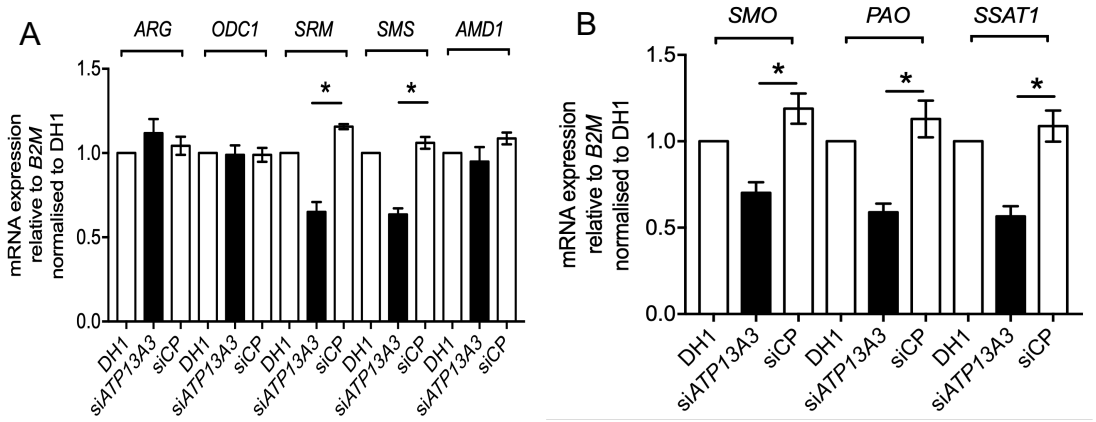

Figure 4-17 ATP13A3 deficiency affects the mRNA expression of polyamine metabolic pathway enzymes in BOECs

mRNA expression of different polyamine catabolic enzymes (A) and polyamine biosynthesis enzymes (B) in BOECs transfected with DharmaFECT1 (DH1) alone, si*ATP13A3* or non-targeting siRNA control (siCP) (n=4). Data are presented as fold-change relative to *B2M* and further normalised to DH1. Mean ± SEM are shown and data were analysed using a One-way ANOVA with Tukey's post hoc test for multiple comparisons. *P<0.05, compared to siCP.

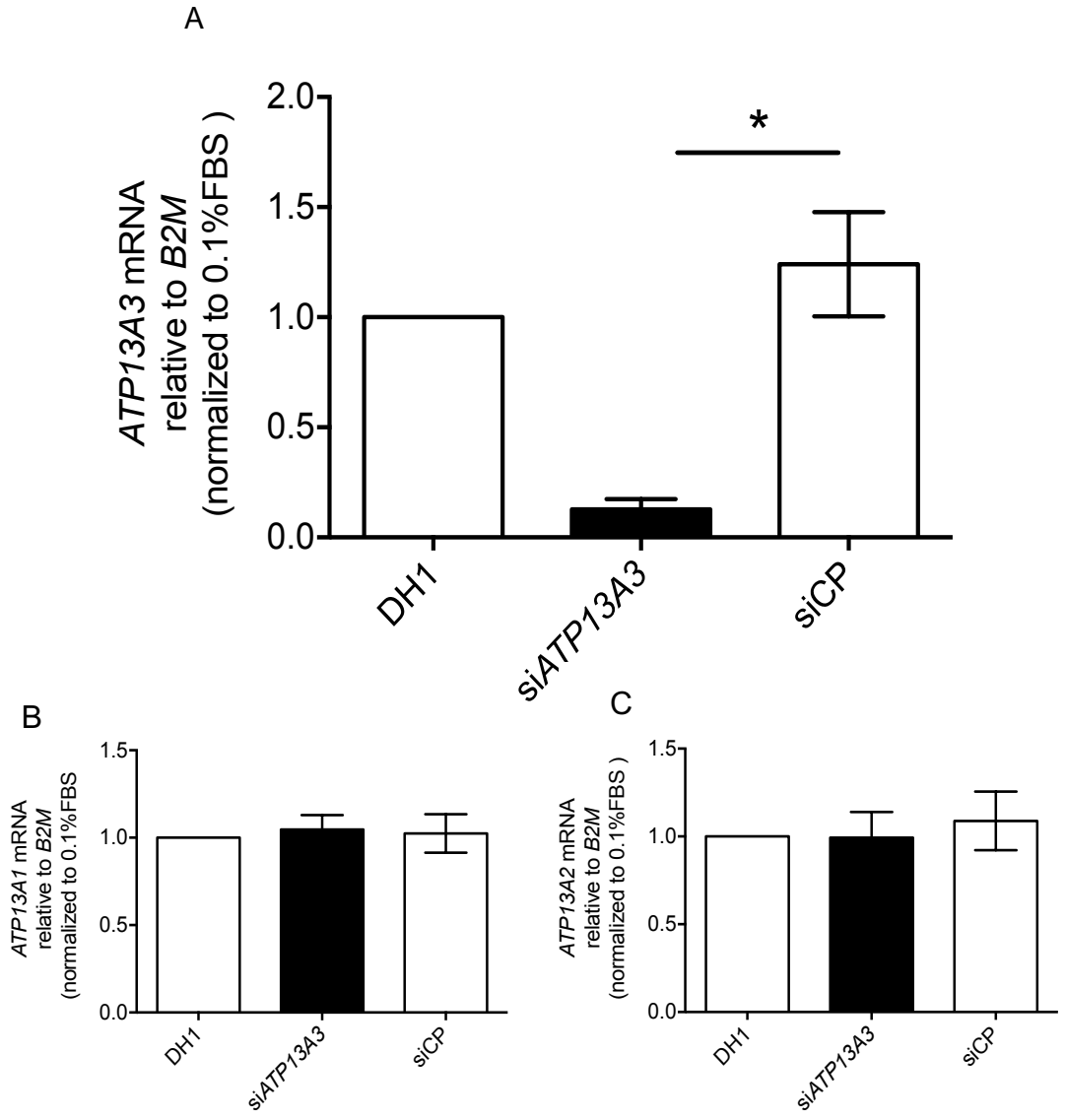

Figure 4-18 ATP13A3 depletion in BOECs does not alter the mRNA expression of other P5-ATPases

mRNA expression of (A) *ATP13A3*, (B) *ATP13A1*, and (C) *ATP13A2* of BOECs transfected with DharmaFECT1 (DH1) alone, si*ATP13A3* or non-targeting siRNA control (siCP) (n=4). Data are presented as fold-change relative to *B2M* and further normalised to DH1. Mean ± SEM are shown and data were analysed using a One-way ANOVA with Tukey's post hoc test for multiple comparisons. *P<0.05, compared to siCP.

4.2.3.2 *ATP13A3* depletion upregulates ornithine decarboxylase (ODC) protein expression in endothelial cells

Ornithine decarboxylase (ODC) is essential for polyamine biosynthesis, and its regulation is heavily reliant on polyamine levels. Increased cellular polyamine trigger the proteasomal degradation of ODC mediated by antizyme while reduced polyamine levels preserve ODC by suppressing functional antizyme expression (Figure 4-19). As *ATP13A3* depletion reduces polyamine levels in endothelial cells, I then question if ODC may be altered by ATP13A3 deficiency. Intriguingly, *ATP13A3* depletion did not affect *ODC* mRNA in hPAECs (Figure 4-19 B). Instead, ODC protein level was upregulated by approximately two-fold, indicating a post-translational regulation of ODC by *ATP13A3* depletion (Figure 4-20). Similar observations were also found in BOECs (Figure 4-19 C; Figure 4-21). Immunostaining of ODC in hPAECs further confirmed its upregulation by *ATP13A3* deficiency (Figure 4-23).

As mentioned earlier, ODC degradation is dynamically monitored via the regulation of antizyme (Figure 4-19). Since *ATP13A3* depletion reduced the polyamine content, I then questioned if antizyme (OAZ) participated in ODC regulation in this context. Consistent with this hypothesis, *OAZ* mRNA was reduced in both BOECs (42%) and hPAECs (50%) with si*ATP13A3* transfection (Figure 4-20 B, C), suggesting that upregulation of ODC1 protein is potentially a consequence of the downregulation of OAZ1 mRNA levels. mRNA level of antizyme inhibitor (AZIN), which competes ODC for antizyme, was not altered (Figure 4-20 B, C), indicating that ODC upregulation mediated by *ATP13A3* loss is more likely via the downregulation of antizyme. Interestingly, unlike endothelial cells, *ATP13A3* deficiency did not cause ODC upregulation in hPASMCs (Figure 4-22), suggesting a cell-type dependent effect of *ATP13A3* on ODC regulation.

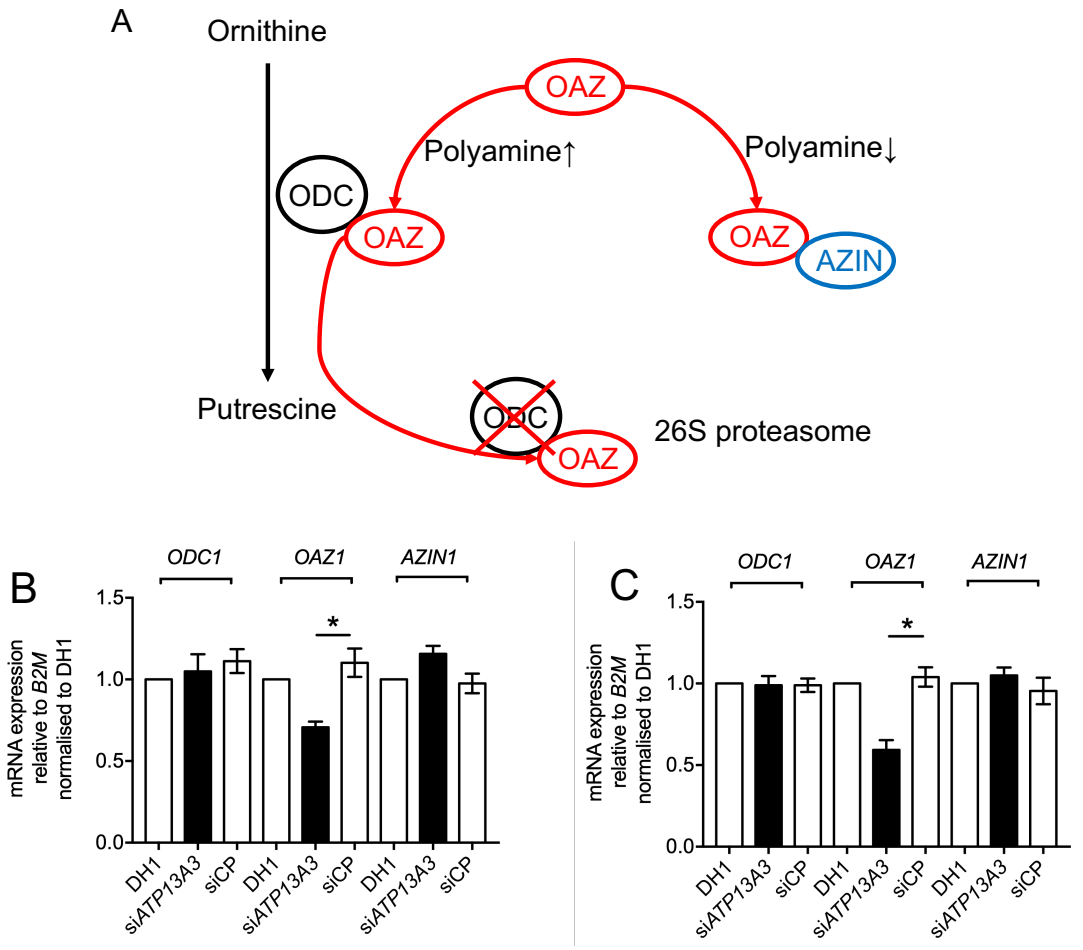

Figure 4-19 ATP13A3 depletion did not alter ODC1 but reduced OAZ1 at transcriptional level

(A) schematic of ornithine decarboxylase regulation in cells. ODC is highly regulated by antizyme through a polyamine dependent manner. Increased cellular polyamine levels trigger the production of functional antizyme (OAZ1) by mediating a ribosomal frameshift event. The resulting antizyme forms a complex with ODC, mediating ubiquitin-independent degradation through the 26S proteasome. When polyamine levels drop, the antizyme inhibitor competitively binds to antizyme and therefore releases ODC for polyamine biosynthesis. *ODC1, OAZ1, AZIN1* mRNA expression in BOECs (B) or hPAECs (C) transfected with DH1, siATP13A3 or siCP (n=4). Data are presented as fold change relative to B2M and further normalised to DH1. Mean ± SEM are shown and data were analysed using a One-way ANOVA with Tukey's post hoc test for multiple comparisons. *P<0.05 compared to siCP.

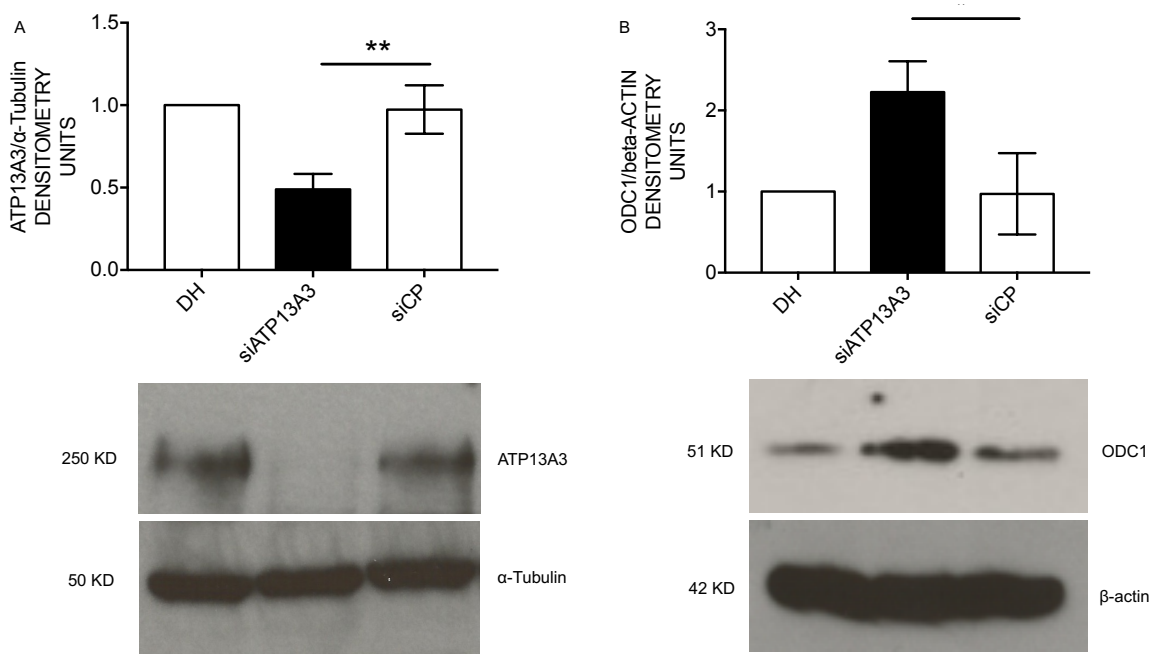

Figure 4-20 ATP13A3 depletion upregulates ODC1 protein expression in human pulmonary artery endothelial cells

Immunoblotting of (A) ATP13A3 (B) ODC1 in cell lysates harvested from hPAECs 48-hours post-transfection of DharmaFECT1(DH1) alone, si*ATP13A3* or non-targeting siRNA control (siCP) (N=3). Densitometric analysis of ATP13A3 and ODC are presented as fold change relative to α-tubulin and β-actin respectively and further normalised to DH1. Mean ± SEM are shown and data were analysed using a One-way ANOVA with Tukey's post hoc test for multiple comparisons. *P<0.05, **P<0.01 compared to siCP.

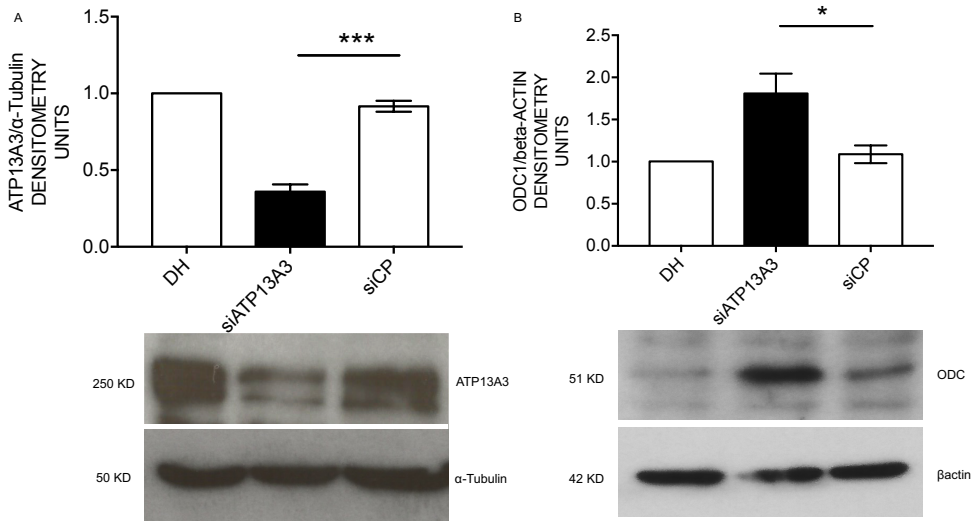

Figure 4-21 *ATP13A3* depletion upregulates ODC1 protein expression in human blood outgrowth endothelial cells

Immunoblotting of (A) ATP13A3 (B) ODC1 in BOECs 48-hours post-transfection (N=3). Densitometry analysis of ATP13A3 and ODC are presented as fold change relative to α-tubulin and β-actin respectively and further normalised to DH1. Mean ± SEM are shown and data were analysed using a One-way ANOVA with Tukey's post hoc test for multiple comparisons. *P<0.05, ***P<0.001 compared to siCP.

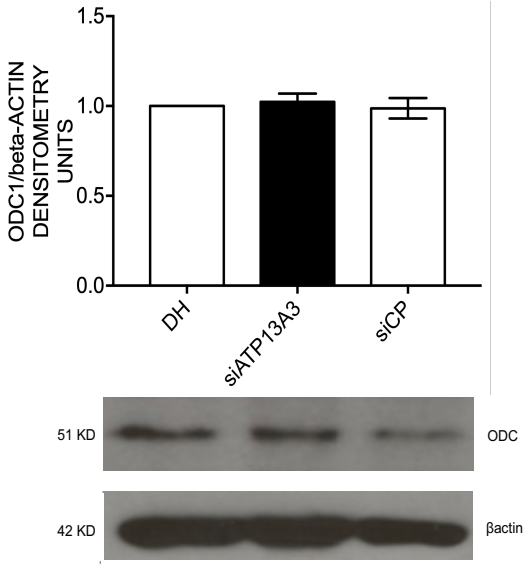

Figure 4-22 ATP13A3 depletion does not alter ODC protein expression in human pulmonary artery smooth muscle cells

Immunoblotting of ODC and βactin in hPASMCs 48-hours post-transfection (N=3). Densitometry analysis of ODC are presented as fold change relative to β-actin and further normalised to DH1. Mean ± SEM are shown and data were analysed using a One-way ANOVA with Tukey's post hoc test for multiple comparisons.

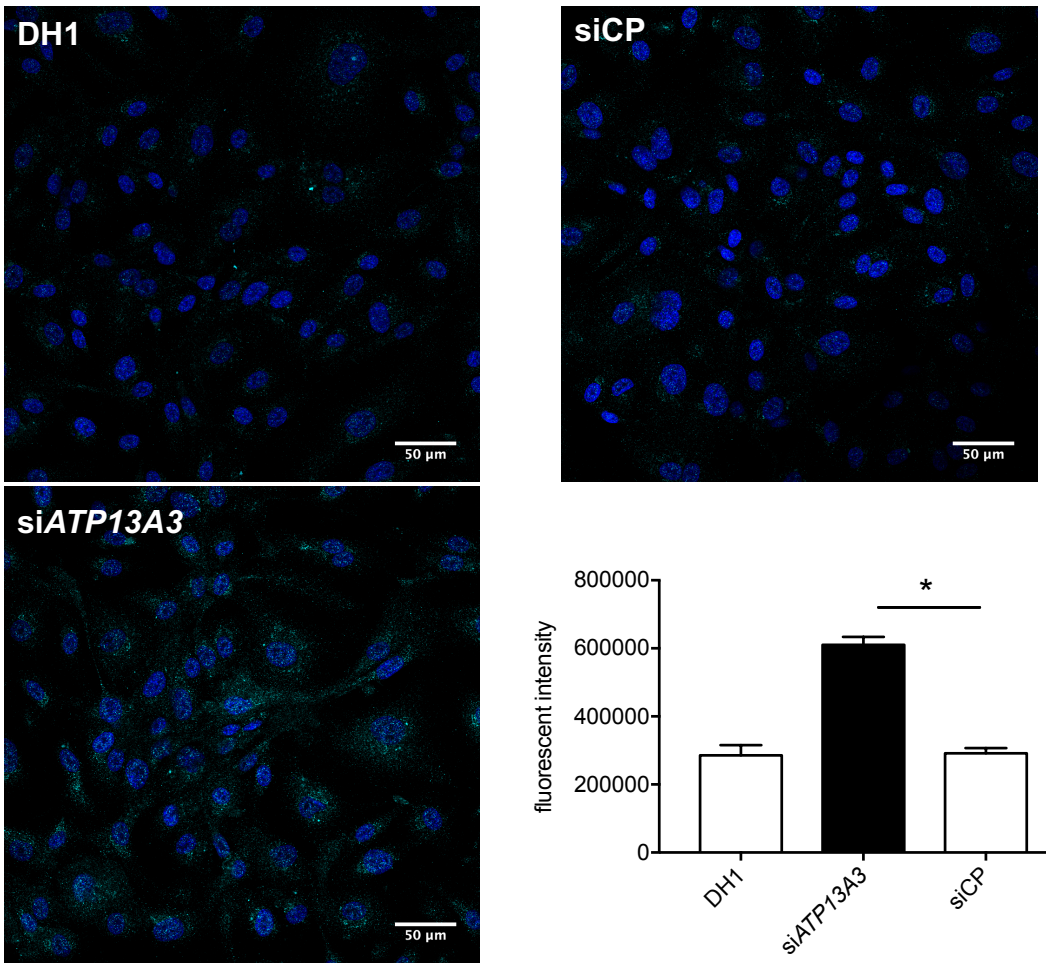

Figure 4-23 Immunofluorescent staining of ODC in human pulmonary artery endothelial cells (hPAECs)

hPAECs were transfected with DharmaFECT1(DH1) alone, si*ATP13A3* or non-targeting siRNA control (siCP) before staining with mouse anti-Ornithine Decarboxylase/ODC (abcam 1:100) and rabbit anti-mouse Alexa Fluor®488 (1:100) Representative images were taken at 20X (N=3). Fluorescent intensity was quantified using ImageJ. Data were analysed using a One-way ANOVA with Tukey's post hoc test for multiple comparisons. *P<0.05, compared to siCP.

4.2.3.3 Ornithine exacerbates apoptosis by promoting putrescine accumulation in hPAECs lacking *ATP13A3*

Polyamine biosynthesis is initiated by converting ornithine into putrescine with ODC. The induction of ODC has been demonstrated to contribute to the apoptosis of CEM T leukaemia cells [308]. Upregulation of ODC was also observed in cardiomyocytes under ischemic conditions, leading to an increase of apoptosis [309]. It has been shown (Chapter 3) that *ATP13A3* deficiency led to endothelial cells apoptosis, which was accompanied by ODC overproduction. Therefore, I questioned whether ODC is involved in this apoptotic phenotype. As shown in Figure 4.24 A, overnight Ornithine incubation did not induce apoptosis in hPAECs (DH1 or siCP) with normal *ATP13A3* expression levels. However, when transfected with si*ATP13A3*, hPAECs displayed a dose-dependent increase of apoptosis in response to ornithine incubation. To assess if this was due to aberrant polyamine homeostasis, the cellular polyamine contents of hPAECs incubated with 10mM ornithine were measured by LC-MS. As illustrated in Figure 4-23, exogenous ornithine substantially increased (~2 fold) putrescine content in *ATP13A3*-deficient cells, whereas hPAECs with normal *ATP13A3* expression (DH1 and siCP) were less affected (Figure 4-23 B). Spermidine and spermine, however, remained lower in si*ATP13A3* transfected hPAECs without being affected by ornithine incubation. Interestingly, DFMO by inhibiting ODC activities only neutralised the apoptosis induced by exogenous ornithine but not the basal apoptosis triggered by si*ATP13A3* in hPAECs (Figure 4-25).

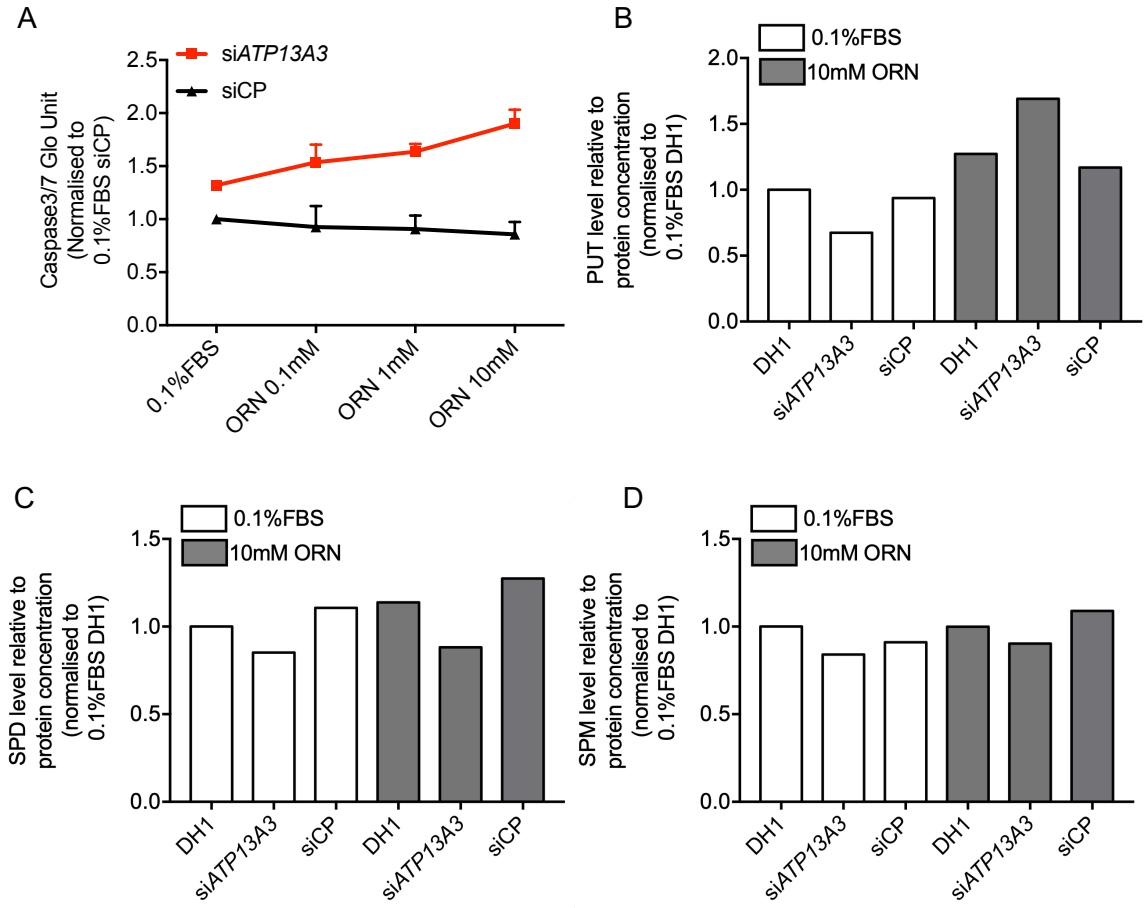

Figure 4-24 Ornithine exacerbates apoptosis by mediating putrescine accumulation in hPAECs lacking ATP13A3

(A) hPAECs transfected with si*ATP13A3* or non-targeting siRNA control (siCP) were incubated with 0.1-10mM of ornithine overnight and assessed for cellular caspase activities (N=2). Data are presented as fold changes normalised to siCP in 0.1%FBS. hPAECs were incubated overnight with 10mM ornithine and assessed for cellular (B) putrescine, (C) spermidine and (D) spermine by LC-MS (N=1). Data are presented as levels relative to protein concentration and further normalised to DH1 in 0.1%FBS.

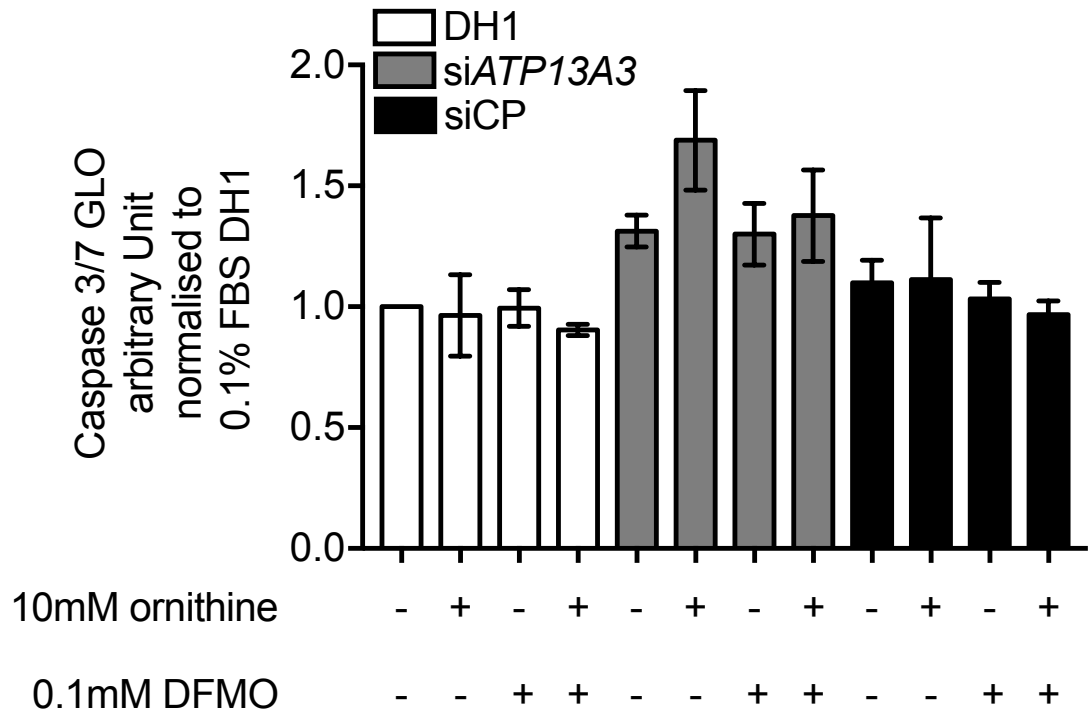

Figure 4-25 DFMO alleviates ornithine-induced apoptosis in hPAECs

hPAECs transfected with DharmaFECT1(DH1) alone, si*ATP13A3* or non-targeting siRNA control (siCP) were cultured in 0.1%FBS EBM2 with or without the presence of 10mM ornithine, 100μM DFMO or in combination overnight. Cellular caspase activity was assessed in the following morning as described in chapter 2.3.3 (N=2). Data are presented as fold change normalised to DH1 hPAECs cultured in 0.1%FBS EBM2.

4.2.4 Characterisation of a BOEC line derived from a PAH patient with a germ-line ATP13A3 mutation

ATP13A3 mutations have previously been identified as being associated with PAH [27]. As described above, ATP13A3 is likely to function as a polyamine transporter in maintaining endothelial cell homeostasis. Polyamine uptake analysis in hPAECs has revealed that polyamine transport capacity is impaired in *ATP13A3* mutants with polyamines. A limitation of my studies up to this point is that they were reliant on overexpression and knockdown studies. Therefore, to further validate my observations in the context of endogenous ATP13A3 mutations, a mutant BOEC line was generated from a PAH patient bearing a heterozygous frameshift mutation (LK726X, c.2176_2180delTTAAA) in *ATP13A3*. The genotype of *ATP13A3*^{LK726X} BOECs was confirmed by Sanger sequencing (Figure 4-26)

4.2.4.1 *ATP13A3*-LK726X frameshift mutation is likely to cause nonsense-mediated mRNA decay (NMD)

Nonsense-mediated mRNA decay (NMD) is a cellular surveillance mechanism that selectively eliminates genetically defective mRNA with premature terminate codon induced by nonsense or frameshift mutations. In comparison to wild type BOECs, *ATP13A3*^{LK726X} BOECs displayed overlapping peaks at the mutation site in both genomic DNA (gDNA) and cDNA sequencing chromatograms (Figure 4-27), indicating a mismatch of the wild type and mutant allele. Interestingly, the ratio of mutant peak height/WT allele peak height (~1/5) in the *ATP13A3*-LK726X cDNA chromatogram was lower than that of in the gDNA (~1/2). The difference in peak height ratios suggests the degradation of mutant mRNA transcripts mediated by NMD.

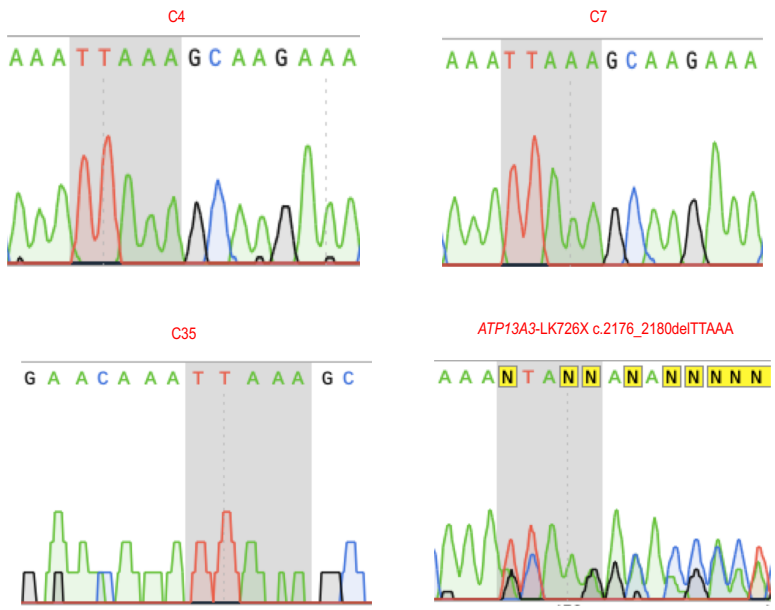

Figure 4-26 Genotyping of control and ATP13A3^{LK726X} BOECs

Sanger sequencing data of the PCR products amplified from the genomic DNA of control BOECs (C4, C7, C35) and *ATP13A3*^{LK726X} BOECs using the strategy described in the material and method section. *ATP13A3*^{LK726X} BOECs showed the heterozygous deletion of TTAAA at the mutation site.

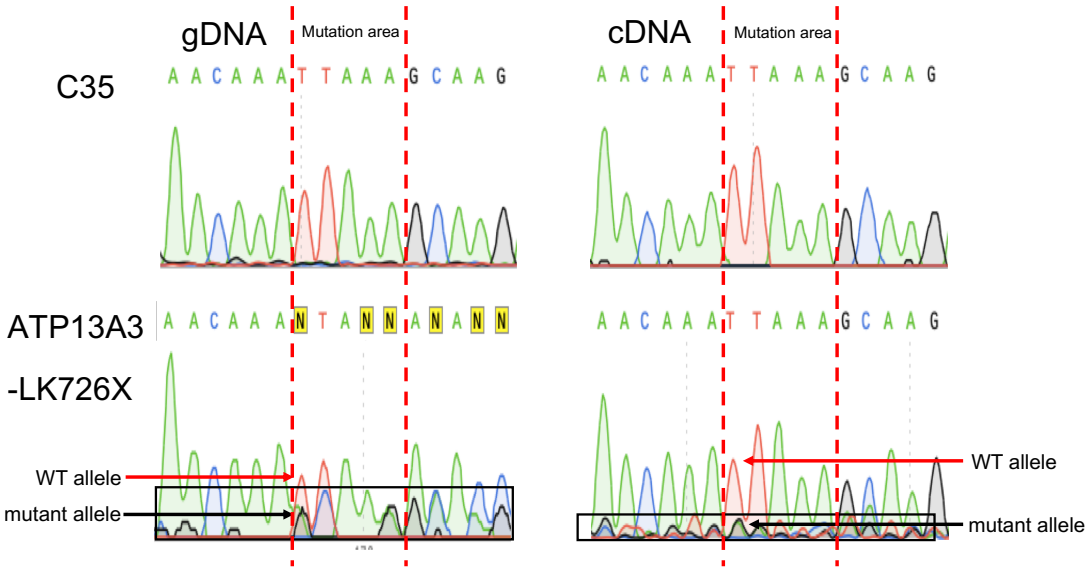

Figure 4-27 ATP13A3-LK726X frameshift mutation may induce nonsense-mediated mRNA decay (NMD) in BOECs

Sanger sequencing data of the PCR products amplified from the genomic DNA (gDNA) and cDNA of control BOECs (C35) and *ATP13A3*^{LK726X} BOECs using the strategy described in the material and methods section. Wild type (WT) and mutant alleles are indicated by red and black arrow respectively.

4.2.4.2 *ATP13A3*^{LK726X} BOECs showed reduced protein and mRNA expression of *ATP13A3*

The frameshift mutation LK726X creates a premature stop codon (TGA 733X) in *ATP13A3* and was therefore predicted to disrupt its mRNA expression through nonsense-mediated decay (NMD) (Figure 4-27). To assess this, three control BOECs lines derived from healthy volunteers (Chapter 2) were used for comparing ATP13A3 protein and mRNA expression with *ATP13A3*-LK726X BOEC line. Consistent with the hypothesis, mutant BOECs showed approximately 60% less *ATP13A3* mRNA compared to the control lines, suggesting this mutation leads to haploinsufficiency. The *ATP13A3* protein level in LK726X BOECs was also lower than that in (~1/3) control BOEC lines. Comparison of the mRNA expression of other P5-ATPases revealed no apparent difference between control and mutant (LK726X) BOECs (Figure 4-30).

4.2.4.3 LK726X frameshift mutation impairs polyamine homeostasis in BOECs

I then questioned if LK726X mutation also impaired ATP13A3 mediated polyamine uptake in BOECs. To assess this, mutant (LK726X) and control BOECs were cultured with or without the presence of 1mM putrescine, 10μM spermidine, or 10μM spermine overnight before measured for cellular polyamines. Similar to the findings in *ATP13A3*-deficient control endothelial cells (Figure 4-8), LK726X, by causing ATP13A3 reduction, also significantly impaired the putrescine uptake without affecting spermidine and spermine levels (Figure 4-29). Interestingly, unlike si*ATP13A3* which affected basal level of all polyamine types, *ATP13A3*^{LK726X} BOECs only exhibited lower putrescine level compared with control BOECs (Figure 4-29). Again, this is likely to be an ATP13A3-specific effect, as *P5B-ATPases* mRNA of *ATP13A3*^{LK726X} BOECs was similar to those of the control lines (Figure 4-30).

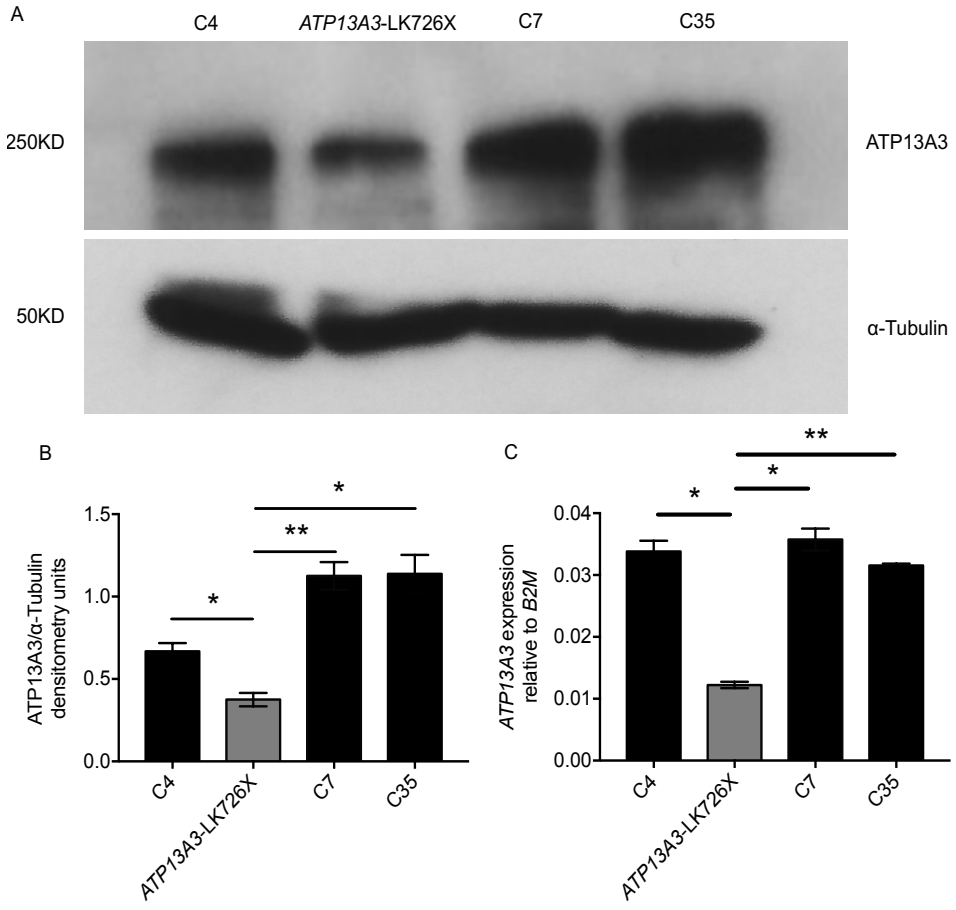

Figure 4-28 ATP13A3^{LK726X} BOECs showed reduced level of protein and mRNA expression of ATP13A3

(A) immunoblotting of ATP13A3 and α-Tubulin in control BOEC lines (C4, C7, C35) and ATP13A3-LK726X BOEC line (n=3). (B) Densitometric analysis of ATP13A3 are presented as fold change relative to α -Tubulin. Mean ± SEM are shown and data were analysed using a One-way ANOVA with Tukey's post hoc test for multiple comparisons. (C)mRNA expression of ATP13A3 are presented as fold change relative to B2M expression. Mean ± SEM are shown and data were analysed using a One-way ANOVA with Tukey's post hoc test for multiple comparisons. *P<0.05, **P<0.01 compared to ATP13A3-LK726X.

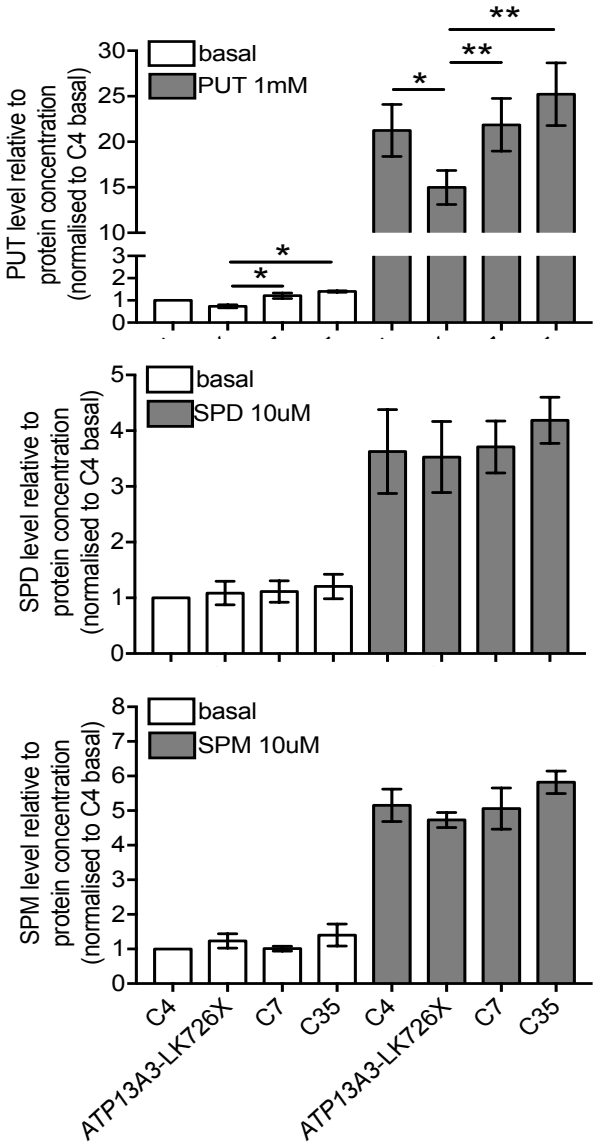

Figure 4-29 LK726X frameshift mutation impairs polyamine homeostasis in BOECs

Mutant (LK726X) or control BOECs were cultured with or without the addition of 1mM putrescine, 10μM spermidine, or 10μM spermine overnight before measured for cellular Putrescine (A), Spermidine (B), or (C) Spermine by Liquid chromatography-mass spectrometry (LC-MS). (N=3). Data are presented as polyamine peak area ratio relative to sample protein concentration, and further normalised to C4 control BOECs. One-way ANOVA was used for statistical analysis among different BOECs with or without polyamine supplement. *P<0.05 **P<0.01 compared with *ATP13A3*-LK726X BOECs.

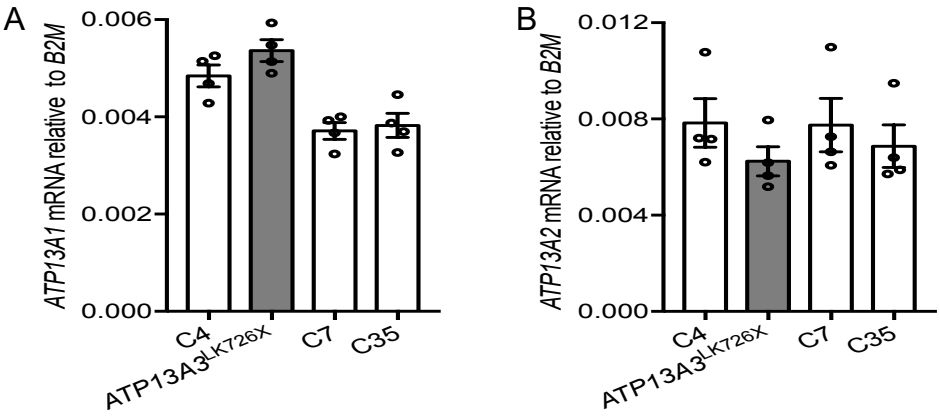

Figure 4-30 *ATP13A1, ATP13A2* mRNA expression in control and ATP13A3^{LK726X} BOECs

(A) ATP13A1, (B) ATP13A2 mRNA expression was assessed in control BOECs (C4, C7, C35) from healthy subjects and the ATP13A3-LK726X BOEC line (n=4). Data are presented as relative expression normalised to B2M expression. Mean ± SEM are shown and data were analysed using a One-way ANOVA with Tukey's post hoc test for multiple comparisons.

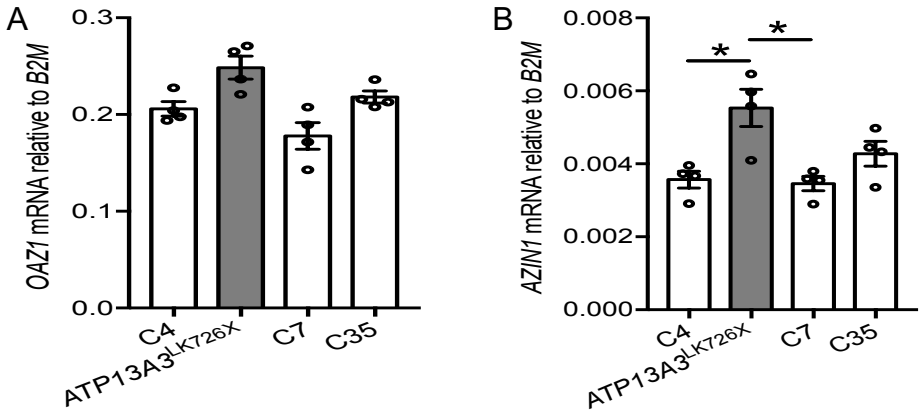

Figure 4-31 *OAZ1, AZIN1* mRNA expression in control and ATP13A3^{LK726X} BOECs

(A) antizyme (OAZ1) (B) AZIN1 (Antizyme inhibitor) mRNA expression was assessed in control BOECs (C4, C7, C35) from healthy subjects and the ATP13A3-LK726X BOEC line (n=4). Data are presented as relative expression normalised to B2M expression.

4.2.4.4 *ATP13A3*^{LK726X} BOECs display increased *ODC1* mRNA and protein expression

I demonstrated earlier in this chapter that *ATP13A3* deficiency could upregulate ODC1 protein in BOECs (Figure 4-21). Since *ATP13A3*^{LK726X} BOECs exhibited impaired ATP13A3 expression, I then questioned if ODC was also altered as a result of ATP13A3 reduction in these mutant BOECs. Unlike transient *ATP13A3* knockdown in BOECs, which post-translationally upregulated ODC1 protein expression, *ATP13A3*^{LK726X} BOECs also showed an average of ~50% higher *ODC1* mRNA expression than control BOECs (Figure 4-32 C). ODC1 protein level was also increased by approximately 2-fold (Figure 4-32 A, B). Different from the observation in si*ATP13A3* transfected control BOECs., antizyme mRNA level was comparable among *ATP13A3*^{LK726X} BOECs and control BOECs (Figure 4-31). Interestingly, higher mRNA expression of antizyme inhibitor (*AZIN1*) was observed in *ATP13A3*^{LK726X} BOECs (Figure 4-31).

4.2.4.5 *ATP13A3*^{LK726X} BOECs showed increased expression of polyamine biosynthesis enzymes

ATP13A3 deficiency (achieved by siRNA transfection) has been demonstrated to polyamine related enzymes in endothelial cells (Figure 4-16, 4-17). To further characterise the LK726X frameshift mutation, mRNA expression of these enzymes was assessed in both *ATP13A3*^{LK726X} and control BOECs. Opposite to the expectation, both adenosylmethionine decarboxylase (*AMD1*) and spermidine synthase (*SRM*) were upregulated by ~ 2-fold in *ATP13A3*^{LK726X} BOECs (Figure 4-33 B, C). spermine synthase (*SMS*) was ~70% higher in LK726X mutant BOECs (Figure 4-33 D). *Arginase* 1 mRNA expression was also slightly elevated (~30%) in LK726X BOECs though the expression level of control BOECs was variable (Figure 4-33 A). In comparison, expression of polyamine catabolic enzymes, namely spermidine/spermine acetyltransferase 1 (*SAT1*), polyamine oxidase (*PAO*) and spermine oxidase

(*SMOX*) were only marginally different among *ATP13A3*^{LK726X} and control BOECs (Figure 4-34). Taken together, LK726X BOECs displayed in general a higher level of biosynthesis enzyme while the expression of the catabolic enzyme remained similar to control BOECs.

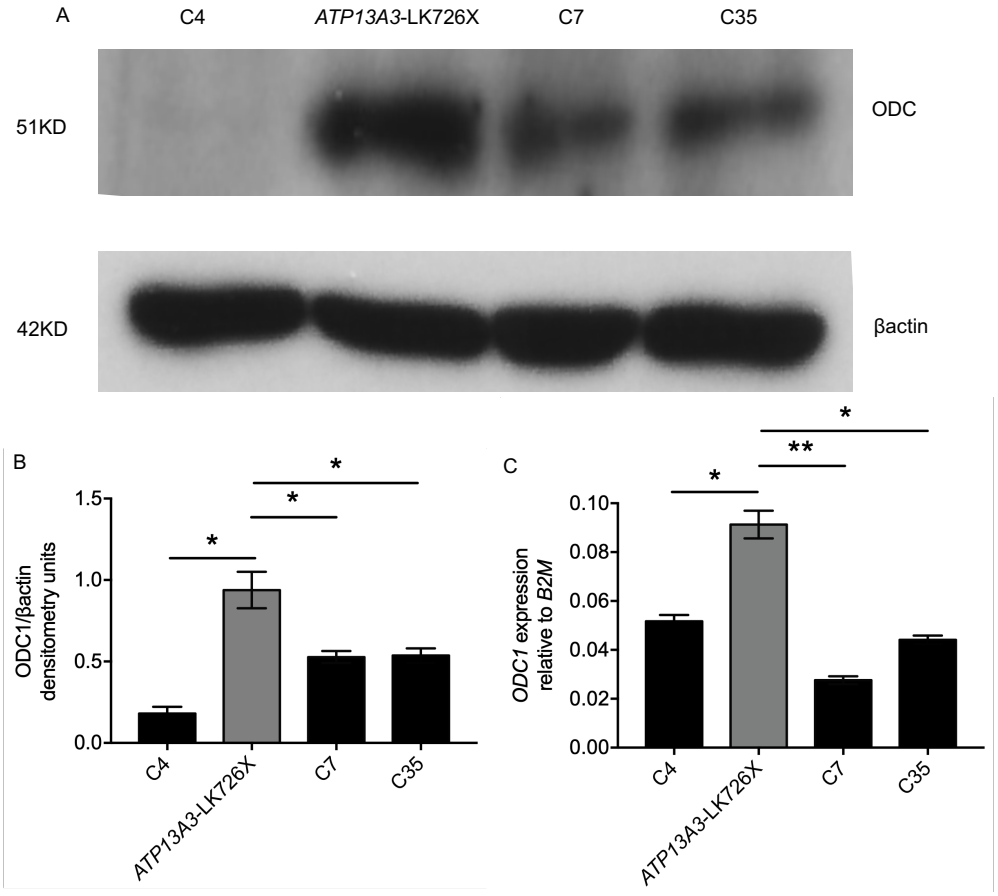

Figure 4-32 *ATP13A3*^{LK726X} BOECs displayed increased ODC1 protein and mRNA expression levels

(A) immunoblotting of ODC1, β-actin in control (C4, C7, C35) and *ATP13A3*^{LK726X} BOEC line (n=3). (B) Densitometry analyses of ODC1 are presented as fold changes relative to β-actin. Mean ± SEM are shown and data were analysed using a One-way ANOVA with Tukey's post hoc test for multiple comparisons. (C)mRNA expression of *ODC1* is presented as fold change relative to *B2M* expression. Mean ± SEM are shown and data were analysed using a One-way ANOVA with Tukey's post hoc test for multiple comparisons. *P<0.05, **P<0.01 compared to *ATP13A3*^{LK726X} BOEC.

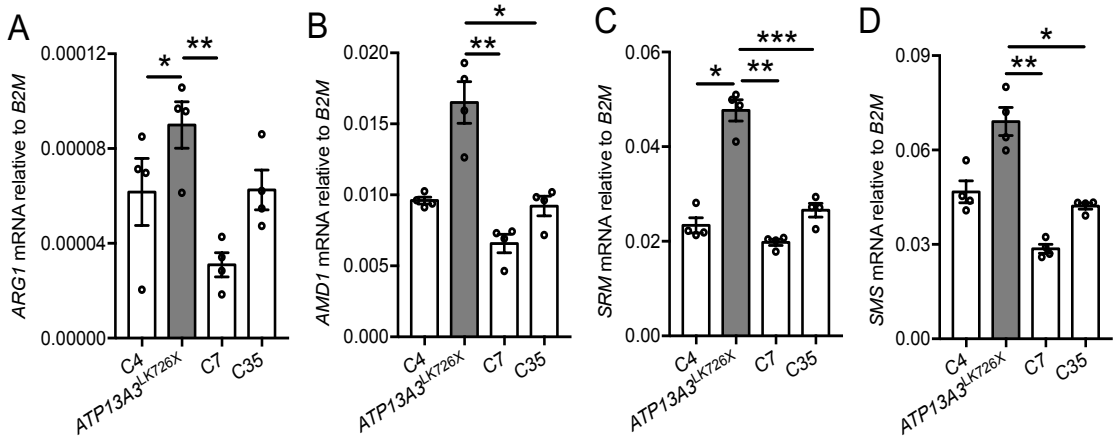

Figure 4-33 *ATP13A3*^{LK726X} BOECs display increased mRNA expression of polyamine biosynthesis enzymes.

mRNA expression of polyamine biosynthesis related enzymes (A) Arginase 1 (ARG1) (B) Adenosylmethionine decarboxylase (AMD1) (C) Spermidine synthase (SRM) (D) spermine synthase (SMS) in control BOEC lines (C4, C7, C35) and ATP13A3-LK726X BOEC line (n=2). Data are presented as fold change relative to *B2M*. Mean ± SEM are shown and data were analysed using a One-way ANOVA with Tukey's post hoc test for multiple comparisons. *P<0.05, **P<0.01, ***P<0.01 compared to ATP13A3LK726X BOEC.

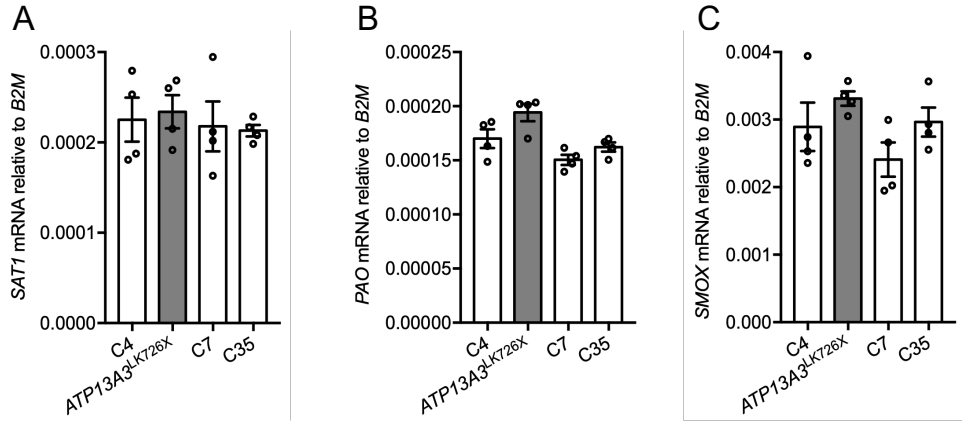

Figure 4-34 *ATP13A3*^{LK726X} BOECs displayed increased mRNA expression of polyamine biosynthesis enzymes

mRNA expression of polyamine catabolic enzymes (A) Spermidine/spermine acetyltransferase1 (SAT1) (B) polyamine oxidase (PAO) (C) Spermine oxidase (SMOX) in control BOEC lines (C4, C7, C35) and ATP13A3-LK726X BOEC line (n=2). Data are presented as fold changes relative to *B2M*. Mean ± SEM are shown and data were analysed using a One-way ANOVA with Tukey's post hoc test for multiple comparisons.

4.2.4.6 *ATP13A3*^{LK726X} BOECs displayed higher sensitivity to serum-deprivation induced apoptosis

Having shown that the LK726X frameshift mutation causes *ATP13A3* reduction in BOECs, I then questioned if this predisposes cells to apoptosis. As shown in Figure 4-35 A, when grown in EGM2 supplemented with 10% FBS, *ATP13A3*^{LK726X} BOECs displayed similar cellular caspase activity to control BOECs. Increased caspase activity was observed in BOECs cultured in EBM2 supplemented with 5% FBS, with no significant difference among mutant and control BOECs (Figure 4-35 B). When further exposed to serum-free condition (0.1% FBS EBM2), the caspase activity of *ATP13A3*^{LK726X} BOECs was significantly higher than that of the control BOECs (C35), similar to that observed in si*ATP13A3* transfected BOECs (Figure 4-35 C).

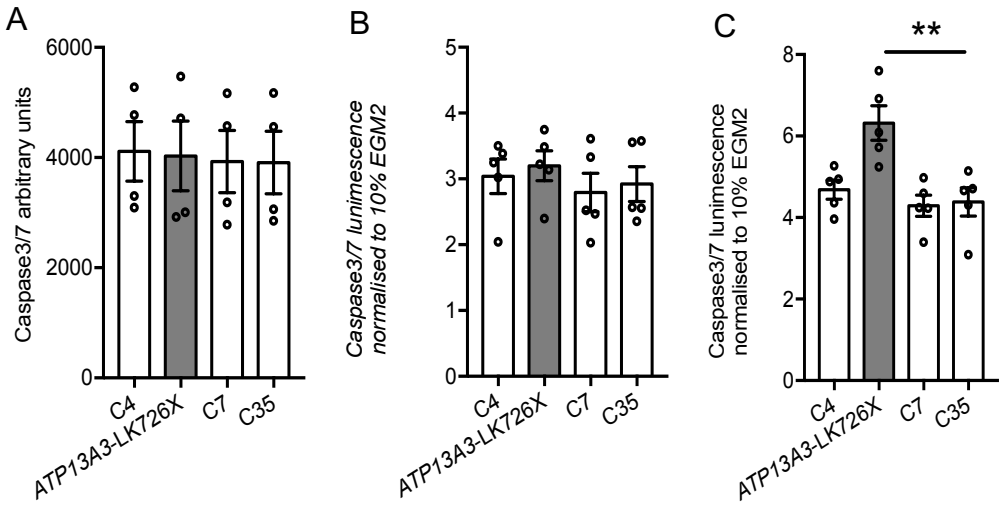

Figure 4-35 *ATP13A3*^{LK726X} BOECs display higher sensitivity to serum-deprivation induced apoptosis

Cellular caspase activity of BOECs cultured in (A) 10% EGM2 (B) 5% EBM2 and (C) 0.1% EBM2 was assessed by Caspase3/7 Glo kit (Promega) (n=3). Data in (A) are presented as raw arbitrary units. Data in (B) and (C) are presented as fold changes relative to the corresponding caspase activity in (A). Mean ± SEM are shown and data were analysed using a One-way ANOVA with Tukey's post hoc test for multiple comparisons. **P<0.01, compared to *ATP13A3*^{LK726X} BOECs.

4.3 Discussion

In this result section, I have demonstrated that ATP13A3 functions as a polyamine transporter in endothelial cells and reveal functional impairments of PAH-associated mutations on ATP13A3 mediated polyamine uptake.

Similar to the previous findings in Hela cells [141], subcellular localisation analysis revealed ATP13A3 as residing in the recycling endosome (Rab11) of endothelial cells. Mammalian polyamine transport systems are extremely understudied. The endocytic pathway has been proposed as one potential route for mediating cellular polyamine trafficking [190]. In line with this theory, here I have observed that *ATP13A3* deficiency in endothelial cells substantially reduced the basal levels of putrescine and the uptake of exogenous putrescine. Basal spermidine and spermine contents were also reduced, but to a lesser extent in si*ATP13A3* hPAECs while the uptake capacity remained relatively intact. These observations, provide strong evidence for ATP13A3 as a polyamine transporter with a higher selectivity towards putrescine than spermidine and spermine in endothelial cells. Different to my findings, *ATP13A3* levels were previously shown correlating to spermidine uptake in pancreatic cancer cells [147]. However, the authors did not rule out the possibility of spermidine transport activities being affected by other P5-ATPases. Previously, in silico analysis of P5B-ATPases protein sequences revealed a conserved putative substrate-binding region [134], suggesting similar transport substrates may be shared. However, the fact that ATP13A2 mainly transport spermine in neuron cells [148] while ATP13A3 mediates putrescine translocation in endothelial cells reveals the complexity of the transport activities of P5-ATPases, which may be cell-type dependent.

In addition to the transport systems, cellular polyamine content is also fine-tuned by the metabolism pathways. Transient *ATP13A3* knockdown significantly reduced polyamine content in endothelial cells, predominantly

affecting putrescine level. As a potential compensatory mechanism, endothelial cells activate their polyamine biosynthesis pathway by post-translationally upregulating ODC1. This is likely achieved via the downregulation of *OAZ1* mRNA, which preserves ODC expression by suppressing proteasomal degradation. Interestingly, increased Odc activity was reported in MCT treated rat lung tissues, with DFMO, the irreversible ODC inhibitor, blunted the RVSP elevation [255]. This suggests a pathogenic role of ODC elevation in PAH and also indicates a possible involvement of *ATP13A3* deficiency in PAH pathogenesis. Other biosynthesis enzymes such as spermidine synthase (*SRM*) and spermine synthase (*SMS*) mRNA were also reduced by *ATP13A3* deficiency, possibly in compensation for the precursor (putrescine) loss. This also partially explains the basal reduction of spermidine and spermine by *ATP13A3* reduction in hPAECs.

Polyamines are essential for cell growth. Elevated polyamine level sustains hyperproliferation in cancer cells [104, 171] while depletion of the polyamine pool causes cell cycle arrest in different phases [105, 191, 228]. In line with this theory, we have observed that *ATP13A3* deficiency, by reducing cellular polyamine contents, suppressed vascular cell proliferation and caused downregulation of *cyclin A, E and B* mRNA expression in BOECs. The reduction of these cyclins, but not cyclin D, suggests a degree of repression on G1-S transition and DNA synthesis. Aside from affecting cell growth, polyamines were also revealed in the regulation of cell apoptosis. Flavonoid was previously reported causing DNA fragmentation in HL-60 cells by reducing putrescine and cells with higher putrescine levels were resistant to this stimulus [310]. Moreover, etoposide by causing polyamine depletion activated NF-κB and increased caspase activity in fibroblasts [311]. Coincide with these findings, I have also observed that *ATP13A3* deficiency predisposed hPAECs to apoptosis (chapter3), suggesting a protective role of polyamine to endothelial cell viability. Another potential interpretation for the apoptosis driven by

ATP13A3 deficiency is the overproduction of ODC. It was demonstrated that increased ODC contributed to the apoptosis of CEM T leukaemia cells [308]. Also, Ischemia can cause cardiomyocyte apoptosis by ODC upregulation [309]. Interestingly, here my preliminary data also show upregulated ODC in *ATP13A3*-deficient hPAECs while ornithine supplementation can exaggerate their apoptosis. However, DFMO co-administration only partially reversed the cell apoptosis, suggesting the basal apoptosis increase observed in *ATP13A3* deficient endothelial cells is more likely caused by the polyamine loss. In addition to cell growth and apoptosis, polyamines were also demonstrated essential for cell-cell junctions. Polyamine depletion was shown to induce permeability in human small intestine epithelial cells by affecting the expression of E-Cadherin [244] and occludins [245]. Similarly, here we also observed that loss of *ATP13A3* in hPAECs exacerbated endothelial leakage in the presence of thrombin stimulation, indicating an important role of *ATP13A3* in maintaining endothelial integrity under pathogenic conditions.

ATP13A3 was previously identified as a novel PAH associated gene [27]. Functional assessment of deleterious missense variants revealed L675V, M850I, V885M as severe pathogenic modifiers causing impairments on ATP13A3 mediated putrescine uptake. This provides strong evidence for the involvement of ATP13A3 genetic defects in PAH pathogenesis. The impairments of other two variants (R858H, L965P) on the putrescine transport were milder. The variable effects of *ATP13A3* mutations suggest other modifiers may participate in disease progression. Interestingly, Lerche M et al.[109] has recently reported that an IFN-β induced PAH case in a multiple sclerosis patient with a nonsense *ATP13A3* mutation (Glu514*). The fact that IFN-β withdrawal improved PAH symptoms in this patient suggests that additional factors, such as aberrant inflammation, may confer PAH development in *ATP13A3* mutation carriers. One disadvantage of using the overexpression system for characterising the impact of mutations is that it may

not fully represent the endogenous biological state. To overcome this, BOECs were generated from a PAH patient bearing a frameshift mutation (LK726X) in *ATP13A3*. Interestingly, LK726X frameshift mutation disrupted ATP13A3 expression by causing NMD. As a result, mutant BOECs exhibited lower basal putrescine level and uptake capacity, predisposing cells to apoptosis under serum-free condition [27]. Similar to ATP13A3-deficient control BOECs, ODC protein expression was also significantly increased in LK726X BOECs, further indicating a regulatory role of ATP13A3 on ODC. Moreover, the polyamine synthesis pathway in LK726X BOECs was also activated, as manifested by the elevated mRNA expression of *ODC1*, *AMD1, SRM, SMS*. The increased *SRM* and *SMS* mRNA may have exaggerated the putrescine loss by consuming more putrescine to produce spermidine and spermine. This may partially explain the basal reduction of putrescine but not spermidine or spermine observed in LK726X BOECs. However, it is noteworthy that cells derived from PAH-patients may have acquired some changes due to the somatic changes associated with the disease state leading to additional DNA damage. This may serve as a rational interpretation for the different transcriptional fingerprints observed in transient *ATP13A3* loss (siRNA transfection) compared the chronic deficiency (genetic defects).

In summary, here I have demonstrated that ATP13A3 functions as a putrescine transporter with its disruption leading to endothelial dysfunctions. PAH associated mutations were shown to impair ATP13A3 mediated polyamine transport, with a frameshift mutation predisposed BOECs to apoptosis by affecting the polyamine homeostasis. These findings provide for the first time a pathogenic link between ATP13A3 genetic defects and PAH and shed lights for the underlying mechanism of polyamine dysregulation in the pathobiology of PAH.

Chapter 5 Results III- Regulation of ATP13A3 by BMPs and inflammatory cytokines

5.1 Introduction

Bone morphogenetic proteins (BMPs) are a group of at least 14 secreted ligands belongs to the transforming growth factor β (TGFβ) superfamily [79]. The first BMPs discovered were identified as calcification inducers in bone [312] while later studies have revealed more family members with a diverse range of functions, including embryogenesis and development [313], metabolism [314, 315]and maintaining homeostasis of the cardiovascular system [79, 316]. These secreted ligands exert cell-specific effects primarily through autocrine and paracrine signalling while ligands such as BMP6, BMP9 and BMP10 also present in the circulation system [285, 317-319]. BMP signalling is initiated by the binding of - BMPs to cell surface heteromeric receptor complexes formed by type II and type I receptors [320, 321]. For BMPs, there are four known Type I receptors and four known Type II receptors, specific combinations of these defining the selectivity for BMPs [322]. This selectivity is further controlled by Type III accessory receptors, such as endoglin [323]. Upon binding of a dimeric BMP ligand to its specific receptor complex, the constitutively active kinase domain of the type II receptor [324] then transphosphorylates the type I receptor, which in turn catalyses C-terminal phosphorylation of the downstream canonical Smad1/5/8 (receptor-regulated Smads(R-Smads)) proteins. Once activated, the R-Smads form a complex with the nuclear chaperone Smad4 and then translocating into the nucleus where they control the transcriptional regulation of target genes [82, 325, 326].

The pathogenesis of PAH is hallmarked by reduced BMP signalling. Genetic analysis in PAH cohorts has revealed disease-associated mutations in several BMP-specific pathway members [27, 102, 103, 327]. Of note, pathogenic mutations in the gene encoding the bone morphogenetic protein type 2 receptor

(BMPR2), a type II receptor for the BMP pathway was identified as the predominant genetic cause, accounting for nearly 80% of the familial PAH [328] and approximately 20% of sporadic cases [329]. Reduced BMPR2 expression in pulmonary vasculature is also observed in PAH patients without genetic defects [16], suggesting a broader role of the BMP pathway in disease pathobiology.

Cell surface receptors of the BMP/TGFβ pathway are constitutively internalised, degraded or recycled through the endo/lysosome system [330]. BMPR2 was demonstrated to be degraded through E3 ligase-mediated lysosomal degradation [331]. Chloroquine was shown to Inhibit this effect, resulting in increases expression of BMPR2 in hPAECs [332, 333]. Rab 11 was reported to mediate the recycling of TGFβ receptor Type II/I, or the receptor complex back to the plasma membrane [334], suggesting an essential role for the recycling endosome in TGFβ/BMP receptor trafficking. Intriguingly, ATP13A3 has been demonstrated to reside in the early/recycling endosome of Hela cells [141]. This points to a potential link between ATP13A3 and endosome functions. Moreover, microarray analysis following 4-hour TGFβ incubation revealed upregulated *ATP13A3* expression in hPASMCs from HPAH patients bearing BMPR2 mutations [165], further suggesting a potential involvement of ATP13A3 in the TGFβ/BMP signalling pathway. Therefore, in this chapter, I will investigate the potential regulation of ATP13A3 by different BMP ligands in pulmonary vascular cells and assess the effects of ATP13A3 deficiency on BMP downstream signalling.

5.2 Results

5.2.1 ATP13A3 and BMP signalling

5.2.1.1 BMP9 and BMP10 selectively induce mRNA expression of ATP13A3, but not other P5-ATPases, in BOECs

To characterise the regulation of *ATP13A3 by* BMP ligands, BOECs were cultured with or without BMP9, BMP10 or BMP6 for 8 hours and assessed for mRNA expression of *ATP13A1-5*. *ATP13A3* mRNA expression, consistent with previous observations, was significantly increased by 8-hour incubation of BMP9 in a dose-dependent manner (Figure 5-1 A). Although *ATP13A3* was not altered by 0.3ng/ml BMP10, it was increased by BMP10 at 1ng/ml. BMP6, on the other hand, did not alter *ATP13A3* expression (Figure 5-1 A). Interestingly, unlike *ATP13A3*, the transcription of *ATP13A1* and *ATP13A2* were only marginally increased by 20% and 15% respectively in response to 1ng/ml BMP9, but not by other BMP ligands (Figure 5-1 C, D). Both *ATP13A4* and *ATP13A5* were expressed at very low levels in vascular cells and there was no response to BMP ligands. Taken together, these results suggested a selective increase of *ATP13A3* mRNA by BMP9 and BMP10.

5.2.1.2 BMP9 and BMP10 induce *ATP13A3* expression in BOECs via the *ALK1* receptor

Given that BMP9 and BMP10 selectively induce *ATP13A3* but not other P5-ATPases in BOECs, I questioned which BMP receptors are involved in this effect. *BMPR2* is abundantly expressed in BOECs and is partially responsible for the BMP9-dependent induction of *ID2* mRNA in endothelial cells [322]. Although *ID2* mRNA induction by 8-hour incubation of 1ng/ml BMP9 was significantly impaired by si*BMPR2* transfection compared to siCP (Figure 5-2 B), BMP9 induced *ATP13A3* mRNA to the same extent in BOECs with or without *BMPR2* deficiency (Figure 5-2 B). I then questioned whether *ALK1*, a type I receptor for BMP9 or BMP10, was involved in *ATP13A3* induction by these BMP ligands. As shown in Figure 5.3, loss of *ALK1* significantly impaired

the induction of *ATP13A3* mRNA by 1ng/ml BMP9. A similar effect was also seen in BOECs incubated with 1ng/ml BMP10, with a lower *ATP13A3* mRNA expression in cells transfected with si*ALK1* (Figure 5-3).

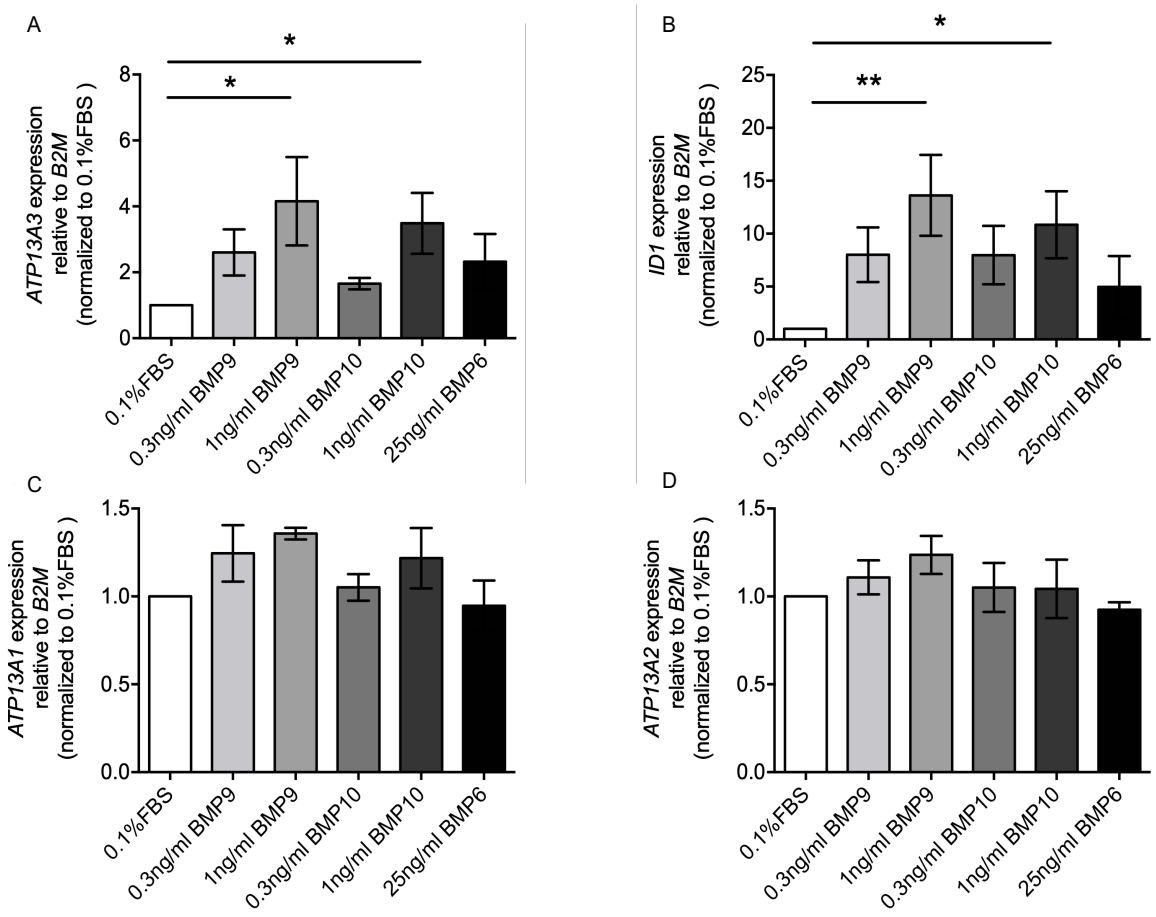

Figure 5-1 Selective up-regulation of ATP13A3 by BMP9 and BMP10 in BOECs

mRNA expression of (A) *ATP13A3,* (B) *ID1,* (C) *ATP13A1,* (D*) ATP13A2,* in response to different concentrations of BMP9, BMP10 and BMP6. BOECs were serum restricted in 0.1% FBS overnight before treating with 0.3ng/ml or 1ng/ml BMP9 or BMP10, or 25ng/ml BMP6 for 8 hours (n=3). Data are presented as fold-change relative to 0.1%FBS. Mean ± SEM was shown. One-way ANOVA with Tukey's post hoc test for multiple comparisons was used for data analysis. *P<0.05, **P<0.01 compared to 0.1% FBS

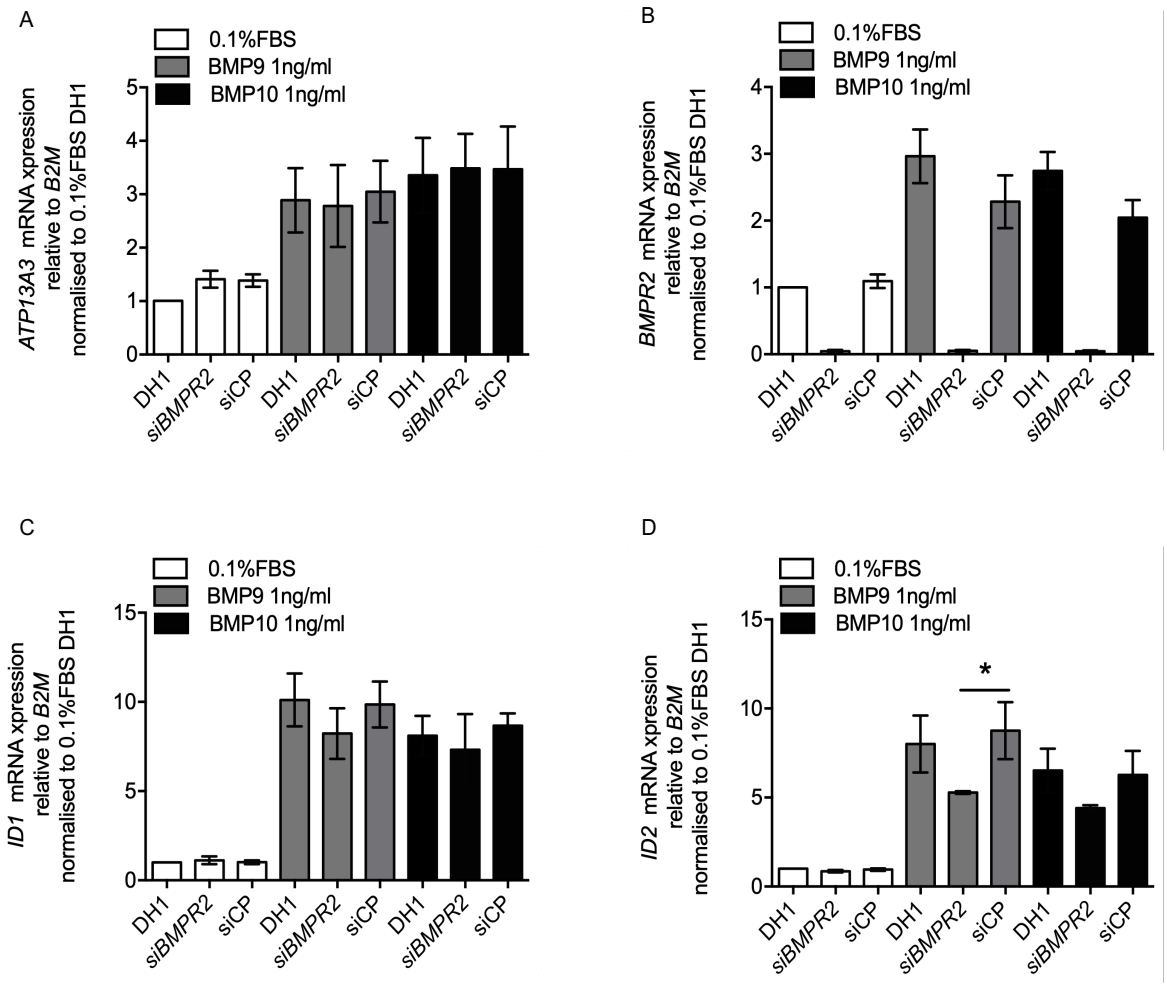

Figure 5-2 BMPR2 knockdown in BOECs does not affect the induction of ATP13A3 mRNA by BMP9 or BMP10

Relative expression of (A) *ATP13A3* (B) *BMPR2*, (C) *ID1,* and (D) *ID2* in BOECs transfected with DharmaFECT1 (DH1) alone, si*BMPR2* or non-targeting siRNA control (siCP) followed by treating with 0.1%FBS with or without the addition of 1ng/ml BMP9 or 1ng/ml BMP10 (n=4). Data are presented as fold-change relative to *B2M* and normalised to DH1. Mean ± SEM was shown. One-way ANOVA with Tukey's post hoc test for multiple comparisons was used for data analysis. *P<0.05, compared to DH1.

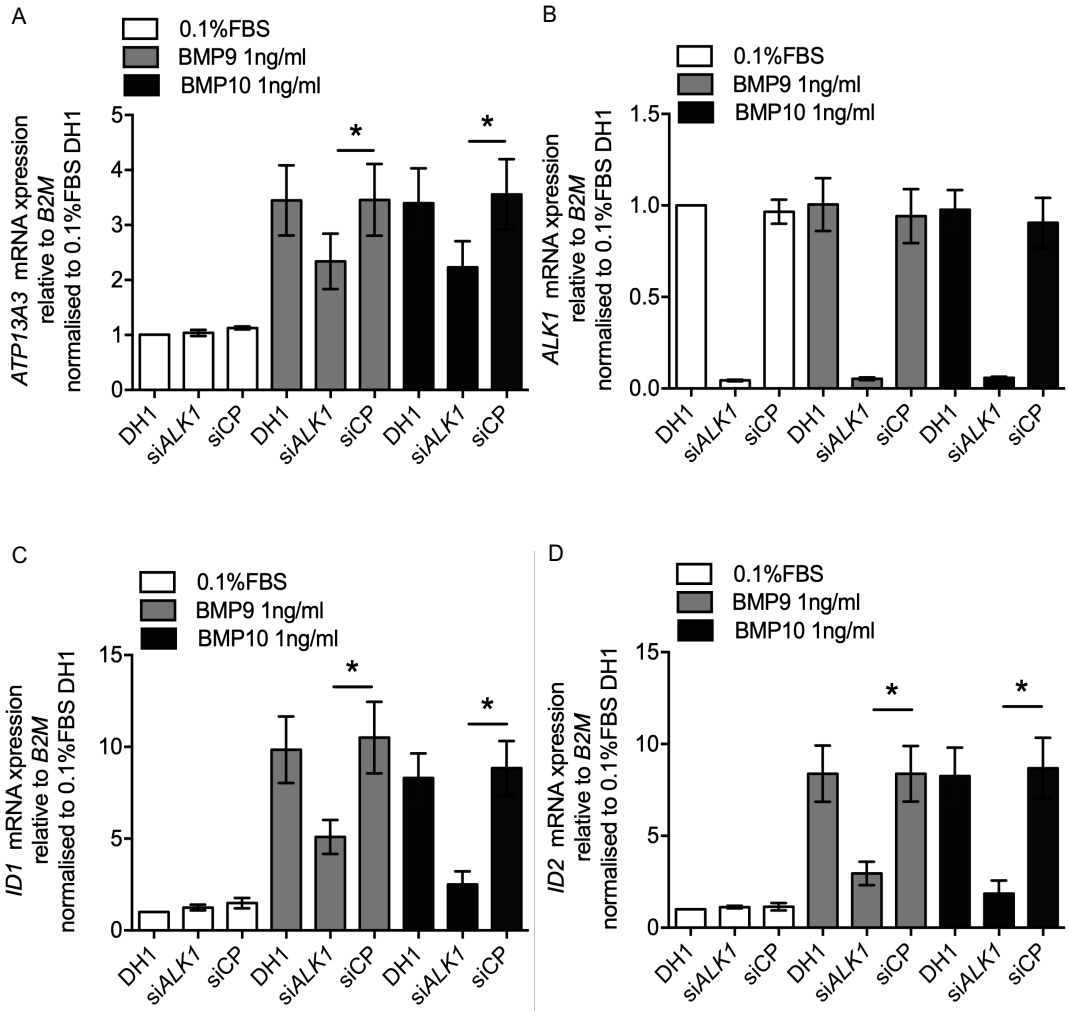

Figure 5-3 ALK-1 deficiency impairs the induction of ATP13A3 mRNA by BMP9 or BMP10 in BOECs

Relative expression of (A) *ATP13A3* (B) *ALK1*, (C) *ID1,* and (D) *ID2* in BOECs transfected with DharmaFECT1 (DH1) alone, si*ALK1* or non-targeting siRNA control (siCP) followed by treating with 0.1%FBS with or without the addition of 1ng/ml BMP9 or 1ng/ml BMP10 (n=4). Data are presented as fold-change relative to *B2M* and normalised to DH1. Mean ± SEM was shown. One-way ANOVA with Tukey's post hoc test for multiple comparisons was used for data analysis. *P<0.05, compared to DH1.

5.2.1.3 *ATP13A3* depletion in endothelial cells did not affect BMP signalling

It is widely acknowledged that the dysregulated BMP signalling contributes to PAH pathogenesis [31, 79]. Receptors of the pathway are actively trafficking from the cell surface into cellular compartments, mediating BMP signalling transduction [330]. As ATP13A3 resides in the recycling endosome and its mRNA could be induced by BMP9/10, I assessed if ATP13A3 deficiency affects BMP signalling in endothelial cells. ATP13A3 deficiency in hPAECs did not alter the mRNA of the BMP type I (ALK1, ALK2) and type II (BMPR2) receptors (Figure 5-4). 8-hour BMP9 treatment induced a concentration-dependent induction of ATP13A3 mRNA expression (Figure 5-5 A). However, ATP13A3 deficiency did not alter the BMP9 mediated ID2 response (figure 5.5 C). The ID1 response to 0.1ng/ml and 0.3ng/ml BMP9 was marginally reduced (10% and 15% respectively) by ATP13A3 deficiency, though no statistical significance was revealed (Figure 5-5 B).

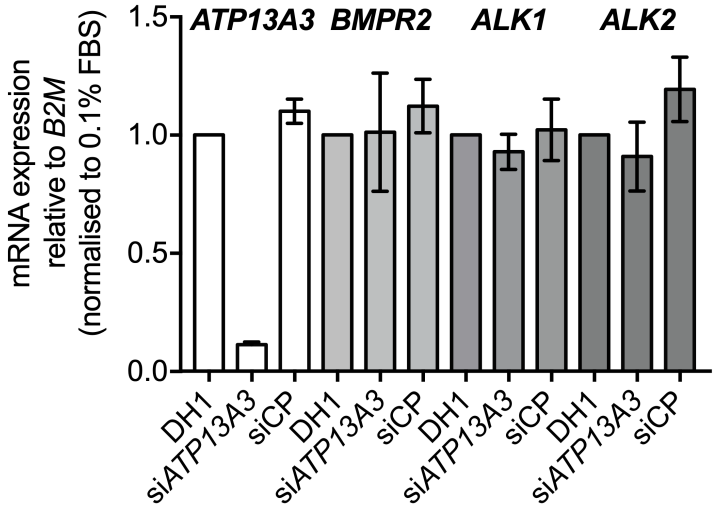

Figure 5-4 ATP13A3 deficiency does not altered mRNA expression of BMP receptors in hPAECs.

mRNA expression of ATP13A3, BMPR2, ALK1 and ALK2 in hPAECs transfected with DH1, siATP13A3 or siCP. Data are presented as fold-change relative to DH1. Mean ± SEM was shown. One-way ANOVA with Tukey's post hoc test for multiple comparisons was used for data analysis. *P<0.05, compared to siCP.

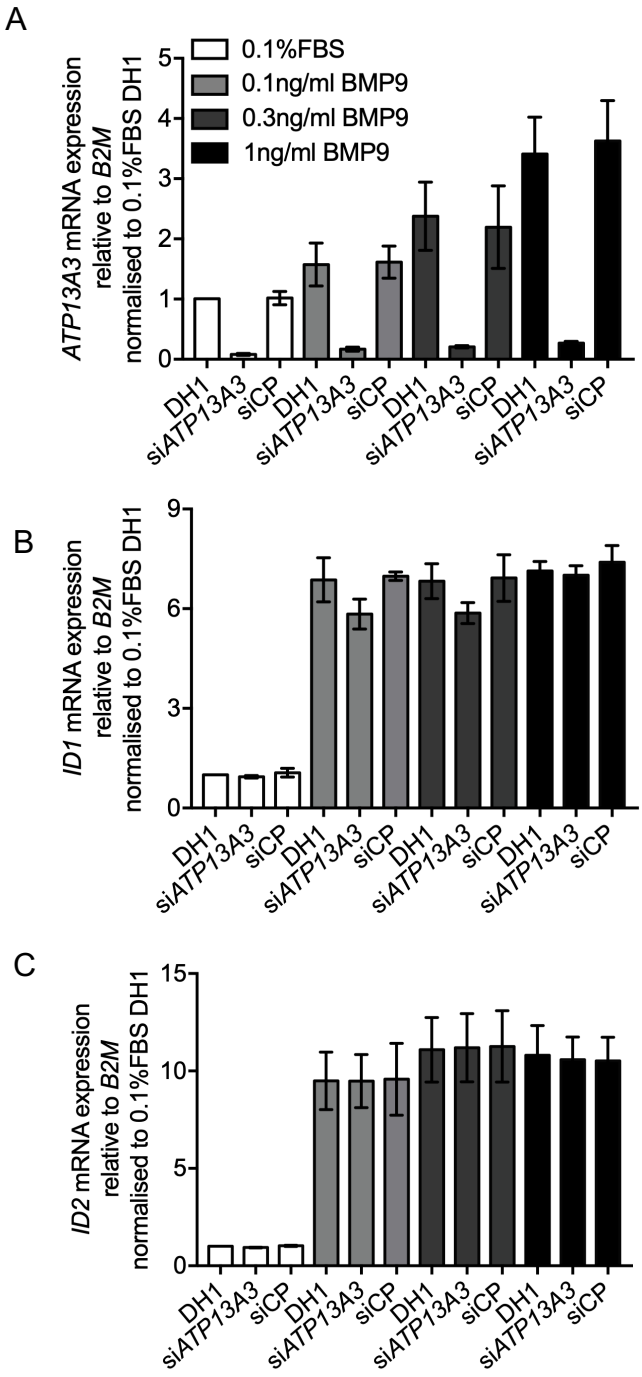

Figure 5-5 *ATP13A3* depletion in endothelial cells does not affect BMP signalling in hPAECs.

mRNA expression of (A) *ATP13A3,* (B*) ID1,* (C) *ID2* of hPAECs transfected with si*ATP13A3* in response to 0.1ng-1ng/ml BMP9 for 8 hours (n=4). Data are presented as fold-change relative to 0.1% FBS. Mean ± SEM was shown. One-way ANOVA with Tukey's post hoc test for multiple comparisons was used for data analysis.

5.2.2 *ATP13A1-5* mRNA expression in response to different cytokine

Recently, a growing body of evidence has linked inflammation to the pathogenesis of PAH with perivascular inflammation observed in all forms of PAH. Therefore, cytokines such as Interleukin-1 beta (IL-1β) and Tumour necrosis factor alpha (TNFα), which have been reported to be elevated in the serum/plasma from PAH patients [74] were assessed for the regulation of *ATP13A3*. Transforming Growth Factor Beta (TGFβ) has previously been reported to upregulating *ATP13A3* expression in hPASMCs from HPAH patients [165]. Therefore, TGFβ was also included for the assessment of P5-ATPases regulation.

5.2.2.1 Interleukin-1 beta selectively induced *ATP13A3* expression, but not other *P5-ATPases* in hPASMCs

To assess the regulatory effects of different cytokines on *ATP13A1-5*, control hPASMCs were cultured with TNFα (0.05ng/ml, 1ng/ml), IL-1β (1ng/ml) or TGFβ (1ng/ml, 5ng/ml) for 4 hours and assessed for mRNA expression. IL-1β at 1ng/ml induced *ATP13A3* mRNA by approximately 4-fold without affecting the expression levels of the other *P5-ATPases*. TNFα and TGFβ did not alter the expression of *P5-ATPases* in hPASMCs at 4-hour time point (Figure 5-6 A, B, C). To confirm that hPASMCs could respond to the cytokines mentioned above, *ID1/PAI-1, Interleukin-6 (IL-6) and Interleukin-8 (IL-8)* were used for assessing TGFβ, IL-1β and TNFα responses, respectively. As shown in Figure 5-7, at 4-hour time point, *ID1* expression was repressed by 50% with 5 ng/ml TGFβ treatment while *IL-6* and *IL-8* were induced by ~10 fold or ~7.5 fold with IL-1β (1ng/ml) and TNFα (1ng/ml) treatment respectively, indicating the successful response to these cytokines in hPASMCs.

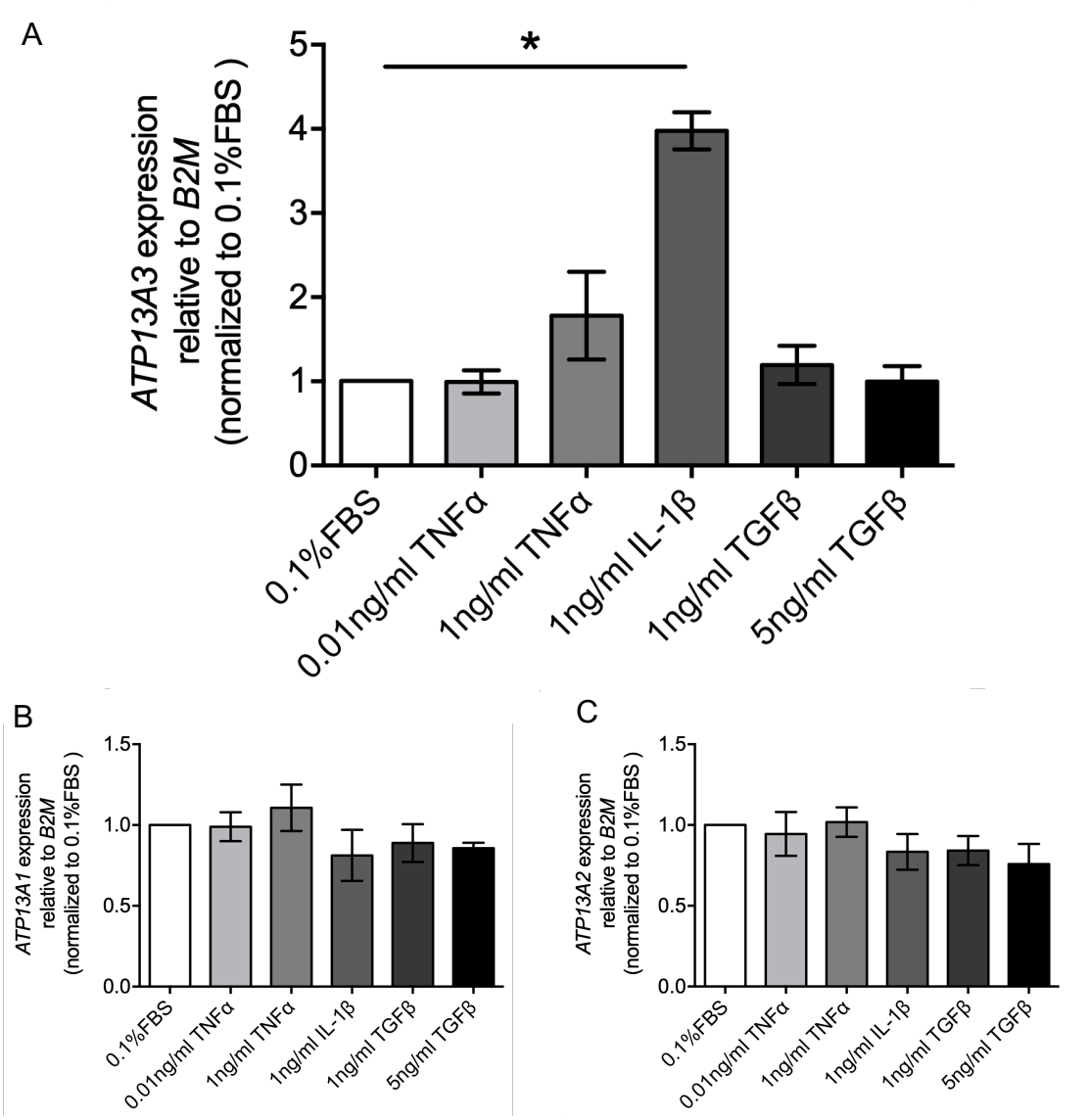

Figure 5-6 P5-ATPase mRNA expression in response to different cytokines in hPASMCs

mRNA expression of (A) *ATP13A3,* (B) *ATP13A1* (C) *ATP13A2* in hPASMCs cultured in 0.1% FBS supplemented DMEM with or without the presence of different concentrations of TNFα, IL-1β and TGFβ for 4 hours (n=3). Data were presented as fold change relative to *B2M* and normalised to 0.1% FBS. Mean ± SEM was shown. One-way ANOVA with Tukey's post hoc test for multiple comparisons was used for data analysis. *P<0.05, compared to 0.1% FBS.

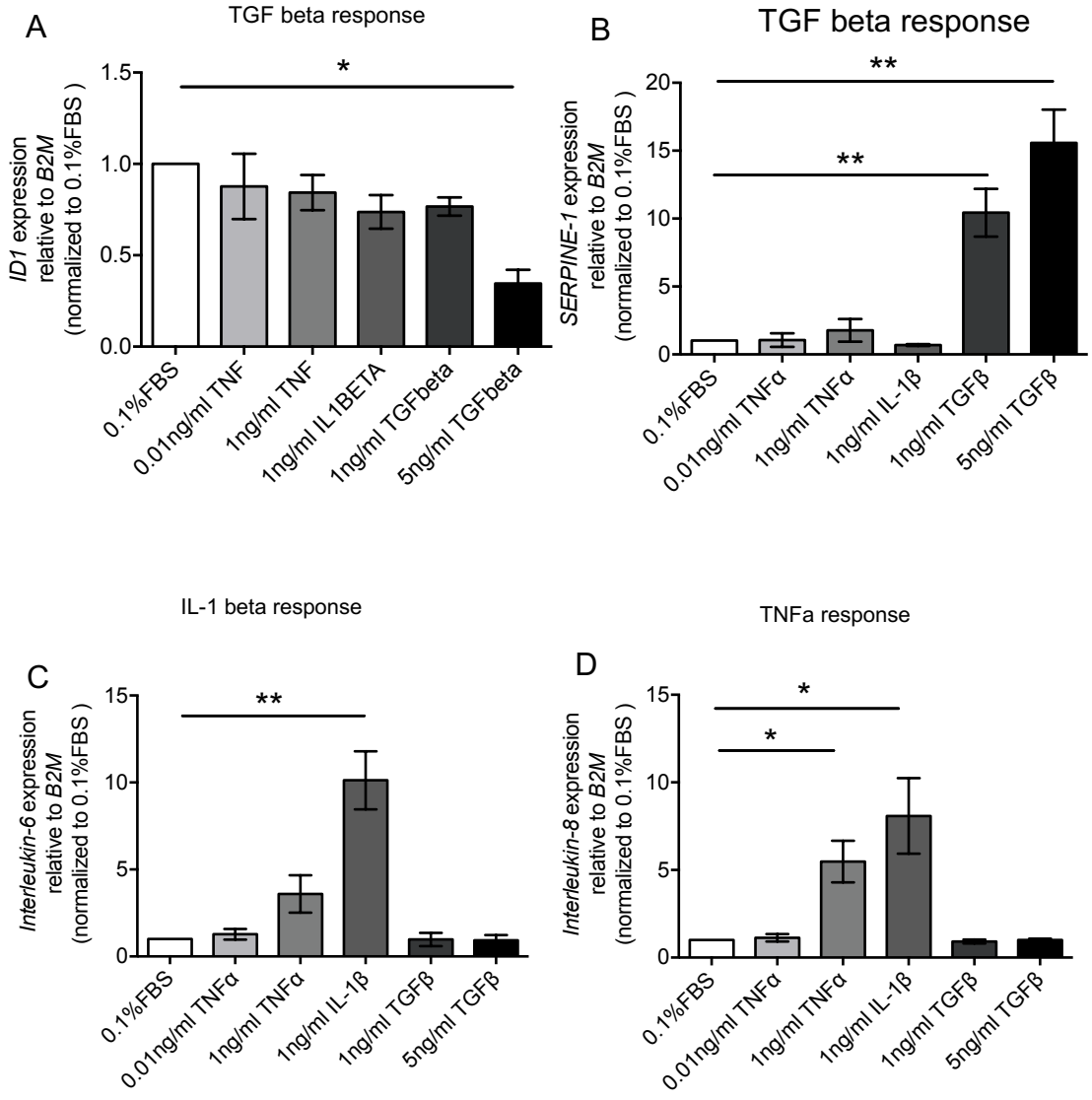

Figure 5-7 *ID1, IL-6, IL-8, SERPINE-1* mRNA expression in response to different cytokines in hPASMCs

mRNA expression of (A) *ID1,* (B) *SERPINE1 (*PAI-1*)* (C) *Interleukin-6* (D) *Interleukin-8* in hPASMCs cultured in 0.1% FBS supplemented DMEM with or without the presence of different concentrations of TNFα, IL-1β and TGFβ for 4 hours (n=3). Data were presented as fold change relative to *B2M* and normalised to 0.1% FBS. Mean ± SEM was shown. One-way ANOVA with Tukey's post hoc test for multiple comparisons was used for data analysis. *P<0.05, **P<0.01 compared to 0.1% FBS.

5.3 Discussion

BMP signalling is critical for maintaining the function and structural integrity of the vasculature. In this chapter, I have shown that in BOECs, BMP9 and BMP10, but not BMP6, selectively increased *ATP13A3* mRNA without affecting the expression of other P5-ATPases. It is well established that BMP9/10 signalling via the BMPR2/ALK1 holds importance for the maintenance of vascular homeostasis [39, 322]. The fact that BMP6 did not affect *ATP13A3* expression suggests that the induction of *ATP13A3* is more likely through ALK1 rather than other BMP type I receptors, such as ALK2 or ALK3 [79]. Interestingly, BMPR2 silencing did not impair this BMP-driven *ATP13A3* induction, probably due to the compensation by other type II receptors, such as activin type II receptors [322]. In contrast, ALK1 depletion substantially attenuated the *ATP13A3* induction by BMP9, indicating the involvement of ALK1 in *ATP13A3* regulation. Whole genome analysis in an I/HPAH patient cohort revealed higher frequency (6/11) of heterozygous protein truncated variants in *ATP13A3* [27], suggesting that *ATP13A3* haploinsufficiency may contribute to the pathogenesis of PAH. Considering that BMP9 transcriptionally upregulates *ATP13A3* in endothelial cells, it is rational to hypothesise that BMP9 may be therapeutically promising for PAH patients bearing *ATP13A3* mutations by enhancing the expression of the non-mutated ATP13A3 allele. Similar effects have been reported by our group that BMP9 blunted PAH phenotypes in *Bmpr2*$^{+/R899X}$ by selectively restoring *Bmpr2* expression in endothelial cells [39]. However, a proof-of-concept study in the *Atp13a3*^{P452fs} mouse model is required to validate the hypothesis.

Here I have shown that *ATP13A3* knockdown did not alter the mRNA expression of *BMPR2*, *ALK1* and *ALK2*. However, since the recycling of these receptors mainly affect their protein level and/or cellular localisation, this does not completely rule out a possible role for ATP13A3 in regulating these receptors, though *ID1* and *ID2* induction by various doses of BMP9 were

unaffected by *ATP13A3* deficiency in hPAECs. Further investigations are necessary to characterise the potential effects of *ATP13A3* deficiency on the canonical Smad pathway, such as the phosphorylation of Smad1/5/8 and on non-canonical kinase pathway signalling. Also, a broader analysis of BMP target genes may reveal a subset of BMP9-responsive genes that are affected by ATP13A3 loss. As revealed by microarray analysis, *ATP13A3* expression was upregulated by 4-hour TGFβ incubation in hPASMCs from HPAH patients harbouring BMPR2 mutation [165]. However, here I have shown that TGFβ did not induce *ATP13A3* upregulation in control hPASMCs, suggesting extra modifiers such as reduced BMPR-II expression by leading to aberrant TGFβ responses may contribute to this effect.

Recently, a growing body of evidence has linked inflammation to the pathogenesis of PAH. My investigation of the regulation of *ATP13A3* in the context of inflammatory cytokines revealed a selective upregulation of *ATP13A3* by IL-1β in hPASMCs. It is noteworthy that IL-1β overproduction promotes PAH in MCT rat models [335]. Moreover, IL-1β was also shown mediating the proliferative response of vascular cells by upregulating FGF2 [336]. In aortic smooth muscle cells, exogenous FGF2 treatment could upregulate polyamine transport and synthesis, resulting in the proliferative effect [337]. However, this study did not specify the polyamine transporter involved in the proliferative effect. Therefore, further investigation of the role of *ATP13A3* in the IL-1β mediated PASMCs proliferation is warranted.

Chapter 6 Results IV- Atp13a3 in rodent models of pulmonary hypertension

6.1 Introduction

Polyamines are a group of polycations dynamically involved in cell growth and apoptosis [104]. Polyamine dysregulation has previously been implicated in the pathogenesis of PAH with polyamines accumulation shown in the lungs of rats treated with both monocrotaline (MCT) and hypoxia [255]. Intriguingly, the two models seem to favour different mechanisms for this polyamine augmentation. In the MCT model, the activation of both ODC and AMD in rat lungs implicates the occurrence of aberrant polyamine biosynthesis. Intervention with DFMO, the irreversible inhibitor of ODC, alleviates the elevation of mPAP in this model, indicating a pathogenic role of ODC overproduction[255]. On the contrary, chronic hypoxia repressed lung ODC activity and hypoxic rats showed no response to a DFMO intervention [255]. This suggests a different mechanism may confer the polyamine elevation in hypoxic rat lungs [256]. Indeed, a later study revealed increased putrescine uptake in rat lung explants under hypoxic conditions [256]. Autoradiographs of [14C]-SPD uptake in rat lung tissues also demonstrated an accumulation of [14C]-SPD in the intimal and media layer of pulmonary arteries from hypoxia treated rats [257]. These findings suggest that hypoxia activates polyamine transport and thus contributes to the development of PAH. However, no polyamine transporters were identified in these studies.

ATP13A3, a putative polyamine transport [139, 147], has recently been identified as a novel PAH-associated gene [27]. However, no study to date has investigated the role of Atp13a3 in the context of PAH in an animal model. Previous studies revealed *Atp13a3* as widely expressed across different mouse tissues, with the peak of expression observed in the embryonic phase [155,

156]. Here, I will describe the expression pattern of *Atp13a3* in lung tissues of MCT and Sugen/hypoxia (SU/Hx) rat models. More importantly, a genetically modified mouse model bearing the PAH-associated frameshift mutation (P452Lfs) will be described for the first time with respect to *Atp13a3* expression, lung polyamine content and pulmonary hemodynamic changes.

6.2 Result

6.2.1 Monocrotaline treated rats display a reduced level of Atp13a3 in lung tissues

I first sought to assess *Atp13a3* mRNA expression in the MCT rat model. Tissues from this model were kindly provided by Dr Elisabet Ferrer with hemodynamic assessment performed by Mr Stephen Moore. Briefly, rats were given a single injection of 40mg/kg MCT, after which they developed a progressive PAH phenotype over 28 days. Hemodynamic parameters were assessed, and tissues were harvested from animals at 7, 14, 21 and 28 days for the monitoring of disease development. As shown in figure 6-1 B, when compared to the saline group, rats injected with MCT displayed elevated right ventricular systolic pressure (RVSP) at day 14, with pressure continuing to rise by day 28. The hemodynamic changes paralleled the right ventricle hypertrophy, manifesting as an increased Fulton index at days 14, 21 and 28 (Figure 6-1 C). Left ventricular end-systolic pressure (LVesp), though fluctuating at week 2, remained similar between MCT and control rats. Interestingly, in the MCT group, the lung expression of *Atp13a3* started to decrease at the 3-week time point and continued to drop to ~ 60% of the level of control rats by day 28 (Figure 6-1 A). The reduction of *Atp13a3* expression tracked the increase of RVSP and the Fulton index (starting from week2), indicating a potential link between *Atp13a3* and the progression of MCT induced PAH.

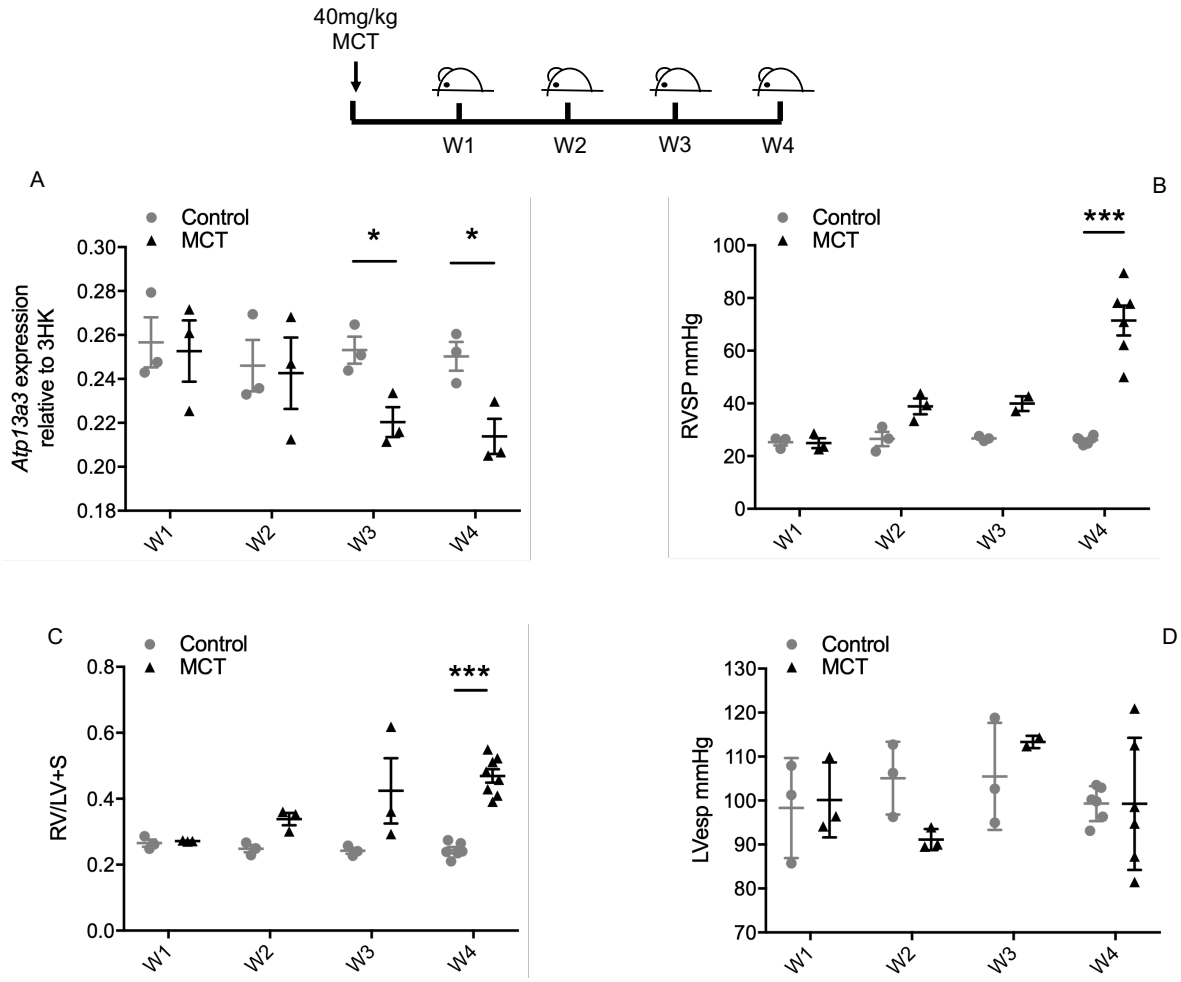

Figure 6-1 *Atp13a3* expression is downregulated in MCT-rat lung tissues.

(A) Relative expression of Atp13a3 in rat lung tissues at days 7 (W1), 14 (W2), 21 (W3) and 28 (W4) after injection of MCT or vehicle (Control) (n=3-8 per group). mRNA expression was normalised to the arithmetic means of the Ct values for three housekeeping genes (3HK) *B2m*, *Actb* and *Hprt*. PAH disease-associated phenotyping by assessing (B) Right ventricle systolic pressure (RVSP) and (C) Fulton index (RV/LV+S). (D) Left ventricular end-systolic pressure (LVesp). Paired t-test was used to compare data from MCT and control rats at each time point. *P<0.05, ***P<0.001 compared with control at each time point.

6.2.2 *Atp13a3* is upregulated in both hypoxia and Sugen/hypoxia rat lungs

I next assessed *Atp13a3* mRNA expression in two other well-established PAH model, the hypoxia rat model and the Sugen/hypoxia rat model. Lung tissues from these models were kindly provided by Dr Lu Long and Dr Xudong Yang. For the hypoxic-rat model, rats were subjected to hypoxia (10% O2) for three weeks. In the Sugen/hypoxia model (SU/Hx), rats were given weekly injection of SU-5416, a vascular endothelial growth factor (VEGF) receptor-2 tyrosine kinase inhibitor, at day 0 followed by exposure to hypoxia (10% O2) for three weeks. Rats were then returned to normoxia for an additional five weeks over which time, a progressive increase in the severity of pulmonary hypertension occurs. As demonstrated in figure 6-2, chronic hypoxia (3-week) induced a ~2-fold increase of *Atp13a3* mRNA in rat lung tissues. In those rats removed from hypoxia after 3 weeks and maintained in normoxia for a further 5 weeks, Atp13a3 levels were similar to control animals. Interestingly, rats in SU/Hx group which underwent the same 8-week duration, exhibited 23.8% increase of lung *Atp13a3* expression compared to the hypoxia/normoxia group (Figure 6-2), suggesting a potential link between Atp13a3 and endothelial injury.

6.2.3 The *Bmpr2*^{R899X} mutation does not lead to altered *Atp13a3* expression in mouse lung tissues

Bmpr2+/R899X knock-in mice have previously reported with impaired BMP signalling and spontaneously develop PAH at the age of 6 months [39]. Having demonstrated that BMP9 selectively induces the expression of *ATP13A3* mRNA in human endothelial cells (Chapter 5) I then assessed whether the *Bmpr2+/R899X* mutation altered *Atp13a3* mRNA in lung tissues kindly provided by Dr Lu Long and Dr Xudong Yang.

Unlike the previous findings in other established PAH models, *Bmpr2+/R899X* mice displayed a similar *Atp13a3* mRNA level to their wild-type littermates (Figure 6-3).

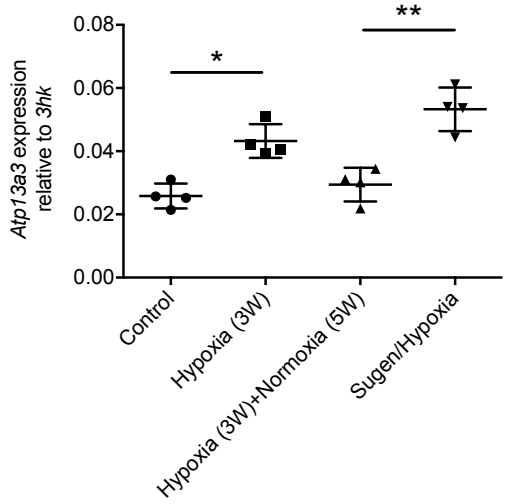

Figure 6-2 *Atp13a3* expression in the lung tissues of hypoxia and the Sugen/hypoxia rat model Relative expression of Atp13a3 in lung tissues of hypoxia or Sugen/hypoxia rat models. The mRNA expression level was normalised to the arithmetic means of the Ct values for three housekeeping genes (3hk) *B2m*, *Actb* and *Hprt* (n=4). One-way ANOVA with Tukey's post hoc test for multiple comparisons was used for data analysis. *P<0.05 compared with control.

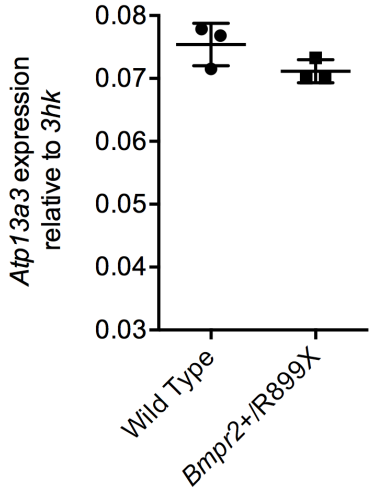

Figure 6-3 *Atp13a3* expression in lung tissues of the Bmpr2R899X mouse Relative expression of *Atp13a3* in lung tissues of *Bmpr2* R899x mice compared to Wild-type littermates (n=3). The mRNA expression level was normalised to the arithmetic means of the Ct values for three housekeeping genes (3hk) *B2m, Actb* and *Hprt*. A paired t-test was used for data analysis.

6.2.4 Characterising of *Atp13a3*-P452Lfs mice

6.2.4.1 Genotyping of Atp13a3-P452Lfs mice

Together with the introduction of the desired P452L frameshift mutation (C>-), one additional silent mutation was also created to prevent the Cas9 protease from "re-cutting" the engineered region. The introduction of these mutations created a de novo BseRI restriction enzyme digestion site which can be used for mouse genotyping. Following PCR amplification of the mutant region, amplicons were further digested with BseRI. As illustrated in figure 6-4 A, Wild type amplicons showed no digestion by BseRI, while heterozygous amplicons were partially digested. Amplicons from the homozygous mice were fully digested by BseRI, resulting in two distinct cleavage bands (Figure 6-4 A). The mouse genotypes were further confirmed by Sanger sequencing.

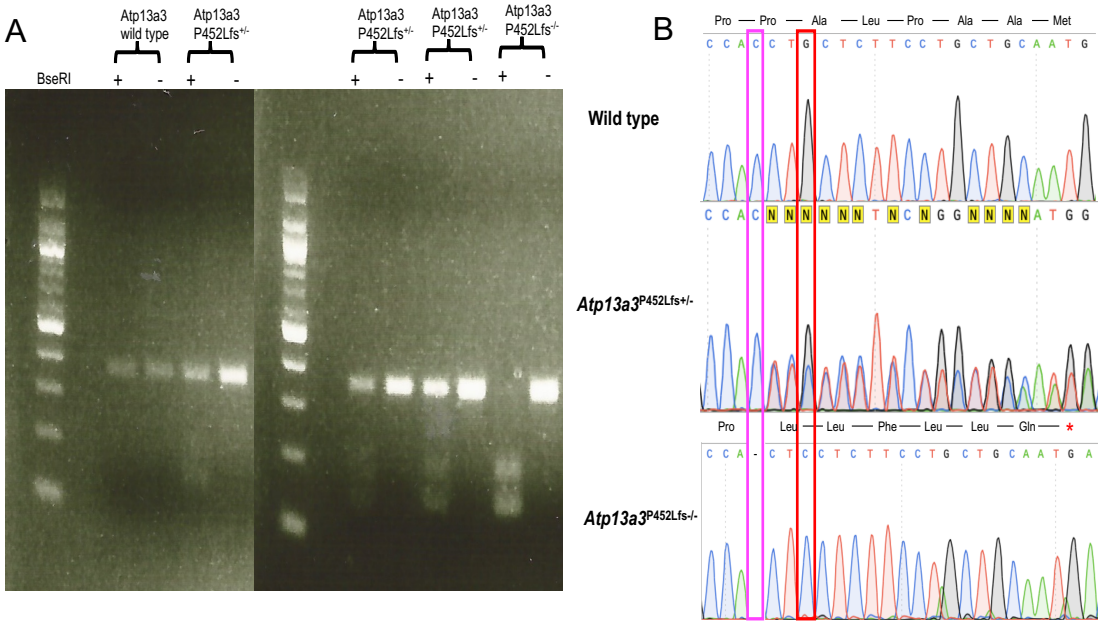

Figure 6-4 Genotyping of Atp13a3 P452Lfs mice

(A) Genomic DNA extracted from mouse tail tip biopsies was amplified by PCR for the region covering the P452Lfs mutation. The resulting amplicons were further digested with BseRI for genotyping. (B) Representative Sanger sequencing results of Atp13a3P452Lfs mice. The targeted P452Lfs C>- mutation is highlighted in the magenta rectangle while the silent mutations are highlighted in red rectangles.

6.2.4.2 *Atp13a3*-P452Lfs mice display reduced *Atp13a3* protein and mRNA expression in lung tissues

The P452Lfs frameshift mutation creates a de novo premature stop codon (TGA), thus is likely to cause mRNA degradation through the nonsense-mediated decay (NMD) pathway (Figure 6-4 B). Indeed, when compared to their wild type littermates, both heterozygous and homozygous mice showed a lower level of *Atp13a3* mRNA and protein expression as revealed by qPCR and immunoblotting (Figure 6-6 A, B). In a homozygous Atp13a3-P452Lfs mouse, both mRNA and protein expression of Atp13a3 were reduced when compared to heterozygous mice. This indicates that this mutation leads to insufficiency of Atp13a3.

6.2.4.3 *Atp13a3*-P452Lfs mice have lower levels of polyamines in lung tissues

I have shown that ATP13A3 deficiency in human pulmonary artery endothelial cells disrupts cellular polyamine homeostasis (Chapter 4). Having demonstrated that Atp13a3-P452Lfs mice display reduced Atp13a3 expression in lung tissue, I asked if the polyamine level was altered in these tissues. Interestingly, preliminary data show that in comparison to the wild type littermates, both heterozygous and homozygous Atp13a3-P452Lfs mice showed lower putrescine, spermidine and spermine levels in their lung tissues (Figure 6-7), suggesting a disruption of polyamine homeostasis in these mice.

6.2.4.4 *Atp13a3*-P452Lfs mice exhibit elevated RVSP at 6-month age

I then moved on to assess if these are sufficient to induce the PAH associated hemodynamic changes in mice. The hemodynamic assessment was performed by Dr Ekaterina Legchenko. As shown in Figure 6-6, at 3-month age, no overt hemodynamic difference were revealed among mice (Figure 6-5A). However, when characterised at 6-month age, both heterozygous and homozygous male Atp13a3-P452Lfs mice exhibit significant higher right ventricle systolic pressure (RVSP) (Figure 6-6 A) without compromising the systemic arterial pressure or

heart rate (Figure 6-6 B, C) when compared with their wild type littermates. Interestingly, only male mice developed increased RVSP while hemodynamic parameters remain similar among female mice (data not shown).

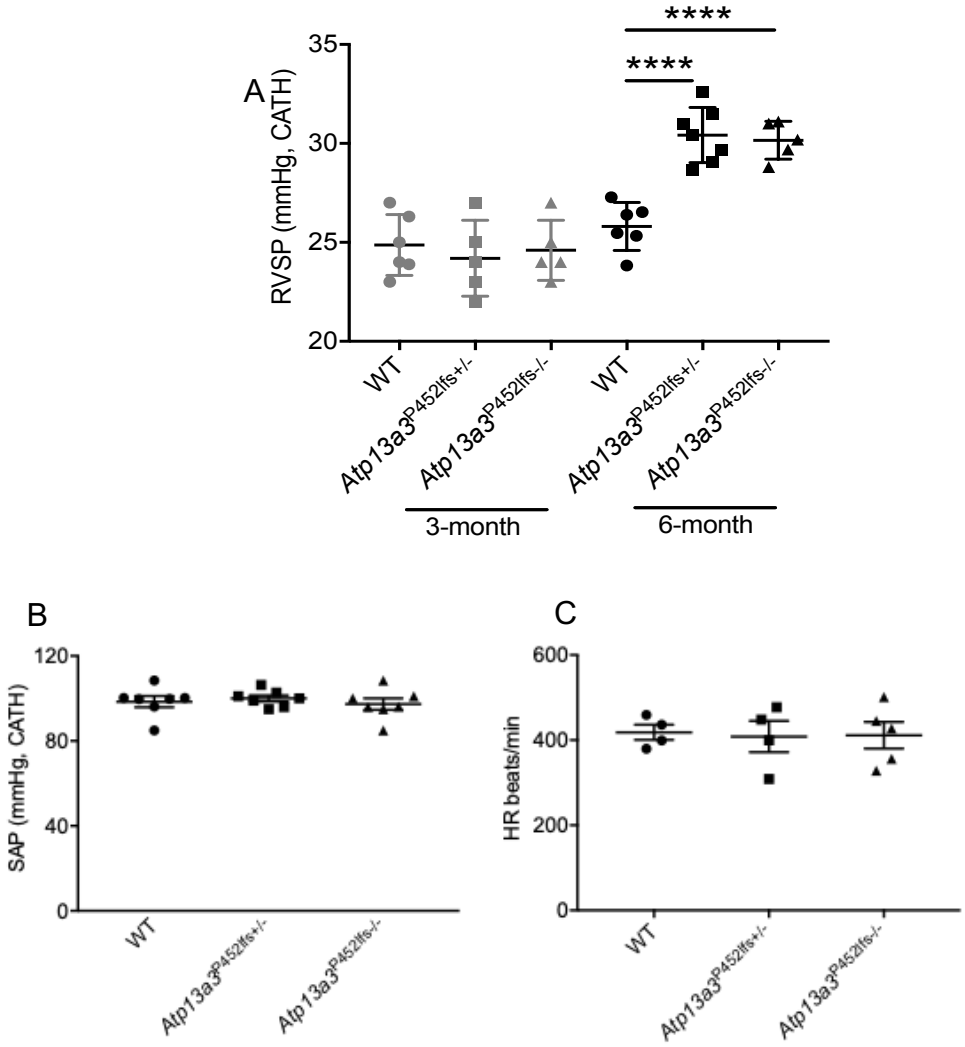

Figure 6-5 Atp13a3-P452Lfs mice exhibit increased RVSP at 6-month age

(A) Right ventricle systolic pressure (RVSP) of male *Atp13a3*$^{P452Lfs+/-}$, *Atp13a3*$^{P452Lfs-/-}$ mice and their wild type littermates was assessed at 3-month and 6-month age (n=5-10). (B) Systemic arterial pressure (SAP) and (C) heart rate (HR) of the mice were also assessed at 6-month age. One-way ANOVA with Tukey's post hoc test for multiple comparisons was used for comparison among genotypes. ****P<0.00001 compared with wild type littermates.

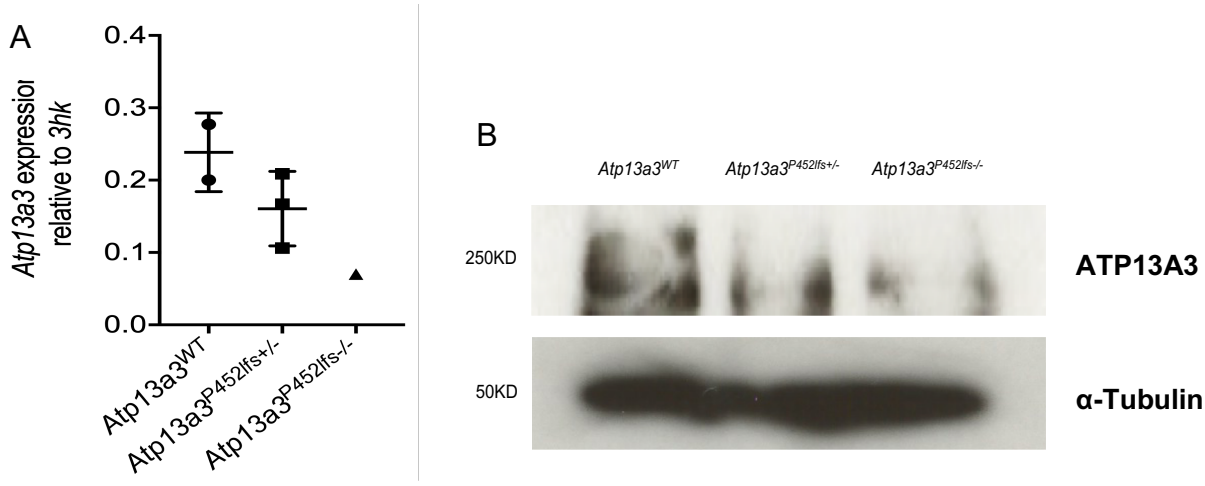

Figure 6-6 Atp13a3-P452Lfs display impair Atp13a3 expression in lung tissues

(A) Atp13a3 mRNA was assessed in lung tissues from 3-month old Atp13a3P452Lfs+/- (N=3), Atp13a3P452Lfs-/- (N=1) mice and their wild type littermates (Atp13a3WT N=2), Data are presented as Atp13a3 expression relative to the arithmetic means of the Ct values three housekeeping genes (3hk) *B2m*, *Actb* and *Hprt*. (B) Immunoblotting of Atp13a3 and α-Tubulin was performed using the lung tissues isolated from wild type, Atp13a3P452Lfs+/- and Atp13a3P452Lfs-/- mice (n=1)

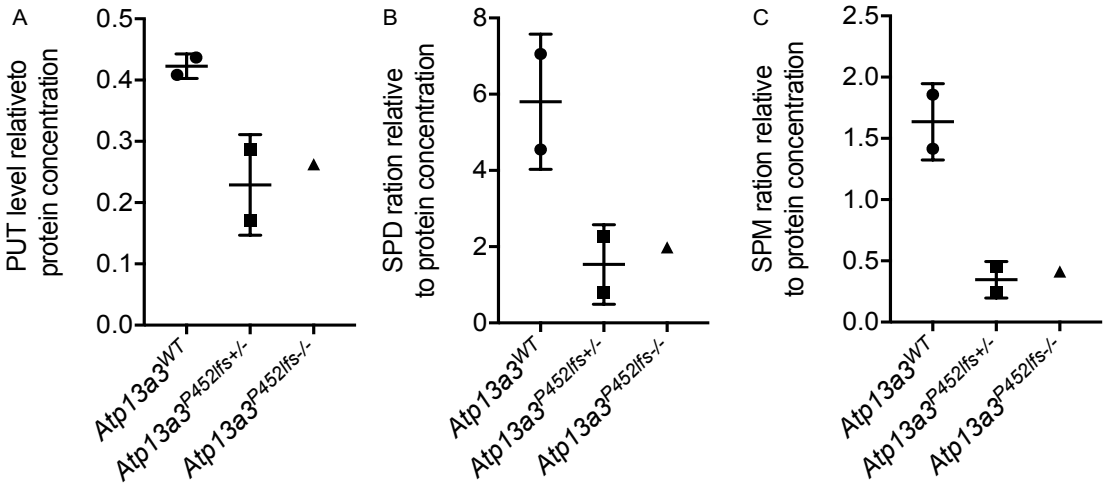

Figure 6-7 *Atp13a3*-P452Lfs mice display reduced polyamine levels in lung tissues

(A) Putrescine (PUT), (B) Spermidine (SPD) and (C) Spermine (SPM) level in lung tissues of wild type (N=2), *Atp13a3*-P452Lfs heterozygous (N=2), homozygous (N=1) mice were measured by LC-MS. Data are presented as the relative level of polyamines normalised to protein concentration.

6.3 Discussion

In this chapter, I have shown different expression patterns of *Atp13a3* mRNA in the MCT- and hypoxia-induced rodent PAH models. In the MCT-treated rat, lung polyamine levels are elevated as a consequence of upregulating de novo polyamine synthesis [255]. This may partially explain the downregulation of *Atp13a3* mRNA, as increased polyamine content was reported to suppress polyamine transport through feedback regulation [213]. Contrary to the MCT PH rat model, *Atp13a3* mRNA was upregulated in the lungs of the hypoxia-induced rat PH model. This is consistent with the observation that hypoxia promotes polyamine transport in rat lung tissues [256] and further suggests that Atp13a3 could be mediating the increase in polyamine content.

Adding to this finding, by using In silico analysis (Pathwaynet online database) I have revealed a functional relationship between HIF1α and ATP13A3 [158]. HIF1α is a subunit of the transcriptional factor hypoxia-induced factor 1 (HIF1). In normoxia, HIF1α is constantly degraded through ubiquitin-mediated proteasomal degradation [159]. However, hypoxia stabilises HIF1α expression by suppressing ubiquitination. By then dimerising with HIF1β and mediating transcription, a set of target genes are transactivated [161]. Intriguingly, the promoter region of ATP13A2, another P5B ATPase, contains hypoxia response elements which can bind to HIF1α [162]. Pharmacological inhibition of HIF1α hydroxylation increases ATP13A2 expression by preserving HIF1α level [163]. Interestingly, the HIF1α pathway has been demonstrated to increase polyamine transport in cancer cells[338]. Considering the high homology shared between ATP13A3 and ATP13A2, it is possible that the stabilisation of HIF-1a in hypoxia is responsible for *Atp13a3* upregulation and hence contributes to the development of PH by affecting polyamine transport. However further investigations are needed to validate this hypothesis. The different regulation of Atp13a3 in MCT versus hypoxia and Sugen-hypoxia may be partly related to the differences in the disease pathology in these models. Although the MCT

challenge causes PH, it also causes hepatic and renal fibrosis [279, 339], which may have additional impacts on polyamine metabolism. Future investigations, such as rebalancing polyamine transport by overexpressing *Atp13a3* in the MCT rat or administration of an Atp13a3 neutralising antibody in the hypoxia and Sugen-hypoxia models may be informative to understand the role of *Atp13a3* and polyamine dysregulation in the pathogenesis of PAH. Moreover, the effects of *Atp13a3* on polyamine homeostasis may be cell type dependent in the lung vasculature. Therefore, to delineate the cell-specific role of *Atp13a3* in these models is of great importance.

Here, by collaborating with Dr Ekaterina Legchenko, we have characterised for the first time that the *Atp13a3* frameshift mutation (P452Lfs) predisposes mice to develop an elevated RVSP. Disruption of *Atp13a3* is likely to confer the phenotypes as reduced *Atp13a3* expression was observed in mutant mice. The fact that RVSP elevation was concluded in comparison with wild type littermates also rules out the possibility that background genetic variation may contribute to phenotypes. Interestingly, preliminary data suggest a lower polyamine content in the lung tissues from *Atp13a3* P452L (+/- and -/-) mice compared to their wild type littermates. These findings, at first glance, differ from the elevated lung polyamine contents reported in MCT and hypoxia-induced PH. However, it is noteworthy that these pathological-insult models may not fully recapitulate the pathobiology of human PAH as they could be a physiological response (hypoxia) or lead to multi-organ injury (MCT administration). On the contrary, genetic models provide a “cleaner” system for investigating PAH pathobiology especially those induced by genetic defects. The fact that the Atp13a3-P452Lfs mice spontaneously developed PAH-like hemodynamic changes strongly suggests that reduced polyamine content caused by the *Atp13a3* mutation contributes to the development of PAH. This also coincides with my previous findings that *ATP13A3* deficiency achieved by siRNA knockdown or mutation (L726X) induced endothelial cell apoptosis by

disrupting polyamine homeostasis (Chapter 4). It is possible that the polyamine elevation observed in the established PH models is the “by-product” of advanced disease rather than the “cause” of PAH, for example, under hypoxic condition, rats may upregulate their lung polyamine transport in response to HIF1a stabilisation while MCT administration metabolically activates the polyamine synthesis by elevating ODC.

ODC is another aspect that worth further attention. As shown previously (Chapter 4), *ATP13A3* deficiency induces ODC upregulation in endothelial cells and DFMO partially alleviate the apoptosis triggered by ornithine supplementation. This suggests that elevated ODC may be an important factor contributing to the development of PAH, especially when polyamine homeostasis is disrupted. Therefore, to investigate the ODC expression and activities in *Atp13a3* P452L mutant mice and to assess the therapeutic value of targeting ODC by DFMO may be of importance in understanding the pathological role of *Atp13a3* mutation. Additionally, it is also worth validating these findings in PAH patients. Recently, a lung metabolomics study has revealed elevated level of ornithine and putrescine in PAH patients [258]. Plasma metabolomics profiling also demonstrated increased levels of polyamine metabolites in idiopathic or heritable PAH patients, with N-acetyl-putrescine being prognostic independent of the established prognostic markers [259]. Considering ATP13A3 is a polyamine transporter in vascular cells, analysing the potential links between ATP13A3 expression and polyamine level in lung tissues or plasma samples from PAH patients may help to decipher any potential broader role of ATP13A3 dysregulation in the pathogenesis of PAH.

Chapter 7 Results V- Generation of the ATP13A3-R858H iPSC lines

7.1 Introduction

Since the discovery of heterozygous germline mutations in *BMPR2*, knowledge of the molecular genetic architecture of PAH patients has expanded greatly. To date, 16 genes [31] have been recognised as associated with PAH, among which *BMPR2* remains the predominant genetic cause. However, insights from recently-identified genes might be anticipated to further the understanding of the pathobiology of PAH and reveal additional treatment targets.

Experimental animal models, especially genetically modified mice, held promise as tools for examining the pathogenesis of PAH-related gene mutations. However, owing to the anatomical and functional differences to human, genetic mouse models have not generally proven to be robust PAH models. Furthermore, those rat models driven by disease-initiating stimuli (i.e. hypoxia, monocrotaline, Sugen-hypoxia) have limitations with respect to extrapolating to human disease [270, 279, 339]. Additionally, age, sex and environmental exposure to disease modifying factors are heterogeneous contributors to the pathobiology of human PAH and hence, make it even harder for animal models to entirely recapitulate the human disease condition. Vascular cells derived from lung tissues or blood samples of the PAH patients complement the rodent model analyses. However, access to these resources can be limited, and following isolation, primary cells only survive for a restricted number of passages before they senesce or change their differentiation state. Also, these cells are generally isolated from patients with end-stage disease, where changes due to chronic disease may lead to responses[340, 341] that are not directly due to the genetic mutation. Therefore, additional models that

can overcome these limitations and thus represent a complementary system to the above models will be beneficial for studying PAH.

Induced pluripotent stem cells (iPSC) reprogrammed from somatic cells can be propagated indefinitely and can be differentiated into endothelial [342] and smooth muscle-like cells[343, 344]. These properties make iPSCs an appropriate alternative for modelling PAH. Indeed, several groups have pioneered the use of patient-derived iPSCs in studying the reduced penetrance of *BMPR2* mutations in PAH [345]. iPSCs generated by reprogramming skin fibroblasts of PAH patients that are then differentiated into endothelial cells share similar traits to hPAECs derived from the same patient [346]. Our group has also reported that control iPSCs engineered to harbour a *BMPR2* mutation using CRISPR-Cas9 editing recapitulate some PAH phenotypes after differentiation into endothelial cells and smooth muscle cells [273, 347]. Collectively, these studies demonstrate the feasibility of studying PAH with iPSC models.

In this chapter, I will describe the generation of an iPSC line engineered with the CRISPR-CAs9 editing system to harbour an *ATP13A3* missense mutation (R858H) identified in a PAH patient. Comparative phenotyping of the mutant iPSC line with the isogenic wild-type line it derived from following endothelial differentiation will also be discussed.

7.2 Results

7.2.1 Generation of the C2-*ATP13A3*^{R858H} iPSC line by CRISPR-Cas9 gene editing

To general the mutant iPSC line, a PAH-associated *ATP13A3* missense mutation (R858H) was introduced into a control iPSC line (C2-*ATP13A3*^{WT}) generated from BOECs from a healthy individual using the CRISPR-Cas9 gene editing system (Figure 7.1). A detailed method is described in Chapter 2.9.

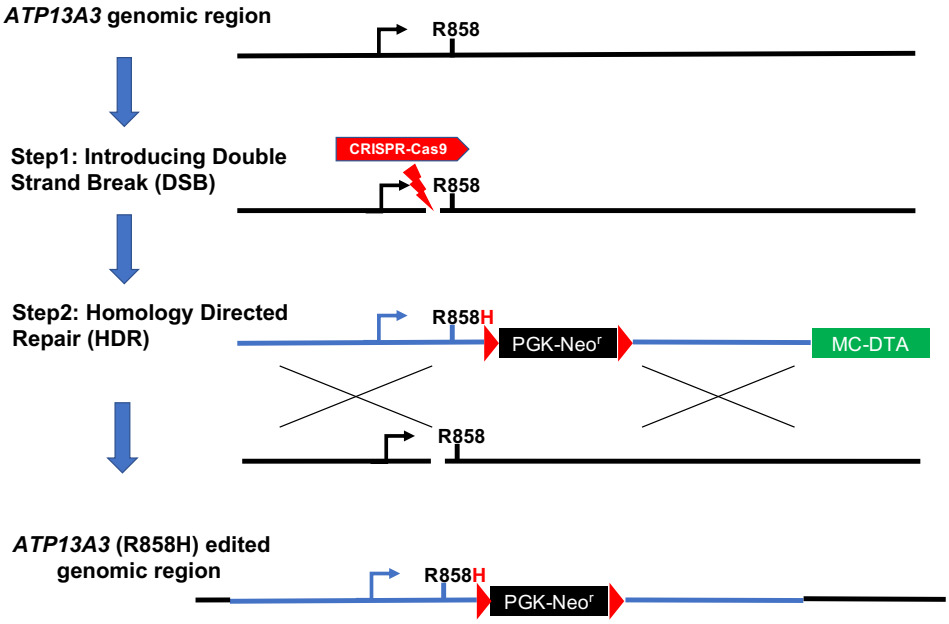

Figure 7-1 Strategy overview for introducing the ATP13A3-R858H mutation using the CRISPR-Cas9 system

7.2.1.1 CRISPR-Cas9 nuclease vector efficiency test

Prior to the introduction of the *ATP13A3* R858H mutation, CRISPR-Cas9 guide RNAs (gRNA) were designed using the online platform, benchling (www.benchling.com), based on the algorithm considering the target efficiency and off-target possibility. Two CRISPR nuclease vectors containing the gRNAs (listed in Chapter 2, Table2-11) targeting different loci of human *ATP13A3* were then tested for their cleavage efficiencies in the control iPSC (C2-*ATP13A3*^{WT}) line. The orange fluorescent protein (OFP) signal was visualised at both 24-hour and 48-hours after transfection (Figure 7-2),

indicating the successful delivery of both vectors. *ATP13A3*-R858H CRISPR vector-2 exhibited a higher transfection efficiency than vector-1, as revealed by a larger OFP positive cell population. To further compare the two vectors, cleavage efficiency was assessed (detailed method described in Chapter 3). As shown in Figure 7-3, insertions and/or deletions (Indels) introduced by CRISPR cleavage were detected by the digestion of the mismatched amplicons with the cleavage detection enzyme, resulting in two cleaved bands (~200bp and ~250bp respectively). The *ATP13A3*-R858H CRISPR vector-2 yielded a higher cleavage efficiency (40%) than vector-1 (20%) (Figure 7-3). Taken together, these findings suggest that the desired human *ATP13A3* genomic loci are "editable" by CRISPR-Cas9 nuclease and that vector-2 displayed higher cleavage efficiency than vector-1.

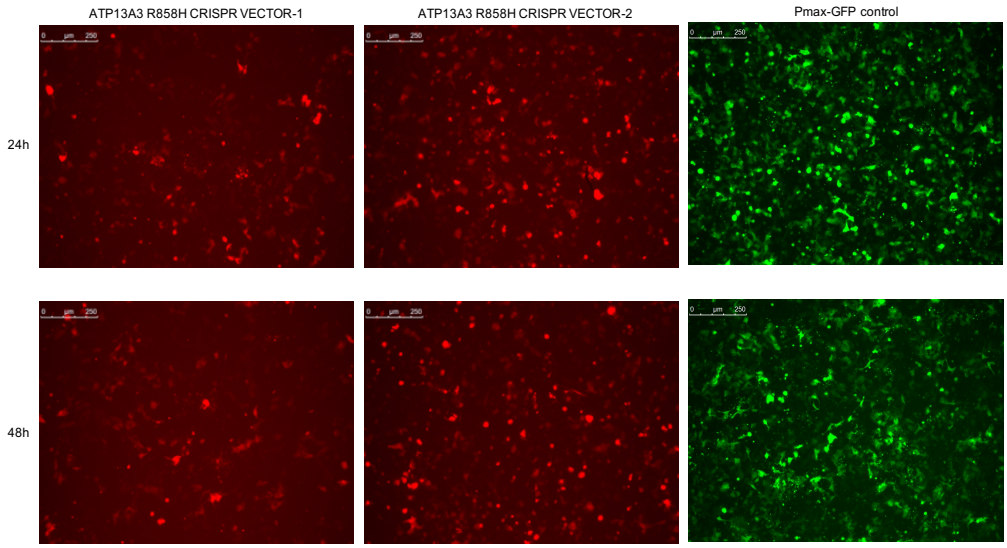

Figure 7-2 Orange Fluorescent Protein (OFP) signal in control iPSCs (C2) electroporated with ATP13A3-R858H CRISPR-Cas9 nuclease vectors

Control iPSCs (C2-*ATP13A3*^{WT}) were electroporated with GeneArt CRISPR Nuclease Vectors-1/2 using Nucleofector® electroporation system (Lonza). At 24-hour and 48-hours post-transfection, the OFP signal were visualised by fluorescence microscopy. Representative images are shown (20x, scale bar = 250 µm). PmaxGFP vector

(Thermo Fisher scientifics) was transfected as a positive control into C2-*ATP13A3*^{WT} iPSCs and visualised together with the *ATP13A3*-R858H CRISPR-targeted cells (N=3).

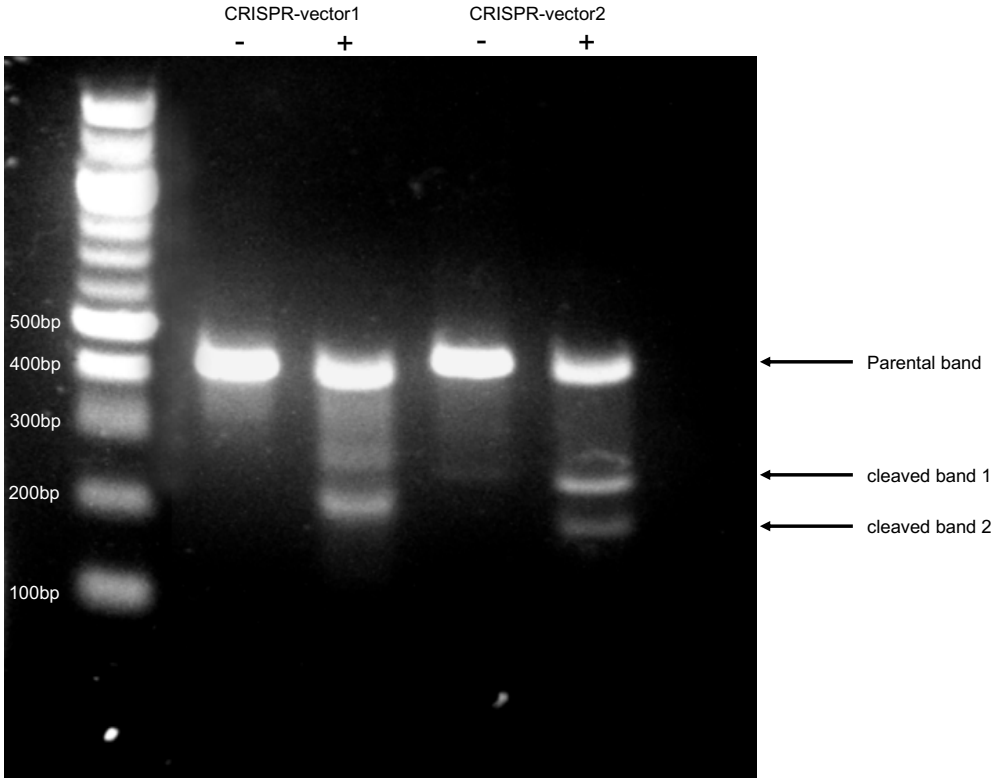

Figure 7-3 Genomic Cleavage Detection Assay for ATP13A3-R858H CRISPR-Cas9 vectors in control iPSCs (C2)

Representative gel image of cleavage detection assay (N=3). Following immunofluorescent imaging, transfected C2-*ATP13A3*^{WT} iPSCs were harvested for genomic DNA and were PCR amplified using primers flanking the CRISPR-Cas9 targeting regions (Chapter2, Table. 2.10.2.1). After re-annealing, samples were treated with or without cleavage detection enzyme and fractionated on a 2% agarose gel. Band densitometry was performed on each lane using Image J. The cleavage efficiency was calculated according to the following equations:

ATP13A3-R858H CRISPR-Cas9 vector-1 cleavage efficiency=

$1 - (1 - \text{fraction cleaved})^{1/2} = 1 - (1 - 0.36)^{1/2} = 20\%$.

ATP13A3-R858H CRISPR-Cas9 vector-2 cleavage efficiency:

$1 - (1 - \text{fraction cleaved})^{1/2} = 1 - (1 - 0.64)^{1/2} = 40\%$;

7.2.1.2 Introducing the *ATP13A3*-R858H mutation into control iPSCs (C2)

To introduce the *ATP13A3*-R858H mutation into the C2-*ATP13A3*^{WT} control iPSC line, 3 µg CRISPR nuclease vector and 3 µg linearised *ATP13A3*-R858H-LNDA repair vector were co-transfected into cells by electroporation. As indicated in figure 7-8A, the introduction of the R858H mutation created a *de novo* NdeI digestion site and a neomycin resistance cassette. Following Geneticin (G418, 50 µg/ml) selection (details described in Chapter 2.9), forty-eight remaining colonies were further genotyped by PCR amplifying the 1kb LHA fragments using the primers listed previously (Chapter2, Table2-11). NdeI digestion screening revealed three positive colonies with cleaved bands at 900bp and 100bp (Figure 7-8 B), indicating the successful homology-directed integration. Genotyping samples of the three colonies were further sequenced by Sanger sequencing. All lines were confirmed as carrying the homozygous *ATP13A3*-R858H mutation (Figure 7-8 C). Following expansion, these iPSC lines were further tested for their efficiency to differentiate into endothelial cells. As a result, line 33 with an average efficiency of 40-55% iPSC-EC production was chosen for further functional assessment.

7.2.2 Pluripotency assessment of the C2-*ATP13A3*^{R858H} iPSC line

Following genotyping, iPSC lines with the confirmed *ATP13A3*^{R858H} mutation were expanded into 6-well plates and maintained for further use. To assess the pluripotency of the mutant C2- *ATP13A3*^{R858H} iPSC lines, immunostaining was performed to assess the endogenous level of the pluripotency markers, Nanog, OCT4, Tra-1-60. As shown in figure 7-9, all three pluripotency markers were abundantly expressed in the C2-*ATP13A3*^{R858H} iPSCs, indicating the mutation does not affect pluripotent differentiation potential in these lines.

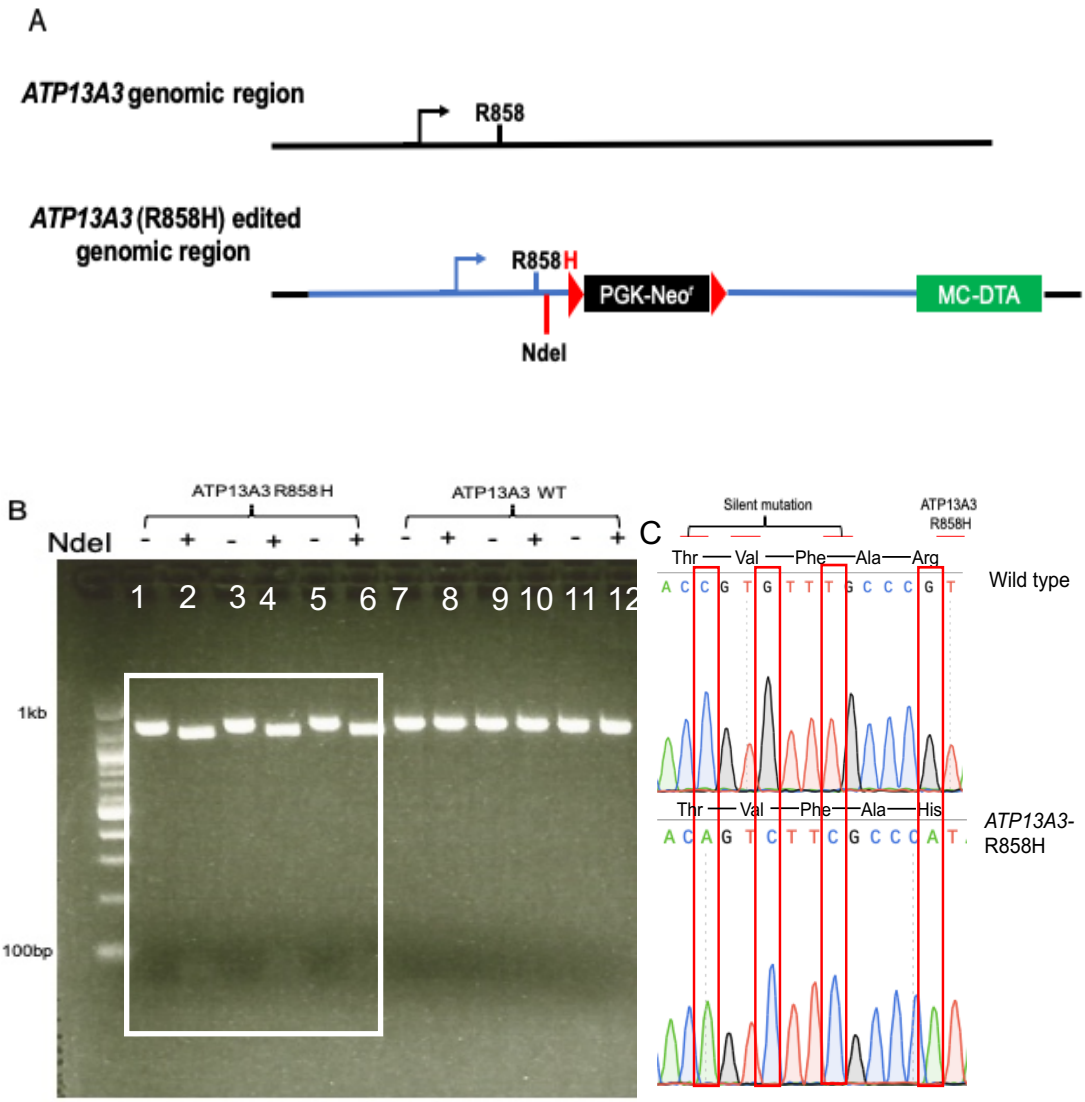

Figure 7-4 Introducing the ATP13A3-R858H mutation into C2-ATP13A3WT control iPSCs (A) Schematic for the introduction of the ATP13A3-R858H mutation by CRISPR-mediated homology recombination. R858H G>C mutation introduced a de novo NdeI restriction enzyme site. (B) Representative gel image of the NdeI genotyping screening. Genomic DNA from emerging cell colonies were PCR amplified as described in chapter 2. PCR products with or without NdeI digestion were run on a 1.5% agarose gel. Samples in lane 1- 6 were from correctly targeted iPSC colonies as the DNA product can be digested by NdeI. (C) Representative result from Sanger sequencing. ATP13A3 R858H (G>A) mutation as well as three silent mutations (C>A, G>C, T>C) are highlighted in the red rectangles.

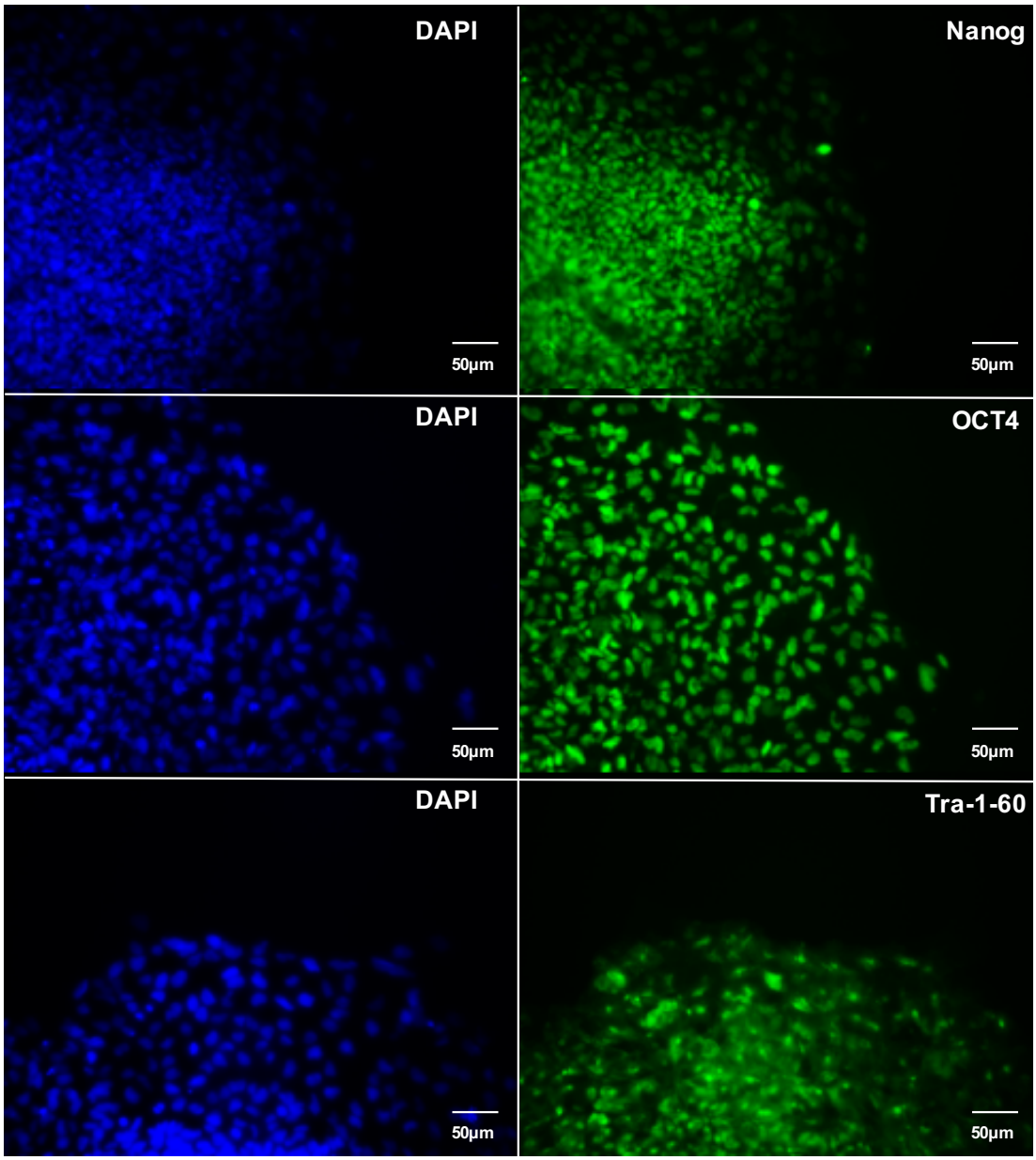

Figure 7-5 Immunostaining of pluripotency markers in C2-ATP13A3R858H iPSC lines

C2-*ATP13A3*^{R858H} iPSCs were seeded into 24-well plates at a density of 30,000/well and stained for the pluripotency markers Nanog, OCT4, TRA-1-60 (Reprocell 1:100) (Green). Nuclei were counterstained with DAPI (Blue) before being visualised (20X magnification, scale bar = 50 µm) using a Leica DMI3000 B manual inverted microscope (N=3).

7.2.3 Generation of C2-*ATP13A3*^{R858H} iPSC-derived endothelial cells (iPSC-ECs)

To examine the potential contribution of *ATP13A3* mutations to the pathogenesis of PAH, C2-*ATP13A3*^{R858H} iPSCs were first assessed for their ability to differentiate into endothelial cells. At the end of the 10-day differentiation period, immunostaining revealed efficient expression of the endothelial-specific markers CD31, VE-cadherin, von Willebrand factor (VWF) in both the C2-*ATP13A3*^{WT} control and C2-*ATP13A3*^{R858H} mutant iPSC-derived endothelial cells, indicating the successful differentiation of iPSC-ECs (Figure 7-10).

7.2.4 Generation of C2-*ATP13A3*^{R858H} iPSC-derived smooth muscle cells (iPSC-SMCs)

As described in Chapter 3, *ATP13A3* is expressed at similar levels in human pulmonary arterial endothelial cells and smooth muscle cells. Therefore, I assessed C2-*ATP13A3*^{R858H} iPSCs for their capacity to differentiate into smooth muscle cells and compared these to C2-*ATP13A3*^{WT} iPSCs. At the end of this differentiation period, iPSC-SMCs were assessed for endogenous smooth muscle cell markers by immunostaining. As shown in figure 7-11, both C2-*ATP13A3*^{WT} control and C2-*ATP13A3*^{R858H} iPSC derived smooth muscle cells abundantly expressed both smooth muscle actin (SMA) and myosin heavy chain (MHC), indicating the successful generation of iPSC-SMCs.

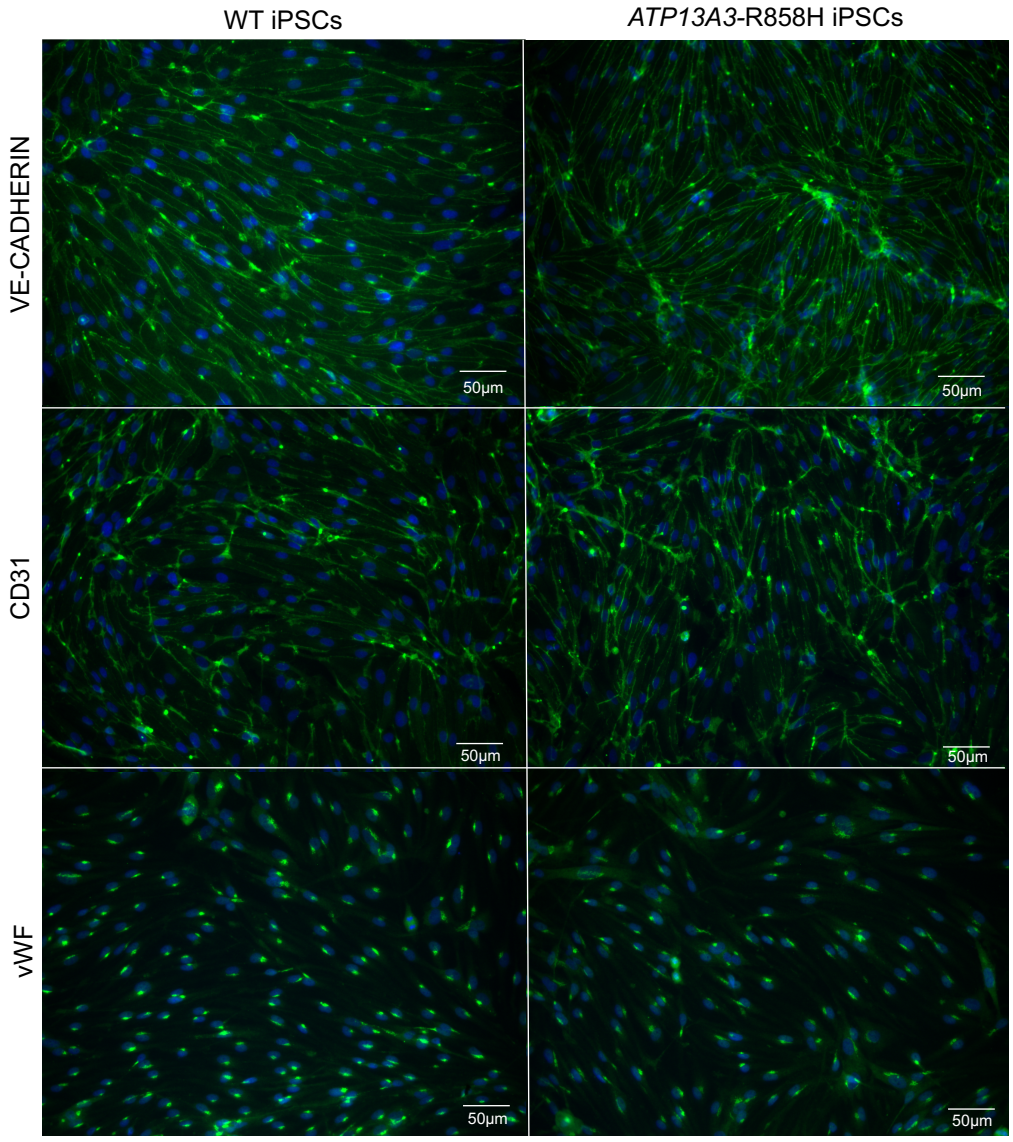

Figure 7-6 Immunostaining of endothelial markers in C2-ATP13A3WT and C2-ATP13A3R858H iPSC-derived endothelial cells (iPSC-ECs)

C2-*ATP13A3*^{WT} and C2-*ATP13A3*^{R858H} iPSC-ECs, following differentiation, were seeded into 4 chamber slides (Thermo fisher Scientific) at a density of 50,000/well and stained for the endothelial markers: VE-Cadherin, CD31, von Willebrand factor (VWF) (BD Biosciences) (Green) overnight. Nuclei were counterstained with DAPI (Blue) before visualisation (20X magnification, scale bar = 50µm) using a Leica DMI3000 B manual inverted microscope (N=3).

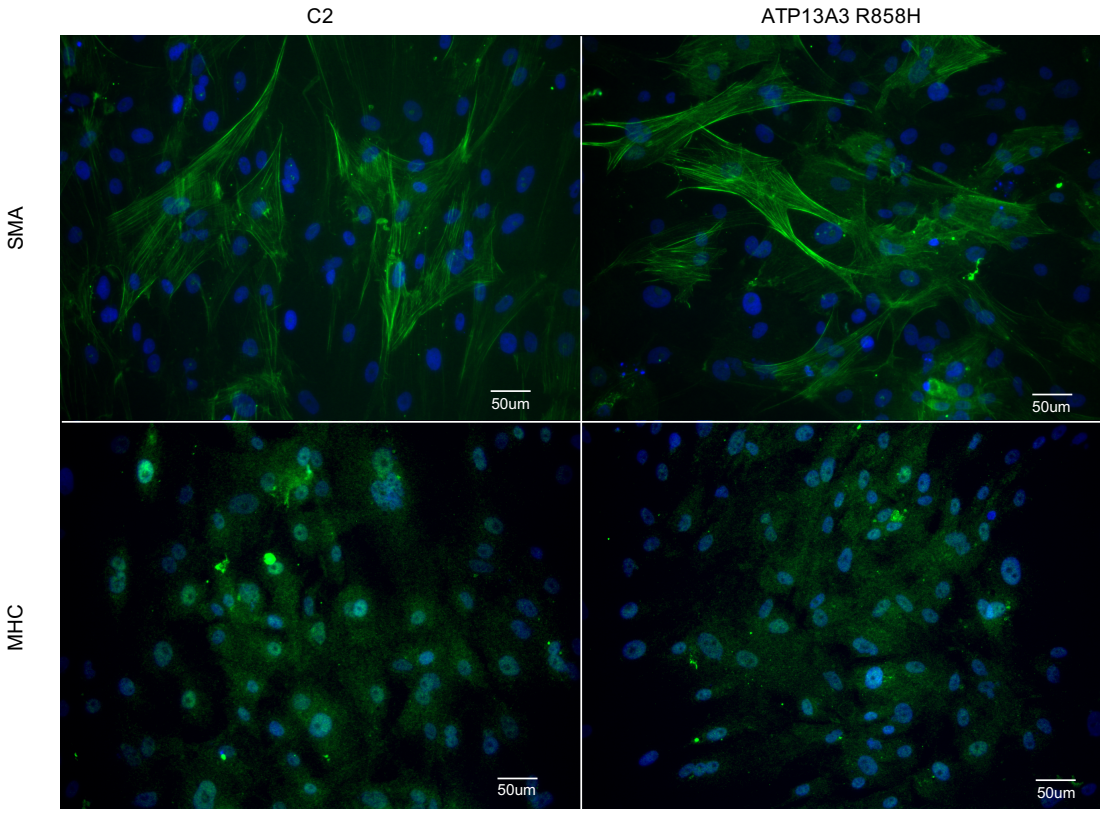

Figure 7-7 Immunostaining of smooth muscle markers in C2-ATP13A3WT and C2-ATP13A3R858H iPSC-derived smooth muscle cells (iPSC-SMCs)

C2-*ATP13A3*^{WT} and C2-*ATP13A3*^{R858H} iPSC-SMCs, following differentiation, were seeded into 4 chamber slides (Thermo fisher Scientific) at a density of 50,000/well and stained with the smooth muscle markers: smooth muscle actin (SMA) and myosin heavy chain (MHC) (Sigma-Aldrich) (Green) overnight. Nuclei were counterstained with DAPI (Blue) before being visualised (20X magnification, scale bar = 50μm) using a Leica DMI3000 B manual inverted microscope (N=3).

7.2.5 C2-*ATP13A3*^{R858H} iPSC-ECs did not display a pro-apoptotic phenotype in comparison to C2-*ATP13A3*^{WT} iPSC-ECs

As demonstrated in Chapter 3, *ATP13A3* silencing by siRNA increased the rate of apoptosis in hPAECs. Therefore, to assess the impact of this missense *ATP13A3* mutation on endothelial cell apoptosis, C2-*ATP13A3*^{R858H} iPSCs and C2-*ATP13A3*^{WT} control iPSCs were differentiated into endothelial cells in parallel and assessed for cell apoptosis following serum-free exposure. As shown in Figure 7-12, unlike *ATP13A3* deficiency in hPAECs, C2-*ATP13A3*^{R858H} iPSC-ECs displayed similar Caspase3/7 Glo activity to C2-*ATP13A3*^{WT} control iPSC-ECs both under E+ complete media or serum-free EBM2 (Figure 7-12).

7.2.6 The R858H missense mutation does not affect *ATP13A3* expression or polyamine uptake capacity in the C2-*ATP13A3*^{R858H} iPSCs

Since I have observed that C2-*ATP13A3*^{R858H} iPSCs exhibited similar cellular apoptosis rates to C2-*ATP13A3*^{WT} wild type iPSCs, I then questioned if the mutation affects *ATP13A3* expression and cellular polyamine uptake. RNA samples were directly isolated from iPSC lines without further differentiation. qPCR data reveals a similar *ATP13A3* mRNA level between the two iPSC lines, indicating the missense mutation (R858H) does not cause transcriptional disruption of *ATP13A3* (figure 7-13). To assess the polyamine uptake capacity, both iPSC lines were cultured in iPSC culture media (recipe listed in chapter 2, appendix) with or without the addition of 1mM putrescine, 10 μM spermidine and 10μM spermine overnight. As shown in Figure 7-13, both C2-*ATP13A3*^{WT} and C2-*ATP13A3*^{R858H} iPSCs display similar cellular polyamine levels either in the basal condition or following polyamine supplementation. These suggest that the R858H mutation does not cause an overt impairment of cellular polyamine transport.

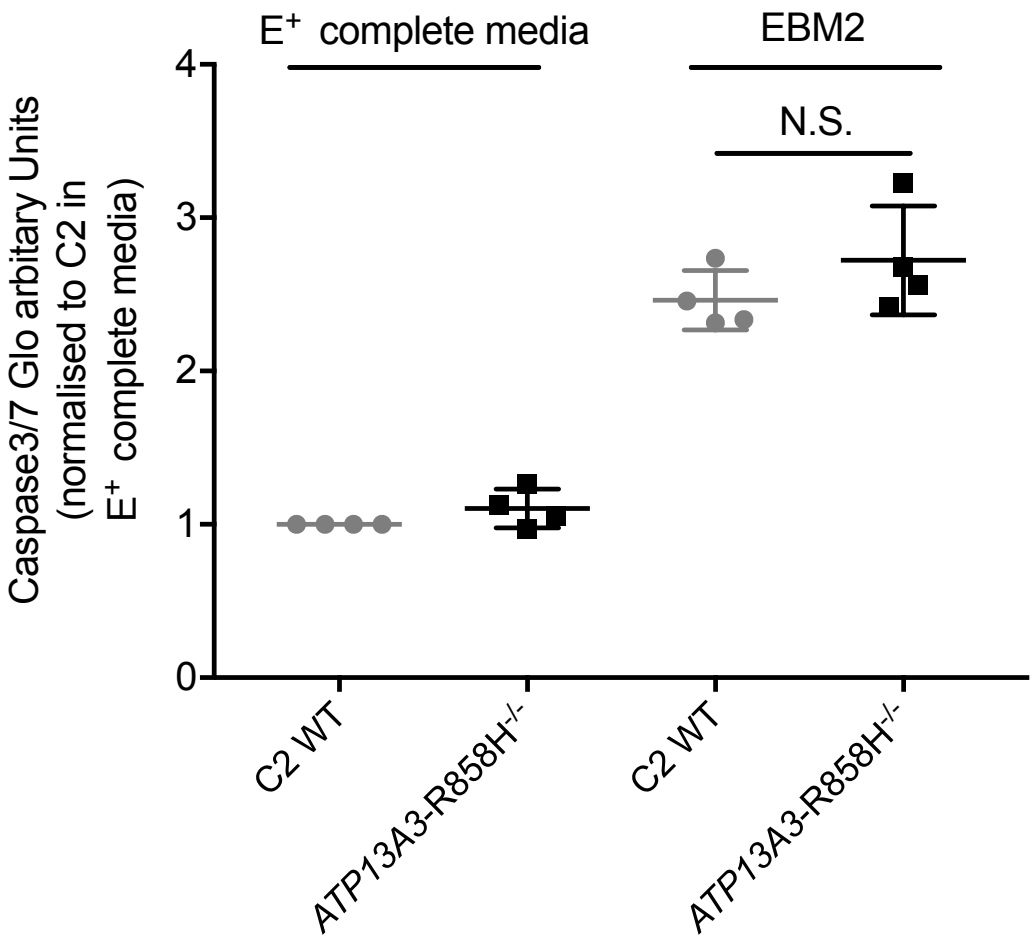

Figure 7-8 Caspase3/7 Glo activities of iPSC-EC differentiated from C2-ATP13A3R858H and C2-ATP13A3WT iPSCs

C2-*ATP13A3*^{R858H} iPSC-ECs and control C2-*ATP13A3*^{WT} iPSC-ECs were seeded into 96-well plates at a density of 15,000/well before being exposed to either E+ complete media (Chapter 2, appendix) or serum-free EBM2 overnight. Cellular apoptosis was assessed by Caspase3/7 Glo (Promega) (N=4). Data are presented as fold-change normalised to the raw value of C2-*ATP13A3*^{WT} control iPSC-ECs cultured in E+ complete media for each experiment. Two-tailed Student's t-test was used for statistical analysis

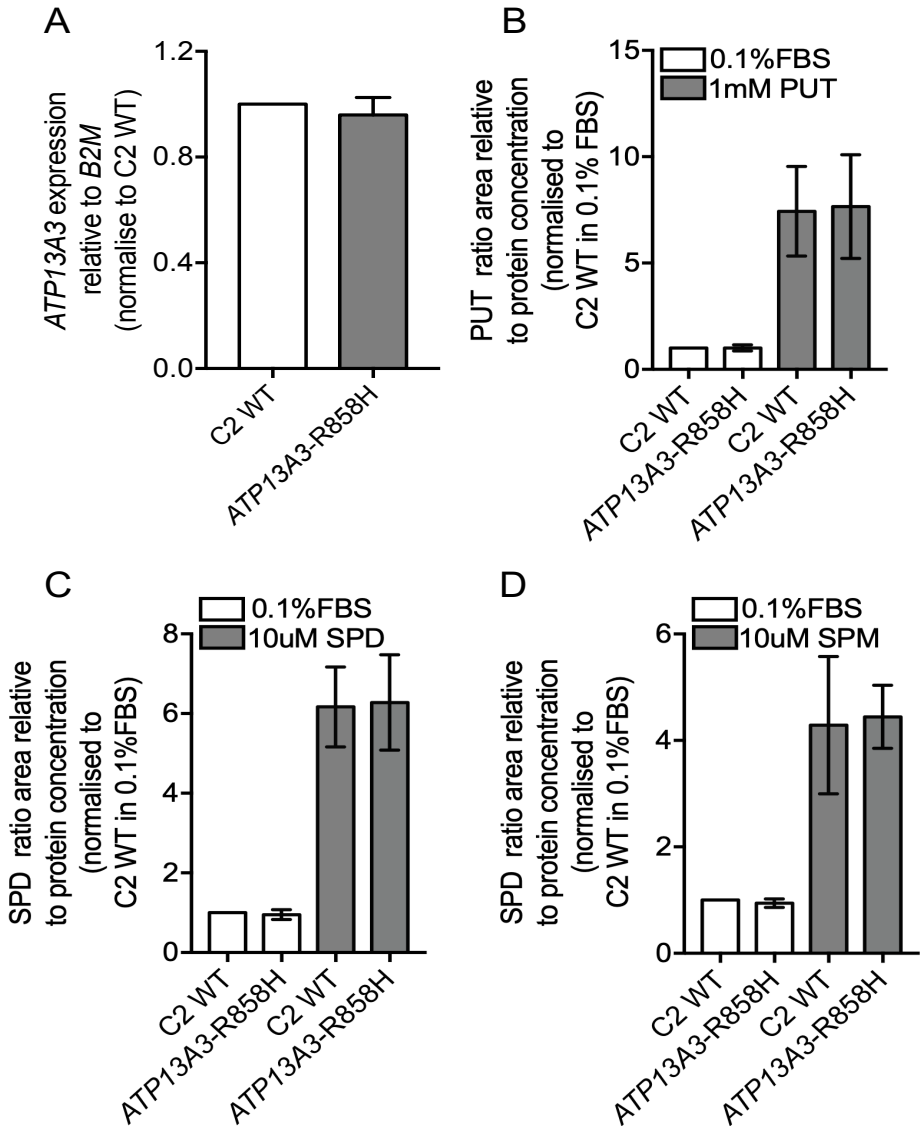

Figure 7-9 ATP13A3 mRNA expression and polyamine uptake capacity of C2-ATP13A3WT and C2-ATP13A3R858H iPSCs (A) ATP13A3 mRNA expression in C2-ATP13A3WT and C2-ATP13A3R858H iPSCs (N=3). Data are presented as fold change relative to B2M and further normalised to C2 wild type (WT) in 0.1%FBS. C2-ATP13A3WT and C2-ATP13A3R858H iPSCs were cultured in 0.1%FBS EBM2 with or without the addition of 1mM putrescine, 10μM spermidine and 10μM spermine overnight. Cellular (B) putrescine (C) spermidine and (D) spermine levels were measured using LC-MS (N=3) and data are presented as the polyamine peak area ratio relative to sample protein concentration, and further normalised to the C2-ATP13A3WT (WT) control in 0.1%FBS. Two-tailed Student's t-test was used for statistical analysis between C2-ATP13A3WT and C2-ATP13A3R858H iPSC.

7.3 Discussion

In this chapter, I have demonstrated the generation of an iPSC subclone harbouring an *ATP13A3* missense mutation (R858H). Comparison of this mutant iPSC line with the isogenic wild-type parental line enables the assessment of the functional impact of specific mutations without the confounding aspect of genetic and epigenetic variation between biological replicates from controls and disease patients. *Atp13a3* was previously reported to be highly expressed during mouse embryonic development [156], indicating a potential role in organogenesis. Here, the introduction of the R858H mutation did not affect the pluripotency of the iPSC line as revealed by immunostaining of Nanog, OCT4 and Tra1-60. Additionally, the C2-*ATP13A3*^{R858H} iPSC line was also able to successfully differentiate into endothelial and smooth muscle cells. However, unlike *ATP13A3* knockdown in hPAECs, the *ATP13A3*-R858H mutation alone did not lead to exaggerated apoptosis in iPSC-ECs. One explanation would be that the R858H missense mutation causes a milder impairment on *ATP13A3* function, without affecting its expression. Moreover, C2-*ATP13A3*^{R858H} iPSCs also exhibit similar polyamine uptake capacity to the isogenic parental C2-*ATP13A3*^{WT} control line. Of note, hPAECs overexpressing the *ATP13A3*-R858H mutation displayed a less robust reduction of putrescine uptake compared with the impact of the catalytically inactivated *ATP13A3* mutant (D498N), suggesting the R858H mutant might have a mild effect (Chapter 4).

So far, genetic studies [19, 27, 348] in F/HPAH cohorts have revealed an autosomal dominant transmission of gene variants with incomplete penetrance in PAH patients. Although *BMPR2* mutations account for 70–80% of familial [328] and 10–20% of sporadic PAH cases [329], the disease penetrance only ranges between 14-42% [348, 349]. The heterozygous R858H mutation was identified from a PAH patient and chosen for the generation of the mutant iPSC line, which is a lengthy process. My parallel overexpression experiments have suggested that this may represent a mild mutation. If I were to generate a

second mutant line, I would select one of those mutations identified as having a stronger effect in my in vitro assays. However, it is also possible that the R858H missense mutation serves as predisposing mutation, and additional disease-promoting stimuli are required for disease occurrence. Recently, Lerche M et al.[109]has reported that an IFN-β induced PAH case in a multiple sclerosis patient with a nonsense *ATP13A3* mutation (Glu514*). The fact that withdrawing IFN-β improved PAH symptoms in this patient suggests that additional factors may confer PAH development in *ATP13A3* mutation carriers. Interestingly, type I interferon was shown to induce the development of PAH in the mouse by activating Interferon Alpha and Beta Receptor Subunit 1 (IFNAR1) [350]. The IFNAR1 protein is rapidly turned over via internalization and recycling through the endocytic system [351]. Therefore, investigating a potential link between ATP13A3 and IFNAR1, especially in the presence of type I interferon may be informative in uncovering the underlying mechanism of *ATP13A3* mutations penetrance in PAH pathobiology. This could be assessed in C2-*ATP13A3*^{R858H} iPSCs and compared to the response in C2-*ATP13A3*^{WT} iPSCs. Interestingly, I have demonstrated an upregulation of *ATP13A3* mRNA by IL-1β in hPASMC (chapter 5). However, how this may affect polyamine dysregulation is still unknown, especially on the background of an *ATP13A3* mutation. Additionally, cells with or without genetic defects may respond to stimuli differently. For example, the transcriptional fingerprint of hPASMCs bearing *BMPR2* mutation in response to TGFβ is distinct to control hPASMCs [165], with TGFβ–dependent upregulation of *ATP13A3* mRNA transcription observed in mutant, but not in control hPASMCs (Chapter 5). Elevated plasma IL-1β level was also documented in PAH patients and correlated with worse clinical outcomes [74]. In addition, both in vivo [352, 353] and in vitro [354-356] data have suggested IL-1β as a potent inflammatory disease driver for PAH. Therefore, to investigate the response to IL-1β in C2-*ATP13A3*^{R858H} iPSCs and in C2-*ATP13A3*^{WT} iPSCs and how this affects cellular polyamine levels may lead to a further understanding of *ATP13A3* mutation in PAH pathogenesis.

Chapter 8 General Discussion and Future Work

8.1 Summary of findings and limitations

Pulmonary arterial hypertension (PAH) is a devastating vascular disorder characterised by the progressive remodelling of small pulmonary arteries. Although the aetiologies of PAH can be diverse, genetic defects are a major cause, accounting for approximately one-third of the IPAH patient population [31, 357]. Recently, *ATP13A3*, the gene encoding an enigmatic cation transporter, was identified as a novel PAH associated gene [27]. My thesis focussed mainly on characterising the functions of *ATP13A3* in the pulmonary vasculature and the underlying mechanism of how disease-associated mutations contribute to PAH pathogenesis.

Some prior evidence has suggested a tentative link between ATP13A3 and polyamines [139, 147]. Similar to that in Hela cells [141], ATP13A3 was shown to reside in the recycling endosome of endothelial cells. This is consistent with ATP13A3 being a cellular polyamine transporter as the endocytic system is proposed to be essential for polyamine trafficking [190]. Indeed, my studies of cellular polyamine measurement revealed ATP13A3 as mediating polyamine transporter in endothelial cells with a higher selectivity towards putrescine than spermidine and spermine (Chapter 4). In addition to transport, ATP13A3 deficiency in endothelial cells also affects polyamine metabolism, manifesting by post-translational upregulation of ODC1.

Polyamines are essential for cell growth [104, 171] while their depletion causes cell cycle arrest [191]. In line with these findings, I observed that *ATP13A3* deficiency, by reducing cellular polyamine content (Chapter 4), suppressed vascular cell proliferation and downregulated *cyclin A, E and B* mRNA expression in BOECs (Chapter 3). The reduction of these cyclins, but not cyclin D, suggests repression of G1-S transition and DNA synthesis. Aside from affecting cell proliferation, *ATP13A3* loss also predisposed endothelial

cells to apoptosis. One potential explanation for this finding includes the polyamine reduction via ATP13A3 loss as decreased polyamines may promote cell apoptosis under pathogenic insults [310][311]. ODC overproduction might also play a part in the apoptosis driven by ATP13A3 loss, since high ODC level was reported in cells undergoing apoptosis [308][309]. However, DFMO co-administration only partially reversed this apoptotic phenotype, suggesting that EC apoptosis driven by ATP13A3 deficiency is more likely related to the polyamine deficiency rather than ODC overproduction. Moreover, I also observed that *ATP13A3* loss exacerbated thrombin-dependent hPAECs monolayer permeability. Interestingly, studies have demonstrated polyamines as crucial factors for maintaining cell-cell junctions [244][245]. Therefore, further investigations of the impact of ATP13A3 loss on adherens or tight junction molecules, such as VE-Cadherin and Zo-1, may provide further mechanistic insights.

Having demonstrated that ATP13A3 deficiency can disrupt endothelial homeostasis, I next sought to characterise the functional impacts of PAH-associated ATP13A3 mutations using a lentiviral overexpression system. Interestingly, L675V, M850I, V885M mutations exhibited substantial impairment on ATP13A3 mediated putrescine uptake while the impacts of R858H, L965P were milder. A disadvantage of using overexpression systems for characterising mutations is that it might not represent the endogenous biological state. As a surrogate, BOECs generated from a PAH patient bearing an *ATP13A3* frameshift mutation (LK726X) were characterised. Importantly, LK26X, by reducing ATP13A3 expression via nonsense-mediated mRNA decay of the mutant transcript, recapitulated the pathological phenotypes such as reduced putrescine uptake and increased apoptosis observed in ATP13A3-deficent BOECs. These findings reinforced the hypothesis that genetic defects in ATP13A3 participate in PAH pathobiology via the disruption of polyamine homeostasis. However, cells derived from PAH-patients may have acquired disease-associated somatic changes such as DNA damage [84, 340].

Therefore, to functionally assess specific mutations without confounding these aspects, an iPSC subclone harbouring an *ATP13A3* missense mutation (R858H) was generated. However, R858H did not affect polyamine uptake capacity, nor did it exacerbate apoptosis in *ATP13A3*^{R858H} iPSC-ECs. A likely explanation is that R858H impairs *ATP13A3* function only mildly, supported by no disruption on *ATP13A3* expression and a marginal reduction of putrescine uptake in hPAECs (Chapter 4). In this context, incomplete disease penetrance for *ATP13A3* missense mutations, similar to *BMPR2* [348], might mean that additional stimuli are required to reveal disease-associated phenotypes. Of note, IFN-β promoted PAH in a multiple sclerosis patient harbouring a nonsense *ATP13A3* mutation (Glu514*) [109]. Therefore, the impact of IFN-β on the function of C2-*ATP13A3*^{R858H} warrants further investigation. Collectively, the in vitro data generated in my studies have demonstrated that ATP13A3 is a polyamine transporter with a higher preference towards putrescine. ATP13A3 deficiency or mutation, by affecting cell polyamine homeostasis, leads to endothelial dysfunction. These findings provide strong evidence for a pathogenic link between ATP13A3 genetic defects and PAH, providing new insights into the involvement of polyamine dysregulation in the pathobiology of PAH.

Adding to my in vitro data, in collaboration with Dr. Ekaterina Legchenko, we have observed elevated RVSP in mice with the *Atp13a3*$^{P452Lfs/P452Lfs}$ frameshift mutation compared to wild-type litter mates at 6 months of age. The mutant mice have reduced *Atp13a3* expression in their lungs, suggesting a link between Atp13a3 loss of function and hemodynamic alterations. Although preliminary, I have also observed lower polyamine contents in the lungs of *Atp13a3*$^{P452Lfs/P452Lfs}$ and *Atp13a3*$^{P452Lfs/+}$ mice compared to their wild type littermates. At first glance, these findings contradict the elevated lung polyamine contents reported in MCT [358]and hypoxia-induced PH [255]. However, the polyamine elevation observed in these PH models may represent a “by-product” of advanced disease due to upregulation of their lung polyamine

transport (hypoxia) or polyamine synthesis (MCT). Conversely, genetic rodent models may provide a "cleaner" system for investigating the pathobiology of PAH and our data suggest that, *Atp13a3*$^{P452Lfs/P452Lfs}$ mice spontaneously develop PAH-like hemodynamic changes. Given that *ATP13A3* deficiency (Chapter 4) increased ODC in endothelial cells and inhibition with DFMO alleviated the apoptosis triggered by ornithine, the regulation and therapeutic inhibition of *Odc* warrants investigation. Furthermore, polyamine dysregulation has been documented in human PAH via metabolomic profiling of human lung samples [258] or plasma samples [259], so analysis of plasma polyamine contents in PAH patients harbouring *ATP13A3* mutations may be informative. This might also be assessed regarding correlation to ATP13A3 expression in blood-derived cells from these PAH patients to explore a potential broader role of ATP13A3 dysregulation in the pathogenesis of PAH.

8.2 Conclusions and Future directions

In my studies, I have demonstrated that ATP13A3, residing in the recycling endosome, functions as a polyamine transporter in human vascular endothelial cells with putrescine as the preferred substrate. Deficiency of ATP13A3 induces endothelial dysfunction via the impairment of polyamine transport and subsequent ODC overproduction. PAH-associated ATP13A3 mutations compromise polyamine homeostasis and hence promote PAH. Notably, BOECs isolated from a PAH patient harbouring a frameshift ATP13A3^{LK726X} mutation exhibited disease-associated phenotypes, possibly due to the disruption of cellular polyamine homeostasis. Collectively, these findings suggest a crucial role of ATP13A3 in maintaining vascular homeostasis with pathogenic mutations in the gene contributing to the pathobiology of PAH.

Based on the current findings, the investigation of ATP13A3 and its role in PAH might proceed in a number of directions.

8.2.1 Biochemical characterisation of ATP13A3

Although I have demonstrated that ATP13A3 mediates polyamine uptake in vascular cells, a potential disadvantage of unlabelled polyamine supplementation combined with cellular polyamine measurement is that it does not exclude the possibility of compensation by polyamine metabolism. Therefore, further validation using supplementation with fluorescent-labelled (Bodipy-) or radioactive-labelled polyamines would further strengthen my findings.

Additionally, characterising the biochemical transport function of ATP13A3 regarding to the aspartyl site autophosphorylation/dephosphorylation and the activation of ATP hydrolysis, both of which are heavily reliant on substrate binding, requires further study. These can be examined via [γ-32P] ATP based autophosphorylation assay using full-length ATP13A3 purified in a yeast overexpression system [141] or a luminescence ATPase activity assay using cell microsomal fractionation [148]. These two assays will enable a further comparison of the preferable polyamine for ATP13A3, and provide a means to screening additional transport substrates. Once developed, these together with the LC-MS based assay I have demonstrated earlier, may facilitate a more comprehensive functional assessment of the PAH associated mutations in ATP13A3.

8.2.2 ATP13A3 in human pulmonary arterial smooth muscle cells

My current study has mainly focussed on investigating the role of ATP13A3 in endothelial cells. However, hPASMC dysfunction also contributes to the pathogenesis of PAH. Preliminary data from my study suggests that ATP13A3 deficiency reduces hPASMCs growth, but whether this is due to disrupted

polyamine homeostasis is unclear. Notably, unlike endothelial cells, ODC protein was not increased by ATP13A3 deficiency in hPASMCs, which may indicate either a heavier reliance on the polyamine biosynthesis or a different substrate preference by ATP13A3 in hPASMC. Therefore, a comprehensive assessment of whether ATP13A3 mediates polyamine transport and its substrate specificity in hPASMCs would be informative. Interestingly, spermine was recently shown to induce hPASMC proliferation via the upregulation of spermine synthase (SMS) [360], so investigation of a potential link between ATP13A3 and SMS would also provide a further direction for exploring polyamine dysregulation in PAH.

8.2.3 *Atp13a3* P452Lfs mice

Promisingly, we observe an elevated RVSP in *Atp13a3* P452Lfs mice at 6-months of age. However, deeper phenotyping of these mice is required, including lung morphometric analysis of these mice to assess vessel remodelling. Moreover, as the hemodynamic elevation presents at 6-months of age, but not 3 months, it would be interesting to track the polyamine changes over time to establish if polyamine dysregulation might contribute to the disease phenotype. Furthermore, as observed in my in vitro study, ATP13A3 deficiency causes substantial upregulation of endothelial ODC, so determination of Odc expression in endothelial cells from the *Atp13a3*^{P452Lfs}.mice would be of interest. If endothelial Odc is elevated, the therapeutic potential of targeting ODC by DFMO in these mice would be assessed. Finally, as BMP9 selectively induces *ATP13A3* mRNA expression in BOECs, a proof-of-concept study to enhance the expression of the non-mutated *Atp13a3* allele with BMP9 in heterozygous *Atp13a3*$^{P452Lfs/+}$ mice and assess how it affects polyamine homeostasis and disease progression would be interesting.

Reference

1. Hatano, S., T. Strasser, and W.H. Organization, *Primary pulmonary hypertension: report on a WHO meeting, Geneva, 15-17 October 1973*. 1975: World Health Organization.
2. Kovacs, G., A. Berghold, S. Scheidl, and H. Olschewski, *Pulmonary arterial pressure during rest and exercise in healthy subjects: a systematic review.* Eur Respir J, 2009. **34**(4): p. 888-894.
3. Valerio, C.J., et al., *Borderline mean pulmonary artery pressure in patients with systemic sclerosis: transpulmonary gradient predicts risk of developing pulmonary hypertension.* Arthritis Rheum, 2013. **65**(4): p. 1074-1084.
4. Douschan, P., et al., *Mild elevation of pulmonary arterial pressure as a predictor of mortality.* Am J Respir Crit Care Med, 2018. **197**(4): p. 509-516.
5. Yıldızeli, Ş.O., et al., *Pulmonary endarterectomy for patients with chronic thromboembolic disease.* Anatolian journal of cardiology, 2018. **19**(4): p. 273.
6. Simonneau, G., et al., *Haemodynamic definitions and updated clinical classification of pulmonary hypertension.* Eur Respir J, 2019. **53**(1).
7. Humbert, M., et al., *Pulmonary arterial hypertension in France: results from a national registry.* Am J Respir Crit Care Med, 2006. **173**(9): p. 1023-1030.
8. Peacock, A., et al., *An epidemiological study of pulmonary arterial hypertension.* Eur Respir J, 2007. **30**(1): p. 104-109.
9. Thenappan, T., S.J. Shah, S. Rich, and M. Gomberg-Maitland, *A USA-based registry for pulmonary arterial hypertension: 1982–2006.* Eur Respir J, 2007. **30**(6): p. 1103-1110.
10. Badesch, D.B., et al., *Pulmonary arterial hypertension: baseline characteristics from the REVEAL Registry.* Chest, 2010. **137**(2): p. 376-387.
11. Humbert, M., et al., *Pathology and pathobiology of pulmonary hypertension: state of the art and research perspectives.* Eur Respir J, 2019. **53**(1).
12. Tuder, R.M., et al., *Pathology of pulmonary hypertension.* Clin Chest Med, 2007. **28**(1): p. 23-42.
13. Tuder, R.M., et al., *Development and pathology of pulmonary hypertension.* J Am Coll Cardiol, 2009. **54**(1 Supplement): p. S3-S9.
14. Humbert, M., *Pulmonary arterial hypertension and chronic thromboembolic pulmonary hypertension: pathophysiology.* European Respiratory Review, 2010. **19**(115): p. 59-63.
15. Simonneau, G., A. Torbicki, P. Dorfmüller, and N. Kim, *The pathophysiology of chronic thromboembolic pulmonary hypertension.* European Respiratory Review, 2017. **26**(143): p. 160112.

16. Atkinson, C., et al., *Primary pulmonary hypertension is associated with reduced pulmonary vascular expression of type II bone morphogenetic protein receptor.* Circulation, 2002. **105**(14): p. 1672-1678.
17. von Romberg, E., *Über sklerose der lungenarterie.* Dtsch Arch Klin Med, 1891. **48**: p. 197-206.
18. Loyd, J., R. Primm, and J. Newman, *Transmission of familial primary pulmonary hypertension.* Am Rev Respir Dis, 1984. **129**: p. 194-197.
19. Lane, K.B., et al., *Heterozygous germline mutations in BMPR2, encoding a TGF-β receptor, cause familial primary pulmonary hypertension.* Nat Genet, 2000. **26**(1): p. 81-84.
20. Trembath, R.C., et al., *Clinical and molecular genetic features of pulmonary hypertension in patients with hereditary hemorrhagic telangiectasia.* N Engl J Med, 2001. **345**(5): p. 325-334.
21. Chaouat, A., et al., *Endoglin germline mutation in a patient with hereditary haemorrhagic telangiectasia and dexfenfluramine associated pulmonary arterial hypertension.* Thorax, 2004. **59**(5): p. 446-448.
22. Nasim, M.T., et al., *Molecular genetic characterization of SMAD signaling molecules in pulmonary arterial hypertension.* Hum Mutat, 2011. **32**(12): p. 1385-1389.
23. Shintani, M., et al., *A new nonsense mutation of SMAD8 associated with pulmonary arterial hypertension.* J Med Genet, 2009. **46**(5): p. 331-337.
24. Austin, E.D., et al., *Whole exome sequencing to identify a novel gene (caveolin-1) associated with human pulmonary arterial hypertension.* Circ Cardiovasc Genet, 2012. **5**(3): p. 336-343.
25. Ma, L., et al., *A novel channelopathy in pulmonary arterial hypertension.* N Engl J Med, 2013. **369**: p. 351-361.
26. Kerstjens-Frederikse, W.S., et al., *TBX4 mutations (small patella syndrome) are associated with childhood-onset pulmonary arterial hypertension.* J Med Genet, 2013. **50**(8): p. 500-506.
27. Gräf, S., et al., *Identification of rare sequence variation underlying heritable pulmonary arterial hypertension.* Nature communications, 2018. **9**(1): p. 1-16.
28. Eyries, M., et al., *Widening the landscape of heritable pulmonary hypertension mutations in paediatric and adult cases.* Eur Respir J, 2019. **53**(3).
29. Hodgson, J., et al., *Characterization of GDF2 mutations and levels of BMP9 and BMP10 in pulmonary arterial hypertension.* Am J Respir Crit Care Med, 2020. **201**(5): p. 575-585.
30. Morrell, N.W., et al., *Genetics and genomics of pulmonary arterial hypertension.* Eur Respir J, 2019. **53**(1): p. 1801899.
31. Southgate, L., R.D. Machado, S. Gräf, and N.W. Morrell, *Molecular genetic framework underlying pulmonary arterial hypertension.* Nature Reviews Cardiology, 2019: p. 1-11.

32. Humbert, M., et al., *Cellular and molecular pathobiology of pulmonary arterial hypertension.* J Am Coll Cardiol, 2004. **43**(12 Supplement): p. S13-S24.
33. Tuder, R.M., et al., *The pathobiology of pulmonary hypertension: endothelium.* Clin Chest Med, 2001. **22**(3): p. 405-418.
34. Giaid, A. and D. Saleh, *Reduced expression of endothelial nitric oxide synthase in the lungs of patients with pulmonary hypertension.* N Engl J Med, 1995. **333**(4): p. 214-221.
35. Gaine, S.P. and L.J. Rubin, *Primary pulmonary hypertension.* The Lancet, 1998. **352**(9129): p. 719-725.
36. Hervé, P., et al., *Increased plasma serotonin in primary pulmonary hypertension.* The American journal of medicine, 1995. **99**(3): p. 249-254.
37. Rabinovitch, M., *Pathobiology of pulmonary hypertension.* Annu Rev Pathol Mech Dis, 2007. **2**: p. 369-399.
38. Tuder, R.M. and K.R. Stenmark, *Perspective: pathobiological paradigms in pulmonary hypertension, time for reappraisal.* American Journal of Physiology-Lung Cellular and Molecular Physiology, 2020. **318**(6): p. L1131-L1137.
39. Long, L., et al., *Selective enhancement of endothelial BMPR-II with BMP9 reverses pulmonary arterial hypertension.* Nat Med, 2015. **21**(7): p. 777.
40. Thenappan, T., M.L. Ormiston, J.J. Ryan, and S.L. Archer, *Pulmonary arterial hypertension: pathogenesis and clinical management.* BMJ, 2018. **360**: p. j5492.
41. Xue, C., M. Sowden, and B.C. Berk, *Extracellular cyclophilin A, especially acetylated, causes pulmonary hypertension by stimulating endothelial apoptosis, redox stress, and inflammation.* Arterioscler Thromb Vasc Biol, 2017. **37**(6): p. 1138-1146.
42. Farkas, D., et al., *Toll-like receptor 3 is a therapeutic target for pulmonary hypertension.* Am J Respir Crit Care Med, 2019. **199**(2): p. 199-210.
43. Agarwal, S., H. Sharma, L. Chen, and N.K. Dhillon, *NADPH oxidase-mediated endothelial injury in HIV-and opioid-induced pulmonary arterial hypertension.* American Journal of Physiology-Lung Cellular and Molecular Physiology, 2020. **318**(5): p. L1097-L1108.
44. Wilson, D.W., et al., *Mechanisms and pathology of monocrotaline pulmonary toxicity.* Crit Rev Toxicol, 1992. **22**(5-6): p. 307-325.
45. Taraseviciene-Stewart, L., et al., *Inhibition of the VEGF receptor 2 combined with chronic hypoxia causes cell death-dependent pulmonary endothelial cell proliferation and severe pulmonary hypertension.* The FASEB Journal, 2001. **15**(2): p. 427-438.
46. Campbell, A.I., Y. Zhao, R. Sandhu, and D.J. Stewart, *Cell-based gene transfer of vascular endothelial growth factor attenuates monocrotaline-*

induced pulmonary hypertension. Circulation, 2001. **104**(18): p. 2242-2248.

47. Partovian, C., et al., *Adenovirus-mediated lung vascular endothelial growth factor overexpression protects against hypoxic pulmonary hypertension in rats.* Am J Respir Cell Mol Biol, 2000. **23**(6): p. 762-771.
48. Teichert-Kuliszewska, K., et al., *Bone morphogenetic protein receptor-2 signaling promotes pulmonary arterial endothelial cell survival: implications for loss-of-function mutations in the pathogenesis of pulmonary hypertension.* Circ Res, 2006. **98**(2): p. 209-217.
49. Masri, F.A., et al., *Hyperproliferative apoptosis-resistant endothelial cells in idiopathic pulmonary arterial hypertension.* American Journal of Physiology-Lung Cellular and Molecular Physiology, 2007. **293**(3): p. L548-L554.
50. Caruso, P., et al., *Identification of microRNA-124 as a major regulator of enhanced endothelial cell glycolysis in pulmonary arterial hypertension via PTBP1 (polypyrimidine tract binding protein) and pyruvate kinase M2.* Circulation, 2017. **136**(25): p. 2451-2467.
51. Jurasz, P., D. Courtman, S. Babaie, and D.J. Stewart, *Role of apoptosis in pulmonary hypertension: from experimental models to clinical trials.* Pharmacol Ther, 2010. **126**(1): p. 1-8.
52. Burton, V.J., et al., *Bone morphogenetic protein receptor II regulates pulmonary artery endothelial cell barrier function.* Blood, 2011. **117**(1): p. 333-341.
53. Eddahibi, S., et al., *Imbalance between platelet VEGF and PDGF in pulmonary hypertension, effects of prostacyclin infusion.* Am J Respir Crit Care Med, 2000. **162**: p. 1493-1499.
54. Tuder, R.M. and N.F. Voelkel, *Plexiform lesion in severe pulmonary hypertension: association with glomeruloid lesion.* The American journal of pathology, 2001. **159**(1): p. 382.
55. Nagashima, T., et al., *BMPR2 is required for postimplantation uterine function and pregnancy maintenance.* The Journal of clinical investigation, 2013. **123**(6): p. 2539-2550.
56. Hwangbo, C., et al., *Modulation of endothelial bone morphogenetic protein receptor type 2 activity by vascular endothelial growth factor receptor 3 in pulmonary arterial hypertension.* Circulation, 2017. **135**(23): p. 2288-2298.
57. Huertas, A., et al., *Immune dysregulation and endothelial dysfunction in pulmonary arterial hypertension: a complex interplay.* Circulation, 2014. **129**(12): p. 1332-1340.
58. Soon, E., et al., *Bone morphogenetic protein receptor type II deficiency and increased inflammatory cytokine production. A gateway to pulmonary arterial hypertension.* Am J Respir Crit Care Med, 2015. **192**(7): p. 859-872.

59. Le Hiress, M., et al., *Proinflammatory signature of the dysfunctional endothelium in pulmonary hypertension. Role of the macrophage migration inhibitory factor/CD74 complex.* Am J Respir Crit Care Med, 2015. **192**(8): p. 983-997.
60. Ricard, N., et al., *Increased Pericyte coverage mediated by endothelial-derived fibroblast growth Factor-2 and Interleukin-6 is a source of smooth muscle–like cells in pulmonary hypertension.* Circulation, 2014. **129**(15): p. 1586-1597.
61. Yang, X., et al., *Dysfunctional Smad signaling contributes to abnormal smooth muscle cell proliferation in familial pulmonary arterial hypertension.* Circ Res, 2005. **96**(10): p. 1053-1063.
62. Hurst, L.A., et al., *TNFα drives pulmonary arterial hypertension by suppressing the BMP type-II receptor and altering NOTCH signalling.* Nature communications, 2017. **8**(1): p. 1-14.
63. Savai, R., et al., *Pro-proliferative and inflammatory signaling converge on FoxO1 transcription factor in pulmonary hypertension.* Nat Med, 2014. **20**(11): p. 1289-1300.
64. Suzuki, Y.J., et al., *Activation of GATA-4 by serotonin in pulmonary artery smooth muscle cells.* J Biol Chem, 2003. **278**(19): p. 17525-17531.
65. Biasin, V., et al., *Endothelin-1 driven proliferation of pulmonary arterial smooth muscle cells is c-fos dependent.* The international journal of biochemistry & cell biology, 2014. **54**: p. 137-148.
66. Tajsic, T. and N.W. Morrell, *Smooth muscle cell hypertrophy, proliferation, migration and apoptosis in pulmonary hypertension.* Comprehensive Physiology, 2010. **1**(1): p. 295-317.
67. Shimoda, L.A. and S.S. Laurie, *Vascular remodeling in pulmonary hypertension.* J Mol Med, 2013. **91**(3): p. 297-309.
68. Barst, R.J., *PDGF signaling in pulmonary arterial hypertension.* The Journal of clinical investigation, 2005. **115**(10): p. 2691-2694.
69. Hoeper, M.M., et al., *Imatinib mesylate as add-on therapy for pulmonary arterial hypertension: results of the randomized IMPRES study.* Circulation, 2013. **127**(10): p. 1128-1138.
70. Tang, H., et al., *Pathogenic role of mTORC1 and mTORC2 in pulmonary hypertension.* JACC: Basic to Translational Science, 2018. **3**(6): p. 744-762.
71. Stenmark, K.R., et al., *The adventitia: essential role in pulmonary vascular remodeling.* Comprehensive Physiology, 2010. **1**(1): p. 141-161.
72. Dorfmüller, P., F. Perros, K. Balabanian, and M. Humbert, *Inflammation in pulmonary arterial hypertension.* Eur Respir J, 2003. **22**(2): p. 358-363.
73. Perros, F., et al., *Pulmonary lymphoid neogenesis in idiopathic pulmonary arterial hypertension.* Am J Respir Crit Care Med, 2012. **185**(3): p. 311-321.

74. Soon, E., et al., *Elevated levels of inflammatory cytokines predict survival in idiopathic and familial pulmonary arterial hypertension.* Circulation, 2010. **122**(9): p. 920-7.
75. Tian, W., et al., *Blocking macrophage leukotriene b4 prevents endothelial injury and reverses pulmonary hypertension.* Sci Transl Med, 2013. **5**(200): p. 200ra117-200ra117.
76. Steiner, M.K., et al., *Interleukin-6 overexpression induces pulmonary hypertension.* Circ Res, 2009. **104**(2): p. 236-244.
77. Savale, L., et al., *Impact of interleukin-6 on hypoxia-induced pulmonary hypertension and lung inflammation in mice.* Respir Res, 2009. **10**(1): p. 6.
78. Hagen, M., et al., *Interaction of interleukin-6 and the BMP pathway in pulmonary smooth muscle.* American Journal of Physiology-Lung Cellular and Molecular Physiology, 2007. **292**(6): p. L1473-L1479.
79. Morrell, N.W., et al., *Targeting BMP signalling in cardiovascular disease and anaemia.* Nat Rev Cardiol, 2016. **13**(2): p. 106-20.
80. Lowery, J.W. and M.P. de Caestecker, *BMP signaling in vascular development and disease.* Cytokine Growth Factor Rev, 2010. **21**(4): p. 287-298.
81. Cai, J., E. Pardali, G. Sánchez-Duffhues, and P. ten Dijke, *BMP signaling in vascular diseases.* FEBS Lett, 2012. **586**(14): p. 1993-2002.
82. Shi, Y. and J. Massagué, *Mechanisms of TGF-β signaling from cell membrane to the nucleus.* Cell, 2003. **113**(6): p. 685-700.
83. Austin, E.D., et al., *Alterations in oestrogen metabolism: implications for higher penetrance of familial pulmonary arterial hypertension in females.* Eur Respir J, 2009. **34**(5): p. 1093-1099.
84. Federici, C., et al., *Increased mutagen sensitivity and DNA damage in pulmonary arterial hypertension.* Am J Respir Crit Care Med, 2015. **192**(2): p. 219-228.
85. Drake, K.M., et al., *Correction of nonsense BMPR2 and SMAD9 mutations by ataluren in pulmonary arterial hypertension.* Am J Respir Cell Mol Biol, 2013. **49**(3): p. 403-409.
86. Copeland, C.A., et al., *A disease-associated frameshift mutation in caveolin-1 disrupts caveolae formation and function through introduction of a de novo ER retention signal.* Mol Biol Cell, 2017. **28**(22): p. 3095-3111.
87. Marsboom, G., et al., *Aberrant caveolin-1–mediated Smad signaling and proliferation identified by analysis of adenine 474 deletion mutation (c. 474delA) in patient fibroblasts: a new perspective on the mechanism of pulmonary hypertension.* Mol Biol Cell, 2017. **28**(9): p. 1177-1185.
88. Achcar, R.O., et al., *Loss of caveolin and heme oxygenase expression in severe pulmonary hypertension.* Chest, 2006. **129**(3): p. 696-705.

89. Wertz, J.W. and P.M. Bauer, *Caveolin-1 regulates BMPRII localization and signaling in vascular smooth muscle cells.* Biochem Biophys Res Commun, 2008. **375**(4): p. 557-561.
90. Zhao, Y.-Y., et al., *Defects in caveolin-1 cause dilated cardiomyopathy and pulmonary hypertension in knockout mice.* Proc Natl Acad Sci U S A, 2002. **99**(17): p. 11375-11380.
91. Yuan, X.-J., et al., *Attenuated K+ channel gene transcription in primary pulmonary hypertension.* Lancet (British edition), 1998. **351**(9104): p. 726-727.
92. Bohnen, M.S., et al., *The Impact of Heterozygous KCNK 3 Mutations Associated With Pulmonary Arterial Hypertension on Channel Function and Pharmacological Recovery.* Journal of the American Heart Association, 2017. **6**(9): p. e006465.
93. Eyries, M., et al., *EIF2AK4 mutations cause pulmonary veno-occlusive disease, a recessive form of pulmonary hypertension.* Nat Genet, 2014. **46**(1): p. 65-69.
94. Dever, T.E., et al., *Phosphorylation of initiation factor 2α by protein kinase GCN2 mediates gene-specific translational control of GCN4 in yeast.* Cell, 1992. **68**(3): p. 585-596.
95. Hadinnapola, C., et al., *Phenotypic characterization of EIF2AK4 mutation carriers in a large cohort of patients diagnosed clinically with pulmonary arterial hypertension.* Circulation, 2017. **136**(21): p. 2022-2033.
96. Zhu, N., et al., *Rare variants in SOX17 are associated with pulmonary arterial hypertension with congenital heart disease.* Genome Med, 2018. **10**(1): p. 1-11.
97. Schuoler, C., et al., *Aquaporin 1 controls the functional phenotype of pulmonary smooth muscle cells in hypoxia-induced pulmonary hypertension.* Basic Res Cardiol, 2017. **112**(3): p. 30.
98. Saadoun, S., M.C. Papadopoulos, M. Hara-Chikuma, and A. Verkman, *Impairment of angiogenesis and cell migration by targeted aquaporin-1 gene disruption.* Nature, 2005. **434**(7034): p. 786-792.
99. Yun, X., et al., *Aquaporin 1-mediated changes in pulmonary arterial smooth muscle cell migration and proliferation involve β-catenin.* American Journal of Physiology-Lung Cellular and Molecular Physiology, 2017. **313**(5): p. L889-L898.
100. Rhodes, C.J., et al., *Genetic determinants of risk in pulmonary arterial hypertension: international genome-wide association studies and meta-analysis.* The Lancet Respiratory Medicine, 2019. **7**(3): p. 227-238.
101. Hiraide, T., et al., *SOX17 mutations in Japanese patients with pulmonary arterial hypertension.* Am J Respir Crit Care Med, 2018. **198**(9): p. 1231-1233.
102. Wang, X.-J., et al., *Germline BMP9 mutation causes idiopathic pulmonary arterial hypertension.* Eur Respir J, 2019. **53**(3): p. 1801609.

103. Zhu, N., et al., *Novel risk genes and mechanisms implicated by exome sequencing of 2572 individuals with pulmonary arterial hypertension.* Genome Med, 2019. **11**(1): p. 69.
104. Pegg, A.E., *Functions of polyamines in mammals.* J Biol Chem, 2016. **291**(29): p. 14904-14912.
105. Oredsson, S.M., *Polyamine dependence of normal cell-cycle progression.* Biochem Soc Trans, 2003. **31**(2): p. 366-70.
106. Seiler, N. and F. Raul, *Polyamines and apoptosis.* J Cell Mol Med, 2005. **9**(3): p. 623-42.
107. Liu, B., et al., *ATP13A3 Loss of Function Disrupts Polyamine Homeostasis in Pulmonary Arterial Endothelial Cells.* Circulation, 2019. **140**(Suppl_1): p. A14378-A14378.
108. Liu, B., et al., *S42 Characterizing ATP13A3 loss of function in pulmonary arterial hypertension (PAH)*. 2018, BMJ Publishing Group Ltd.
109. Lerche, M., et al., *Mutually reinforcing effects of genetic variants and interferon-beta 1a therapy for pulmonary arterial hypertension development in multiple sclerosis patients.* Pulm Circ, 2019. **9**(3): p. 2045894019872192.
110. Palmgren, M.G. and P. Nissen, *P-type ATPases.* Annual review of biophysics, 2011. **40**: p. 243-266.
111. Skou, J.C., *The influence of some cations on an adenosine triphosphatase from peripheral nerves.* Biochim Biophys Acta, 1957. **23**: p. 394-401.
112. Post, R., et al., *Flexibility of an active center in sodium-plus-potassium adenosine triphosphatase.* The Journal of general physiology, 1969. **54**(1): p. 306-326.
113. Albers, R., *Biochemical aspects of active transport.* Annu Rev Biochem, 1967. **36**(1): p. 727-756.
114. Laimins, L.A., D.B. Rhoads, K. Altendorf, and W. Epstein, *Identification of the structural proteins of an ATP-driven potassium transport system in Escherichia coli.* Proc Natl Acad Sci U S A, 1978. **75**(7): p. 3216-3219.
115. Nucifora, G., L. Chu, T.K. Misra, and S. Silver, *Cadmium resistance from Staphylococcus aureus plasmid pI258 cadA gene results from a cadmium-efflux ATPase.* Proc Natl Acad Sci U S A, 1989. **86**(10): p. 3544-3548.
116. Rensing, C., B. Mitra, and B.P. Rosen, *Insertional inactivation of dsbA produces sensitivity to cadmium and zinc in Escherichia coli.* J Bacteriol, 1997. **179**(8): p. 2769-2771.
117. Vulpe, C., et al., *Isolation of a candidate gene for Menkes disease and evidence that it encodes a copper–transporting ATPase.* Nat Genet, 1993. **3**(1): p. 7-13.
118. Tanzi, R., et al., *The Wilson disease gene is a copper transporting ATPase with homology to the Menkes disease gene.* Nat Genet, 1993. **5**(4): p. 344-350.

119. Berchtold, M.W., H. Brinkmeier, and M. Muntener, *Calcium ion in skeletal muscle: its crucial role for muscle function, plasticity, and disease.* Physiol Rev, 2000. **80**(3): p. 1215-1265.
120. Grover, A. and I. Khan, *Calcium pump isoforms: diversity, selectivity and plasticity.* Cell Calcium, 1992. **13**(1): p. 9-17.
121. Odermatt, A., et al., *Mutations in the gene–encoding SERCA1, the fast–twitch skeletal muscle sarcoplasmic reticulum Ca 2+ ATPase, are associated with Brody disease.* Nat Genet, 1996. **14**(2): p. 191-194.
122. Wagner, A.J., C. Meyers, L.A. Laimins, and N. Hay, *c-Myc induces the expression and activity of ornithine decarboxylase.* Cell growth & differentiation: the molecular biology journal of the American Association for Cancer Research, 1993. **4**(11): p. 879-883.
123. Martin, V., et al., *Three novel sarco/endoplasmic reticulum Ca2+-ATPase (SERCA) 3 isoforms expression, regulation, and function of the members of the SERCA3 family.* J Biol Chem, 2002. **277**(27): p. 24442-24452.
124. Morth, J.P., et al., *A structural overview of the plasma membrane Na+, K+-ATPase and H+-ATPase ion pumps.* Nature reviews Molecular cell biology, 2011. **12**(1): p. 60-70.
125. Sen, A.K. and R. Post, *Stoichiometry and localization of adenosine triphosphate-dependent sodium and potassium transport in the erythrocyte.* J Biol Chem, 1964. **239**(1): p. 345-352.
126. Jorgensen, P.L., K.O. Håkansson, and S.J. Karlish, *Structure and mechanism of Na, K-ATPase: functional sites and their interactions.* Annu Rev Physiol, 2003. **65**(1): p. 817-849.
127. Pardo, J.M. and R. Serrano, *Structure of a plasma membrane H+-ATPase gene from the plant Arabidopsis thaliana.* J Biol Chem, 1989. **264**(15): p. 8557-8562.
128. Snavely, M., C. Miller, and M. Maguire, *The mgtB Mg2+ transport locus of Salmonella typhimurium encodes a P-type ATPase.* J Biol Chem, 1991. **266**(2): p. 815-823.
129. Axelsen, K.B. and M.G. Palmgren, *Evolution of substrate specificities in the P-type ATPase superfamily.* J Mol Evol, 1998. **46**(1): p. 84-101.
130. Pomorski, T., et al., *Drs2p-related P-type ATPases Dnf1p and Dnf2p are required for phospholipid translocation across the yeast plasma membrane and serve a role in endocytosis.* Mol Biol Cell, 2003. **14**(3): p. 1240-1254.
131. Strautnieks, S.S., et al., *A gene encoding a liver-specific ABC transporter is mutated in progressive familial intrahepatic cholestasis.* Nat Genet, 1998. **20**(3): p. 233-238.
132. Lopez-Marques, R.L., L. Theorin, M.G. Palmgren, and T.G. Pomorski, *P4-ATPases: lipid flippases in cell membranes.* Pflügers Archiv-European Journal of Physiology, 2014. **466**(7): p. 1227-1240.

133. Møller, A.B., T. Asp, P.B. Holm, and M.G. Palmgren, *Phylogenetic analysis of P5 P-type ATPases, a eukaryotic lineage of secretory pathway pumps.* Mol Phylogenet Evol, 2008. **46**(2): p. 619-634.
134. Sorensen, D.M., M.J. Buch-Pedersen, and M.G. Palmgren, *Structural divergence between the two subgroups of P5 ATPases.* Biochim Biophys Acta, 2010. **1797**(6-7): p. 846-55.
135. Rosenzweig, A.C. and J.M. Argüello, *Toward a molecular understanding of metal transport by P1B-Type ATPases*, in *Current topics in membranes*. 2012, Elsevier. p. 113-136.
136. Holemans, T., et al., *A lipid switch unlocks Parkinson's disease-associated ATP13A2.* Proc Natl Acad Sci U S A, 2015. **112**(29): p. 9040-9045.
137. Vashist, S., C.G. Frank, C.A. Jakob, and D.T. Ng, *Two distinctly localized p-type ATPases collaborate to maintain organelle homeostasis required for glycoprotein processing and quality control.* Mol Biol Cell, 2002. **13**(11): p. 3955-3966.
138. Façanha, A.L.O., et al., *The endoplasmic reticulum cation P-type ATPase Cta4p is required for control of cell shape and microtubule dynamics.* The Journal of cell biology, 2002. **157**(6): p. 1029-1040.
139. Heinick, A., et al., *Caenorhabditis elegans P5B-type ATPase CATP-5 operates in polyamine transport and is crucial for norspermidine-mediated suppression of RNA interference.* The FASEB Journal, 2010. **24**(1): p. 206-217.
140. Gitler, A.D., et al., *α-Synuclein is part of a diverse and highly conserved interaction network that includes PARK9 and manganese toxicity.* Nat Genet, 2009. **41**(3): p. 308-315.
141. Sørensen, D.M., et al., *Parkinson disease related ATP13A2 evolved early in animal evolution.* PLoS One, 2018. **13**(3).
142. Sørensen, D.M., et al., *Towards defining the substrate of orphan P5A-ATPases.* Biochimica et Biophysica Acta (BBA)-General Subjects, 2015. **1850**(3): p. 524-535.
143. Sørensen, D.M., et al., *Ca2+ induces spontaneous dephosphorylation of a novel P5A-type ATPase.* J Biol Chem, 2012. **287**(34): p. 28336-28348.
144. Park, J.-S., et al., *Parkinson's disease-associated human ATP13A2 (PARK9) deficiency causes zinc dyshomeostasis and mitochondrial dysfunction.* Hum Mol Genet, 2014. **23**(11): p. 2802-2815.
145. Tan, J., et al., *Regulation of intracellular manganese homeostasis by Kufor-Rakeb syndrome-associated ATP13A2 protein.* J Biol Chem, 2011. **286**(34): p. 29654-29662.
146. Schmidt, K., D.M. Wolfe, B. Stiller, and D.A. Pearce, *Cd2+, Mn2+, Ni2+ and Se2+ toxicity to Saccharomyces cerevisiae lacking YPK9p the orthologue of human ATP13A2.* Biochem Biophys Res Commun, 2009. **383**(2): p. 198-202.

147. Madan, M., et al., *ATP13A3 and caveolin-1 as potential biomarkers for difluoromethylornithine-based therapies in pancreatic cancers.* Am J Cancer Res, 2016. **6**(6): p. 1231.
148. van Veen, S., et al., *ATP13A2 deficiency disrupts lysosomal polyamine export.* Nature, 2020. **578**(7795): p. 419-424.
149. Ramirez, A., et al., *Hereditary parkinsonism with dementia is caused by mutations in ATP13A2, encoding a lysosomal type 5 P-type ATPase.* Nat Genet, 2006. **38**(10): p. 1184-1191.
150. Di Fonzo, A., et al., *ATP13A2 missense mutations in juvenile parkinsonism and young onset Parkinson disease.* Neurology, 2007. **68**(19): p. 1557-1562.
151. Kwasnicka-Crawford, D.A., et al., *Characterization of a novel cation transporter ATPase gene (ATP13A4) interrupted by 3q25–q29 inversion in an individual with language delay.* Genomics, 2005. **86**(2): p. 182-194.
152. Worthey, E.A., et al., *Whole-exome sequencing supports genetic heterogeneity in childhood apraxia of speech.* J Neurodev Disord, 2013. **5**(1): p. 1-16.
153. Vallipuram, J., J. Grenville, and D.A. Crawford, *The E646D-ATP13A4 mutation associated with autism reveals a defect in calcium regulation.* Cell Mol Neurobiol, 2010. **30**(2): p. 233-246.
154. Raredon, M.S.B., et al., *Single-cell connectomic analysis of adult mammalian lungs.* Science Advances, 2019. **5**(12): p. eaaw3851.
155. Schultheis, P.J., et al., *Characterization of the P5 subfamily of P-type transport ATPases in mice.* Biochem Biophys Res Commun, 2004. **323**(3): p. 731-738.
156. Weingarten, L.S., H. Dave, H. Li, and D.A. Crawford, *Developmental expression of P 5 ATPase mRNA in the mouse.* Cell Mol Biol Lett, 2012. **17**(1): p. 153-170.
157. Schaum, N., et al., *Single-cell transcriptomics of 20 mouse organs creates a Tabula Muris: The Tabula Muris Consortium.* Nature, 2018. **562**(7727): p. 367.
158. Park, C.Y., et al., *Tissue-aware data integration approach for the inference of pathway interactions in metazoan organisms.* Bioinformatics, 2015. **31**(7): p. 1093-1101.
159. Kallio, P.J., et al., *Activation of hypoxia-inducible factor 1α: posttranscriptional regulation and conformational change by recruitment of the Arnt transcription factor.* Proc Natl Acad Sci U S A, 1997. **94**(11): p. 5667-5672.
160. Sutter, C.H., E. Laughner, and G.L. Semenza, *Hypoxia-inducible factor 1α protein expression is controlled by oxygen-regulated ubiquitination that is disrupted by deletions and missense mutations.* Proc Natl Acad Sci U S A, 2000. **97**(9): p. 4748-4753.
161. Semenza, G.L., *HIF-1 and human disease: one highly involved factor.* Genes Dev, 2000. **14**(16): p. 1983-1991.

162. Xu, Q., et al., *Hypoxia regulation of ATP13A2 (PARK9) gene transcription.* J Neurochem, 2012. **122**(2): p. 251-259.
163. Rajagopalan, S., A. Rane, S.J. Chinta, and J.K. Andersen, *Regulation of ATP13A2 via PHD2-HIF1α signaling is critical for cellular iron homeostasis: implications for Parkinson's disease.* J Neurosci, 2016. **36**(4): p. 1086-1095.
164. Habtemichael, N. and G. Kovacs, *Cloning the AFURS1 gene which is up-regulated in senescent human parenchymal kidney cells.* Gene, 2002. **283**(1-2): p. 271-275.
165. Davies, R.J., et al., *BMP type II receptor deficiency confers resistance to growth inhibition by TGF-β in pulmonary artery smooth muscle cells: role of proinflammatory cytokines.* American Journal of Physiology-Lung Cellular and Molecular Physiology, 2012. **302**(6): p. L604-L615.
166. Ong, C.-A.J., et al., *A three gene immunohistochemical panel serves as an adjunct to clinical staging of patients with head and neck cancer.* Oncotarget, 2017. **8**(45): p. 79556.
167. Leeuwenhoek, A.v., *1678: Observationes D.* Anthonii Lewenhoeck, de, 1678.
168. Williams-Ashman, H.G. and Z.N. Canellakis, *Polyamines in mammalian biology and medicine.* Perspect Biol Med, 1979. **22**(3): p. 421-453.
169. Shah, P. and E. Swiatlo, *A multifaceted role for polyamines in bacterial pathogens.* Mol Microbiol, 2008. **68**(1): p. 4-16.
170. Pegg, A.E., *Toxicity of polyamines and their metabolic products.* Chem Res Toxicol, 2013. **26**(12): p. 1782-1800.
171. Casero, R.A., T.M. Stewart, and A.E. Pegg, *Polyamine metabolism and cancer: treatments, challenges and opportunities.* Nature Reviews Cancer, 2018. **18**(11): p. 681-695.
172. Pegg, A.E., *Regulation of ornithine decarboxylase.* J Biol Chem, 2006. **281**(21): p. 14529-14532.
173. Kumar, A.P., et al., *Regulation of rat ornithine decarboxylase promoter activity by binding of transcription factor Sp1.* J Biol Chem, 1995. **270**(9): p. 4341-4348.
174. Qin, C., I. Samudio, S. Ngwenya, and S. Safe, *Estrogen-dependent regulation of ornithine decarboxylase in breast cancer cells through activation of nongenomic cAMP-dependent pathways.* Molecular Carcinogenesis: Published in cooperation with the University of Texas MD Anderson Cancer Center, 2004. **40**(3): p. 160-170.
175. Zhao, B. and A.P. Butler, *Core promoter involvement in the induction of rat ornithine decarboxylase by phorbol esters.* Molecular Carcinogenesis: Published in cooperation with the University of Texas MD Anderson Cancer Center, 2001. **32**(2): p. 92-99.
176. Shantz, L.M., R.-H. Hu, and A.E. Pegg, *Regulation of ornithine decarboxylase in a transformed cell line that overexpresses translation initiation factor eIF-4E.* Cancer Res, 1996. **56**(14): p. 3265-3269.

177. Pyronnet, S., L. Pradayrol, and N. Sonenberg, *Alternative splicing facilitates internal ribosome entry on the ornithine decarboxylase mRNA.* Cellular and Molecular Life Sciences CMLS, 2005. **62**(11): p. 1267-1274.
178. Tabor, C.W. and H. Tabor, *Polyamines.* Annu Rev Biochem, 1984. **53**(1): p. 749-790.
179. Coffino, P., *Regulation of cellular polyamines by antizyme.* Nature reviews Molecular cell biology, 2001. **2**(3): p. 188-194.
180. Hoffman, D.W., D. Carroll, N. Martinez, and M.L. Hackert, *Solution structure of a conserved domain of antizyme: a protein regulator of polyamines.* Biochemistry, 2005. **44**(35): p. 11777-11785.
181. Zhang, M., C.M. Pickart, and P. Coffino, *Determinants of proteasome recognition of ornithine decarboxylase, a ubiquitin-independent substrate.* The EMBO journal, 2003. **22**(7): p. 1488-1496.
182. Gandre, S., Z. Bercovich, and C. Kahana, *Ornithine decarboxylase-antizyme is rapidly degraded through a mechanism that requires functional ubiquitin-dependent proteolytic activity.* Eur J Biochem, 2002. **269**(4): p. 1316-1322.
183. Hayashi, S.-i. and Y. Murakami, *Rapid and regulated degradation of ornithine decarboxylase.* Biochem J, 1995. **306**(Pt 1): p. 1.
184. Palanimurugan, R., H. Scheel, K. Hofmann, and R. Jürgen Dohmen, *Polyamines regulate their synthesis by inducing expression and blocking degradation of ODC antizyme.* The EMBO journal, 2004. **23**(24): p. 4857-4867.
185. Nilsson, J., et al., *Polyamines regulate both transcription and translation of the gene encoding ornithine decarboxylase antizyme in mouse.* Eur J Biochem, 1997. **250**(2): p. 223-231.
186. Fujita, K., Y. Murakami, and S.-i. Hayashi, *A macromolecular inhibitor of the antizyme to ornithine decarboxylase.* Biochem J, 1982. **204**(3): p. 647-652.
187. Murakami, Y., T. Ichiba, S. Matsufuji, and S.-i. Hayashi, *Cloning of antizyme inhibitor, a highly homologous protein to ornithine decarboxylase.* J Biol Chem, 1996. **271**(7): p. 3340-3342.
188. Nilsson, J., B. GRAHN, and O. HEBY, *Antizyme inhibitor is rapidly induced in growth-stimulated mouse fibroblasts and releases ornithine decarboxylase from antizyme suppression.* Biochem J, 2000. **346**(3): p. 699-704.
189. Ivanov, I.P., G. Loughran, and J.F. Atkins, *uORFs with unusual translational start codons autoregulate expression of eukaryotic ornithine decarboxylase homologs.* Proc Natl Acad Sci U S A, 2008. **105**(29): p. 10079-10084.
190. Poulin, R., R.A. Casero, and D. Soulet, *Recent advances in the molecular biology of metazoan polyamine transport.* Amino Acids, 2012. **42**(2-3): p. 711-723.

191. Miller-Fleming, L., V. Olin-Sandoval, K. Campbell, and M. Ralser, *Remaining mysteries of molecular biology: the role of polyamines in the cell.* J Mol Biol, 2015. **427**(21): p. 3389-3406.
192. Nicolet, T.G., et al., *Characterization of putrescine-and spermidine-transport systems of a rat pancreatic acinar tumoral cell line (AR4-2J).* Biochem J, 1990. **269**(3): p. 629-632.
193. Poulin, R., G. Pelletier, and A. Pegg, *Induction of apoptosis by excessive polyamine accumulation in ornithine decarboxylase-overproducing L1210 cells.* Biochem J, 1995. **311**(3): p. 723-727.
194. Osborne, D.L. and E.R. Seidel, *Gastrointestinal luminal polyamines: cellular accumulation and enterohepatic circulation.* American Journal of Physiology-Gastrointestinal and Liver Physiology, 1990. **258**(4): p. G576-G584.
195. Minchin, R.F. and R.L. Martin, *Extracellular calcium stimulates Na+-dependent putrescine uptake in B16 melanoma cells.* The international journal of biochemistry & cell biology, 1997. **29**(3): p. 447-454.
196. Busch, A.E., et al., *Electrogenic properties and substrate specificity of the polyspecific rat cation transporter rOCT1.* J Biol Chem, 1996. **271**(51): p. 32599-32604.
197. MITCHELL, J.L., J. Rupert, A. Leyser, and G.G. JUDD, *Mammalian cell polyamine homeostasis is altered by the radioprotector WR1065.* Biochem J, 1998. **335**(2): p. 329-334.
198. Poulin, R., R. Wechter, and A. Pegg, *An early enlargement of the putrescine pool is required for growth in L1210 mouse leukemia cells under hypoosmotic stress.* J Biol Chem, 1991. **266**(10): p. 6142-6151.
199. Torossian, K., M. AUDETTE, and R. POULIN, *Substrate protection against inactivation of the mammalian polyamine-transport system by 1-ethyl-3-(3-dimethylaminopropyl) carbodi-imide.* Biochem J, 1996. **319**(1): p. 21-26.
200. Winter, T.N., W.F. Elmquist, and C.A. Fairbanks, *OCT2 and MATE1 provide bidirectional agmatine transport.* Mol Pharm, 2011. **8**(1): p. 133-142.
201. Gründemann, D., C. Hahne, R. Berkels, and E. Schömig, *Agmatine is efficiently transported by non-neuronal monoamine transporters extraneuronal monoamine transporter (EMT) and organic cation transporter 2 (OCT2).* J Pharmacol Exp Ther, 2003. **304**(2): p. 810-817.
202. Uemura, T., et al., *Identification and characterization of a diamine exporter in colon epithelial cells.* J Biol Chem, 2008. **283**(39): p. 26428-26435.
203. Daigle, N.D., et al., *Molecular characterization of a human cation-Cl− cotransporter (SLC12A8A, CCC9A) that promotes polyamine and amino acid transport.* J Cell Physiol, 2009. **220**(3): p. 680-689.

204. Aouida, M., R. Poulin, and D. Ramotar, *The human carnitine transporter SLC22A16 mediates high affinity uptake of the anticancer polyamine analogue bleomycin-A5.* J Biol Chem, 2010. **285**(9): p. 6275-6284.
205. Abdulhussein, A.A. and H.M. Wallace, *Polyamines and membrane transporters.* Amino Acids, 2014. **46**(3): p. 655-660.
206. Hiasa, M., et al., *Identification of a mammalian vesicular polyamine transporter.* Sci Rep, 2014. **4**: p. 6836.
207. Soulet, D., et al., *A fluorescent probe of polyamine transport accumulates into intracellular acidic vesicles via a two-step mechanism.* J Biol Chem, 2004. **279**(47): p. 49355-49366.
208. Belting, M., et al., *Glypican-1 is a vehicle for polyamine uptake in mammalian cells a pivotal role for nitrosothiol-derived nitric oxide.* J Biol Chem, 2003. **278**(47): p. 47181-47189.
209. Uemura, T., D.E. Stringer, K.A. Blohm-Mangone, and E.W. Gerner, *Polyamine transport is mediated by both endocytic and solute carrier transport mechanisms in the gastrointestinal tract.* American Journal of Physiology-Gastrointestinal and Liver Physiology, 2010. **299**(2): p. G517-G522.
210. Drab, M., et al., *Loss of caveolae, vascular dysfunction, and pulmonary defects in caveolin-1 gene-disrupted mice.* Science, 2001. **293**(5539): p. 2449-2452.
211. Lessard, M., C. Zhao, S.M. Singh, and R. Poulin, *Hormonal and feedback regulation of putrescine and spermidine transport in human breast cancer cells.* J Biol Chem, 1995. **270**(4): p. 1685-1694.
212. Blais, Y., et al., *Growth-independent induction of spermidine transport by IL-4 and IL-13 in ZR-75-1 human breast cancer cells.* Int J Cancer, 1996. **67**(4): p. 532-538.
213. Mitchell, J., G. Judd, A. Bareyal-Leyser, and S. Ling, *Feedback repression of polyamine transport is mediated by antizyme in mammalian tissue-culture cells.* Biochem J, 1994. **299**(Pt 1): p. 19.
214. Igarashi, K. and K. Kashiwagi, *Modulation of cellular function by polyamines.* The international journal of biochemistry & cell biology, 2010. **42**(1): p. 39-51.
215. Childs, A., D. Mehta, and E. Gerner, *Polyamine-dependent gene expression.* Cellular and Molecular Life Sciences CMLS, 2003. **60**(7): p. 1394-1406.
216. Wei, G., et al., *Polyamine-mediated regulation of protein acetylation in murine skin and tumors.* Molecular Carcinogenesis: Published in cooperation with the University of Texas MD Anderson Cancer Center, 2007. **46**(8): p. 611-617.
217. Igarashi, K., T. Uemura, and K. Kashiwagi, *Acrolein: An effective biomarker for tissue damage produced from polyamines*, in *Polyamines*. 2018, Springer. p. 459-468.

218. Ouameur, A.A., P. Bourassa, and H.-A. Tajmir-Riahi, *Probing tRNA interaction with biogenic polyamines.* RNA, 2010. **16**(10): p. 1968-1979.
219. Wang, Y., W. Devereux, T.M. Stewart, and R.A. Casero, *Cloning and characterization of human polyamine-modulated factor-1, a transcriptional cofactor that regulates the transcription of the spermidine/spermine N 1-acetyltransferase gene.* J Biol Chem, 1999. **274**(31): p. 22095-22101.
220. Liu, L., et al., *Polyamine-modulated expression of c-myc plays a critical role in stimulation of normal intestinal epithelial cell proliferation.* American Journal of Physiology-Cell Physiology, 2005. **288**(1): p. C89-C99.
221. Meksuriyen, D., et al., *Formation of a Complex Containing ATP, Mg2+, and Spermine STRUCTURAL EVIDENCE AND BIOLOGICAL SIGNIFICANCE.* J Biol Chem, 1998. **273**(47): p. 30939-30944.
222. Bachrach, U., Y.-C. Wang, and A. Tabib, *Polyamines: new cues in cellular signal transduction.* Physiology, 2001. **16**(3): p. 106-109.
223. Igarashi, K., K. Hikami, K. Sugawara, and S. Hirose, *Effect of polyamines on polypeptide synthesis in rat liver cell-free system.* Biochimica et Biophysica Acta (BBA)-Nucleic Acids and Protein Synthesis, 1973. **299**(2): p. 325-330.
224. Kashiwagi, K., et al., *Spermidine biosynthesis in Saccharomyces cerevisiae. Biosynthesis and processing of a proenzyme form of S-adenosylmethionine decarboxylase.* J Biol Chem, 1990. **265**(36): p. 22321-22328.
225. Schmidt, C., et al., *Structure of the hypusinylated eukaryotic translation factor eIF-5A bound to the ribosome.* Nucleic Acids Res, 2016. **44**(4): p. 1944-1951.
226. Casero, R.A. and L.J. Marton, *Targeting polyamine metabolism and function in cancer and other hyperproliferative diseases.* Nature reviews Drug discovery, 2007. **6**(5): p. 373-390.
227. Russell, D. and S.H. Snyder, *Amine synthesis in rapidly growing tissues: ornithine decarboxylase activity in regenerating rat liver, chick embryo, and various tumors.* Proc Natl Acad Sci U S A, 1968. **60**(4): p. 1420.
228. Thomas, T. and T.J. Thomas, *Polyamines in cell growth and cell death: molecular mechanisms and therapeutic applications.* Cell Mol Life Sci, 2001. **58**(2): p. 244-58.
229. Mamont, P.S., et al., *Alpha-methyl ornithine, a potent competitive inhibitor of ornithine decarboxylase, blocks proliferation of rat hepatoma cells in culture.* Proc Natl Acad Sci U S A, 1976. **73**(5): p. 1626-1630.
230. Samal, K., et al., *AMXT-1501, a novel polyamine transport inhibitor, synergizes with DFMO in inhibiting neuroblastoma cell proliferation by targeting both ornithine decarboxylase and polyamine transport.* Int J Cancer, 2013. **133**(6): p. 1323-1333.

231. Bettuzzi, S., et al., *Coordinate changes of polyamine metabolism regulatory proteins during the cell cycle of normal human dermal fibroblasts.* FEBS Lett, 1999. **446**(1): p. 18-22.
232. Heby, O. and L. Persson, *Molecular genetics of polyamine synthesis in eukaryotic cells.* Trends Biochem Sci, 1990. **15**(4): p. 153-158.
233. Fredlund, J.O., M.C. Johansson, E. Dahlberg, and S.M. Oredsson, *Ornithine decarboxylase and S-adenosylmethionine decarboxylase expression during the cell cycle of Chinese hamster ovary cells.* Exp Cell Res, 1995. **216**(1): p. 86-92.
234. Wallace, H.M., A.V. Fraser, and A. Hughes, *A perspective of polyamine metabolism.* Biochem J, 2003. **376**(1): p. 1-14.
235. Kramer, D.L., et al., *Polyamine depletion in human melanoma cells leads to G1 arrest associated with induction of p21WAF1/CIP1/SDI1, changes in the expression of p21-regulated genes, and a senescence-like phenotype.* Cancer Res, 2001. **61**(21): p. 7754-7762.
236. Grassilli, E., et al., *Is polyamine decrease a common feature of apoptosis? Evidence from γ rays-and heat shock-induced cell death.* Biochem Biophys Res Commun, 1995. **216**(2): p. 708-714.
237. Penning, L.C., et al., *Sensitization of tnf-induced apoptosis with polyamine synthesis inhibitors in different human and murine tumour cell lines.* Cytokine, 1998. **10**(6): p. 423-431.
238. Thomas, T., et al., *Effects of epidermal growth factor on MDA-MB-468 breast cancer cells: Alterations in polyamine biosynthesis and the expression of p21/CIP1/WAF1.* J Cell Physiol, 1999. **179**(3): p. 257-266.
239. Flamigni, F., et al., *Polyamine biosynthesis as a target to inhibit apoptosis of non-tumoral cells.* Amino Acids, 2007. **33**(2): p. 197-202.
240. Packham, G. and J.L. Cleveland, *Ornithine decarboxylase is a mediator of c-Myc-induced apoptosis.* Mol Cell Biol, 1994. **14**(9): p. 5741-5747.
241. TOME, E.M., M.S. FISER, M.C. PAYNE, and W.E. GERNER, *Excess putrescine accumulation inhibits the formation of modified eukaryotic initiation factor 5A (eIF-5A) and induces apoptosis.* Biochem J, 1997. **328**(3): p. 847-854.
242. Ambroziak, W., G. Izaguirre, and R. Pietruszko, *Metabolism of retinaldehyde and other aldehydes in soluble extracts of human liver and kidney.* J Biol Chem, 1999. **274**(47): p. 33366-33373.
243. Pledgie, A., et al., *Spermine oxidase SMO (PAOh1), Not N1-acetylpolyamine oxidase PAO, is the primary source of cytotoxic H2O2 in polyamine analogue-treated human breast cancer cell lines.* J Biol Chem, 2005. **280**(48): p. 39843-39851.
244. Wang, J.Y., *Polyamines regulate expression of E-cadherin and play an important role in control of intestinal epithelial barrier function.* Inflammopharmacology, 2005. **13**(1-3): p. 91-101.

245. Guo, X., et al., *Polyamines are necessary for synthesis and stability of occludin protein in intestinal epithelial cells.* Am J Physiol Gastrointest Liver Physiol, 2005. **288**(6): p. G1159-69.
246. Russell, D.H., *Increased polyamine concentrations in the urine of human cancer patients.* Nature new biology, 1971. **233**(39): p. 144-145.
247. Bello-Fernandez, C., G. Packham, and J.L. Cleveland, *The ornithine decarboxylase gene is a transcriptional target of c-Myc.* Proc Natl Acad Sci U S A, 1993. **90**(16): p. 7804-7808.
248. Ozfiliz, P., et al., *Bag-1 promotes cell survival through c-Myc-mediated ODC upregulation that is not preferred under apoptotic stimuli in MCF-7 cells.* Cell Biochem Funct, 2015. **33**(5): p. 293-307.
249. Koomoa, D.-L.T., et al., *DFMO/eflornithine inhibits migration and invasion downstream of MYCN and involves p27Kip1 activity in neuroblastoma.* Int J Oncol, 2013. **42**(4): p. 1219-1228.
250. Gerner, E.W. and F.L. Meyskens, *Polyamines and cancer: old molecules, new understanding.* Nature Reviews Cancer, 2004. **4**(10): p. 781-792.
251. Nakanishi, S. and J.L. Cleveland, *Targeting the polyamine-hypusine circuit for the prevention and treatment of cancer.* Amino Acids, 2016. **48**(10): p. 2353-2362.
252. Zabala-Letona, A., et al., *mTORC1-dependent AMD1 regulation sustains polyamine metabolism in prostate cancer.* Nature, 2017. **547**(7661): p. 109-113.
253. Ignatenko, N.A., et al., *Suppression of polyamine catabolism by activated Ki-ras in human colon cancer cells.* Molecular Carcinogenesis: Published in cooperation with the University of Texas MD Anderson Cancer Center, 2004. **39**(2): p. 91-102.
254. Ou, Y., et al., *Activation of SAT1 engages polyamine metabolism with p53-mediated ferroptotic responses.* Proc Natl Acad Sci U S A, 2016. **113**(44): p. E6806-E6812.
255. Olson, J.W., et al., *Polyamine content in rat lung during development of hypoxia-induced pulmonary hypertension.* Biochem Pharmacol, 1986. **35**(4): p. 714-716.
256. Shiao, R.-T., H.B. Kostenbauder, J.W. Olson, and M.N. Gillespie, *Mechanisms of lung polyamine accumulation in chronic hypoxic pulmonary hypertension.* American Journal of Physiology-Lung Cellular and Molecular Physiology, 1990. **259**(6): p. L351-L358.
257. Babal, P., S.M. Manuel, J.W. Olson, and M.N. Gillespie, *Cellular disposition of transported polyamines in hypoxic rat lung and pulmonary arteries.* American Journal of Physiology-Lung Cellular and Molecular Physiology, 2000. **278**(3): p. L610-L617.
258. Zhao, Y.D., et al., *A biochemical approach to understand the pathogenesis of advanced pulmonary arterial hypertension: metabolomic profiles of arginine, sphingosine-1-phosphate, and heme of human lung.* PLoS One, 2015. **10**(8).

259. Rhodes, C.J., et al., *Plasma metabolomics implicates modified transfer RNAs and altered bioenergetics in the outcomes of pulmonary arterial hypertension.* Circulation, 2017. **135**(5): p. 460-475.
260. Stearman, R.S., et al., *Systems Analysis of the Human Pulmonary Arterial Hypertension Lung Transcriptome.* Am J Respir Cell Mol Biol, 2019. **60**(6): p. 637-649.
261. Cason, A.L., et al., *X-linked spermine synthase gene (SMS) defect: the first polyamine deficiency syndrome.* Eur J Hum Genet, 2003. **11**(12): p. 937-944.
262. Gomes-Trolin, C., I. Nygren, S.-M. Aquilonius, and H. Askmark, *Increased red blood cell polyamines in ALS and Parkinson's disease.* Exp Neurol, 2002. **177**(2): p. 515-520.
263. Roede, J.R., et al., *Serum metabolomics of slow vs. rapid motor progression Parkinson's disease: a pilot study.* PLoS One, 2013. **8**(10).
264. Inoue, K., et al., *Metabolic profiling of Alzheimer's disease brains.* Sci Rep, 2013. **3**(1): p. 1-9.
265. Ormiston, M.L., et al., *Generation and culture of blood outgrowth endothelial cells from human peripheral blood.* JoVE (Journal of Visualized Experiments), 2015(106): p. e53384.
266. Morrell, N.W., et al., *Angiotensin II activates MAPK and stimulates growth of human pulmonary artery smooth muscle via AT1 receptors.* American Journal of Physiology-Lung Cellular and Molecular Physiology, 1999. **277**(3): p. L440-L448.
267. Ades, E.W., et al., *HMEC-1: establishment of an immortalized human microvascular endothelial cell line.* J Invest Dermatol, 1992. **99**(6): p. 683-690.
268. Kutner, R.H., X.-Y. Zhang, and J. Reiser, *Production, concentration and titration of pseudotyped HIV-1-based lentiviral vectors.* Nat Protoc, 2009. **4**(4): p. 495.
269. Barczak, W., W. Suchorska, B. Rubiś, and K. Kulcenty, *Universal real-time PCR-based assay for lentiviral titration.* Mol Biotechnol, 2015. **57**(2): p. 195-200.
270. Maarman, G., et al., *A comprehensive review: the evolution of animal models in pulmonary hypertension research; are we there yet?* Pulmonary circulation, 2013. **3**(4): p. 739-756.
271. Vallier, L., et al., *Activin/Nodal signalling maintains pluripotency by controlling Nanog expression.* Development, 2009. **136**(8): p. 1339-1349.
272. Ran, F.A., et al., *Genome engineering using the CRISPR-Cas9 system.* Nat Protoc, 2013. **8**(11): p. 2281.
273. Kiskin, F.N., et al., *Contributions of BMPR2 mutations and extrinsic factors to cellular phenotypes of pulmonary arterial hypertension revealed by induced pluripotent stem cell modeling.* Am J Respir Crit Care Med, 2018. **198**(2): p. 271-275.

274. Morrell, N.W., et al., *Cellular and molecular basis of pulmonary arterial hypertension.* J Am Coll Cardiol, 2009. **54**(1 Supplement): p. S20-S31.
275. Humbert, M., et al., *Pathology and pathobiology of pulmonary hypertension: state of the art and research perspectives.* Eur Respir J, 2019. **53**(1): p. 1801887.
276. Hong, K.-H., et al., *Genetic ablation of the BMPR2 gene in pulmonary endothelium is sufficient to predispose to pulmonary arterial hypertension.* Circulation, 2008. **118**(7): p. 722.
277. Itokawa, T., et al., *Antiangiogenic Effect by SU5416 Is Partly Attributable to Inhibition of Flt-1 Receptor Signaling 1 Supported by grant-in-aid for Cancer Research from the Ministry of Education, Culture, Sports, Science and Technology, Japan. 1.* Mol Cancer Ther, 2002. **1**(5): p. 295-302.
278. Fong, T.A.T., et al., *SU5416 is a potent and selective inhibitor of the vascular endothelial growth factor receptor (Flk-1/KDR) that inhibits tyrosine kinase catalysis, tumor vascularization, and growth of multiple tumor types.* Cancer Res, 1999. **59**(1): p. 99-106.
279. Stenmark, K.R., et al., *Animal models of pulmonary arterial hypertension: the hope for etiological discovery and pharmacological cure.* American Journal of Physiology-Lung Cellular and Molecular Physiology, 2009. **297**(6): p. L1013-L1032.
280. Kühlbrandt, W., *Biology, structure and mechanism of P-type ATPases.* Nature reviews Molecular cell biology, 2004. **5**(4): p. 282-295.
281. Yamasaki, Y., et al., *Weekly dosing with the platelet-derived growth factor receptor tyrosine kinase inhibitor SU9518 significantly inhibits arterial stenosis.* Circ Res, 2001. **88**(6): p. 630-636.
282. Morrell, N.W., et al., *Altered growth responses of pulmonary artery smooth muscle cells from patients with primary pulmonary hypertension to transforming growth factor-β1 and bone morphogenetic proteins.* Circulation, 2001. **104**(7): p. 790-795.
283. Tajsic, T. and N.W. Morrell, *Cellular and Molecular Mechanisms of Pulmonary Vascular Smooth Muscle Cell Proliferation*, in *Textbook of Pulmonary Vascular Disease*. 2011, Springer. p. 323-334.
284. Voelkel, N.F. and J. Gomez-Arroyo, *The role of vascular endothelial growth factor in pulmonary arterial hypertension. The angiogenesis paradox.* Am J Respir Cell Mol Biol, 2014. **51**(4): p. 474-484.
285. David, L., et al., *Bone morphogenetic protein-9 is a circulating vascular quiescence factor.* Circ Res, 2008. **102**(8): p. 914-922.
286. Suzuki, Y., et al., *BMP-9 induces proliferation of multiple types of endothelial cells in vitro and in vivo.* J Cell Sci, 2010. **123**(10): p. 1684-1692.
287. FRANKLIN, S., R. FERRY, and P. COHEN, *IGFBP-3 Inhibits VEGF-Induced Survival of Endothelial Cells, Independently from the Type 1*

IGF Receptor, through the PI3K/Akt Signal Transduction Pathway. Diabetes, 2001. **50**.

288. Gerber, H.-P., V. Dixit, and N. Ferrara, *Vascular endothelial growth factor induces expression of the antiapoptotic proteins Bcl-2 and A1 in vascular endothelial cells.* J Biol Chem, 1998. **273**(21): p. 13313-13316.
289. Burton, V.J., et al., *Attenuation of leukocyte recruitment via CXCR1/2 inhibition stops the progression of PAH in mice with genetic ablation of endothelial BMPR-II.* Blood, The Journal of the American Society of Hematology, 2011. **118**(17): p. 4750-4758.
290. Huang, J., et al., *Pyrrolidine dithiocarbamate restores endothelial cell membrane integrity and attenuates monocrotaline-induced pulmonary artery hypertension.* American Journal of Physiology-Lung Cellular and Molecular Physiology, 2008. **294**(6): p. L1250-L1259.
291. Good, R.B., et al., *Endothelial to mesenchymal transition contributes to endothelial dysfunction in pulmonary arterial hypertension.* The American journal of pathology, 2015. **185**(7): p. 1850-1858.
292. Marcos-Ramiro, B., D. García-Weber, and J. Millán, *TNF-induced endothelial barrier disruption: beyond actin and Rho.* Thromb Haemost, 2014. **112**(12): p. 1088-1102.
293. Konstantoulaki, M., P. Kouklis, and A.B. Malik, *Protein kinase C modifications of VE-cadherin, p120, and β-catenin contribute to endothelial barrier dysregulation induced by thrombin.* American Journal of Physiology-Lung Cellular and Molecular Physiology, 2003. **285**(2): p. L434-L442.
294. Mehta, D., K. Ravindran, and W.M. Kuebler, *Novel regulators of endothelial barrier function.* American Journal of Physiology-Lung Cellular and Molecular Physiology, 2014. **307**(12): p. L924-L935.
295. Pegg, A.E., *Mammalian polyamine metabolism and function.* IUBMB life, 2009. **61**(9): p. 880-894.
296. Kahana, C., *The antizyme family for regulating polyamines.* J Biol Chem, 2018. **293**(48): p. 18730-18735.
297. Dever, T.E. and I.P. Ivanov, *Roles of polyamines in translation.* J Biol Chem, 2018. **293**(48): p. 18719-18729.
298. Stewart, T.M., T.T. Dunston, P.M. Woster, and R.A. Casero, *Polyamine catabolism and oxidative damage.* J Biol Chem, 2018. **293**(48): p. 18736-18745.
299. Sharma, C., et al., *Antimicrobial resistance: its surveillance, impact, and alternative management strategies in dairy animals.* Frontiers in veterinary science, 2018. **4**: p. 237.
300. Bachmann, A.S. and D. Geerts, *Polyamine synthesis as a target of MYC oncogenes.* J Biol Chem, 2018. **293**(48): p. 18757-18769.
301. Shantz, L.M. and A.E. Pegg, *Translational regulation of ornithine decarboxylase and other enzymes of the polyamine pathway.* The

international journal of biochemistry & cell biology, 1999. **31**(1): p. 107-122.
302. Pyronnet, S., L. Pradayrol, and N. Sonenberg, *A cell cycle–dependent internal ribosome entry site.* Mol Cell, 2000. **5**(4): p. 607-616.
303. Ambroziak, W. and R. Pietruszko, *Human aldehyde dehydrogenase. Activity with aldehyde metabolites of monoamines, diamines, and polyamines.* J Biol Chem, 1991. **266**(20): p. 13011-13018.
304. Igarashi, K. and K. Kashiwagi, *Characteristics of cellular polyamine transport in prokaryotes and eukaryotes.* Plant Physiol Biochem, 2010. **48**(7): p. 506-512.
305. Igarashi, K., K. Ito, and K. Kashiwagi, *Polyamine uptake systems in Escherichia coli.* Res Microbiol, 2001. **152**(3-4): p. 271-278.
306. Park, J.S., et al., *Pathogenic effects of novel mutations in the P-type ATPase ATP13A2 (PARK9) causing Kufor-Rakeb syndrome, a form of early-onset parkinsonism.* Hum Mutat, 2011. **32**(8): p. 956-64.
307. Li, C., et al., *Spermine synthase deficiency causes lysosomal dysfunction and oxidative stress in models of Snyder-Robinson syndrome.* Nat Commun, 2017. **8**(1): p. 1257.
308. Tiberio, L., J.A. Maier, and L. Schiaffonati, *Down-modulation of c-myc expression by phorbol ester protects CEM T leukaemia cells from starvation-induced apoptosis: role of ornithine decarboxylase and polyamines.* Cell Death Differ, 2001. **8**(10): p. 967-76.
309. Tantini, B., et al., *Involvement of polyamines in apoptosis of cardiac myoblasts in a model of simulated ischemia.* J Mol Cell Cardiol, 2006. **40**(6): p. 775-82.
310. Nakamura, C., et al., *Changes in intracellular concentrations of polyamines during apoptosis of HL-60 cells.* Anticancer Res, 2003. **23**(6C): p. 4797-803.
311. Stefanelli, C., et al., *Caspase activation in etoposide-treated fibroblasts is correlated to ERK phosphorylation and both events are blocked by polyamine depletion.* FEBS Lett, 2002. **527**(1-3): p. 223-28.
312. Urist, M., *A morphogeneric matrix for differentiation of bone tissue.* Calcif Tissue Res, 1970. **4**(1): p. 98-101.
313. Paul, B.Y., et al., *Dorsomorphin inhibits BMP signals required for embryogenesis and iron metabolism.* Nat Chem Biol, 2008. **4**(1): p. 33.
314. Grgurevic, L., G.L. Christensen, T.J. Schulz, and S. Vukicevic, *Bone morphogenetic proteins in inflammation, glucose homeostasis and adipose tissue energy metabolism.* Cytokine Growth Factor Rev, 2016. **27**: p. 105-118.
315. Blázquez-Medela, A.M., M. Jumabay, and K.I. Boström, *Beyond the bone: Bone morphogenetic protein signaling in adipose tissue.* Obes Rev, 2019. **20**(5): p. 648-658.

316. Goumans, M.-J., A. Zwijsen, P. Ten Dijke, and S. Bailly, *Bone morphogenetic proteins in vascular homeostasis and disease.* Cold Spring Harb Perspect Biol, 2018. **10**(2): p. a031989.
317. Vukicevic, S. and L. Grgurevic, *BMP-6 and mesenchymal stem cell differentiation.* Cytokine Growth Factor Rev, 2009. **20**(5-6): p. 441-448.
318. Laux, D.W., et al., *Circulating Bmp10 acts through endothelial Alk1 to mediate flow-dependent arterial quiescence.* Development, 2013. **140**(16): p. 3403-3412.
319. Herrera, B. and G.J. Inman, *A rapid and sensitive bioassay for the simultaneous measurement of multiple bone morphogenetic proteins. Identification and quantification of BMP4, BMP6 and BMP9 in bovine and human serum.* BMC Cell Biol, 2009. **10**(1): p. 20.
320. Yadin, D., P. Knaus, and T.D. Mueller, *Structural insights into BMP receptors: Specificity, activation and inhibition.* Cytokine Growth Factor Rev, 2016. **27**: p. 13-34.
321. Mueller, T.D. and J. Nickel, *Promiscuity and specificity in BMP receptor activation.* FEBS Lett, 2012. **586**(14): p. 1846-1859.
322. Upton, P.D., R.J. Davies, R.C. Trembath, and N.W. Morrell, *Bone morphogenetic protein (BMP) and activin type II receptors balance BMP9 signals mediated by activin receptor-like kinase-1 in human pulmonary artery endothelial cells.* J Biol Chem, 2009. **284**(23): p. 15794-15804.
323. Castonguay, R., et al., *Soluble endoglin specifically binds bone morphogenetic proteins 9 and 10 via its orphan domain, inhibits blood vessel formation, and suppresses tumor growth.* J Biol Chem, 2011. **286**(34): p. 30034-30046.
324. Huse, M., Y.-G. Chen, J. Massagué, and J. Kuriyan, *Crystal structure of the cytoplasmic domain of the type I TGF β receptor in complex with FKBP12.* Cell, 1999. **96**(3): p. 425-436.
325. Hill, C.S., *Transcriptional control by the SMADs.* Cold Spring Harb Perspect Biol, 2016. **8**(10): p. a022079.
326. Ross, S. and C.S. Hill, *How the Smads regulate transcription.* The international journal of biochemistry & cell biology, 2008. **40**(3): p. 383-408.
327. Machado, R.D., et al., *Pulmonary arterial hypertension: a current perspective on established and emerging molecular genetic defects.* Hum Mutat, 2015. **36**(12): p. 1113-1127.
328. Machado, R.D., et al., *Mutations of the TGF-β type II receptor BMPR2 in pulmonary arterial hypertension.* Hum Mutat, 2006. **27**(2): p. 121-132.
329. Thomson, J.R., et al., *Sporadic primary pulmonary hypertension is associated with germline mutations of the gene encoding BMPR-II, a receptor member of the TGF-β family.* J Med Genet, 2000. **37**(10): p. 741-745.

330. Ehrlich, M., *Endocytosis and trafficking of BMP receptors: Regulatory mechanisms for fine-tuning the signaling response in different cellular contexts.* Cytokine Growth Factor Rev, 2016. **27**: p. 35-42.
331. Durrington, H.J., et al., *Identification of a lysosomal pathway regulating degradation of the bone morphogenetic protein receptor type II.* J Biol Chem, 2010. **285**(48): p. 37641-37649.
332. Dunmore, B.J., et al., *The lysosomal inhibitor, chloroquine, increases cell surface BMPR-II levels and restores BMP9 signalling in endothelial cells harbouring BMPR-II mutations.* Hum Mol Genet, 2013. **22**(18): p. 3667-3679.
333. Long, L., et al., *Chloroquine prevents progression of experimental pulmonary hypertension via inhibition of autophagy and lysosomal bone morphogenetic protein type II receptor degradation.* Circ Res, 2013. **112**(8): p. 1159-1170.
334. Mitchell, H., A. Choudhury, R.E. Pagano, and E.B. Leof, *Ligand-dependent and-independent transforming growth factor-β receptor recycling regulated by clathrin-mediated endocytosis and Rab11.* Mol Biol Cell, 2004. **15**(9): p. 4166-4178.
335. Voelkel, N., R. Tuder, J. Bridges, and W. Arend, *Interleukin-1 receptor antagonist treatment reduces pulmonary hypertension generated in rats by monocrotaline.* Am J Respir Cell Mol Biol, 1994. **11**(6): p. 664-675.
336. Izikki, M., et al., *Endothelial-derived FGF2 contributes to the progression of pulmonary hypertension in humans and rodents.* The Journal of clinical investigation, 2009. **119**(3): p. 512-523.
337. Endean, E., et al., *Regulation of polyamine synthesis and transport by fibroblast growth factor in aortic smooth muscle cells.* Growth Factors, 1996. **13**(3-4): p. 229-242.
338. Svensson, K.J., et al., *Hypoxia-mediated induction of the polyamine system provides opportunities for tumor growth inhibition by combined targeting of vascular endothelial growth factor and ornithine decarboxylase.* Cancer Res, 2008. **68**(22): p. 9291-9301.
339. Gomez-Arroyo, J.G., et al., *The monocrotaline model of pulmonary hypertension in perspective.* American Journal of Physiology-Lung Cellular and Molecular Physiology, 2012. **302**(4): p. L363-L369.
340. Ranchoux, B., et al., *DNA damage and pulmonary hypertension.* Int J Mol Sci, 2016. **17**(6): p. 990.
341. Aldred, M.A., et al., *Somatic chromosome abnormalities in the lungs of patients with pulmonary arterial hypertension.* Am J Respir Crit Care Med, 2010. **182**(9): p. 1153-1160.
342. Gu, M., *Efficient differentiation of human pluripotent stem cells to endothelial cells.* Current protocols in human genetics, 2018. **98**(1): p. e64.

343. Patsch, C., et al., *Generation of vascular endothelial and smooth muscle cells from human pluripotent stem cells.* Nat Cell Biol, 2015. **17**(8): p. 994-1003.
344. Rana, A.A., F.N. Kiskin, and C.-H. Chang, *Modeling Pulmonary Arterial Hypertension Using Induced Pluripotent Stem Cells*, in *Molecular Mechanism of Congenital Heart Disease and Pulmonary Hypertension*. 2020, Springer. p. 139-145.
345. Gu, M., et al., *Patient-specific iPSC-derived endothelial cells uncover pathways that protect against pulmonary hypertension in BMPR2 mutation carriers.* Cell stem cell, 2017. **20**(4): p. 490-504. e5.
346. Sa, S., et al., *Induced pluripotent stem cell model of pulmonary arterial hypertension reveals novel gene expression and patient specificity.* Am J Respir Crit Care Med, 2017. **195**(7): p. 930-941.
347. Shih, J., et al., *SOX17 Deficiency Impairs Tube Network Formation Through the Reduction of Arterial Identity in Pulmonary Arterial Hypertension*, in *A67 STRUCTURE-FUNCTION RELATIONSHIPS*. 2020, American Thoracic Society. p. A2366-A2366.
348. Larkin, E.K., et al., *Longitudinal analysis casts doubt on the presence of genetic anticipation in heritable pulmonary arterial hypertension.* Am J Respir Crit Care Med, 2012. **186**(9): p. 892-896.
349. Evans, J.D., et al., *BMPR2 mutations and survival in pulmonary arterial hypertension: an individual participant data meta-analysis.* The lancet Respiratory medicine, 2016. **4**(2): p. 129-137.
350. George, P.M., et al., *Evidence for the involvement of type I interferon in pulmonary arterial hypertension.* Circ Res, 2014. **114**(4): p. 677-688.
351. Claudinon, J., et al., *Palmitoylation of interferon-α (IFN-α) receptor subunit IFNAR1 is required for the activation of Stat1 and Stat2 by IFN-α.* J Biol Chem, 2009. **284**(36): p. 24328-24340.
352. Tuder, R.M., et al., *Prostacyclin synthase expression is decreased in lungs from patients with severe pulmonary hypertension.* Am J Respir Crit Care Med, 1999. **159**(6): p. 1925-1932.
353. Mullin, C.J., G.J. Kato, and C.E. Ventetuolo, *Anakinra, What Is Thy Bidding in Pulmonary Hypertension?* 2019, American Thoracic Society.
354. Itoh, A., et al., *Effects of IL-1β, TNF-α, and macrophage migration inhibitory factor on prostacyclin synthesis in rat pulmonary artery smooth muscle cells.* Respirology, 2003. **8**(4): p. 467-472.
355. Bradbury, D.A., et al., *Effect of bradykinin, TGF-β1, IL-1β, and hypoxia on COX-2 expression in pulmonary artery smooth muscle cells.* American Journal of Physiology-Lung Cellular and Molecular Physiology, 2002. **283**(4): p. L717-L725.
356. Wen, F., K. Watanabe, H. Tanaka, and M. Yoshida, *Cytokines and lipopolysaccharide enhance basal and thrombin-stimulated production of PGI2 by cultured human pulmonary artery smooth muscle cells.*

Prostaglandins, leukotrienes and essential fatty acids, 1997. **56**(3): p. 185-192.

357. Galiè, N., et al., *2015 ESC/ERS guidelines for the diagnosis and treatment of pulmonary hypertension: the Joint Task Force for the Diagnosis and Treatment of Pulmonary Hypertension of the European Society of Cardiology (ESC) and the European Respiratory Society (ERS): endorsed by: Association for European Paediatric and Congenital Cardiology (AEPC), International Society for Heart and Lung Transplantation (ISHLT).* Eur Heart J, 2016. **37**(1): p. 67-119.
358. Olson, J.W., A.D. Hacker, R.J. Altiere, and M.N. Gillespie, *Polyamines and the development of monocrotaline-induced pulmonary hypertension.* American Journal of Physiology-Heart and Circulatory Physiology, 1984. **247**(4): p. H682-H685.
359. Abdul-Salam, V.B., et al., *CLIC4/Arf6 pathway: a new lead in BMPRII inhibition in pulmonary hypertension.* Circ Res, 2019. **124**(1): p. 52-65.
360. He, Y.-Y., et al., *Spermine Promotes Pulmonary Vascular Remodelling and Its Synthase is a Therapeutic Target for Pulmonary Arterial Hypertension.* Eur Respir J, 2020.

Appendix

Materials and buffer recipes

Mouse Genomic DNA extraction reagents:

Digestion buffer recipe:50mM Tris-HCl, pH 8.0; 5mM EDTA, pH 8.0; 100mM NaCl; 1% sodium dodecyl sulfate (SDS)

RNA extraction from cells/tissues material

Cell RNA extraction

Silica membrane column: EconoSpin® All-In-One Mini Spin Columns for DNA/RNA extraction

Buffer recipe:

Cell lysis buffer: RLT buffer (Qiagen) 1:100 diluted with β-Mercaptoethanol.

RNase-Free DNase solution (Qiagen): One vial of RNase-Free DNase dissolved in 550µl of nuclease-free water**.**

Tissue RNA extraction

TissueLyser II (Qiagen), Stainless steel beads (Qiagen)

5PRIME Phase Lock Gel tubes (Quantabio)

Tissue lysis buffer: QIAzol Lysis Reagent (Qiagen)

Immunoblotting

Materials:

EDTA-free protease inhibitor cocktail (Roche): Two tablets per 1 ml dH2O. Aliquoted 50µl/tube and stored at -20ºC.

Lysis Buffer recipe:

SDS Lysis buffer: 125mM Tris HCl pH 7.4, 2% SDS, 10% glycerol. Aliquoted 950µl/tube and store at -20°C. One aliquot (50µl) EDTA-free protease inhibitor cocktail was added into one aliquot (950µl) SDS Lysis buffer before used.

Radioimmunoprecipitation buffer (RIPA buffer): 50mM Tris HCl pH7.4, 0.5% Sodium deoxycholate, 150mM NaCl, 0.1%SDS, 1% IGEPAL CA-630. Aliquoted 950µl/tube and store at -20°C. One aliquot (50µl) EDTA-free protease inhibitor cocktail was added into one aliquot (950 µl) RIPA Lysis buffer before used.

Buffer recipe for Western blotting:

5x Sample loading buffer: 312.5mM Tris.HCl pH6.8, 10%SDS, 50%Glycerol, 0.0075%(w/v) bromophenol blue, 25%(v/v) β-Mercaptoethanol

Tris(tris(hydroxymethyl)aminomethane) buffered saline, Tween20 (TBS-T):

10mM Tris.HCl, 150mM NaCl; pH7.4, 0.05% Tween 20

Protein Electrophoresis buffer:

25mM Tris, 192mM Glycine, 0.01%SDS

Protein transfer buffer:

25mM Tris, 192mM Glycine, 0.01% SDS, 20%Methanol

Immunocytochemistry

Materials:

Slides: 4-chambered Nunc™ Lab-Tek™ II Chamber Slides™ (Thermo Fisher Scientific)

Slide coating buffer: Type I Rat Tail Collagen (BD biosciences) 1:100 (v/v) in 0.02N acetic acid

Buffer recipe:

Fixation

4% Paraformaldehyde solution:

39% Formaldehyde solution (Sigma) 1:10 diluted with PBS buffer.

Permeabilisation

0.05% Saponin solution:

0.05% (w/v) Saponin (Sigma) in 0.5% (w/v) BSA (sigma) in PBS buffer.

Blocking: 0.5-3% (w/v) BSA (sigma) in PBS buffer.

Human induced pluripotent stem cell (iPSCs)

Cell culture media recipes

Chemically defined medium (CDM):

Ham's F-12 Nutrient Mixture (49.5%v/v, Thermo Fisher Scientific)

Iscove's Modified Dulbecco's Medium (IMDM) (49.5%v/v, Thermo Fisher Scientific)

Chemically defined lipid concentrates (1%v/v, Thermo Fisher Scientific)

Transferrin from human serum (15µg/ml, Roche)

Recombinant human insulin (7µg/ml, Roche)

1-thioglycerol (450 µM, Sigma)

Knockout Serum Replacement (KSR) medium:

Advanced DMEM/F12 (79.5%v/v, Thermo Fisher Scientific)

Knockout Serum Replacement (19.5% v/v, Thermo Fisher Scientific)

MEM Non-Essential Amino Acids Solution (1%v/v, Thermo Fisher Scientific)

L-glutamine (2mM, Thermo Fisher Scientific)

FGF2(10ng/ml)

CDM-BSA: CDM media supplemented with 5mg/ml bovine serum albumin (BSA, Sigma).

CDM-PVA: CDM media supplemented with 1.2mg/ml polyvinyl alcohol(sigma)

Feeder-dependent iPSC culture medium (25% media):

CDM-BSA (25% v/v), KSR (50% v/v), Conditioned media from iMEFs cultured in CDM-BSA supplemented with 4ng/ml FGF-2 for 24 hours (25% v/v), Activin A(12.5ng/ml), FGF-2(15ng/ml), L-ascorbic acid(50ng/ml)

Feeder-free iPSC culture medium (CDM-BSA/KSR, BK):

CDM-BSA (50% v/v), KSR (50% v/v), Activin A(12.5ng/ml), FGF-2(15ng/ml), L-ascorbic acid (50ng/ml, Sigma)

iPSC-ECs differentiation basal media(E^+):

EGM2-MV2 serum-free media (Promocell) supplemented with Chemically defined lipid concentrate (1%v/v, Thermo Fisher Scientific), vitamin C (2.5ul/ml,

Sigma), Transferrin from human serum (15µg/ml, Roche) and Recombinant human insulin(7µg/ml, Roche)

iPSC-ECs full growth media (E^+ FGM):

E^+ media supplemented with 2% FBS(Lonza), 5ng/ml FGF2, 20ng/ml human $VEGFA_{165}$, 10uM SB 431542 and 5uM DAPT.